Prestressed Cold-formed Steel Beams

by

Nicolaos Hadjipantelis

A thesis submitted to Imperial College London

for the degree of Doctor of Philosophy

Department of Civil and Environmental Engineering

Imperial College London

London SW7 2AZ

February 2019

Declaration of Originality

This thesis presents a record of my own original research and any material from others is acknowledged by appropriately referencing the published or unpublished sources. This research has been carried out in the Department of Civil & Environmental Engineering at Imperial College London under the supervision of Professor Leroy Gardner and Professor Ahmer Wadee. This thesis is submitted to Imperial College London for the degree of Doctor of Philosophy and has not been submitted for a degree or any other qualification at another university.

<div style="text-align: right">

Nicolaos Hadjipantelis

February 2019

</div>

Copyright Declaration

Abstract

A novel concept, whereby prestressing techniques are utilised to enhance the load-carrying capacity and serviceability performance of cold-formed steel beams, is proposed. The prestressing is applied by means of a high-strength steel cable located within the bottom hollow flange of the cold-formed steel beam at an eccentric location with respect to its strong geometric axis. Since the initial stresses generated by the prestressing are opposite in sign to those induced during the subsequent imposed vertical loading stage, the development of instabilities is delayed and thus the capacity of the cold-formed steel beam is enhanced. Owing to the pre-camber that is induced along the member during the prestressing stage and the contribution of the cable to the system bending stiffness, the overall vertical deflections of the member are reduced significantly.

Prestressed cold-formed steel beams can provide highly-efficient structural solutions. Owing to their enhanced structural performance, for a given span and imposed vertical load, a smaller cross-section is required and thus a more lightweight solution is achievable. Potentially, the proposed beams can open up new applications for cold-formed steel in construction, particularly in cases where increased load-carrying capacities, longer spans and reduced deflections are desired.

The current thesis presents the conceptual development of prestressed cold-formed steel beams. The mechanical behaviour of the proposed structural system is explored using analytical and numerical models with the origin of the obtained structural benefits being demonstrated. Finite element modelling is employed to simulate the behaviour of the proposed beams during the prestressing and imposed vertical loading stages and parametric studies are conducted to investigate the influence of the key controlling parameters, such as the prestress level, cable size, section slenderness and centroid location. Finally, design recommendations and failure criteria, which define the permissible design zone for the prestressed system, are developed with their implementation being demonstrated through practical a worked example.

To Agathi and Pantelis

Acknowledgements

I would like to express my deepest gratitude to Professor Leroy Gardner and Professor Ahmer Wadee, who I was incredibly lucky to have as supervisors. Their doors were always open for me and they have always been willing to provide me with their guidance and expert knowledge. Thank you both for trusting me with the PhD position in the first place and I am looking forward to continue collaborating with you. I would also like to acknowledge the President's PhD Scholarship scheme from Imperial College London for its financial support.

My PhD thesis is dedicated to my parents, Agathi and Pantelis, as a mean of expressing my gratefulness for the love and support they offered me all these years. It makes me incredibly happy that, by successfully finishing my PhD, I can make them proud. Mum, thank you for all the positive energy that you have transmitted to me over the last seven years. Your support and advice have been instrumental in having a nice experience during my undergraduate and PhD studies. Dad, thank you for always believing in me. You never had a doubt that I would do great and this provided me with the strength to work hard and with the confidence to face all the difficulties with persistence.

This PhD thesis is also dedicated to my love, Marina. Because this marathon would simply not have been such a positive experience without her. Marina provided the perfect balance in my day-to-day life. From the moment I would see her after going home, I would just forget anything related to my research – most of the times at least. And even when things were bad, she was always willing to hear about my models that have not been running. My sweetheart, thank you for supporting me in the most challenging period of my life, so far. But, most importantly, thank you for all the beautiful moments that we have had together over the last years; from the everyday endless laughter to the several-week long trips.

My Giagia, my sisters, Kyriaki, Andria and Christiana, and my brothers-in-law, Paul and

Contents

List of Figures

17

List of Tables

Nomenclature

α_{th} Coefficient of thermal expansion of the cable

β Reliability index

β_0 Target reliability index

ΔP Incremental increase in the prestressing force

ΔP^{D} Increase in the prestressing force due to dead loading

ΔP^{L} Increase in the prestressing force due to live loading

ΔT Temperature difference

$\delta_{\text{mid,y}}$ Vertical deflection of the bare cold-formed steel beam at the point of first yield

δ_{mid} Vertical deflection at midspan

δ_{mid}^{II} Overall vertical deflection at midspan at the end of Stage II

δ_{mid}^{I} Vertical deflection at midspan at the end of Stage I

δ_{perm} Vertical deflection due to permanent loads

δ_{serv} Vertical deflection due to service loads

ϵ Engineering strain

$\epsilon_{\text{ln}}^{\text{pl}}$ Logarithmic plastic strain

$\epsilon_{\text{t0.2}}$ Total strain at 0.2% proof stress

$\epsilon_{\text{t1.0}}$ Total strain at 1.0% proof stress

γ_{i} Load factors

λ Member slenderness

λ_{d} Distortional slenderness for columns or beams

λ_{l} Local slenderness for columns or beams

$\bar{\sigma}$ Overall compressive stress level due to combined axial loading and bending

$\overline{\sigma}_\mathrm{a}$ Compressive stress level due to axial compression

$\overline{\sigma}_\mathrm{b}$ Compressive stress level due to bending

$\overline{M}$ Applied bending moment based on factored loads

$\overline{M}_\mathrm{x}$ Applied bending moment based on factored loads about the major centroidal axis

$\overline{M}_\mathrm{y}$ Applied bending moment based on factored loads about the minor centroidal axis

$\overline{P}$ Applied axial compressive force based on factored loads

ϕ Resistance factor

ϕ_b Resistance factor for bending resistance

ϕ_c Resistance factor for axial compressive resistance

ϕ_t Resistance factor for tensile resistance

σ Engineering stress

σ Standard deviation

$\sigma_\mathrm{b,av}$ Average membrane axial stress level across the width of the bottom flange of the cold-formed steel beam

$\sigma_\mathrm{b,p}$ Net axial stress level within the bottom flange of the cross-section at the end of Stage I

σ_b Net axial stress level within the bottom flange of the cross-section at the end of Stage II

$\sigma_\mathrm{c,p}$ Additional tensile stress induced in the cable in Stage II

$\overline{\sigma}_\mathrm{c}$ Axial stress level within the cable

$\sigma_\mathrm{t,av}$ Average membrane axial stress level across the width of the top flange of the cold-formed steel beam

$\sigma_\mathrm{t,DSM}$ Direct Strength Method (DSM) failure stress

$\sigma_\mathrm{t,p}$ Net axial stress level within the top flange of the cross-section at the end of Stage I

σ_true Truss stress

σ_t Net axial stress level within the top flange of the cross-section at the end of Stage II

$\sigma_\mathrm{0.2,corner}$ 0.2% proof stress in the corner regions

$\sigma_\mathrm{0.2,flat}$ 0.2% proof stress in the flat regions

$\sigma_\mathrm{0.2}$ 0.2% proof stress

23

F_{cre} Elastic critical global buckling stress

F_{crl} Elastic critical local buckling stress

F_{m} Mean value of fabrication factor

F_{n} Material ultimate strength

$F_{\mathrm{y,c}}$ Yield stress of the cable

$F_{\mathrm{y,s}}$ Yield stress of the cold-formed steel

F_{y} Material yield strength

h Total height of the cross-section

I_{eff} Effective second moment of area of cold-formed steel section

I_{s} Second moment of area of the cold-formed steel cross-section about the strong geometric axis

k_{c} Axial stiffness of the cable

k_{s} Axial stiffness of the steel beam

L Length of the member

L_{crd} Critical distortional buckling half-wavelength

L_{crd}^{+} Critical distortional buckling half-wavelength for positive bending

L_{crd}^{-} Critical distortional buckling half-wavelength for negative bending

$L_{\mathrm{cre,r}}$ Critical half-wavelength for global torsional buckling

$L_{\mathrm{cre,x}}$ Critical half-wavelength for global flexural buckling about the x–x axis

$L_{\mathrm{cre,y}}$ Critical half-wavelength for global flexural buckling about the y–y axis

L_{cre} Critical half-wavelength for lateral-torsional buckling

L_{crl} Critical local buckling half-wavelength

L_{crl}^{+} Critical local buckling half-wavelength for positive bending

L_{crl}^{-} Critical local buckling half-wavelength for negative bending

M Applied bending moment

M_1 Bending moment about the major principal axis of the cross-section

M_2 Bending moment about the minor principal axis of the cross-section

M_{ax} Factored bending resistance about the major centroidal axis

M_{ax} — Factored bending resistance about the minor centroidal axis

M_{ax} — Factored bending resistance about the strong geometric axis

M_{ay} — Factored bending resistance about the weak geometric axis

M_{a} — Factored bending resistance of the cold-formed steel member

M_{crd} — Elastic critical moment for distortional buckling

M_{crd}^{+} — Elastic critical moment for distortional buckling under positive bending

M_{crd}^{-} — Elastic critical moment for distortional buckling under negative bending

M_{cre} — Elastic critical moment for lateral-torsional buckling

M_{cre}^{+} — Elastic critical moment for lateral-torsional buckling under positive bending

M_{cre}^{-} — Elastic critical moment for lateral-torsional buckling under negative bending

M_{crl} — Elastic critical moment for local buckling

M_{crl}^{+} — Elastic critical moment for local buckling under positive bending

M_{crl}^{-} — Elastic critical moment for local buckling under negative bending

M_{cr} — Elastic critical buckling moment

M_{DSM} — Moment capacity predictions based on the Direct Strength Method (DSM) for the validation process

M_{d} — Nominal bending resistance of cold-formed steel member, but with the yield moment M_{y} in all the DSM expressions replaced by M_{serv}

$M_{\mathrm{end,x}}^{II}$ — Net factored (hogging) bending moment at the end sections in Stage II

M_{FE} — Ultimate moment capacity achieved by the finite element (FE) modes in the validation process

M_{II} — Bending moment component of the Stage II coordinate system on the axial force versus bending moment (P–M) interaction diagram

M_{I} — Bending moment component of the Stage I coordinate system on the axial force versus bending moment (P–M) interaction diagram

M_{max} — Maximum bending moment induced at the critical cross-section due to imposed vertical loading

$M_{\mathrm{max}}^{\mathrm{D}}$ — Bending moment at midspan due to unfactored dead loading

$M_{\mathrm{max}}^{\mathrm{L}}$ — Bending moment at midspan due to unfactored live loading

$M_{\mathrm{max}}^{\mathrm{L}}$ — Sagging moment due to the live loading

M_{m} Mean value of material factor

M_{nd} Nominal bending resistance for distortional buckling

M_{nd}^{+} Nominal bending resistance for distortional buckling under positive bending

M_{nd}^{-} Nominal bending resistance for distortional buckling under negative bending

$M_{\mathrm{net,x}}$ Net bending moment at the critical cross-section about the strong geometric axis

M_{net}^{II} Net bending moment about the strong geometric axis of the critical cross-section in Stage II

M_{net}^{I} Net bending moment about the strong geometric axis of the critical cross-section in Stage I

M_{ne} Nominal bending resistance for lateral-torsional buckling

M_{ne}^{+} Nominal bending resistance for lateral-torsional buckling under positive bending

M_{ne}^{-} Nominal bending resistance for lateral-torsional buckling under negative bending

M_{nl} Nominal bending resistance for local buckling

M_{nl}^{+} Nominal bending resistance for local buckling under positive bending

M_{nl}^{-} Nominal bending resistance for local buckling under negative bending

M_{nx} Nominal bending resistance of the cold-formed steel member about the strong geometric axis

M_{nx}^{+} Nominal bending resistance of the cold-formed steel member about the strong geometric axis under positive bending

M_{nx}^{-} Nominal bending resistance of the cold-formed steel member about the strong geometric axis under negative bending

M_{n} Nominal bending resistance of the cold-formed steel member

M_{serv} Applied moment due to unfactored service loading

M_{test} Ultimate moment achieved in tests on laterally braced cold-formed steel beams

$M_{\mathrm{ult,Pr1}}$ Ultimate moment capacity of the original bare steel beam with Profile 1

$M_{\mathrm{ult,p}}$ Ultimate moment capacity of prestressed cold-formed steel beams

M_{ult} Ultimate moment capacity of bare cold-formed steel beams

M_{x} Applied bending moment about the strong geometric axis of the cross-section

M_{y} Yield moment

M_{y}^{-} Yield moment under negative bending

q_D Dead loading component of uniformly distributed load

Q_i Load effects

q_L Live loading component of uniformly distributed load

Q_m Mean value of load effects

R Internal radius in corner regions of cold-formed steel cross-sections

r Radius of gyration of cold-formed steel cross-section

r_1 Internal radius of web stiffeners

r_2 Internal radius of corner regions

r_c Radius of cable

R_DSM Distance of design prediction point from the Stage II origin on the axial force versus bending moment (P–M) interaction diagram

R_FE Distance of FE ultimate point from the Stage II origin on the axial force versus bending moment (P–M) interaction diagram

R_m Mean value of nominal resistances of cold-formed steel member

R_n Nominal resistance of cold-formed steel member

S_b Elastic section modulus corresponding to first yield of the bottom extreme fibre

S_fy Elastic section modulus corresponding to the extreme fibre in first yield

S_t Elastic section modulus corresponding to first yield of the top extreme fibre

t Thickness of cold-formed steel cross-section

U Total strain energy stored in the system

u_1 Axial deformation at the member end

U_A2 Strain energy due to axial shortening of cable

U_A2 Strain energy due to axial shortening of cold-formed steel beam

v_eff Effective Poisson's ratio

V_FEM Coefficient of variation of FE validation results

V_F Coefficient of variation of fabrication factor

V_M Coefficient of variation of material factor

V_P Coefficient of variation of FE-to-predicted ratio

V_Q Coefficient of variation of load effects

Chapter 1

INTRODUCTION

1.1 Motivation

At least four of the seventeen Sustainable Development Goals of the United Nations (UN General Assembly, 2015), otherwise known as Global Goals, are directly dependent on the construction industry and its impact on the natural and built environment. These goals include climate action, life on land, sustainable cities and communities, alongside industry, innovation and infrastructure. Sustainable and efficient structural solutions are therefore needed more than ever in the construction industry to decrease its carbon-footprint on the environment.

With the purpose of offering such a solution and thus contributing towards a more sustainable construction industry, the current thesis presents the conceptual development of a simple, yet innovative, structural system, namely prestressed cold-formed steel beams. In the proposed concept, prestressing techniques are utilised to enhance the performance of cold-formed steel beams with the aim of offering a novel and highly efficient solution for structural design.

1.2 Initial concept

Prestressing techniques are often employed to enhance the load-carrying capacity and serviceability performance of structural members and systems. Although typically employed in concrete

structures, prestressing can also offer benefits in the case of steel structures, as initially proposed by Magnel (1950). The underlying principle in both cases is essentially the same, where the application of prestress results in the partial or even full cancellation of the stresses that arise at specific regions within the members under loading. In the case of concrete structures the primary aim of prestressing is to impose compressive stresses on parts of the cross-section to overcome the intrinsically weak tensile performance and thus prevent flexural cracking. However, in the proposed prestressed cold-formed steel beams, the purpose is to enhance the performance of the members by applying tensile stresses to parts of the cross-section that are prone to instability.

Cold-formed steel members offer lightweight and efficient solutions in a range of structural applications because of their intrinsic high strength-to-weight ratio and optimised geometries (Hancock, 2016; Schafer, 2017). However, owing to their thin-walled geometry, cold-formed steel members are highly vulnerable to local instability phenomena that complicate the prediction of their behaviour. Local, distortional and global buckling together with their interactions may occur at stress levels lower than the material yield strength and hence prevent the full utilisation of the cross-sectional capacity of the members.

Cold-formed steel beams carry imposed loading in bending and are typically employed as purlins and rafters in roof systems or as joists in floor systems, as shown in Figure 1.1. In the proposed concept, the occurrence of the aforementioned instability phenomena in cold-formed steel beams is delayed by utilising prestressing techniques. The prestressing is applied using a high-strength steel cable that is housed within the cross-section profile of the cold-formed steel beam, at a location eccentric to the strong geometric axis. An illustration of the proposed beams is shown

Figure 1.1: Cold-formed steel members in construction (CSC Building Systems, 2018).

(a) Prestressing stage

(b) Imposed vertical loading stage
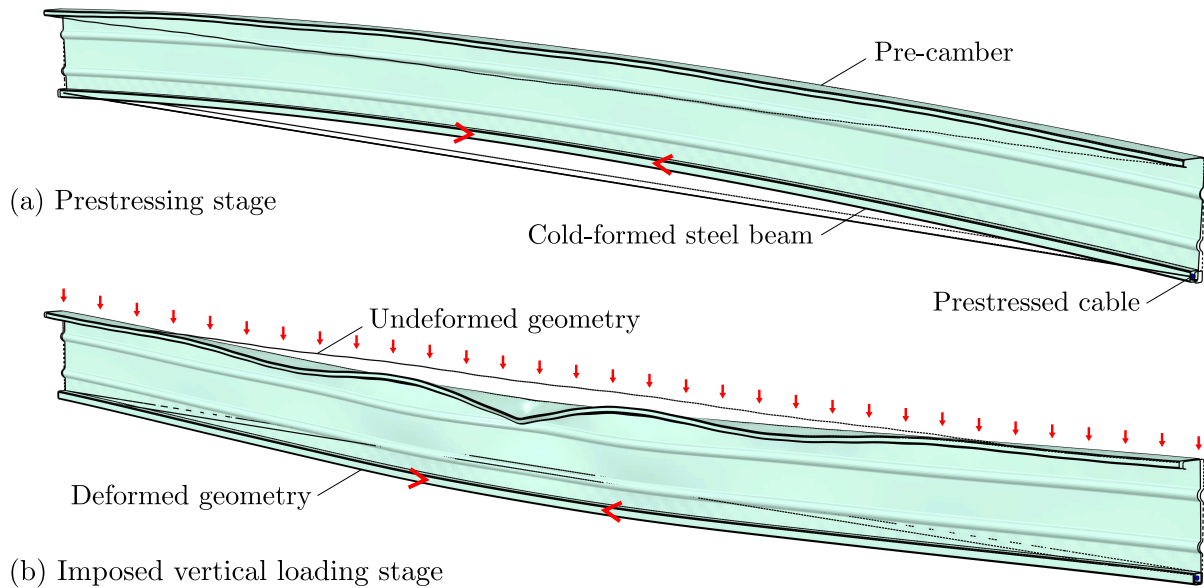
Figure 1.2: 3-D representation of a prestressed cold-formed steel beam at the end of (a) the prestressing stage and (b) the imposed vertical loading stage.

in Figure 1.2.

Owing to the enhanced performance of prestressed cold-formed steel beams, a smaller steel cross-section is required for a given demand in capacity and span length, resulting in material and therefore self-weight savings relative to conventional non-prestressed beams. Potentially, the proposed beams can inspire new applications for cold-formed steel within the construction industry, particularly in cases where increased load-carrying capacities and reduced deflections are desired. For instance, the proposed beams may be employed in thin-slab floor systems or more widely as primary structural elements in the construction of buildings and other structures.

1.3 Aim and objectives

The aim of the current thesis is the conceptual development of prestressed cold-formed steel beams. For this purpose, the following objectives have been established:

(i) To examine in depth the mechanics governing the structural behaviour of prestressed cold-formed steel beams using first principles and to identify the origin of the obtained structural benefits.

(ii) To define failure criteria for the design of the two structural components (*i.e.* the cold-formed steel beam and the prestressed cable) of the system during the two loading stages

(*i.e.* prestressing and imposed vertical loading).

(iii) To simulate the behaviour of the proposed beams during the different loading stages using analytical and numerical modelling.

(iv) To analyse the numerical results, validate them against available experimental data, and compare them with the corresponding analytical results and capacity predictions.

(v) To investigate the effect of the key controlling parameters with the aim of identifying how the benefits obtained from the addition of the prestressed cable can be maximised.

(vi) To provide structural design rules that can be utilised to design the proposed system in practice and to demonstrate their implementation.

(vii) To provide recommendations for further research such that the proposed concept can be developed further.

1.4   Methodology

The research methodology adopted to achieve the objectives listed above utilises the following:

(i) Literature review:

A literature review is conducted first to determine the state-of-the-art regarding the two driving principles of the proposed concept, namely prestressing techniques and cold-formed steel members.

(ii) Analytical modelling:

The mechanical behaviour of prestressed cold-formed steel beams is examined at both cross-section and member levels by applying fundamental principles and analysis techniques of structural mechanics. In this manner, a set of analytical expressions that define the linear elastic behaviour of the studied beams during the prestressing and imposed vertical loading stages is developed.

(iii) Numerical modelling:

Finite element (FE) analysis is the primary tool utilised to develop the proposed concept. Following validation of the FE modelling approach, parametric FE analysis is conducted to investigate the effect of the key controlling parameters. For this purpose, numerous combinations of beam geometries, cable sizes and prestress levels are modelled.

In the present work, the main processes involved in the numerical modelling are: (i) elastic buckling analysis, (ii) creation of the input files, (iii) FE simulation, (iv) data extraction, (v) data analysis, and (vi) post-processing. The order of execution of these processes is illustrated by the flow chart presented in Figure 1.3, where the corresponding software packages, inputs and outputs are also indicated. The interaction of the software packages was fully automated to make the overall modelling process more computationally efficient. The automation required the creation of a number of practical in-house tools that enabled:

- Full parametrisation of the 'Masterfile' such that any desired geometry, prestress level, load case, analysis type etc. could be modelled.

- Automatic extraction of the nodal coordinates, element connectivity and material properties to be inputted into CUFSM (rounded corners) and cFSM (sharp corners).

- Automatic execution of both CUFSM and cFSM for all three loading types.

- Automatic conversion of the obtained imperfection shapes and critical half-wavelengths into imperfection shapes to be introduced into the FE model.

- Automatic extraction of the elastic critical buckling stresses to be used for the determination of the compression and bending strengths of the cold-formed members.

- Automatic creation of the input file, execution of the FE analysis, data extraction and data analysis. This automation was initially established for individual models, as indicated by the 'single model' blocks in Figure 1.3, and was then extended for 'multiple models' to conduct the parametric studies. Note that the purpose and implementation of the elastic buckling analysis and finite element modelling processes is described extensively in the subsequent chapters.

(iv) Design recommendations:

Existing design methods, namely linear interaction equations in conjunction with the Direct Strength Method (DSM) (Schafer, 2008; Camotim et al., 2016), are adapted to structural design
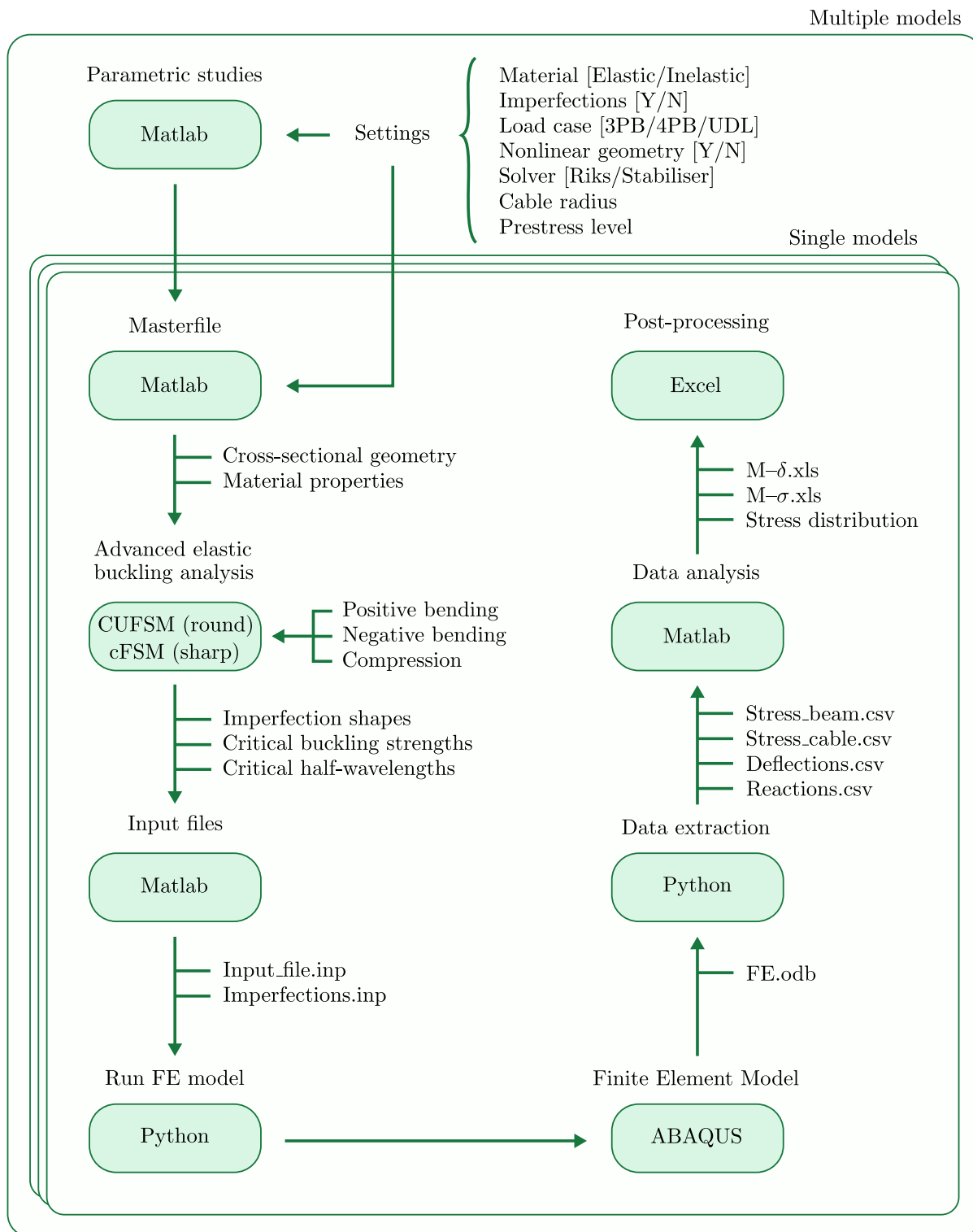
Figure 1.3: Summary of the automated numerical modelling and data analysis processes concerning the FE simulation of prestressed cold-formed steel beams.

rules and failure criteria for the design of prestressed cold-formed steel beams. The implementation of the developed design provisions is demonstrated by means of practical worked examples.

1.5   Sign conventions

Throughout the present thesis, the following sign convention is adopted:

- Axial stresses: Tensile stresses are taken to be positive.
- Axial force diagrams: Compressive forces are indicated to be positive.
- Bending moment diagrams: Sagging bending moments are designated to be positive.
- Vertical member deflections: Downwards vertical deflections are defined to be positive.

1.6   Outline of thesis

The present thesis is structured according to the research methodology presented in Section 1.4. The aim is to achieve the objectives outlined in Section 1.3.

In Chapter 2, essential background knowledge needed to understand the mechanical behaviour of prestressed cold-formed steel beams is presented. The literature review outlines previous research on the two driving principles of the proposed structural system, *i.e.* prestressing and cold-formed steel. Previous research on prestressed steel structures, including prestressed bare steel and composite beams, is discussed first, to be followed by an overview of the properties, behaviour and design of cold-formed steel members.

In Chapter 3, the concept of prestressed cold-formed steel beams is introduced by describing the principal characteristics of the proposed system, such as the structural components, cross-sectional geometry and member restraints. Subsequently, analytical expressions that define the axial stress levels at critical parts of the cross-section and the moment–deflection relationships for the entire member during the different loading stages are developed. Failure criteria for the design of prestressed cold-formed steel beams are then developed by treating the studied members as beam-column members. For this purpose, linear interaction equations, alongside the Direct Strength Method (DSM) (Schafer, 2008), are employed. The failure criteria define the maximum allowable initial prestressing force and bending moment at the critical cross-section

that can be applied in the prestressing and imposed vertical loading stages respectively.

In Chapter 4, FE models are developed to simulate the mechanical behaviour of the proposed system. The key features of the FE models, such as the material response, the beam–cable connection and the boundary conditions, are described. Subsequently, a brief summary regarding previous experimental investigations on cold-formed steel beams with similar cross-sections is presented and the validation of the FE modelling approach is demonstrated. In this manner, it is ensured that the FE models can simulate the behaviour of the proposed beams accurately.

In Chapter 5, the mechanical behaviour of prestressed cold-formed steel beams during the different loading stages is analysed in detail and the origin of the obtained structural benefits is identified. The moment–deflection response, moment–stress response and axial stress distribution at the critical cross-section of sample FE models are compared with the corresponding analytical results and failure criteria. Subsequently, the influence of the key controlling parameters on the behaviour of the studied beams is investigated with the aim of maximising the benefits that can be obtained from the addition of the prestressed cable. A set of parametric studies exploring the effect of the prestress level, cable size, section slenderness and centroid location on the obtained benefits are presented.

In Chapter 6, structural design rules for prestressed cold-formed steel beams are provided. The net axial force and bending moment acting at the critical cross-section during the prestressing and imposed vertical loading stages are defined first. Design recommendations are then presented, whereby the capacities of both structural components (*i.e.* the cold-formed steel and the cable) of the system are checked at both loading stages. The cold-formed steel member is designed as a beam-column using linear interaction equations in conjunction with the DSM, while the prestressed cable is designed by ensuring that its tensile capacity is not violated during the two loading stages. Subsequently, a set of failure criteria are utilised that define the permissible design zone for the prestressed system. The suitability of the proposed design method is then assessed against the parametric FE results, and finally, the implementation of the design recommendations is demonstrated through practical worked examples.

In Chapter 7, the findings of the present work are summarised and conclusions are drawn. The contribution of the current work in the field of structural engineering is subsequently outlined. Finally, recommendations for future research are provided.

1.7 Publications

The research work presented in this thesis has contributed in the following publications:

Journal publications:

- Hadjipantelis, N., Gardner, L., and Wadee, M. A. (2019). Design of prestressed cold-formed steel beams. *Thin-Walled Structures* (Accepted).

- Hadjipantelis, N., Gardner, L., and Wadee, M. A. (2019). Finite element modeling of prestressed cold-formed steel beams. *Journal of Structural Engineering, ASCE* (Accepted).

- Hadjipantelis, N., Gardner, L., and Wadee, M. A. (2018). Prestressed cold-formed steel beams: Concept and mechanical behaviour. *Engineering Structures*, 172:1057-72. https://doi.org/10.1016/j.engstruct.2018.06.027.

Conference publications:

- Hadjipantelis, N., Kyvelou, P., Gardner, L., and Wadee, M. A. (2019). Prestressed composite cold-formed steel flooring systems. *Proceedings of the Seventh International Conference on Structural Engineering, Mechanics and Computation*, Cape Town, South Africa, September 2-4, 2019 (In progress).

- Hadjipantelis, N., Gardner, L., and Wadee, M. A. (2018). Prestressed cold-formed steel beams – parametric studies and design recommendations. In: Chan, S. L., Chan, T. M. , Zhu, S. (Eds.), *Proceedings of the Ninth International Conference on Advances in Steel Structures*, Hong Kong, China, December 5-7, 2018. https://doi.org/10.18057/ICASS2018.P.023.

- Hadjipantelis, N., Gardner, L., and Wadee, M. A. (2018). Prestressed cold-formed steel beams – conceptual development. *Proceedings of the Eight International Conference on Thin-Walled Structures*, Lisbon, Portugal, July 24-27, 2018.

- Hadjipantelis, N. (2018). Prestressed cold-formed steel beams. *Proceedings of the Twentieth Young Researchers' Conference of the Institution of Structural Engineers*, London, United Kingdom, April 10, 2018.

Chapter 2

LITERATURE REVIEW

2.1 Introduction

The literature review was conducted to identify existing research related to the concept of prestressing cold-formed steel beams. The main findings are presented in the current chapter. The first part of the literature review focuses on the first driving principle of the proposed structural system, namely prestressing technologies. The concept of utilising prestressing to enhance the load-carrying capacity and serviceability performance of structures is introduced and its application to steel structures, such as prestressed bare steel and composite beams, is presented. The second part of the literature review concerns the second driving principle of the proposed concept, namely cold-formed steel members. For this purpose, the characteristics of cold-formed steel members, including material properties, buckling phenomena and initial geometric imperfections, are outlined. Finally, an overview of elastic buckling analysis techniques and the Direct Strength Method (DSM), which can be employed for the design of cold-formed steel members, is presented.

2.2 Prestressing technologies

In construction, prestressing technologies are typically used to prestress concrete. However, as discussed in the present section, prestressing steel members or systems can offer similar benefits.

In both cases, the aim of prestressing is to strengthen the member or system by introducing forces that cancel out part of the forces anticipated due to the applied loading.

2.2.1 Historical development

The principle of prestressing can be dated back to 2700 B.C. when the Ancient Egyptians were using a twisting wire rope system to prevent hogging failure in their sailing ships, as shown in Figure 2.1 (Casson, 1971; Troitsky, 1990).
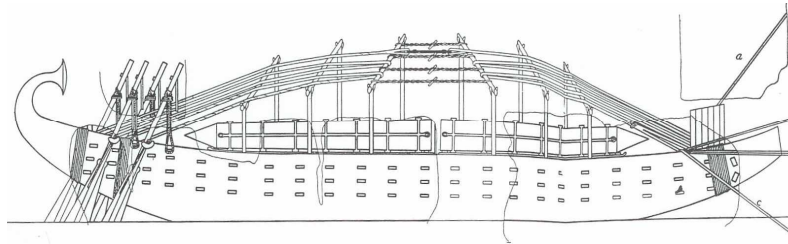
Figure 2.1: Egyptian sailing ships prestressed using a twisting wire rope system (Casson, 1971).

Over the years, prestressing has been employed to strengthen structures made from all kinds of materials including stones, timber and metals. Eventually, prestressing became associated with the construction of long-span structures, such as prestressed segmental bridges, owing to the benefits obtained in terms of both the load-carrying capacity and the serviceability performance of the structure. The development of prestressed steel structures initiated in highly industrialised countries such as the United States, the former Soviet Union, Germany and Belgium (Troitsky, 1990). Nowadays, prestressing is most commonly associated with concrete structures, as discussed below.

2.2.2 Prestressed concrete structures

Prestressing techniques are primarily employed in concrete structures to overcome the weak tensile performance of the concrete. In the case of prestressed concrete beams, a compressive force is applied, before or after concrete casting, using a cable embedded along the member. The aim is the partial or even full cancellation of the tensile stresses that arise in specific regions within the beam under loading. In this manner, flexural cracking within those regions is pre-

Cross-section: Side-view: Axial stress:

(a) Concentric prestressing

(b) Eccentric prestressing
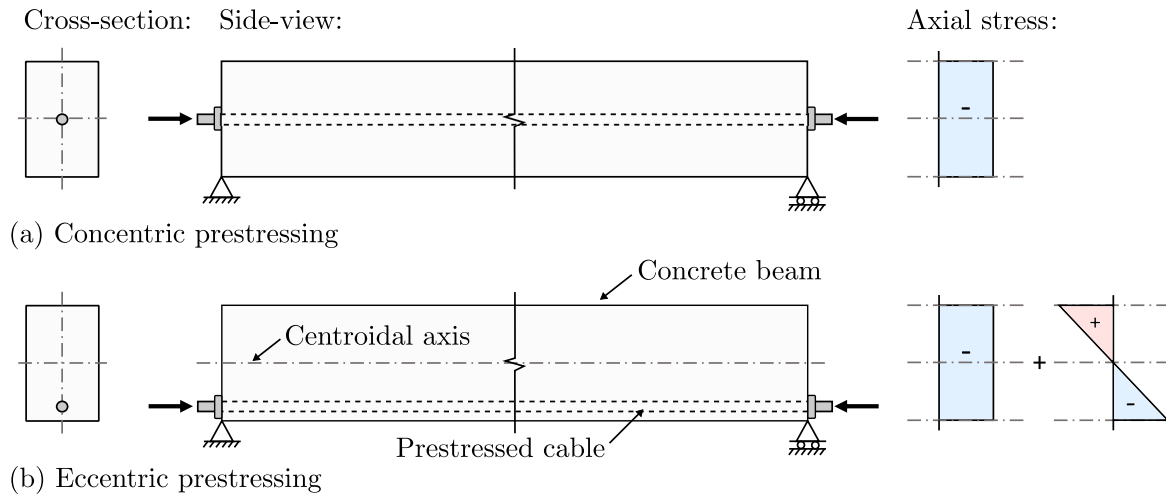
Figure 2.2: Prestressed concrete beam under (a) concentric and (b) eccentric prestressing.

vented. If the prestressed cable is located at a concentric location, a uniform axial compressive stress distribution is imposed across the cross-section, as shown in Figure 2.2(a), while, if the cable is located at an eccentric location, an additional linear stress distribution is induced, as shown in Figure 2.2(b), with the stress level being directly proportional to the eccentricity of the prestressing force.

Applications of prestressed concrete structures include floor slabs in high-rise buildings, bridge decks, offshore structures and nuclear reactor vessels. For long-span structures, such as segmental bridges, prestressing has become the sole option owing to the significant contribution of the self-weight to the vertical deflections of the bridge. Prestressed concrete is generally more expensive than conventional reinforced concrete owing to the use of high strength materials and the higher labour, equipment and installation costs. Nevertheless, these additional costs are often outweighed by the multiple benefits offered by the prestressing process, such as crack control, higher working stress (thus shallower cross-sections, material savings and lighter foundations) and longer spans. The aforementioned benefits led to the idea that the prestressing technologies could also be used in steel structures.

2.2.3   Prestressed steel structures

The concept of prestressing steel structures was initiated by Dischinger (1949) and Magnel (1950) who, both being pioneers in prestressed concrete, realised the potential benefits of using the same principle to prestress steel. Troitsky (1990) also contributed significantly by providing

(a) General view   (b) Anchorage
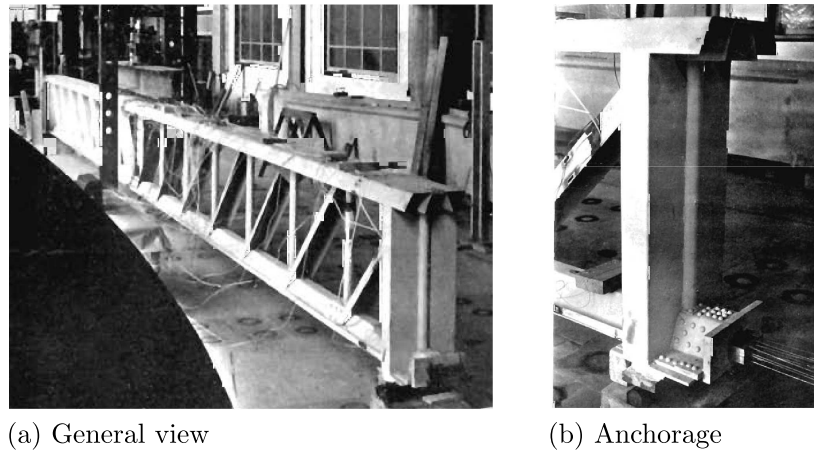
Figure 2.3: Prestressed trussed girder; the first experiment on prestressed steel structures by Magnel (1950).

recommendations for the analysis and design of prestressed bridge systems, plate girders and trusses. The same author estimated that prestressing steel can result in material savings in the range of 10–30% (Troitsky, 1990).

Initially, prestressing has been used in conjunction with steel structures in the form of prestressed truss systems, such as the prestressed trussed girder shown in Figure 2.3, comprising tubular steel elements that housed the post-tensioned cables (Magnel, 1950; Ayyub et al., 1990a; Ellen et al., 2012). More recently, extensive analytical, numerical and experimental research on the tensile and compressive performance of individual prestressed tubular steel elements was conducted by Gosaye et al. (2014; 2016) and Wang et al. (2017). Other applications of prestressed steel structures include prestressed stayed columns (Saito and Wadee, 2008, 2009, 2010; Osofero et al., 2012; Wadee et al., 2013; Yu and Wadee, 2017) and prestressed steel arches (Clarke and Hancock, 1991; Gosaye, 2015). Considerable enhancements in load-carrying capacities and reductions in deflections of the aforementioned members and systems have been reported.

In practice, limited applications of prestressed steel structures have been previously reported. Examples include the reconfiguration of the roof structure of the Sydney Olympic stadium and the Five Star Aviation hangar at Brisbane Airport (Ellen et al., 2012). The design of the latter was based on a patent concerning the construction and erection of post-tensioned trussed arch structures (Ellen, 1987), as shown in Figure 2.4. The use of prestressing in conjunction with cold-formed steel members has been explored when proprietary LiteSteel Beams (Keerthan and Mahendran, 2010; Anapayan et al., 2011) were used to form long-span shell structures (Ellen et al., 2012), with economies in the erection process and significant savings in material reported.
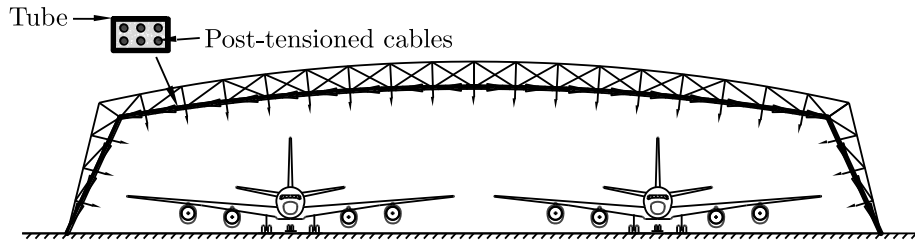
Figure 2.4: Post-tensioning of cables contained within the bottom chord of prestressed steel frame structures (Ellen et al., 2012).

2.2.4   Prestressed bare steel beams

Prestressed bare steel beams are the most relevant application of prestressing in relation to the proposed concept of prestressed cold-formed steel beams. Initially, the following methods of prestressing steel beams were proposed by the Subcommittee 3 on Prestressed Steel of Joint ASCE-AASHO Committee on Steel Flexural Members (1968), with the first method being the most common in practice and the one adopted in the current work:

(i) Prestressing by means of high-strength wires/bars anchored at the beam ends.

(ii) Prestressing by stressing components of hybrid beams – *e.g.* pre-tensioning a high-strength steel plate, and while maintaining the tensile force, welding it to the bottom flange of an unstressed T-section steel beam.

(iii) Prestressing by means of composite action of a concrete slab, also known as the "Preflex technique" – *e.g.* precambering the steel beam and then casting the concrete slab against the beam.

The purpose of prestressing is to induce initial stresses within the steel member or system that counteract the stresses imposed by the external loading. As demonstrated in Figure 2.5(a), in the case of a prestressed bare steel beam with a doubly-symmetric cross-section profile, the overall axial stress distribution comprises three main components. The axial compressive and hogging bending components are induced by the initial prestressing force P_i, while the sagging bending component is imposed by the applied bending moment M. Note that the incremental increase in the prestressing force due to the elongation of the cable under the imposed loading is not shown in Figure 2.5 for illustration purposes. The overall axial stress levels at the top σ_t and bottom σ_b extreme fibres can be evaluated simply by superimposing the aforementioned
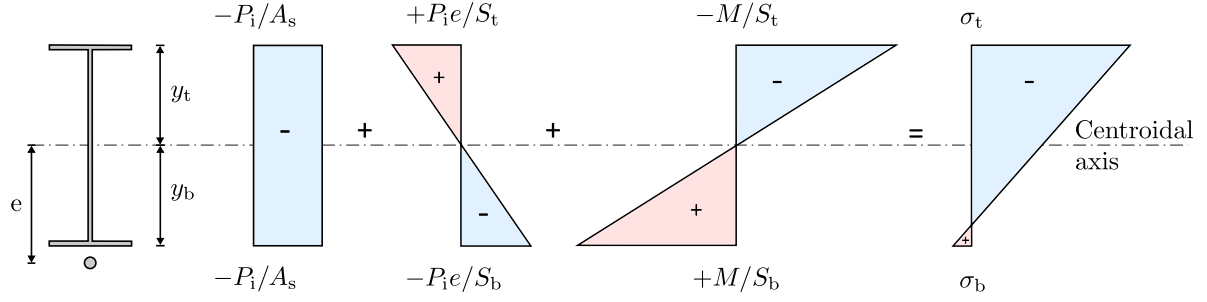
(a) Doubly-symmetric profile
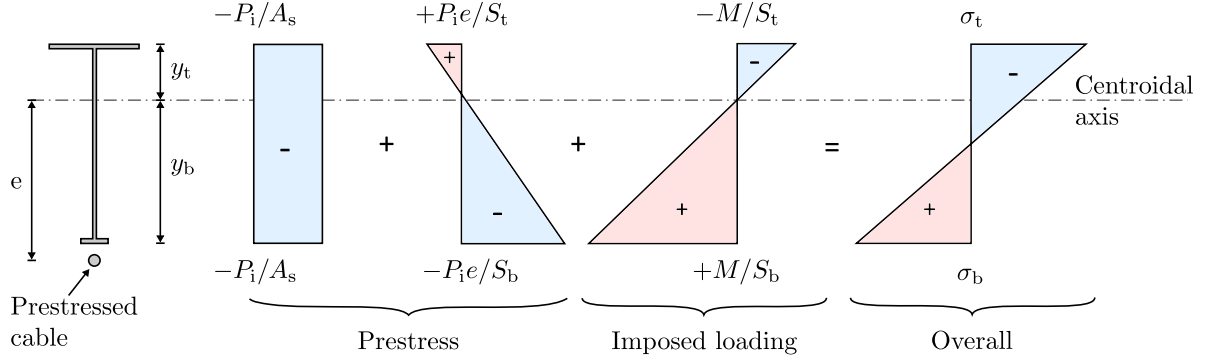
(b) Mono-symmetric profile

Figure 2.5: Axial stress distributions in prestressed (a) doubly-symmetric and (b) mono-symmetric steel girders.

components, *i.e.*:

$$\sigma_t = -\frac{P_\mathrm{i}}{A_\mathrm{s}} + \frac{P_\mathrm{i}e}{S_\mathrm{t}} - \frac{M}{S_\mathrm{t}}, \tag{2.1}$$

$$\sigma_b = -\frac{P_\mathrm{i}}{A_\mathrm{s}} - \frac{P_\mathrm{i}e}{S_\mathrm{b}} + \frac{M}{S_\mathrm{b}}. \tag{2.2}$$

where A_s is the cross-sectional area of the steel; $S_\mathrm{t}{=}I_\mathrm{s}/y_\mathrm{t}$ and $S_\mathrm{b}{=}I_\mathrm{s}/y_\mathrm{b}$ are the elastic section moduli corresponding to first yield of the top and bottom extreme fibres respectively, with I_s being the second moment of area of the steel cross-section about its strong axis of bending.

As discussed by Hoadley (1968) and Troitsky *et al.* (1989), the cross-sectional geometry plays a significant role in the effectiveness of the prestressing force. If the cross-section profile is doubly-symmetric, the overall stress distribution is uneven, as demonstrated in Figure 2.5(a), with the bottom flange not being fully utilised. On the other hand, a well-proportioned cross-section can provide an economical solution by ensuring that the overall stress levels within the top and bottom flanges are equal. This can be achieved by prestressing a mono-symmetric beam, where the major centroidal axis is located within the top half of the cross-section, as shown in
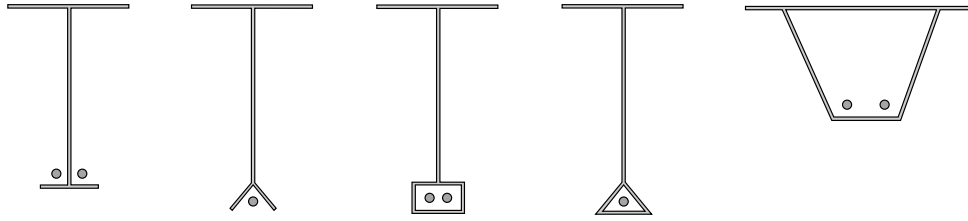
Figure 2.6: Cross-section profiles of mono-symmetric prestressed steel girders (Troitsky et al., 1989).

Figure 2.5(b). Owing to the higher centroidal axis, the eccentricity of the cable (*i.e.* the level arm) is greater and thus the prestressing is more effective. Furthermore, since higher tensile stresses are induced within the bottom flange during the imposed loading stage, the overall contribution of the bottom flange is increased, thus the overall stresses in the two flanges are at similar levels. With the above considerations in mind, Troitsky *et al.* (1989) recommended the mono-symmetric cross-sections shown in Figure 2.6 as possible practical profiles for prestressed steel girders.

Hoadley (1968) also considered the effect of the cable profile on the behaviour of prestressed steel beams. A straight profile, where the cable is located below the centroid of the beam, results in a constant eccentric prestressing force and thus a uniform hogging moment along the member, as illustrated in Figure 2.7(a). In contrast, a parabolic profile, where the cable is profiled as shown in Figure 2.7(b), leads to a variable eccentric prestressing force and, consequently, the induced hogging moment mirrors more closely the moment imposed by the applied loading; hence, greater benefits are obtained from the addition of the prestressed cable.

According to Troitsky (1990), the utilisation of prestressing techniques in conjunction with hot-rolled steel beams can achieve economies of approximately 10–20% and 5–12% in material and cost respectively. The same author provided a general method for the analysis of the mechanical behaviour of continuous prestressed steel girders (Troitsky et al., 1989). The analysis was based on the flexibility method and accounted for variable span lengths and tendon configurations along the girder.

More recently, Belletti and Gasperi (2010) conducted a numerical study to investigate the effect of the number of deviators, which impose the cable profile by fixing the distance between the steel beam and the cable, on the capacity of prestressed bare steel beams. It was concluded that, by increasing the number of deviators, a higher prestressing force can be applied (since any

(a) Straight cable profile

(b) Parabolic cable profile
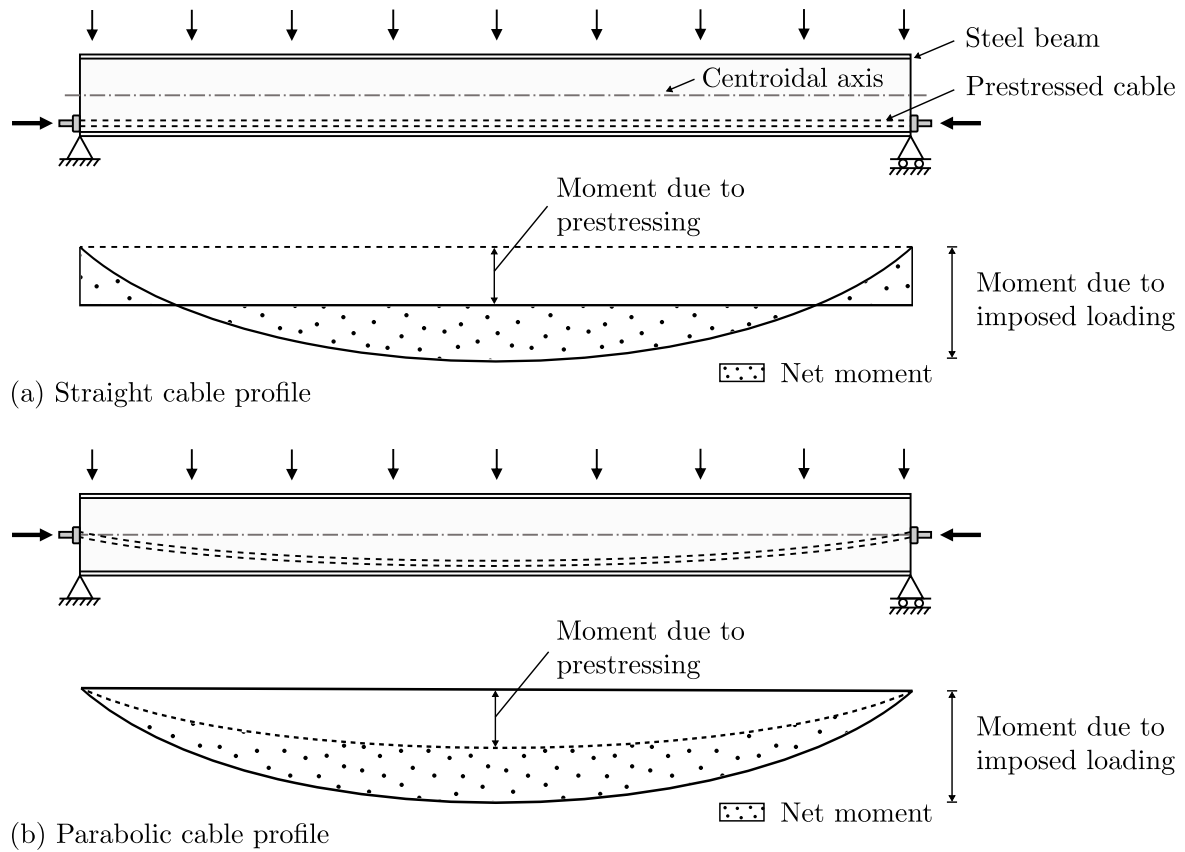
Figure 2.7: Configuration and bending moment diagram corresponding to (a) straight and (b) parabolic cable profiles in prestressed steel beams; adapted from Hoadley (1968).

buckling effects are mitigated more effectively) and thus a greater capacity enhancement can be achieved. However, it was also noted that, a greater number of deviators results in higher fabrication costs. Finally, Kambal and Jia (2018) conducted an experimental and analytical study concerning the bending resistance of steel box girders prestressed with external tendons. The results demonstrated that prestressing can improve the serviceability performance and load-carrying capacity of steel box girders, thus achieving a more lightweight solution.

2.2.5   Prestressed composite steel beams

In contrast to the limited research existing on prestressed bare steel beams, substantial work has been previously conducted on prestressed steel–concrete composite steel beams, which were initially proposed by Dischinger (1949). As illustrated in Figure 2.8, in these systems, the prestressed cables are located externally along the steel member that acts compositely with the concrete slab located above.

(a) Cross-section: (b) Side-view:
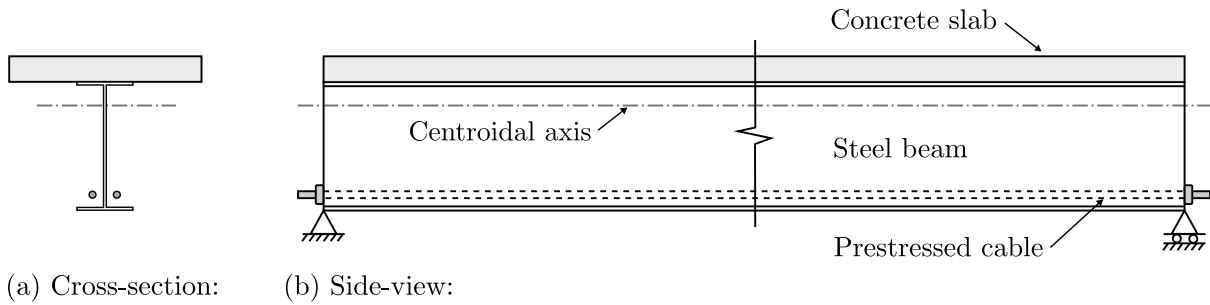
Figure 2.8: Illustration of a simply-supported prestressed steel–concrete composite steel beam.

The behaviour of simply-supported prestressed composite beams was studied by Hoadley (1963). It was demonstrated that, overall, the response of prestressed and conventional composite steel beams is similar, with the difference being that the prestressed beams achieve higher yielding and ultimate moment capacities. Hoadley (1968) concluded that, as in the case of prestressed bare steel beams, fundamental importance is attributed to a well-proportioned cross-section, where the maximum allowable stresses for both the concrete and the steel are reached simultaneously. It should be noted that the construction sequence plays a significant role in the structural behaviour of these prestressed composite beams. For instance, if the composite beam is pre-tensioned (*i.e.* prestressing applied before concrete casting), the prestressing force is carried by the steel beam, while, if the composite beam is post-tensioned (*i.e.* prestressing applied after concrete casting), the prestressing is carried by the composite member. Moreover, Troitsky *et al.* (1990) conducted an analytical and experimental study on pre-tensioned and post-tensioned composite beams with different tendon configurations, concluding that, ideally, the tendon profile needs to vary along the member according to the location of the tensile stresses.

Tong and Saadatmanesh (1992) formulated an analytical model to examine the behaviour of continuous prestressed composite girders with two different tendon profiles, namely straight discontinuous and draped continuous, as shown in Figure 2.9. It should be emphasised that, within the hogging moment regions (*i.e.* between the inflection points on each side of the internal support) of continuous prestressed composite girders, the tendon needs to be located within the top part of the cross-section. Otherwise, the prestressing force amplifies the hogging moment induced by the imposed vertical loading and thus has an adverse effect on the capacity of the member. By analysing the midspan deflections and the stresses at critical parts of the cross-section, Tong and Saadatmanesh (1992) reported that the studied tendon profiles provide similar results. Hence, the choice of tendon profile should be based on the ease of fabrication of the

(a) Straight discontinuous tendon profile

(b) Draped continuous tendon profile

(c) Bending moment diagram

(d) Section A–A: (e) Section B–B:
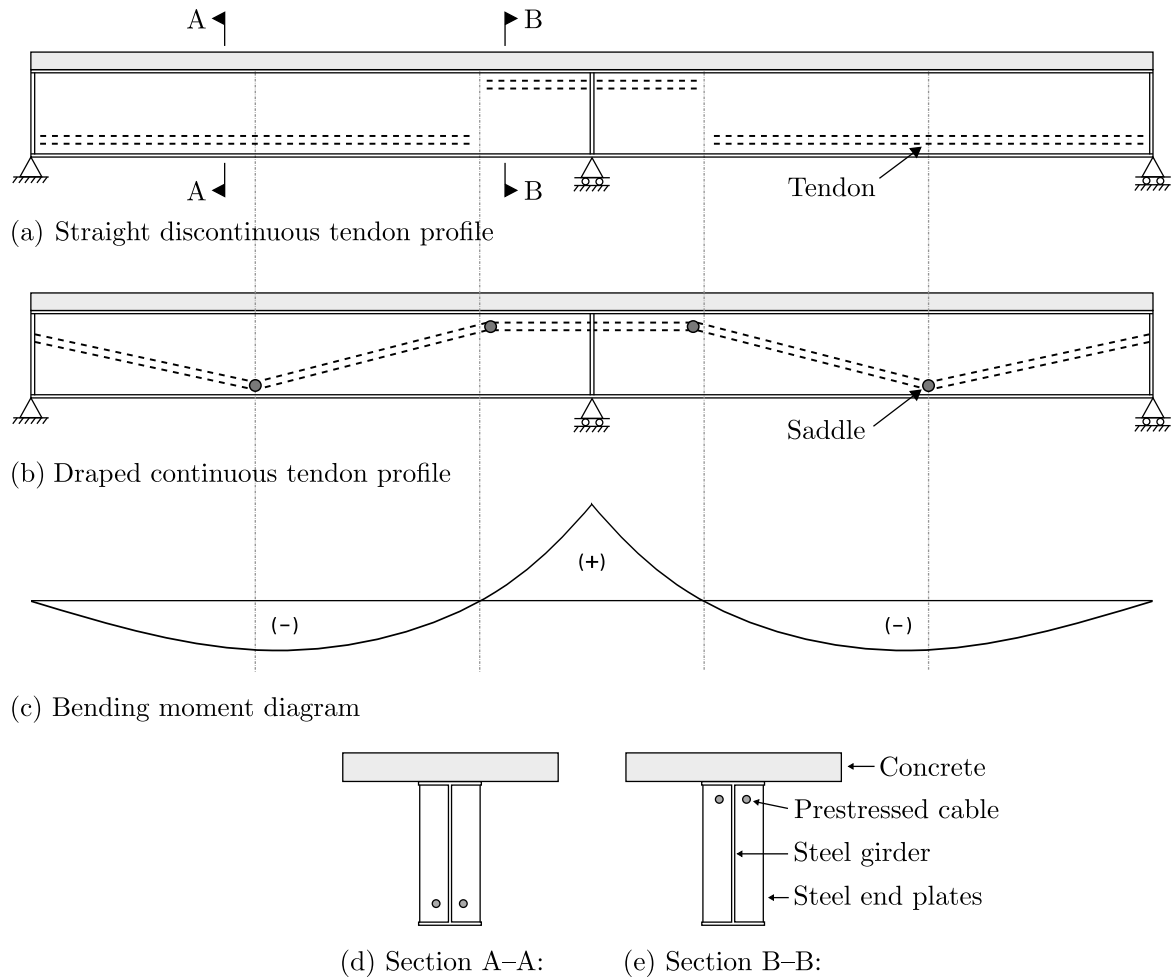
Figure 2.9: Continuous prestressed composite girders with (a) straight discontinuous and (b) draped continuous tendon profiles; (c) bending moment diagram due to the application of imposed vertical loading. Adapted from Tong and Saadatmanesh (1992).

prestressed girder. A parametric study was also conducted to investigate the influence of various parameters, such as the prestressing force, tendon eccentricity and length, prestressing sequence and load patterns on the capacity and vertical deflections of the girder. Finally, the authors indicated that the incremental increase in the prestressing force owing to the application of imposed vertical loading can have a significant effect; hence, this increase should be considered when selecting the initial prestressing force.

Saadatmanesh *et al.* developed analytical models (1989a) and design guidelines (1989c) for simply-supported prestressed composite steel beams subjected to positive and/or negative bending. The analytical results were verified against the test results (1989b) from a girder subjected to positive bending and a girder subjected to negative bending. In the former test, the tendon was placed just above the bottom flange, as shown in Figure 2.9(d), and the prestress was applied before concrete casting. In the latter test, the tendon was placed just below the top flange,

as shown in Figure 2.9(e), and the prestress was applied after concrete casting in order to place the concrete slab under compression. The negative bending test simulated the behaviour within the hogging moment region of continuous prestressed composite steel beams. Saadatmanesh *et al.* (1989b) observed that the addition of the prestressed tendons enhanced the yielding and ultimate capacities of composite steel beams substantially. Furthermore, the authors concluded that this enhancement can be extended by increasing the eccentricity of the tendons further. This principle also governs the design of under-deck cable stayed bridges where struts position the cables as deep within the tension zone as possible (Madrazo-Aguirre et al., 2015b).

Other experimental investigations regarding the mechanical behaviour and failure mechanisms of simply-supported and continuous prestressed composite steel beams include the works of Ayyub *et al.* (1990b), Chen and Gu (2005), Lorenc and Kubica (2006) and Chen *et al.* (2009). More recently, with numerical modelling becoming more prominent, several parametric studies have been conducted to investigate the effect of various parameters on the behaviour of prestressed composite beams, including the works of Chen and Jia (2010), El-Zohairy *et al.* (2015) and Lou *et al.* (2016).

2.2.6 Losses of prestress

Prestressed systems can suffer from losses of prestress, impairing their performance. In practice, as in the case of prestressed concrete, the aforementioned losses need to be considered in the calculation of the effective prestressing force. The magnitudes of these losses depend partly on the specifications of the prestressing system components, which are typically provided by the manufacturer. Prestress losses can be categorised into two groups, as described below.

Immediate prestress losses that take place during the transfer of the prestressing force and, in practice, are compensated by overstressing the cables accordingly. Such losses can arise due to:

(i) Anchorage slippage: During the transfer of the prestress, there is inevitable slip at the anchorages that takes place as the wedges grip on the cable and the anchorage system tightens. The magnitude of slip loss depends on the characteristics of the chosen anchorage system and becomes less significant as the length of the tendons is increased (Troitsky, 1990).

(ii) Friction: Takes place at the locations of the saddles/deviators that are used to enforce the cable profile. Hence, the greater the curvature of the cable profile, the greater the friction losses. By lubricating the saddles and greasing the cable, these losses can be minimised.

(iii) Initial elastic shortening of the steel beam: As the prestress is transferred into the member, elastic axial shortening of the steel beam occurs. As a result, the cable shortens and thus a proportion of the prestressing force is lost.

Time-dependent prestress losses that develop during the service life of the prestressed member can arise due to:

(i) Cable relaxation: Progressive decrease (at a diminishing rate) of the cable stresses over the course of time, owing to the fact that the cable is subjected to a sustained load at constant strain. The percentage of relaxation varies depending on the material properties of the cable and the magnitude of the initial prestressing force. Special low-relaxation wires that ensure no noticeable relaxation losses are available; maximum prestressing force losses of 2.5% at 0.7 Rm (20°C) at 1000h can be achieved (ArcelorMittal WireSolutions, 2018). The cable specifications should satisfy the appropriate design standards, such as EN10138 (2000) and the ASTM Specifications A416 (2012) and A421 (2015).

(ii) Creep in the steel: The tendency of the material to deform permanently when subjected to mechanical stress over a long period of time. This is typically negligible in steel members.

2.3   Cold-formed steel members

As discussed in the present section, cold-formed steel members offer structurally efficient, practical and durable solutions in construction, with their design nowadays being facilitated by modern analysis techniques and design methods, such as advanced elastic buckling analysis and the Direct Strength Method (DSM) (Schafer, 2008; Camotim et al., 2016) respectively.

Recommended sources for further reading with regards to the principal characteristics and design of cold-formed steel members include the Commentary of the North American Specification (AISI S100-16, 2016) and the works of Trebilcock (1994), Grubb and Lawson (1997), Grubb et al. (2001), Hancock et al. (2001), Yu and LaBoube (2010), Davison and Owens (2012) and Yu (2016).

2.3.1 Cold-formed steel in construction

The use of cold-formed steel members in construction initiated in the 1850s (AISI S100-16, 2016). Today, in the United States, cold-formed steel members are used in structural and non-structural framing in 30–35% of all non-residential buildings (Williams, 2016). In the United Kingdom, cold-formed steel members are becoming increasingly more common in residential, educational, commercial and industrial construction (Grubb et al., 2001).

2.3.1.1 Production techniques

The thickness of galvanised cold-formed steel, also known as 'light gauge' steel, commonly ranges from 0.9 mm to 3.2 mm in the case of wall studs, floor joists and roof trusses, and from 1.4 mm to 3.2 mm in the case of purlins and cladding rails (Davison and Owens, 2012). The height of the cold-formed steel cross-sections typically ranges from 50 mm to 300 mm (Trebilcock, 1994).

The production of cold-formed steel members is performed at, or near, room temperature and involves the roll-forming of cold-formed steel coils, as shown in Figure 2.10(a), through a series of stands that gradually produce the desired cross-section shape, as shown in Figure 2.10(b). This takes place in a continuous, automated and highly accurate process, with holes for bolts or services being punched at predetermined locations, if desired.

(a) Coils   (b) Roll forming
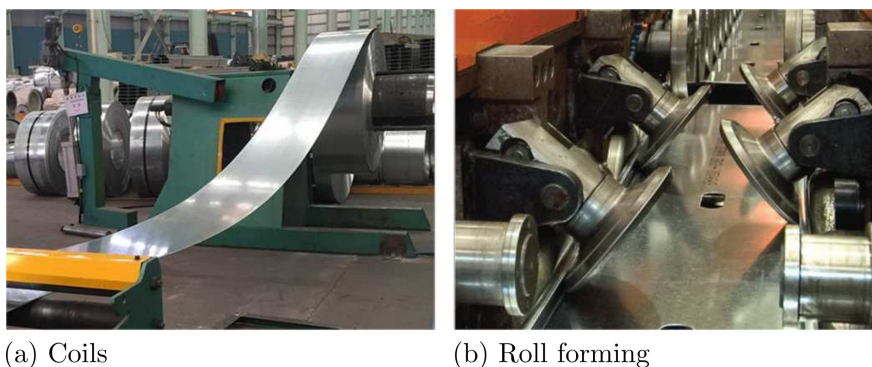
Figure 2.10: Production of cold-formed steel members using roll forming (SFIA, 2018).

The rolling process offers great flexibility regarding the cross-section shape; examples of typical profiles are shown in Figure 2.11. Advanced analysis and optimisation techniques have facilitated the cost-effective production of geometrically complex cross-sections, such as the Swage and

(a) Channel   (b) Lipped channel   (c) SwageBeam   (d) Multibeam   (e) Eaves beam

(f) Lipped zed   (g) Zeta   (h) Hat   (i) Built-up channel   (j) Easibeam
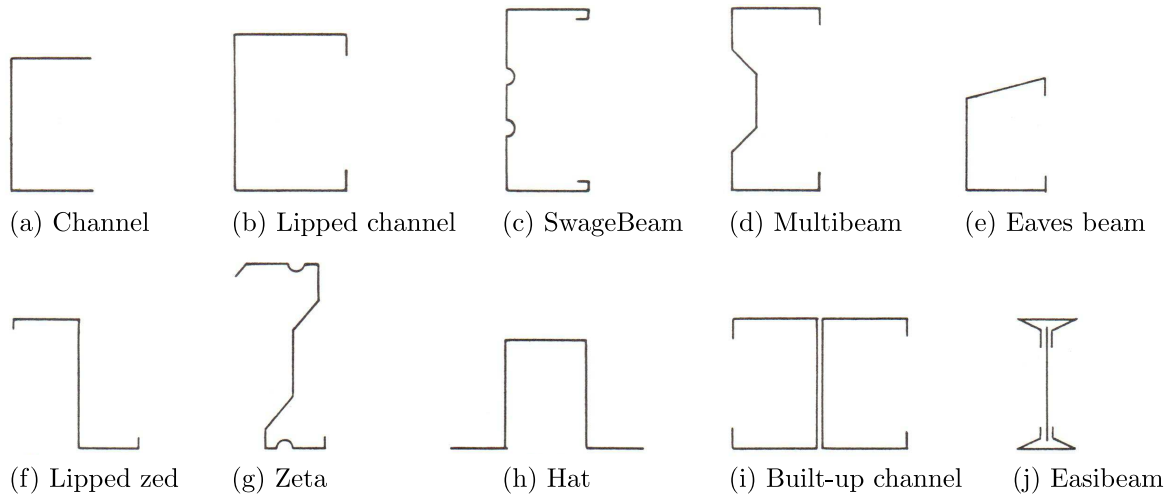
Figure 2.11: Examples of cold-formed steel cross-section profiles. Adapted from Rhodes and Lawson (1992).

Zeta beams in Figures 2.11(c) and (g) respectively, decreasing the vulnerability of the members to local instabilities and thus increasing their load-carrying capacity.

2.3.1.2   Advantages of cold-formed steel

Cold-formed steel members extend the use of structural steel into lighter load-bearing applications and compete directly with masonry and timber construction (Trebilcock, 1994). The advantages of using cold-formed steel members can be categorised as follows:

- Mechanical performance: High strength- and stiffness-to-weight ratios lead to weight reductions and thin floor systems; dimensional accuracy and consistency in material quality.

- Practicality: Prefabrication, as well as ease of transportation, handling and installation, result in quick construction; easily adaptable, no formwork required and services can be integrated.

- Sustainability: Recyclable, reusable and non-combustible (plus fire protection provided by, for example, plasterboard); good thermal and acoustical performances can be achieved.

- Durability: Corrosion protection; not susceptible to shrinkage, fungal and termite attacks.

2.3.1.3 Applications in building construction

In building construction, cold-formed steel members are used in light steel framing that is most commonly employed in residential buildings and low-rise apartment blocks, as shown in Figure 2.12(a). Alternatively, they are utilised as secondary members, for example in industrial, retail or agricultural buildings, as shown in Figure 2.12(b), with the role of providing lateral restraints between primary members while supporting the roof or wall cladding. The most common applications of cold-formed steel members in building construction are the following:

  (i) Load-bearing walls: Used primarily in midrise buildings as structural components to carry gravity and lateral loads, as shown in Figure 2.12(a).

 (ii) Non-load-bearing walls: Used to form the building envelope of steel/concrete frame buildings or as infill walls with the purpose of supporting the plasterboards.

(iii) Floors and roofs: Employed as primary or secondary beams in floors and roofs, as shown in Figure 2.12(b); for this purpose, lipped channel and sigma profiles, shown in Figures 2.11(b) and (d) respectively, are commonly employed.

 (iv) Hybrid systems: Combined easily with other materials, for instance precast concrete, wood framing and structural steel.

  (v) Other uses: Space frames, mezzanine floor systems, portal frames and storage racking.

In the construction process, cold-formed steel members are assembled as: (i) individual components installed on site, also known as 'stick construction', (ii) two-dimensional panelised

(a) Light steel framing   (b) Purlins supporting roof sheeting

Figure 2.12: Applications of (a) light steel framing (SFIA, 2018) and (b) secondary steelwork (Trebilcock, 1994) in building construction.

components to be used as wall, floor or roof systems, or (iii) prefabricated modules built off site from panelised components to serve as the main structural components of the building.

2.3.2   Material behaviour

Material properties play a governing role in the performance of cold-formed steel members. As described below, the cold-forming process induces a few fundamental differences in the material behaviour of cold-formed steel members in comparison with hot-rolled steel members.

2.3.2.1   Stress–strain response

In contrast to the sharp yielding point and yield plateau observed in the stress–strain response of hot-rolled steel (Yun and Gardner, 2017), as shown in Figure 2.13(a), a rounded stress–strain response with gradual yielding and a significant strain hardening period is exhibited by cold-formed steel (Gardner and Yun, 2018), as shown in Figure 2.13(b). In hot-rolled steel, the yielding point is clearly defined, while, in cold-formed steel, it can be obtained by the offset method, with an offset of 0.2% being typically utilised, as demonstrated in Figure 2.13(b). The rounded response of the cold-formed steel is attributed to the cold working process, which, as described below, has two additional effects on the material behaviour. Note that the modelling of the stress–strain response of cold-formed steel is described in Section 4.2.3.1.

(a) Hot-rolled steel   (b) Cold-formed steel
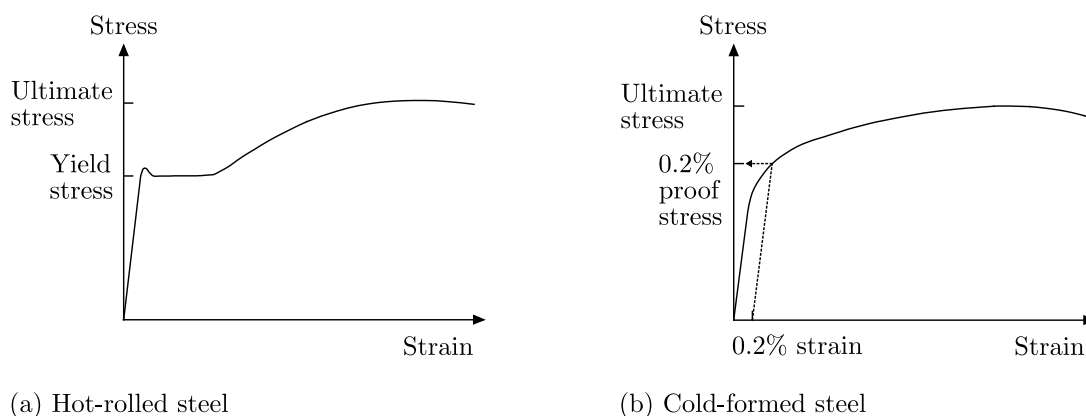
Figure 2.13: Stress–strain curves for (a) hot-rolled and (b) cold-formed steel. Adapted from Yu and LaBoube (2010).

2.3.2.2   Cold-forming effects and strength enhancements in corner regions

To investigate the effect of cold working on the mechanical properties of steel, several studies were conducted at Cornell University in the 1960s (Chajes et al., 1963; Karren, 1967; Karren and Winter, 1967). It was concluded that, owing to the strain-hardening and strain-aging effects, the cold-forming process changes the properties of the parent mild carbon steel mainly in the following ways: (i) the yield strength and ultimate strength of the steel are increased while its ductility is decreased, (ii) the larger the ultimate-to-yield strength ratio, the larger the strain hardening effect during cold-forming, and (iii) the cold work creates anisotropy in the material properties (Hancock et al., 2001). The most critical factor affecting the aforementioned changes is the amount of cold work, which increases as the inner radius-to-thickness ratio of the corner regions R/t reduces (Hancock et al., 2001; Rossi et al., 2013). For instance, to form a corner with a small inner R/t, a larger degree of cold work is required and thus a higher increase in the yield strength is induced.

With these considerations in mind, it follows that different parts of a cold-formed steel cross-section have different material properties. This is illustrated in Figure 2.14, where it can be observed that the ultimate and yield strengths in the corner regions are considerably higher than in the flat regions. In numerical simulations, the strength enhancement in the corner regions can be accounted by increasing the 0.2% proof stress of the material model within those regions, as performed by Hui (2014) and Kyvelou *et al.* (2018).

A set of expressions were derived by Karren (1967) to obtain the ratio between the yield stress in the corner relative to the flat regions. The reliability of these expressions was assessed by comparing the evaluated results with experimental data, with good agreement being demonstrated (Karren and Winter, 1967). Other experimental investigations with regards to the effects of cold-forming include the works of Kyvelou *et al.* (2017) and Afshan *et al.* (2013). A number of similar research studies that investigated the effect of various parameters, such as the R/t ratio, thickness and residual stress distributions are reported by Yu and LaBoube (2010).

(a) Channel section

(b) Joist chord
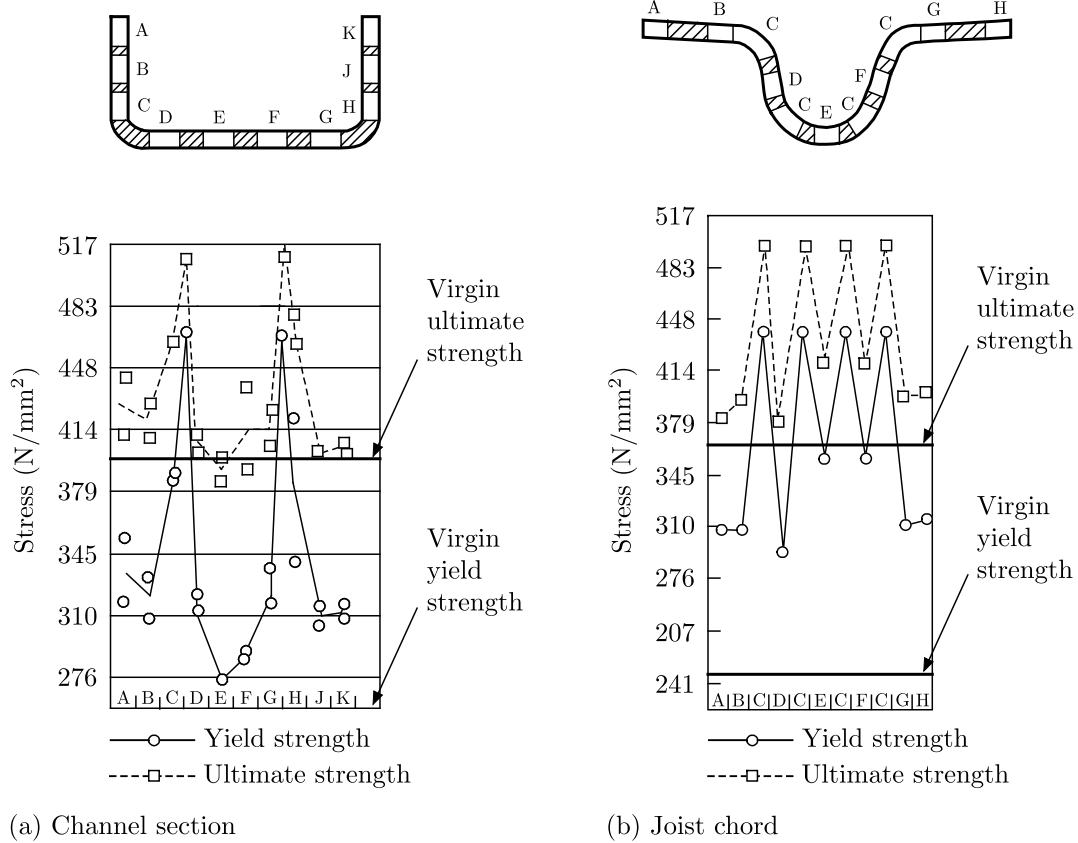
Figure 2.14: Effect of cold working on the mechanical properties of cold-formed steel cross-sections. Adapted from Karren and Winter (1967).

2.3.2.3 Residual stresses

Owing to the development of plastic deformations during the production process, residual stresses and plastic strains are locked in cold-formed steel members (Yu and LaBoube, 2010; Dubina et al., 2012). The residual stresses originate from the coiling-uncoiling and cold-forming processes and, potentially, they can cause premature yielding, thus influencing the load–displacement response and ultimate strength of the members (Moen et al., 2008).

The residual stresses vary nonlinearly across the thickness of the cross-section and are considered to comprise two components, namely the membrane and bending components, as demonstrated in Figure 2.15. The membrane residual stresses are constant across the section thickness and have been found to be relatively low (Cruise and Gardner, 2008) in comparison with the bending residual stresses, which vary linearly across the section thickness in cold-formed sections. According to Schafer and Peköz (1998a), it is not uncommon for the bending residual stresses to be equal to 50% of the material yield stress.
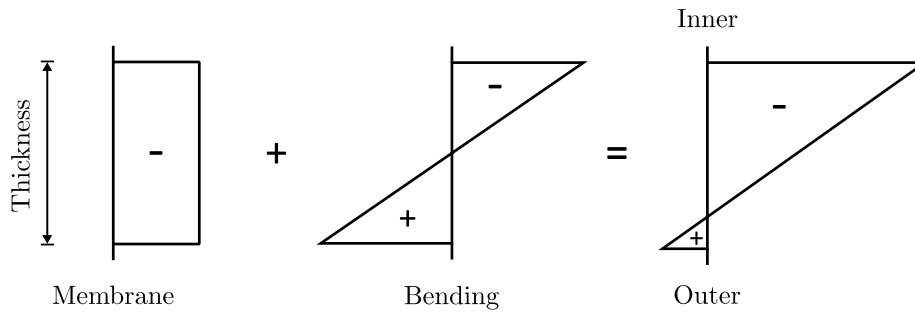
Figure 2.15: Idealisation of residual stresses. Adapted from Schafer and Peköz (1998a).

Even though the variation of the residual stresses across the section thickness is rather complex and depends on the actual manufacturing process, mechanics-based prediction methods for evaluating the residual stresses and strains in cold-formed steel members have been previously developed (Moen et al., 2008). Nevertheless, the inclusion of residual stresses in numerical models is often omitted owing to the lack of data regarding the distributions and magnitudes that should be used (Dubina et al., 2012; Hui, 2014).

According to Schafer et al. (1998a; 2010), the effects of residual stresses and strength enhancements in corner regions offset each other and thus should either be both included in numerical models or they should be both ignored. However, according to Jandera et al. (2008), who conducted experimental and numerical investigations regarding the influence of membrane and bending residual stresses on local and global buckling of cold-rolled stainless steel hollow sections, the bending residual stresses are inherently included in the stress–strain curves obtained from tensile coupon tests and thus should not be re-introduced into the numerical models (this is also supported by Dubina et al. (2012)). In the same study, it has also been reported that, paradoxically, the introduction of residual stresses in the numerical models can even lead to increased load-carrying capacities.

2.3.3 Buckling effects

Owing to their thin-walled geometry, cold-formed steel members are highly vulnerable to local instability phenonmena that complicate the prediction of their behaviour. As discussed in the present sub-section, depending on their slenderness, cold-formed steel members are potentially susceptible to local, distortional and global buckling together with their interactions that may occur at stress levels lower than the material yield stress. Fortunately, as presented in Sec-

(a) Local   (b) Distortional   (c) Flexural (y)   (d) Flexural (x)   (e) Torsion (r)
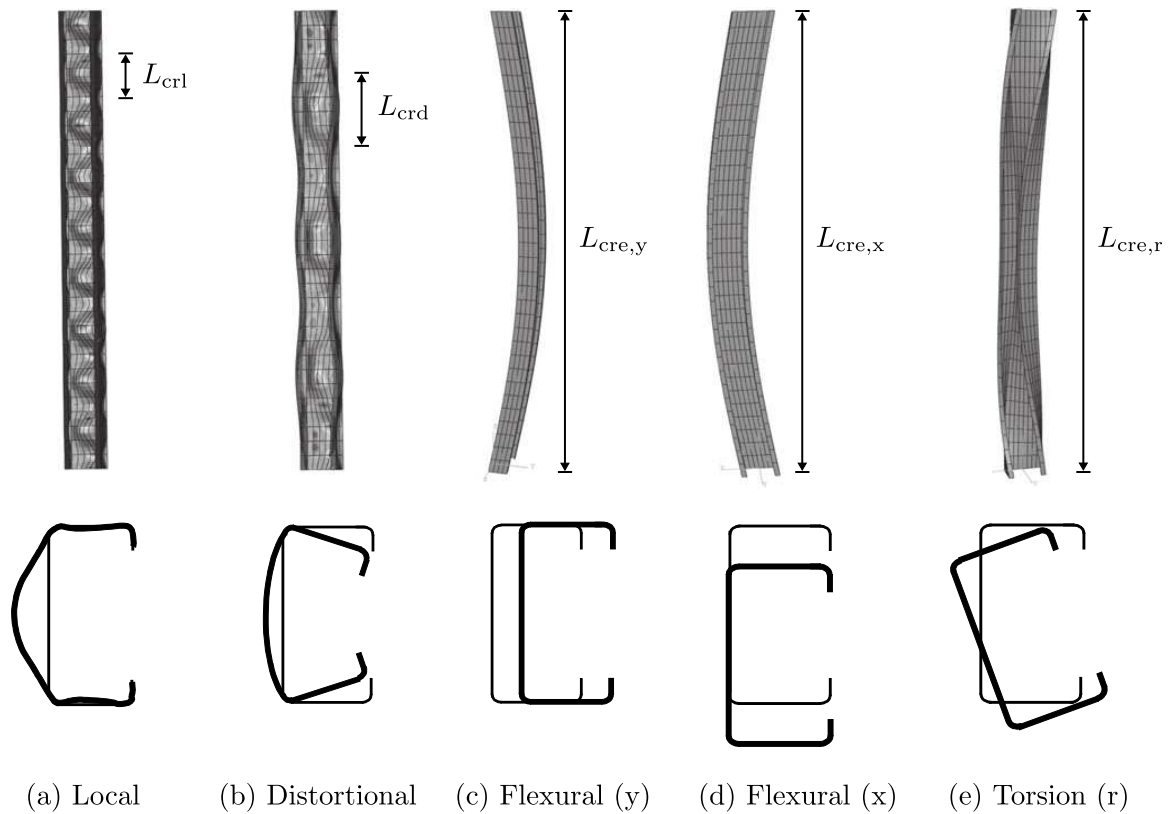
Figure 2.16: Fundamental buckling modes of a thin-walled lipped channel member subjected to axial compression; L_{crl}, L_{crd}, $L_{\text{cre,y}}$, $L_{\text{cre,x}}$ and $L_{\text{cre,r}}$ are the critical half-wavelengths for local, distortional, global flexural about the y–y axis, global flexural about the x–x axis and global torsional buckling respectively. Adapted from Zeinoddini and Schafer (2012).

tion 2.3.5, advanced buckling analysis techniques enable the prediction of the aforementioned buckling effects and facilitate the use of modern design methods, such as the Direct Strength Method (DSM) to determine the ultimate strength of cold-formed steel members.

Cold-formed steel members have three principal elastic buckling modes, namely local, distortional and global buckling; the latter includes flexural, torsional or flexural-torsional buckling for columns and lateral-torsional buckling for beams. The deformed shapes at cross-section and member levels corresponding to the fundamental buckling modes of a thin-walled lipped channel column are illustrated in Figure 2.16, where the corresponding critical half-wavelengths L_{cr}, *i.e.* the longitudinal variation of the buckling shape, are also indicated.

2.3.3.1   Local buckling

Local buckling in plated structures, such as thin-walled cold-formed steel members, has been the subject of extensive research, including the works of Bleich (1952), Timoshenko and Gere (1961),

Bulson (1970) and Allen and Bulson (1980). As shown in Figure 2.16(a), local buckling involves a significant deformation of the cross-section, with only rotation, not translation, taking place at the internal fold lines (*e.g.* at the corners) of the member (AISI S100-16, 2016). The critical half-wavelength for local buckling is typically shorter or equal in length to the largest dimension of the cross-section subjected to compression. For this reason, the local buckling mode cannot be restrained easily, unless the cross-sectional geometry (*e.g.* addition of stiffeners or increase in thickness) or the boundary conditions of the individual cross-section plates (*e.g.* addition of edge stiffeners) are altered. Hence, typically, local buckling needs to be considered in the design of cold-formed steel members.

2.3.3.2 Distortional buckling

Distortional buckling is an instability that occurs most commonly in cold-formed steel members with edge-stiffened flanges, for instance lipped channel and Z-shaped cross-sections (AISI S100-16, 2016). As shown in Figure 2.16(b), distortional buckling involves significant deformation of the cross-section, with both rotation and translation taking place at one or more internal fold lines of the member (AISI S100-16, 2016). For instance, in the lipped channel cross-section shown in Figure 2.16(b), distortional buckling is evident by the instability of the entire flanges, which, together with the edge stiffeners, rotate about the flange/web junctions and thus induce the translations of the flange/lip junctions. As the web becomes deeper, the rotational stiffness provided by the web to the flange/web junction is reduced, hence the distortional buckling strength of the member is decreased (Dubina et al., 2012).

The critical half-wavelength for distortional buckling is longer than the half-wavelength for local buckling and shorter than that for global buckling. Owing to its intermediate half-wavelength, distortional buckling is commonly the controlling mode when: (i) the edge stiffeners are insufficiently stiff to provide stability to the flanges, (ii) global buckling is not the controlling mode owing to short unbraced lengths, and (iii) inadequate rotational restraint is provided by attachments, such as floor sheeting, to the flanges under compression (AISI S100-16, 2016). Furthermore, in comparison with local buckling, distortional buckling has a significantly lower post-buckling stiffness (Schafer and Peköz, 1999). Consequently, distortional buckling may govern the failure of a member even if the elastic critical local buckling strength is lower than the elastic critical distortional buckling strength (Schafer and Peköz, 1999).

Analytical studies regarding the determination of the distortional buckling strength of cold-formed steel members include the works of Lau and Hancock (1987) alongside Schafer and Peköz (1999). The first design curves for thin-walled cross-sections undergoing distortional buckling were proposed by Hancock *et al.* (1994); based on this work, the Direct Strength Method (DSM), which is overviewed in Section 2.3.6, was developed (Schafer, 2008).

2.3.3.3 Global buckling

Global buckling involves the translation and/or rotation of the entire cross-section without any distortion and includes flexural, torsional or flexural-torsional buckling for columns and lateral-torsional buckling for beams. For instance, as shown in Figures 2.16(c)–(d), in flexural buckling, the column deflects laterally with the cross-section shape remaining unchanged. In the case of lateral-torsional buckling, simultaneous out-of-plane deflection and twisting of the cross-section about the shear centre takes place (AISI S100-16, 2016).

The global buckling strength of a member can be enhanced by means of bracing. For instance, a beam is considered to be 'fully braced' when the lateral deformations of its compression flange are restrained and thus lateral-torsional buckling is prevented. In construction, this is typical in the case of cold-formed steel beams due to the attachment of floor sheeting on the compression flange (Davison and Owens, 2012). The critical half-wavelength for global buckling is equal to the unbraced length of the member.

2.3.4 Initial geometric imperfections

Geometric imperfections are deviations of the geometry of a member from the initially perfect geometry and include local deviations (*e.g.* dents), bowing, warping and twisting of the cross-section (Schafer and Peköz, 1998a). Imperfections encourage the early development of the buckling phenomena discussed in Section 2.3.3 and, for this reason, they strongly influence the buckling behaviour and ultimate load-carrying capacity of thin-walled members. As discussed by Schafer *et al.* (2010), the characteristics (*i.e.* shape, magnitude and distribution) of initial geometric imperfections have a significant impact on the results obtained from numerical simulations. Hence, the effects of geometric imperfections need to be understood well and considered with caution.

Initial cross-section level geometric imperfections are most commonly based on the first buckling mode, with their magnitude often being a function of the section thickness (Schafer et al., 2010). Schafer and Peköz (1998a) collected data from a wide range of physical measurements to propose the following empirical rules concerning the magnitude of imperfections. The collected data was categorised into two groups, as shown in Figure 2.17: type 1 imperfections corresponding to local buckling of a stiffened element, and type 2 imperfections corresponding to the maximum deviation from straightness of a lipped/unlipped flange (*i.e.* to distortional buckling). The proposed rules are applicable to thicknesses of less than 3 mm and to plate elements with width to thickness ratios (w/t) less than 200 and 100 for imperfection types 1 and 2 respectively (Schafer and Peköz, 1998a).

(a) Type 1: Local   (b) Type 2: Distortional
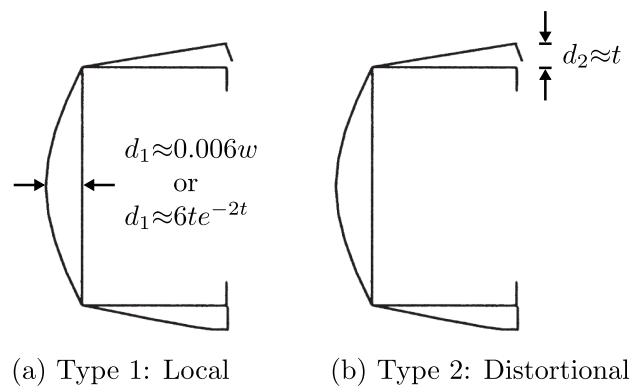
Figure 2.17: Definition of initial geometric imperfections for (a) local and (b) distortional buckling. Adapted from Schafer and Peköz (1998a).

As an alternative to the aforementioned rules, Schafer and Peköz (1998a) proposed a set of cumulative distribution function (CDF) values that account for the probability of occurrence of a particular imperfection magnitude. The CDF values are summarised in Table 4.2. For instance, for a given cold-formed steel member, there is a 75% probability that the maximum magnitude of a type 2 imperfection will be less than d_2/t=1.55. A summary of the available imperfection measurements for cold-formed steel members has been provided by Zeinoddini and Schafer (2012). The authors also introduced three methods of simulating imperfections, with the effect of these methods on the strength of cold-formed steel members being investigated.

For the purpose of modelling the initial geometric imperfections in cold-formed steel members in numerical simulations, the critical buckling mode shapes (at cross-sectional level) and critical half-wavelengths of the member can be utilised. These can be obtained using elastic buckling

Table 2.1: Imperfection magnitudes corresponding to the CDF values proposed by Schafer and Peköz (1998a); d_1 and d_2 are defined in Figure 2.17.

	25% CDF	50% CDF	75% CDF	95% CDF	99% CDF
d_1/t	0.14	0.34	0.66	1.35	3.87
d_2/t	0.64	0.94	1.55	3.44	4.47

analysis, as described in the next sub-section. Note that further background research regarding initial geometric imperfections, as well as a detailed description of the modelling approach adopted for the purpose of the current work, is provided in Section 4.2.4.

2.3.5   Elastic buckling analysis

Elastic buckling analysis techniques can be employed to determine the elastic critical buckling loads/moments, *i.e.* the load/moment at which instability is triggered, of cold-formed steel members. In current design codes, such as the North American (AISI S100-16, 2016), Australian/New Zealand (Standards Australia, 2018) and European (EN 1993-1-3, 2006) specifications, the elastic critical buckling loads/moments are utilised as reference loads for the calculation of the slenderness and ultimate strength of cold-formed steel members. As discussed in Section 2.3.6, elastic buckling analysis facilitates the use of the Direct Strength Method (DSM), which can be employed for the design of cold-formed steel members.

The principal characteristics of the most widely known numerical methods for conducting elastic buckling analysis, namely the Finite Element Method (FEM), Finite Strip Method (FSM), constrained Finite Strip Method (cFSM) and Generalised Beam Theory (GBT) are described below. Further details can be found in the Commentary to Section 2.2 in the North American Specification for 2016 (AISI S100-16, 2016), as well as in the work of Li (2016).

2.3.5.1   Finite Element Method (FEM)

As shown in Figure 2.18(a), in FE modelling, plate or shell elements are utilised for the cross-section discretisation. A three-dimensional model is created and an eigenvalue buckling analysis is performed to determine the elastic buckling loads (eigenvalues) and the buckling mode shapes (eigenvectors). The primary advantage of FE analysis is that all the features of the cold-formed

(a) Finite Element Method   (b) Finite Strip Method
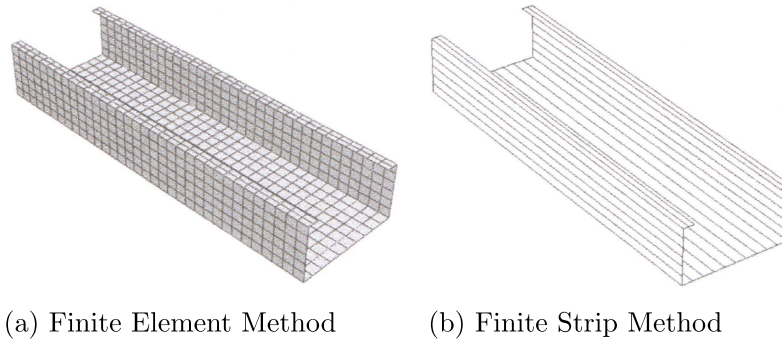
Figure 2.18: (a) Shell finite element mesh and (b) finite strip mesh (Li and Schafer, 2010a).

steel member, for instance boundary conditions, moment gradients, holes, attachments and variations in thickness along the member (Schafer, 2006), can be modelled explicitly.

Examples of using shell FE models to determine the elastic buckling strength of cold-formed steel members and plates with holes include the works of Moen and Schafer (2009a; 2009b). It should be noted that the modelling of boundary conditions in FE models requires careful treatment since features such as longitudinal warping can have a significant impact on elastic buckling analysis results (Dinis et al., 2007). Other features requiring careful consideration include the element type and mesh density (Schafer et al., 2010).

The primary drawback concerning the use of the FEM to conduct elastic buckling analysis is the visual inspection required to identify the characteristic buckling mode shapes out of the numerous obtained modes and the classification of those modes into local, distortional and global buckling. This is a subjective and often tedious process that can make the FEM an inefficient option for the purpose of elastic buckling analysis. Work on the automatic identification of the critical buckling modes in shell FE models has been conducted by Li et al. (2013; 2014).

2.3.5.2   Finite Strip Method (FSM)

As shown in Figure 2.18(b), in the FSM, a series of longitudinal strips are utilised for the cross-section discretisation with the displacement field being defined by shape functions in the transverse and longitudinal directions. Depending on the type of these shape functions, the FSM can be categorised further into: (i) semi-analytical FSM and (ii) spline FSM (Li, 2016); in the former, trigonometric functions are utilised, while, in the latter, spline functions are employed. In comparison with the semi-analytical FSM, the spline FSM is capable of modelling more complex loading and boundary conditions (Li, 2016).
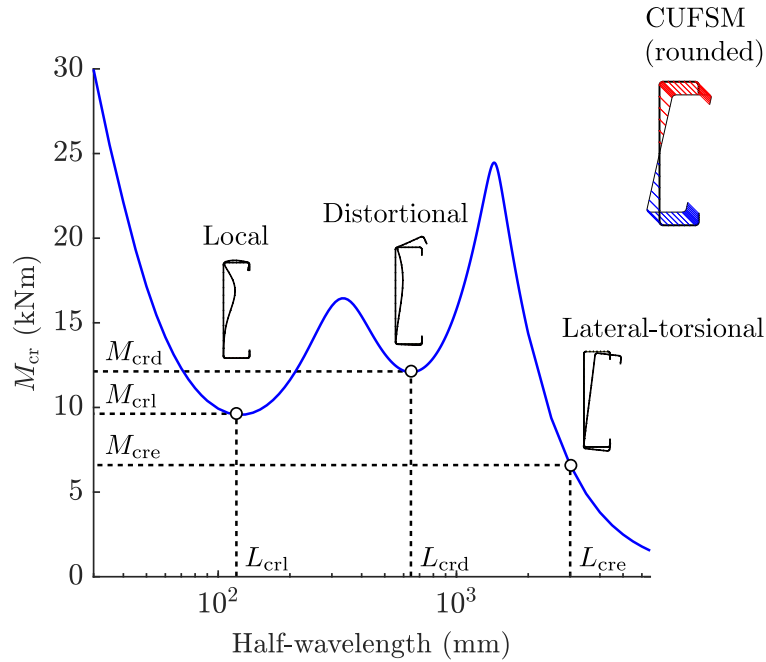
Figure 2.19: Signature curve obtained using CUFSM. Determination of the elastic critical buckling moments and the respective half-wavelengths. Cross-section with rounded corners used.

The theoretical development and stability analysis of the FSM has been described by Cheung and Tham (1997) and Schafer and Ádány (2006) respectively. In the present work, the semi-analytical FSM is employed to obtain the so-called 'signature curve' (Hancock, 1978) that provides the elastic critical buckling loads/moments. The FSM is implemented using the open source software CUFSM (2006), which performs the analysis for a pre-determined number of half-wavelengths based on the assumption that the member buckles along the member (*i.e.* along the x-direction) in half sine waves according to the following expression (Schafer, 2006):

$$\text{Buckling mode} = \text{2D mode shape} \times \sin\left(\frac{\pi x}{\text{half-wavelength}}\right). \tag{2.3}$$

The results are reported in the form of a signature curve, as demonstrated in Figure 2.19 in the case of a reference lipped channel cross-section subjected to positive bending. The critical local and distortional buckling points are indicated by the two minimum points of the curve, while the lateral-torsional buckling point depends on the unbraced length of the member. As demonstrated in Figure 2.19, from these points, the elastic critical local M_{crl}, distortional M_{crd} and lateral-torsional M_{cre} buckling moments are obtained together with the respective critical half-wavelengths L_{crl}, L_{crd} and L_{cre}. As described in Section 2.3.4, the buckling mode shapes at the critical points can be utilised to define the initial geometric imperfections in numerical

simulations of cold-formed steel members.

2.3.5.3 Constrained Finite Strip Method (cFSM)

The cFSM was derived from the semi-analytical FSM and can be employed using the CUFSM software (Li et al., 2014). The two primary applications of the cFSM are modal decomposition and modal identification, which, as described below, originate from the capability of the cFSM to decompose the elastic buckling solution into the pure local, distortional and global modes.

Depending on the cross-sectional geometry and applied stress distribution, the signature curve obtained using the conventional FSM (*i.e.* CUFSM) may have 'indistinct' minimum points. This is demonstrated in Figure 2.20(a), where, on the signature curve corresponding to a reference lipped channel section subjected to pure compression, there is no distinct minimum point corresponding to distortional buckling. This issue can be resolved using modal decomposition, whereby cFSM is employed to determine the pure distortional buckling curve, as shown in Figure 2.20(a). The critical distortional half-wavelength L_{crd} can be determined from the minimum point of the pure distortional buckling curve and, subsequently, the critical distortional buckling load P_{crd} can be obtained from the original signature curve. The above approach was initially proposed by Li and Schafer (2010a) as the "FSM@cFSM-L_{cr}" method. It should be emphasised that the above analysis must be performed using an equivalent cross-section with sharp corners (Li and Schafer, 2010a; Beregszászi and Ádány, 2011; Li et al., 2014), as shown in Figure 2.20(a).

The presence of indistinct minimum points is attributed to the fact that CUFSM considers the interactions between the different buckling modes (Ádány and Beregszászi, 2008). A measure of these interactions can be obtained using the modal identification function of cFSM, whereby the contribution of each mode is visualised as part of the signature curve, as shown in Figure 2.20(b). Similarly, the participation of each mode at each half-wavelength is demonstrated in Figure 2.20(c), where it is observed that, at the critical local buckling point, the participation of the local mode is almost 100%. Conversely, at the critical distortional buckling point there is also an approximately 20% and 5% participation from the local and global modes respectively.

The critical buckling loads/moments obtained using cFSM cannot be used directly in design since the DSM strength expressions are calibrated according to the conventional FSM (Li, 2016).

(a) Modal decomposition

(b) Modal identification

(c) Modal participation
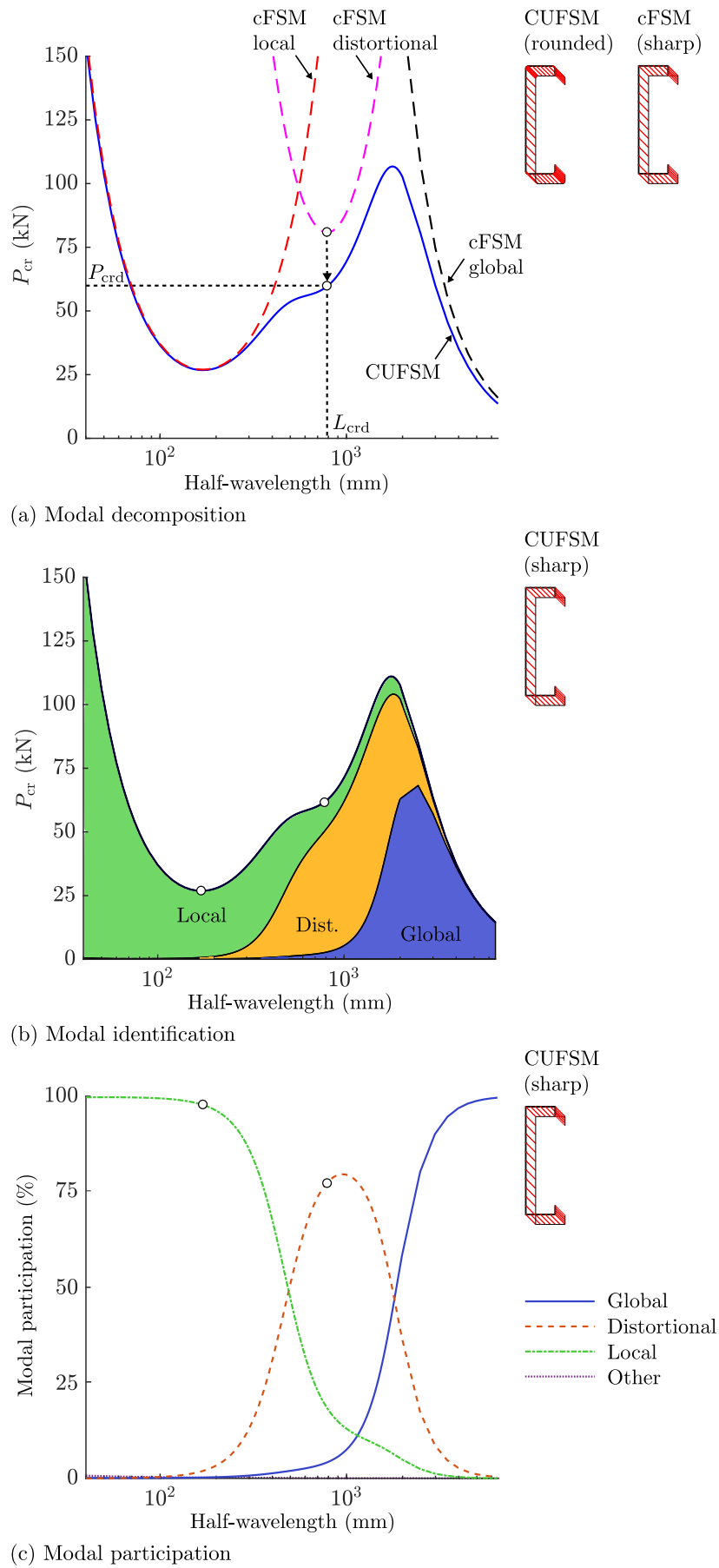
Figure 2.20: (a) Modal decomposition (utilising the FSM@cFSM-L_{cr} method), (b) modal identification and (c) modal participation using the cFSM.

For instance, as shown in Figure 2.20(a), the elastic critical distortional buckling strength obtained from cFSM is considerably higher than that obtained from the CUFSM signature curve. According to Àdàny and Beregszàszi (2008), in the case of distortional buckling, these differences can range from 4% to 50%. Hence, if the critical loads/moments from cFSM were used in design, these over-predictions would be carried forward in the DSM strength expressions, thus leading to unsafe capacity predictions (Ádány and Beregszászi, 2008). Note that, in the case of local buckling, these differences are typically considerably smaller (Ádány and Beregszászi, 2008). This is demonstrated in Figure 2.20(a), where the minimum points of the CUFSM and cFSM local buckling curves coincide.

2.3.5.4 Generalised Beam Theory (GBT)

Generalised Beam Theory (GBT) can be utilised to conduct an elastic buckling analysis for thin-walled members under various loading and boundary conditions. This is achieved by expressing the cross-section displacement field as a linear combination of deformation modes (Basaglia et al., 2011). Furthermore, in a similar manner to cFSM, GBT can provide modal decomposition and identification; a comparison between GBT and cFSM is provided by Àdàny et al. (2009). Originally developed by Schardt (1989), the GBT has been extended over the last few years by many researchers, such as Silvestre and Camotim (2002a; 2002b), with a special GBT-based beam finite element being proposed more recently by Camotim et al. (2008).

2.3.6 Direct Strength Method

The Direct Strength Method (DSM) is a design approach that provides predictions for the ultimate strength of cold-formed steel members, without the use of effective widths (Schafer, 2008). As described below, in the DSM, the critical elastic buckling loads/moments of the member are used as inputs in empirically derived strength equations that account for the post-buckling reserve alongside the interaction between yielding and local, distortional and global buckling. The elastic buckling strength of cold-formed steel members can be determined using elastic buckling analysis, as discussed in Section 2.3.5.

The DSM is an alternative design method to the classical Effective Width Method (EWM), which is currently utilised in most design specifications around the world (Schafer, 2008). In

the latest version of the North American Specification (AISI S100-16, 2016), the DSM has been incorporated into the main chapters (Chapters D to H), as an equivalent method to the EWM. Recommended sources for further reading regarding the DSM include the Commentary on Appendix 1 in the North American Specification for 2012 (AISI S100-12, 2012), the DSM Design Guide (Schafer, 2006) and the works of Schafer (2008) and Camotim *et al.* (2016).

2.3.6.1 The basic idea

The idea of developing a 'direct' approach for the design of cold-formed steel members was initiated by Hancock *et al.* (1994), who proposed strength design curves for cold-formed steel cross-sections experiencing distortional buckling. Later, the DSM was introduced by Schafer and Peköz (1998b) as an alternative to the traditional EWM. The authors calibrated the strength design curves against a collection of experimental data and proposed the use of advanced elastic buckling analysis for the prediction of the elastic buckling strength of cold-formed steel members.

Using the DSM, the resistance of a cold-formed steel member can be determined directly from its elastic critical buckling strength. The fundamental concept is that the ultimate strength F_{n} of the member is a function of the yield stress F_{y} and the elastic critical stresses for local F_{crl}, distortional F_{crd} and global F_{cre} buckling, *i.e.* $F_{\mathrm{n}}=\{F_{\mathrm{crl}}, F_{\mathrm{crd}}, F_{\mathrm{cre}}, F_{\mathrm{y}}\}$ (Camotim et al., 2016). Based on this concept, strength equations that account for different loading configurations (*e.g.* axial compression or bending) and features (*e.g.* with or without holes) have been developed (AISI S100-16, 2016). The only required input in these equations is the elastic critical buckling load/moment of the member, which can be determined using elastic buckling analysis, as discussed Section 2.3.5. The DSM provisions for members subjected to axial compression, bending or combined axial compression and bending are outlined below; a more extensive overview regarding these provisions has been provided by Schafer (2006; 2008; 2018).

Applications and recent advancements regarding the DSM include cold-formed steel columns, beams, beam-columns, angles, shear buckling, built-up members, members with holes, elevated temperatures, member optimisation, as well as other materials, such as stainless steel, hot-rolled steel, aluminium and plastics (Schafer, 2017, 2018; Camotim et al., 2016).

2.3.6.2   Members under axial compression

The development of the DSM strength equations for members in compression was reported by Schafer (2002). To calibrate the proposed design equations, the failure loads P_{test} from several experimental studies on concentrically loaded pin-ended columns were utilised. A list of the references for these studies can be found in the Commentary on Appendix 1 in AISI S100-12 (2012). As shown in Figure 2.21(a), the DSM strength curves are a function of the local $\lambda_{\text{l}}{=}\sqrt{P_{\text{ne}}/P_{\text{crl}}}$ and distortional $\lambda_{\text{d}}{=}\sqrt{P_{\text{y}}/P_{\text{crd}}}$ slendernesses of the columns, with P_{crl} and P_{crd} being the respective elastic critical buckling loads; P_{ne} and P_{y} are the nominal axial resistance for global flexural buckling and the squash (yield) load respectively.

Following the determination of the elastic critical buckling loads, the design equations provided in Chapter E in AISI S100-16 (2016) can be used to evaluate the nominal axial compressive resistance P_{n} of the column, which is equal to the minimum of the nominal axial resistance for local P_{nl}, distortional P_{nd} and global P_{ne} buckling, *i.e.* $P_{\text{n}}{=}\min\{P_{\text{nl}}, P_{\text{nd}}, P_{\text{ne}}\}$.

The expressions for P_{nl} are given by:

$$\text{for} \quad \lambda_{\text{l}} \leqslant 0.776, \quad P_{\text{nl}} = P_{\text{ne}}, \tag{2.4}$$

$$\text{for} \quad \lambda_{\text{l}} > 0.776, \quad P_{\text{nl}} = \left[1 - 0.15\left(\frac{P_{\text{crl}}}{P_{\text{ne}}}\right)^{0.4}\right]\left(\frac{P_{\text{crl}}}{P_{\text{ne}}}\right)^{0.4} P_{\text{ne}}, \tag{2.5}$$

while P_{nd} can be determined using:

$$\text{for} \quad \lambda_{\text{d}} \leqslant 0.561, \quad P_{\text{nd}} = P_{\text{y}}, \tag{2.6}$$

$$\text{for} \quad \lambda_{\text{d}} > 0.561, \quad P_{\text{nd}} = \left[1 - 0.25\left(\frac{P_{\text{crd}}}{P_{\text{y}}}\right)^{0.6}\right]\left(\frac{P_{\text{crd}}}{P_{\text{y}}}\right)^{0.6} P_{\text{y}}. \tag{2.7}$$

The design curves for local and distortional buckling in the case of a fully braced column are shown in Figure 2.22(a). As indicated by the location of the design curves relative to the elastic critical buckling curve, the post-buckling strength related to the local buckling mode is greater than that for the distortional buckling mode. The design provisions for global (flexural, torsional or flexural-torsional) buckling are the same as the recommendations for hot-rolled
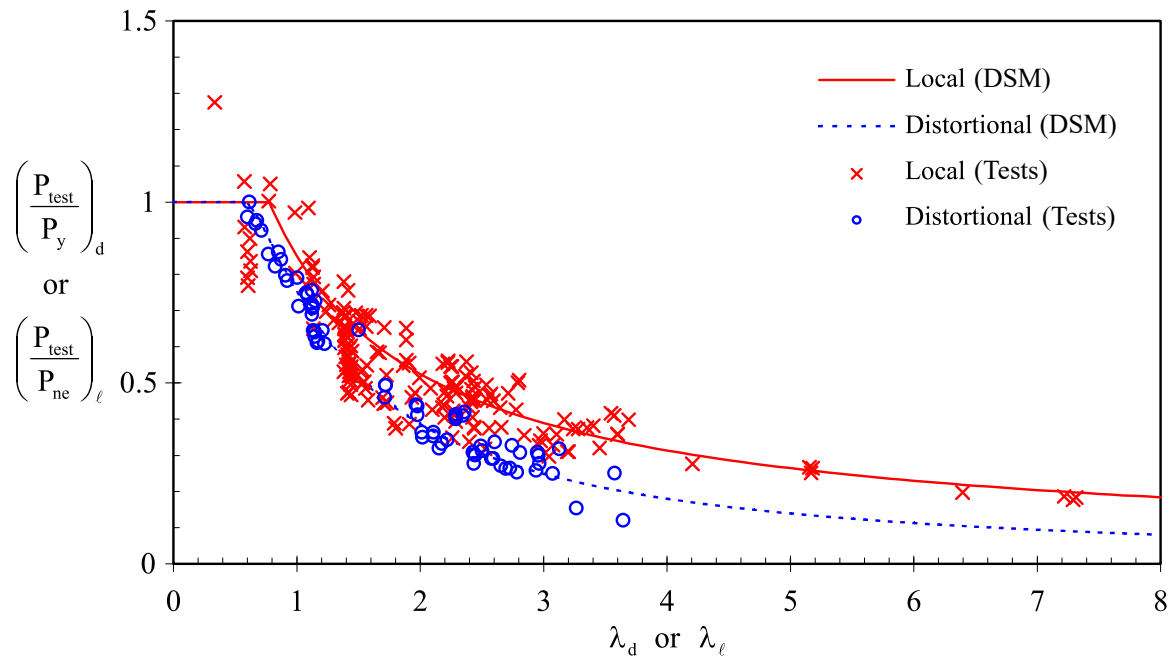
(a) Concentrically loaded pin-ended columns
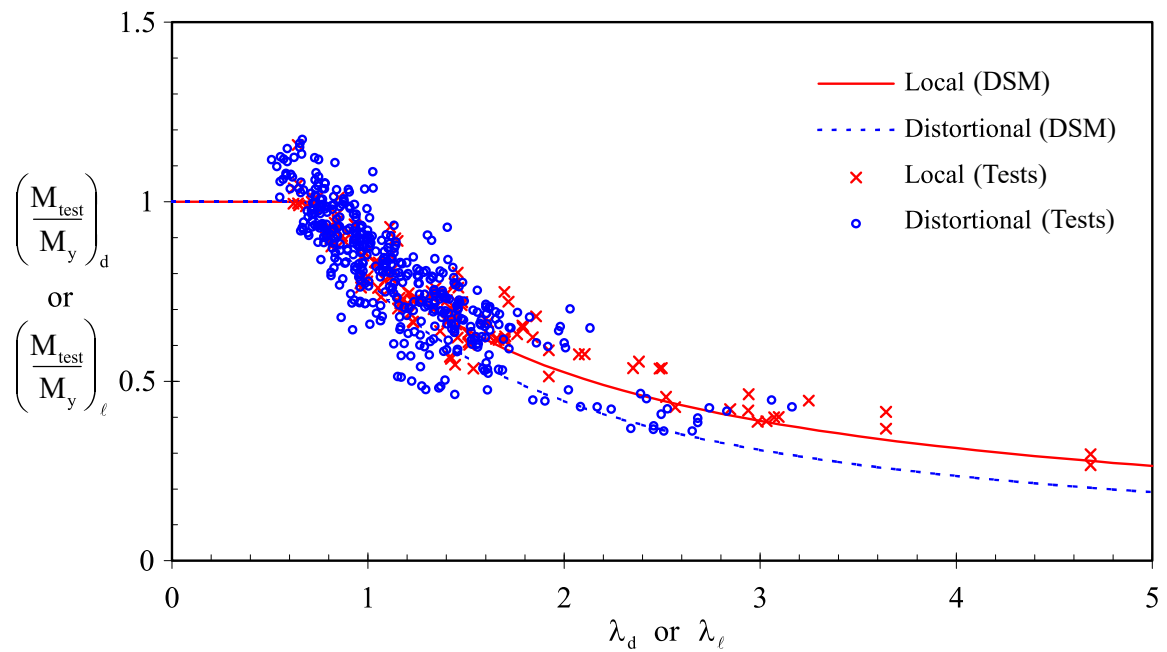
(b) Beams braced against lateral-torsional buckling

Figure 2.21: Direct Strength Method calibration for cold-formed steel columns and beams. Adapted from AISI S100-16 (2016).

(a) Braced column

(b) Laterally braced beam
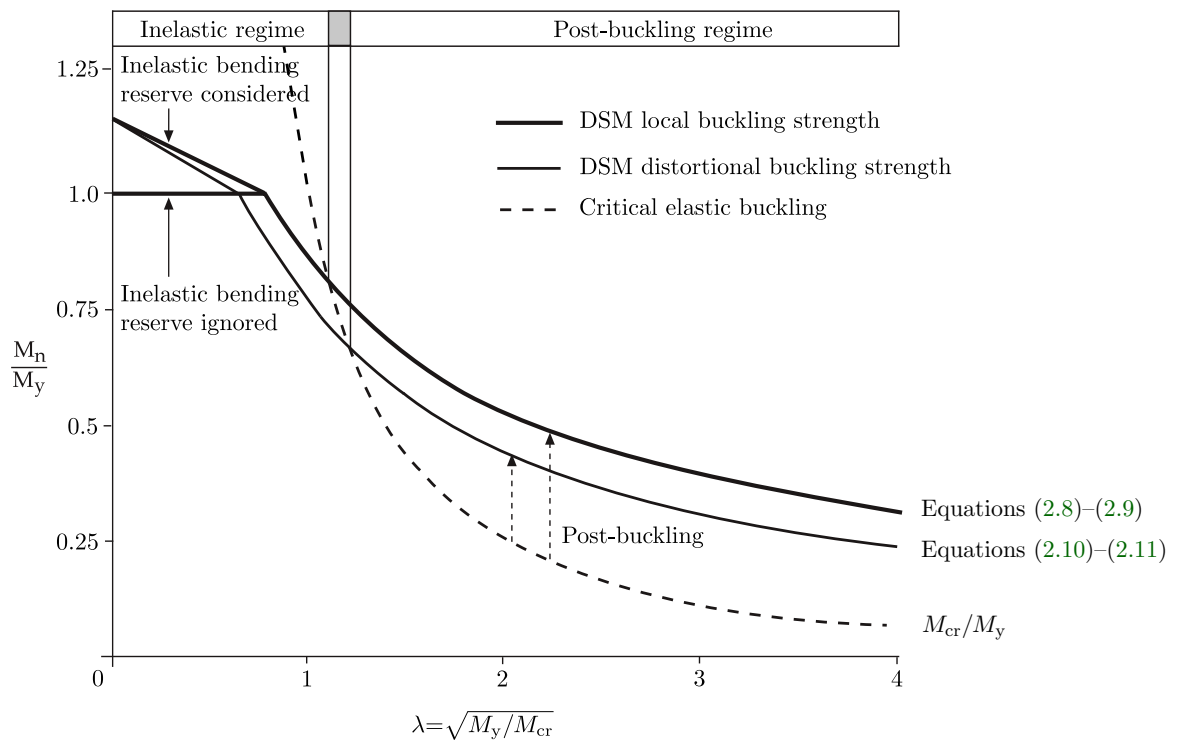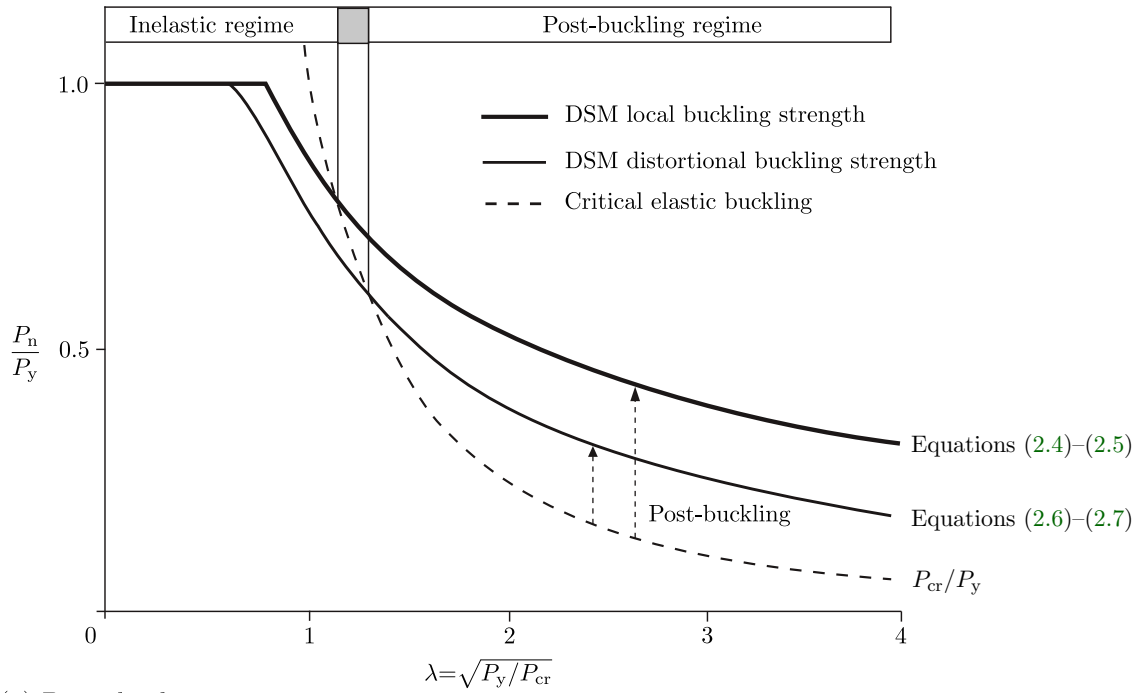
Figure 2.22: Local and distortional direct strength curves for (a) braced columns and (b) laterally braced beams. Adapted from AISI S100-16 (2016).

compact columns. To account for local–global buckling interaction, P_{nl} is limited to P_{ne}, instead of P_y. In contrast, P_{nd} is limited to P_y since the DSM does not consider any distortional–global buckling interaction (AISI S100-16, 2016).

2.3.6.3 Members under bending

The development of the DSM strength equations for members in bending was initiated by Schafer and Peköz (1998b). To calibrate the proposed design equations, the failure moments M_{test} from several experimental studies on laterally braced beams were used. A list of references for these studies can be found in the Commentary on Appendix 1 in AISI S100-12 (2012). Experimental (Yu and Schafer, 2003, 2006) and numerical (Yu and Schafer, 2007) studies were conducted later to provide additional supporting data.

As shown in Figure 2.21(b), the DSM strength curves are a function of the local $\lambda_l = \sqrt{M_{ne}/M_{crl}}$ and distortional $\lambda_d = \sqrt{M_y/M_{crd}}$ slendernesses of the beams, with M_{crl} and M_{crd} being the respective elastic critical buckling moments; M_{ne} and M_y are the nominal bending resistance for lateral-torsional buckling and the yield moment respectively. Following the determination of the elastic critical buckling moments, the nominal bending resistances for local M_{nl}, distortional M_{nd} and global M_{ne} buckling can be evaluated using the DSM expressions provided in Chapter F in AISI S100-16 (2016). The nominal bending resistance of the cold-formed steel beam is equal to the minimum of the nominal resistances for the individual buckling modes, *i.e.* $M_n = \min\{M_{nl}, M_{nd}, M_{ne}\}$. The expressions for M_{nl} are given by:

$$\text{for} \quad \lambda_l \leqslant 0.776, \quad M_{nl} = M_{ne}, \tag{2.8}$$

$$\text{for} \quad \lambda_l > 0.776, \quad M_{nl} = \left[1 - 0.15\left(\frac{M_{crl}}{M_{ne}}\right)^{0.4}\right]\left(\frac{M_{crl}}{M_{ne}}\right)^{0.4} M_{ne}, \tag{2.9}$$

while M_{nd} can be obtained using:

$$\text{for} \quad \lambda_d \leqslant 0.673, \quad M_{nd} = M_y, \tag{2.10}$$

$$\text{for} \quad \lambda_d > 0.673, \quad M_{nd} = \left[1 - 0.22\left(\frac{M_{crd}}{M_y}\right)^{0.5}\right]\left(\frac{M_{crd}}{M_y}\right)^{0.5} M_y. \tag{2.11}$$

The design curves for local and distortional buckling in the case of laterally braced beams are shown in Figure 2.22(b), where it is observed that the post-buckling strength for local buckling is greater than that for distortional buckling. The bending resistance of cold-formed steel beams is limited by either M_{y} or M_{ne}, depending on the unbraced length of the member; for fully braced beams, $M_{\text{ne}}{=}M_{\text{y}}$. Local–global buckling interaction is accounted by limiting M_{nl} to M_{ne}, while, since distortional–global buckling interaction is not considered, M_{nd} is limited to M_{y}. As indicated by the linear approximations in Figure 2.22(b), the DSM also accounts for any inelastic bending reserve in cold-formed steel beams undergoing local (provided that $\lambda_{\text{l}}{\leqslant}0.776$ and $M_{\text{ne}}{\geqslant}M_{\text{y}}$) or distortional buckling (provided that $\lambda_{\text{d}}{\leqslant}0.673$) (Shifferaw and Schafer, 2012).

2.3.6.4 Members under combined axial compression and bending

Cold-formed steel members subjected to combined axial loading and bending are typically referred to as beam-columns. As discussed below, these members can be designed either by employing the linear interaction equations proposed in current design specifications or by utilising the recently developed DSM provision for cold-formed steel beam-columns.

(a) Linear interaction equations

Current design specifications, such as AISI S100-16 (2016), utilise interaction equations for the design of cold-formed steel beam-columns. As presented below, the interaction equations are simply linear combinations of the pure axial P_{n} and pure bending M_{n} resistances of the cold-formed steel member, which can be determined using the DSM (or the EWM), as discussed in Sections 2.3.6.2 and 2.3.6.3 respectively.

Assuming no member second-order effects, the overall compressive stress level $\overline{\sigma}$ within a cross-section subjected to combined axial compression $\overline{P}$ and bending $\overline{M}$ is given by:

$$\overline{\sigma} = \frac{\overline{P}}{A_{\text{s}}} + \frac{\overline{M}}{S} = \overline{\sigma}_{\text{a}} + \overline{\sigma}_{\text{b}} \leqslant F_{\text{a}}, \tag{2.12}$$

where A_{s} and S are the cross-sectional area and elastic section modulus respectively; the overall compressive stress, comprising an axial $\overline{\sigma}_{\text{a}}$ and a bending $\overline{\sigma}_{\text{b}}$ component, is limited by the allowable compressive stress level F_{a}. Re-arranging Equation (2.12) and

accounting for the appropriate resistance factors:

$$\frac{\overline{\sigma}_{\mathrm{a}}}{F_{\mathrm{a,c}}} + \frac{\overline{\sigma}_{\mathrm{b}}}{F_{\mathrm{a,b}}} \leqslant 1.0, \qquad (2.13)$$

where $F_{\mathrm{a,c}}$ and $F_{\mathrm{a,b}}$ are the available stress levels for columns and beams respectively. Multiplying the axial compression and bending components by A_{s} and S respectively, the linear interaction equation can be obtained in terms of the applied axial loading and bending, *i.e.*:

$$\frac{\overline{P}}{P_{\mathrm{a}}} + \frac{\overline{M}}{M_{\mathrm{a}}} \leqslant 1.0, \qquad (2.14)$$

where P_{a} and M_{a} are the available axial compressive and bending resistances respectively.

In Chapter H of AISI S100-16 (2016), Equation (2.14) is reported to have the following form:

$$\frac{\overline{P}}{P_{\mathrm{a}}} + \frac{\overline{M}_{\mathrm{x}}}{M_{\mathrm{ax}}} + \frac{\overline{M}_{\mathrm{y}}}{M_{\mathrm{ay}}} \leqslant 1.0, \qquad (2.15)$$

where, in the numerators, $\overline{P}$ is the axial compressive force based on factored loads (*i.e.* the required axial compressive strength) with due allowance for any global second-order effects and $\overline{M}_{\mathrm{x}}$ and $\overline{M}_{\mathrm{y}}$ are the bending moments based on factored loads (*i.e.* the required flexural strengths) about the major and minor centroidal axes respectively, with due allowance for both global and member second-order effects. In the denominators, P_{a} is the factored axial compressive resistance (*i.e.* the available axial strength) of the member, while M_{ax} and M_{ay} are the factored bending resistances (*i.e.* the available flexural strengths) about the major and minor centroidal axes respectively. The second-order and moment gradient effects are approximated by means of moment amplification factors, which, according to Chapter C1 of AISI S100-16 (2016), need to be included in the determination of $\overline{P}$, $\overline{M}_{\mathrm{x}}$ and $\overline{M}_{\mathrm{y}}$.

(b) DSM for cold-formed steel beam-columns

It has been observed that the current approach for the design of cold-formed steel beam-columns can be overly conservative because the stability of the member under the actual stress distribution that arises owing to the combined axial loading and bending is not
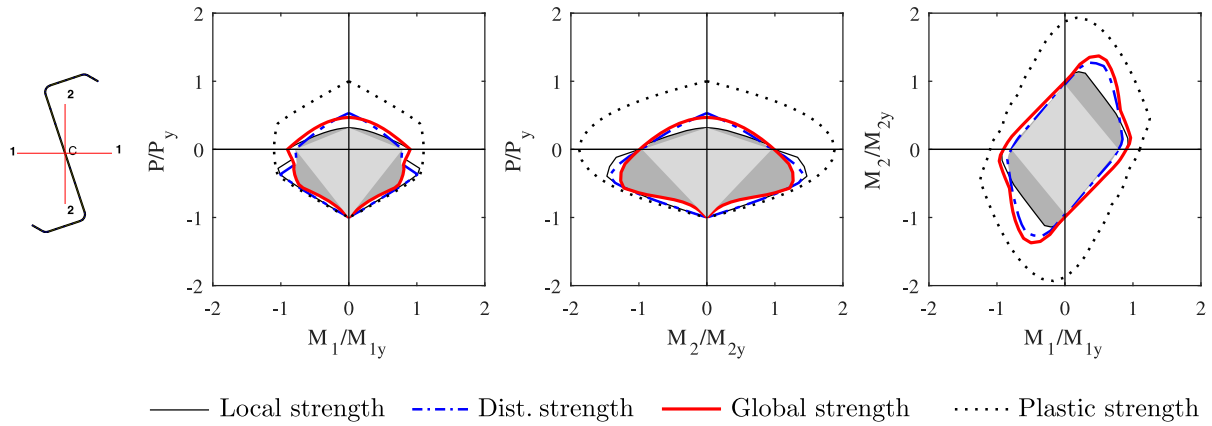
Figure 2.23: Comparison between the currently proposed linear interaction equations (light gray) and the newly proposed DSM provisions for a Z-shaped beam-column; the difference between the two methos is indicated in dark grey (Torabian and Schafer, 2018).

considered directly (Torabian et al., 2014a; Torabian and Schafer, 2018). Instead, as presented above, a linear interaction between the pure axial and pure bending resistance end points is assumed; hence, any nonlinear interaction between the axial and bending resistances of the member is ignored (AISI S100-16, 2016; Torabian and Schafer, 2018). This effect has been investigated experimentally (Torabian et al., 2015, 2016c,b) and numerically (Torabian et al., 2014a, 2016a), with a new extension to the DSM being recently proposed to account for potential strength increases if the actual stress distribution is considered (Torabian and Schafer, 2018; Schafer, 2017, 2018).

The new DSM provision is applicable to members subjected to any combination of axial loading (compression or tension) and bending (major-axis or minor-axis) (Camotim et al., 2016). The method generalises the $P-M_1-M_2$ space, where P represents axial loading while M_1 and M_2 represent bending about the major and minor principal axes respectively (Schafer, 2018). Elastic buckling analysis is utilised to determine the critical buckling loading parameters based on the stress distribution induced by the applied axial loading and bending. It should be noted that the obtained interaction between the axial and bending resistances is cross-section specific (Schafer, 2008).

The effectiveness of the new DSM provisions is demonstrated in Figure 2.23, where the nominal strengths obtained by considering the actual stress distribution are compared with those obtained using the linear interaction equations. It is observed that the actual interaction between the buckling strengths, as determined using the proposed

DSM method, is remarkably different from the linear interaction assumed by the current design specifications. For the majority of the loading combinations, an increased nominal strength is obtained using the DSM (as indicated by the dark grey area), with significant increases being obtained in the case of specific loading combinations. Hence, as reported by Torabian and Schafer (2018), the newly proposed DSM beam-column provisions have the potential of providing more representative predictions of the actual strength of cold-formed steel beam-columns, thus eliminating the conservatism provided by the linear interaction equations.

2.3.6.5 Direct Strength Method versus Effective Width Method

Currently, the EWM and the DSM are the two principal design methods for cold-formed steel members. The EWM was originally proposed by von Kármán (1932) and was later modified by Winter (1947). Essentially, to account for the development of local instabilities in the compressed plates of the cross-section, and thus consider the loss in their effectiveness to carry further axial loading, the EWM reduces the gross cross-section properties to effective cross-section properties. To achieve this, it is assumed that, once local buckling is trigerred, only the edge regions of the compressed plates are capable of carrying axial loading, with the central region of the plates carrying no axial loading; the combined width of the two edge regions comprise the effective width of the plate. The EWM conceptualises the entire member as a collection of plated elements and thus requires the determination of the effective width of each element (AISI S100-16, 2016).

The advantages of the EWM include the fact that it provides an indication of the locations within the cross-section where local buckling has taken place (Schafer, 2008). The shift of the neutral axis within the cross-section due to local buckling is also taken into account. However, the interaction and compatibility between the cross-section elements is ignored, while the consideration of distortional buckling requires tedious procedures. Moreover, the EWM requires lengthy and iterative calculations, especially in case of the geometrically complex cross-sections.

The advantages of the DSM in comparison with the EWM, originate from the fact that the cross-section is considered as a whole (Camotim et al., 2016). In this manner, equilib-

rium and compatibility between the different elements of the cross-section, as well as the effect of stiffeners, are therefore ensured. Furthermore, instead of calculating empirical effective widths, the DSM requires the determination of the elastic buckling strength of the member; this can be readily achieved using elastic buckling analysis tools, such as the Finite Strip Method (FSM), as discussed in Section 2.3.5.2. In the DSM, the gross cross-section properties are used, the shift in the neutral axis of the cross-section is not considered (AISI S100-16, 2016) and no iterations are required. The fact that advanced buckling analysis techniques can be used encourages the optimisation of cold-formed steel members and the extension of the applicability of the DSM. Finally, the DSM was calibrated based on the results from experiments on a broad range of cross-sections with its reliability being considered to be as good, or better than that of the EWM (Schafer, 2008). Further comparisons between the EWM and the DSM can be found in the works of Schafer (2006; 2008), Yu and LaBoube (2010) and Camotim *et al.* (2016).

2.4 Concluding remarks

In the present chapter, a literature review regarding the two driving principles of the proposed prestressed cold-formed steel beams has been presented. The purpose of the literature review was to describe the key technical background relevant to this thesis and to demonstrate how the benefits offered by prestressing techniques can potentially be exploited to enhance the performance of cold-formed steel members.

The utilisation of prestressing techniques to enhance the performance of steel structures, such as bare steel and composite beams, as well as the origin of the obtained benefits, have been the primary focus of the first part of the literature review. It was demonstrated that the fundamental concept in prestressed structures is the introduction of stresses within the structural members that are opposite in sign to the stresses induced during the subsequent loading stages. These initial stresses counteract the stresses imposed by the applied loading and thus enhance the load-carrying capacity and serviceability performance of structural members. Furthermore, the influence of key controlling parameters, such as

the cross-sectional geometry of the prestressed member and the cable profile, on the effectiveness of the prestressing was explored.

The second part of the literature review has considered the principal characteristics, buckling analysis and design of cold-formed steel members. The production process and its influence on the material properties of cold-formed steel members was discussed first, demonstrating that the cold-forming process can have a substantial impact on the material behaviour. Subsequently, the effect of instability phenomena on the behaviour of cold-formed steel members was discussed. For this purpose, the characteristics of local, distortional and global buckling, as well as the effects of initial geometric imperfections, were described. The utilisation of different types of elastic buckling analysis techniques to determine the elastic buckling strength of cold-formed steel members was then outlined. Such techniques facilitate the understanding of the interactions between the different buckling modes in cold-formed steel members and are indispensable for the development of efficient and optimised geometries. Subsequently, an overview of the Direct Strength Method (DSM), which can be employed for the design of cold-formed steel members, was presented. The DSM provisions for columns, beams and beam-columns were outlined and, subsequently, a comparison with the more classical Effective Width Method (EWM) was provided. By utilising advanced elastic buckling analysis, the DSM provides a design approach that is user-friendly and more efficient than the iterative EWM, especially in the cases of geometrically complex cross-sections.

CHAPTER 3

CONCEPT, ANALYTICAL MODELLING AND FAILURE CRITERIA FOR DESIGN

3.1 Introduction

An innovative concept, whereby the load-carrying capacity and serviceability performance of cold-formed steel beams are enhanced by utilising prestressing techniques, is introduced in the present chapter. Firstly, the principal characteristics of the proposed prestressed cold-formed steel beams are described and the assumptions made throughout the present work are reported. Subsequently, analytical expressions are developed to examine the mechanical response of prestressed cold-formed steel beams during both the prestressing and the imposed vertical loading stages. The nature of the axial stress distributions at the critical cross-section during the different stages is studied and the origins of the obtained benefits are demonstrated. Failure criteria for the design of the cold-formed steel beam and the prestressed cable are then proposed by analysing the studied members as beam-columns. For this purpose, interaction equations, alongside the Direct Strength Method (DSM), are employed to determine the capacity of the cold-formed steel member under the combination of axial loads and bending moments. The conceptual development of prestressed cold-formed steel beams presented in this chapter has been published by Hadjipantelis *et al.* (2018a; 2018c).

81

3.2 The concept

Owing to their high strength-to-weight ratio, cold-formed steel members offer lightweight and low-carbon structural solutions in construction. However, as discussed in Section 2.3.3, as a consequence of their thin-walled geometry, cold-formed steel members are highly susceptible to instability phenomena, such as local, distortional and global buckling together with their interactions, which limit their load-carrying capacity.

In the proposed concept, which is illustrated in Figure 3.1, prestressing techniques are employed to delay the occurrence of the aforementioned instability phenomena in cold-formed steel beams. The prestressing force is applied by means of a high-strength steel cable, which is housed at a location eccentric to the strong geometric axis within the bottom hollow flange of the cold-formed steel beam, inducing initial stresses in the member that are opposite in sign to those introduced during the subsequent imposed vertical loading stage. Since these initial stresses need to be overcome first before detrimental compressive stresses develop within the top region of the cold-formed steel beam during the imposed loading stage, the member can carry increased loading before failure occurs, *i.e.* its load-carrying capacity is enhanced. Potentially, this enhancement can enable the use of smaller cross-sections for a given demand in capacity and span length, resulting in material and therefore self-weight savings relative to conventional non-prestressed cold-formed steel beams.

The overall vertical deflections of the member at the end of the imposed loading stage are reduced significantly due to the pre-camber that is naturally induced by the eccentric prestressing force, as shown in Figure 3.1, while the contribution of the high-strength steel cable to the bending stiffness of the system reduces the overall vertical deflections further. Hence, the proposed prestressed cold-formed steel beams also show an enhanced serviceability performance.

Potentially, as a result of their enhanced structural performance, prestressed cold-formed steel beams may be employed more widely as primary structural elements in the construction of buildings and other structures.
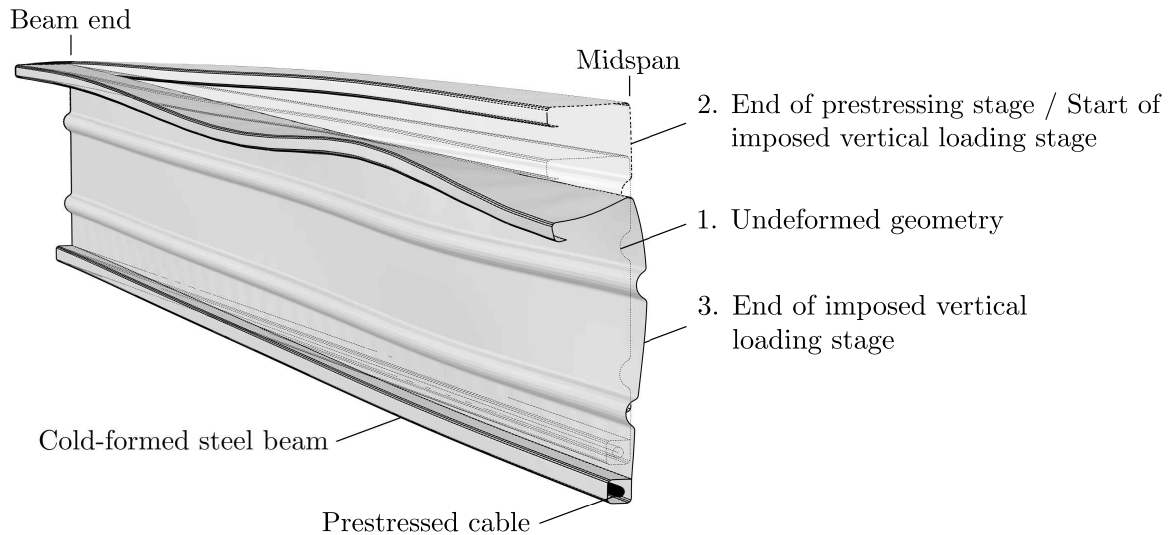
Figure 3.1: Cross-section cut at the midspan of the prestressed cold-formed steel beam showing the deformed geometry at the start and at the end of the two loading stages.

3.3 Principal characteristics

3.3.1 Cross-sectional geometry

In comparison with hot-rolled steel, the fabrication process of cold-formed steel is more rapid and less energy-intensive, while, as discussed in Section 2.3.1.1, the flexibility offered by the rolling or pressing process allows the fabrication of members with complex and tailored cross-sectional geometries. This is exploited in the proposed concept, where a tubular region is formed within the cross-section profile of the cold-formed steel beam to house the prestressing cable.

The proposed cross-section profile is shown in Figure 3.2(a), where the high-strength steel cable resides within the bottom hollow flange of the cold-formed steel beam, at an eccentricity e relative to its strong geometric (x–x) axis. Note that the prestressing cable is eccentric to the strong geometric axis but not to the weak axis of the cross-section. Similar cross-section profiles are currently being used in practice, such as the one tested by Kyvelou *et al.* (2017), as shown in Figures 2.11(c) and 3.2(b).

The cross-sectional geometry is essentially that of a lipped channel section with two longitudinal stiffeners in the web and with the bottom flange being bent back towards
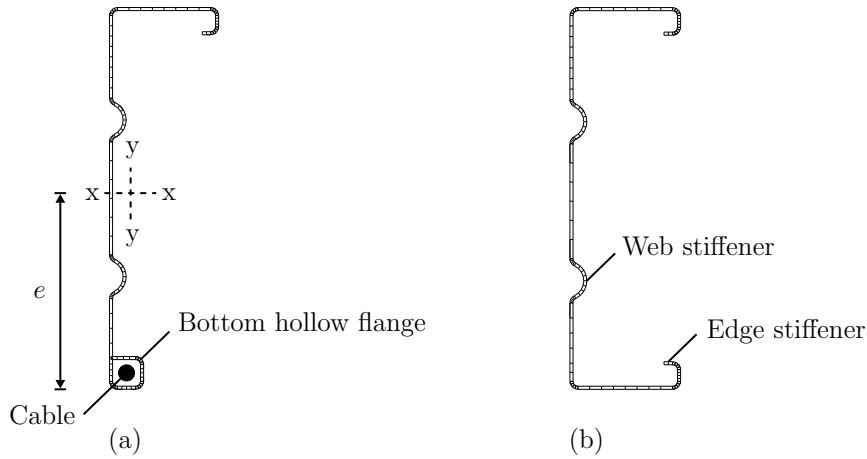
Figure 3.2: (a) Cross-section profile of the proposed prestressed cold-formed steel beams. (b) Lipped channel cross-section with web and edge stiffeners tested by Kyvelou *et al.* (2017).

the web to form the tubular region of the cross-section. The bottom stiffener is required to increase the resistance of the cross-section to local buckling during the prestressing stage while the bottom part of the cross-section is under compression. Similarly, the top stiffener increases the local buckling resistance of the cross-section during the imposed vertical loading stage while the top part of the cross-section is under compression.

The reference cross-section shown in Figure 3.3 is used as an example throughout the present chapter, the dimensions of which are listed in Table 3.1; r_c is the radius of the cable while r_1 and r_2 are the internal radii of the corners and web stiffeners respectively. The x–x and y–y axes shown in Figure 3.3 are the strong and weak geometric axes of the cross-section respectively.

Table 3.1: Dimensions of the reference cross-section profile; the symbols are defined in Figure 3.3.

$h = 280.0$ mm	$b_1 = 28.0$ mm	$t = 2.25$ mm	$r_1 = 3.5$ mm
$d_1 = 28.0$ mm	$b_2 = 70.0$ mm	$a_1 = 82.5$ mm	$r_2 = 12.0$ mm
$d_2 = 20.0$ mm	$b_3 = 12.0$ mm	$a_2 = 115.0$ mm	$r_\mathrm{c} = 5.25$ mm

3.3.2 Structural system

The proposed prestressed system comprises two structural components, namely the cold-formed steel beam and the high-strength steel cable, as shown in Figure 3.4. In the present work, the studied members are assumed to be in the simply-supported configuration.
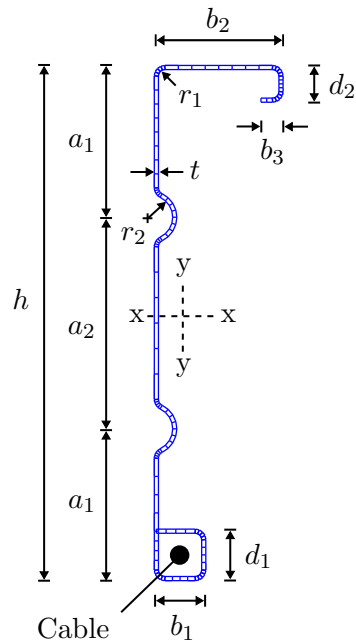
Figure 3.3: Reference cross-section profile of the studied prestressed cold-formed steel beam; external dimensions are shown.
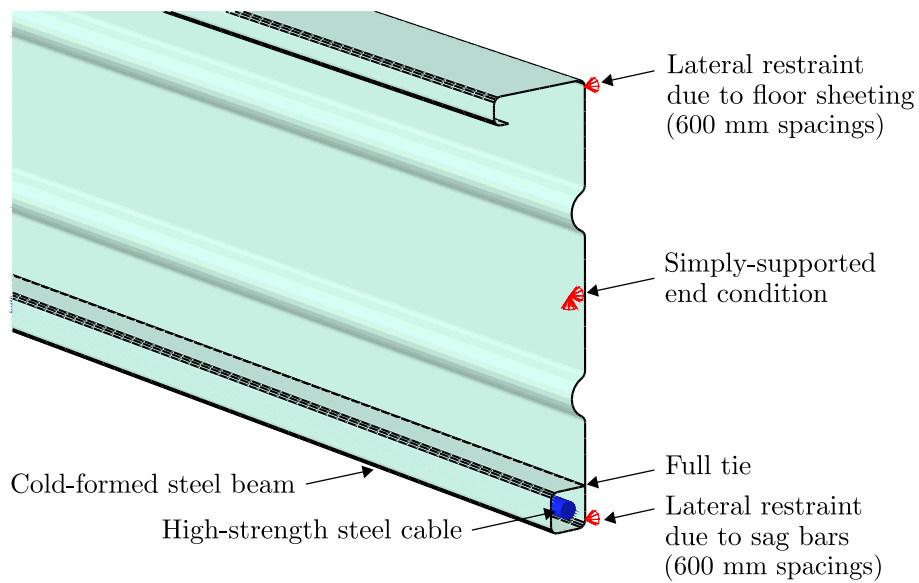
Figure 3.4: Primary features and restraints of the proposed prestressed structural system.

3.3.2.1 Cold-formed steel beam

The edge of the bottom flange of the cold-formed steel beam is assumed to be fully tied to the web, as indicated in Figure 3.4. The means of connection is not explicitly considered herein, but this could be achieved in practice using screws or an automated manufacturing process involving simultaneous cold-forming and electrical resistance welding, as performed in the case of 'LiteSteel' beams (Keerthan and Mahendran, 2010; Anapayan and Mahendran, 2012).

In the present work, it is also assumed that lateral restraints are provided by the presence of floor sheeting and sag bars interconnecting the top and bottom flanges of the cold-formed beam with those of the adjacent beams, as shown in Figure 3.5. These lateral restraints are idealised using boundary conditions and they are assumed to be located at 600 mm intervals along the member, as shown in Figure 3.4. Note that the influence of the presence of the floor sheeting on the response of the top flange when undergoing distortional buckling is not explicitly considered herein.
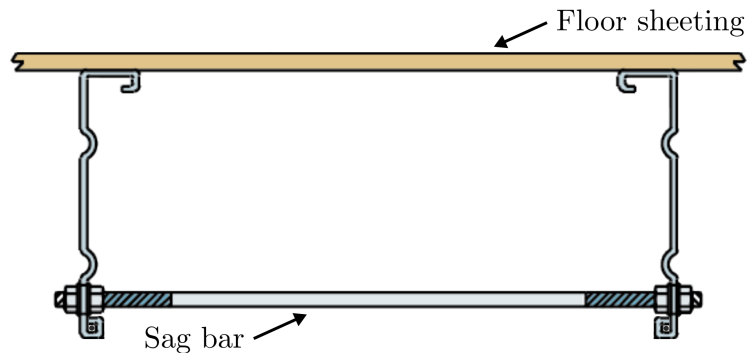
Figure 3.5: Schematic representation of the proposed structural system.

3.3.2.2 High-strength steel cable

In previous research on prestressed hot-rolled steel beams (Belletti and Gasperi, 2010; Kambal and Jia, 2018), the cable was located externally and deviators had to be installed along the beam to hold the cable in place. However, in the proposed system, the high-strength steel cable is housed within the cross-section profile of the member, as shown in Figure 3.4.

The cable is tensioned using a jacking mechanism and anchored at the two ends of the beam, where the transfer of the prestressing force takes place. Along the member, the cable is kept concentric to the bottom hollow flange either by a snug fit or by means of connecting collars that are dimensioned to an outer diameter matching the internal dimensions of the hollow flange and are fitted to the cable at regular intervals. The cable is allowed to elongate freely since no grouting is introduced within the hollow flange. Note that the design of the anchorage system at the two member ends is not explicitly examined herein.

3.3.3 Member restraints

The presence of the floor sheeting, sag bars and cable enhances the stability of the proposed structural system by providing a number of restraints, as discussed below:

(i) The proposed beams are assumed to be fully braced against lateral-torsional buckling during both the prestressing and the imposed vertical loading stages, owing to the lateral restraints provided by the presence of the floor sheeting and sag bars, as shown in Figures 3.4 and 3.5. In the present study, these lateral restraints are assumed to be located at 600 mm intervals along the member.

(ii) The lateral restraints also confine bending about the strong geometric (x–x) axis of the cross-section, thus preventing any asymmetric bending effects. Hence, in-plane bending about the x–x axis is studied herein; this assumption is verified in Section 5.2.7.1.

(iii) The cable enhances the stability of the system by restraining global flexural buckling during the prestressing and the imposed vertical loading stages, since in both stages the only source of axial compression is the prestressing force itself, whose line of action follows the deformation of the member. This has also been investigated in the works of Gosaye *et al.* (2016) and Wang *et al.* (2017), where the behaviour of prestressed steel tubular members was studied analytically, numerically and experimentally. In the aforementioned studies it has been shown that the presence of the cable reduces the effective length of the member and thus increases its global

flexural buckling strength significantly when subjected to an internal compressive prestressing force.

(iv) Distortional buckling arising from negative bending, *i.e.* during the prestressing stage while the bottom part of the cross-section is under compression, is restrained by both the presence of the cable and by the bottom lateral restraints. This is because both of these features prevent the lateral translations of the bottom flange of the member; this assumption is verified in Section 5.2.7.2.

3.3.4   Losses of prestress

Losses of prestress can arise in the proposed prestressed members during the transfer of the prestressing force (*e.g.* due to anchorage slippage, friction and elastic shortening of the cold-formed steel beam) or during the service life of the members (*e.g.* from relaxation of the prestressed cable and creep in the steel). As discussed in Section 2.2.6, these losses depend on the specifications of the system components, which are typically provided by the manufacturer. For instance, the loss due to anchorage slippage depends on the actual design of the anchorage mechanism. Similarly, the loss from the cable relaxation is a function of the mechanical properties of the chosen prestressed cable. Creep is generally negligible in the case of steel, while, owing to the straight profile of the cable, the friction between the cable and the cold-formed steel beam can be assumed to be minimal.

In the current work, prestress losses are not directly considered. Hence, the initial prestressing force is taken simply as the effective prestressing force, *i.e.* the force after account has been taken of the prestress losses.

3.4   Loading stages and analytical modelling

The mechanical behaviour of simply-supported prestressed cold-formed steel beams is explored in the present section with two stages of behaviour being considered, as shown in Figure 1.2. In Stage I, the transfer of the prestressing force into the cold-formed steel beam is assessed. In Stage II, the application of uniformly distributed imposed loading is

Stage I: Prestressing

(a) Loading configuration

(b) Deformed geometry

(c) Bending moment diagram
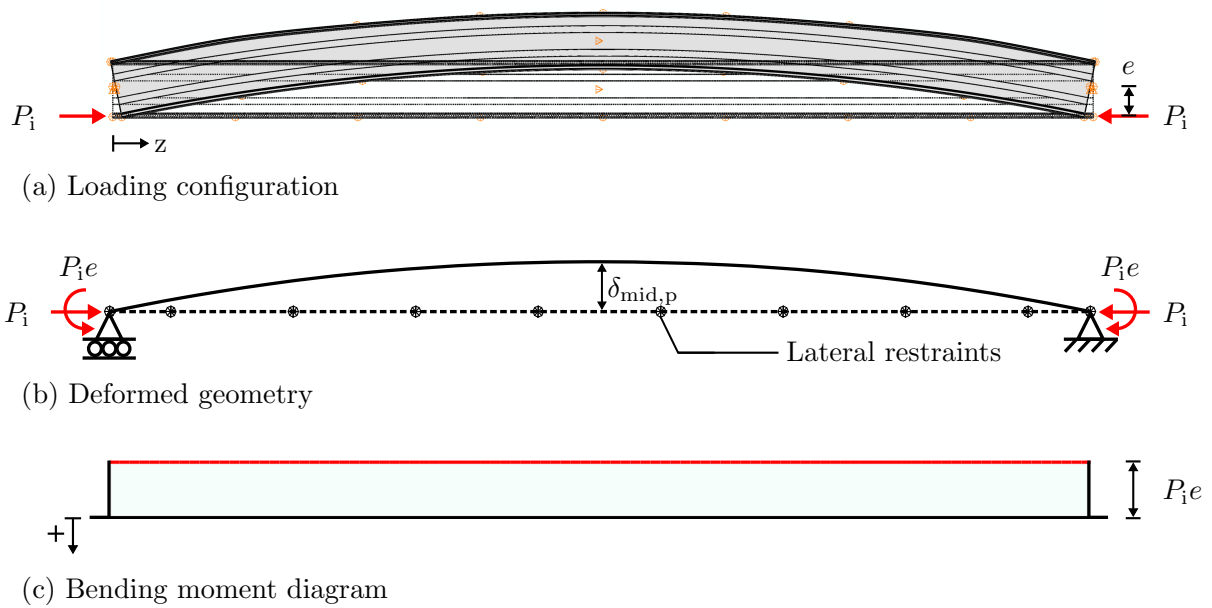
Figure 3.6: (a) Loading configuration, (b) deformed shape and (c) bending moment diagram at the end of Stage I.

investigated. Analytical expressions are employed to describe the elastic behaviour of the beams during these two stages in terms of the stress levels at the critical cross-section, which is located at midspan, and the load–deflection response of the member.

The ultimate response of cold-formed steel members is highly dependent on the applied stress distribution which, especially in the case of cold-formed steel members subjected to combinations of axial load and bending moments, can be considered to be the key controlling parameter (Torabian et al., 2014a; Torabian and Schafer, 2018). Hence, the stress distributions at different stages of loading are carefully assessed herein. A similar approach has been followed in previous research on prestressed steel beams (Hoadley, 1961; Troitsky, 1990) and prestressed composite beams (Hoadley, 1963; Ayyub et al., 1990b; Troitsky et al., 1990), as discussed in Sections 2.2.4 and 2.2.5 respectively.

3.4.1   Stage I: Prestressing

In Stage I, the cable is tensioned using a jacking mechanism and anchored at the two beam ends, where the initial prestressing force is transmitted into the cold-formed steel beam. As shown in Figures 3.6(a) and (b), the resulting eccentric compression is equivalent to a

concentric axial compressive force and a hogging (negative) bending moment applied at the two ends of the member, causing the uniform hogging bending moment distribution shown in Figure 3.6(c).

The axial stress distribution induced within the cold-formed steel cross-section due to the initial prestressing force P_i is shown in Figure 3.7, where tensile stresses are positive. The net stress distribution, shown in Figure 3.7(c), can be decomposed into a uniform compression, shown in Figure 3.7(a), and a linearly varying stress distribution, shown in
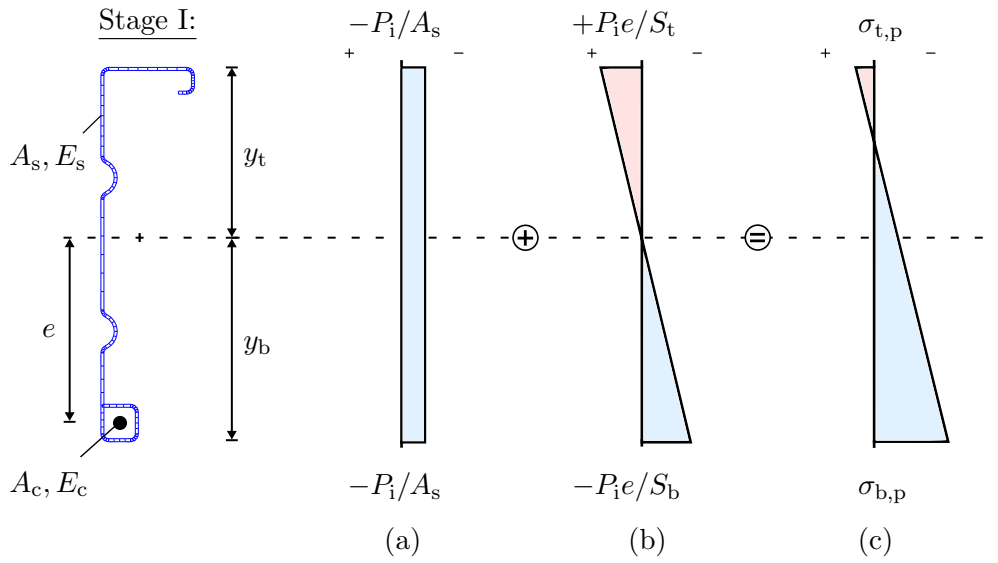
Figure 3.7: Axial stress distribution at the critical cross-section at the end of Stage I. (a) Uniform compression component due to P_i, (b) bending component due to the eccentricity at which P_i is applied and (c) net axial stress distribution.

Figure 3.7(b). The latter is a result of the eccentricity e at which the initial prestressing force is applied. Superposition of the two components leads to a net tensile stress in the top flange $\sigma_{t,p}$ and a net compressive stress in the bottom flange $\sigma_{b,p}$, as illustrated in Figure 3.7(c), thus:

$$\sigma_{t,p} = -\frac{P_i}{A_s} + \frac{P_i e}{S_t}, \tag{3.1}$$

$$\sigma_{b,p} = -\frac{P_i}{A_s} - \frac{P_i e}{S_b}, \tag{3.2}$$

where A_s is the cross-sectional area of the cold-formed steel beam; $S_t = I_s/y_t$ and $S_b = I_s/y_b$ are the elastic section moduli corresponding to first yield of the top and bottom flanges respectively, with y_t and y_b being the distance of the centroid from the top and bottom

extreme fibres respectively, and I_s being the second moment of area of the cold-formed steel cross-section about its strong geometric axis. Note that the initial stresses induced in Stage I have an opposite sign to the stresses imposed due to the subsequent imposed vertical loading in Stage II.

The capacity of the proposed prestressed member in Stage I is limited by either the ultimate capacity of the cold-formed steel beam when subjected to the loading configuration shown in Figure 3.6(b) or the tensile resistance of the cable when subjected to P_i. As shown in Figure 3.7(c), the capacity of the cold-formed steel cross-section is limited by the level of compression at the bottom flange; the initial prestressing force is therefore limited by either yielding or local/distortional buckling (depending on the cross-sectional slenderness) of the bottom part of the cross-section. Hence, possible failure of the compressed bottom flange of the steel cross-section during prestressing needs to be considered.

The uniform hogging moment $P_i e$, induces a pre-camber, *i.e.* an upwards vertical deflection of the member, as shown in Figures 3.6(a) and (b). The pre-camber offers benefits in the serviceability performance of the proposed system since it cancels out part of the deflections induced in the subsequent imposed loading stage. At the end of the prestressing stage, the relationship between the initial prestressing force and the vertical deflection at midspan δ^I_{mid} is given by:

$$\delta^I_{\mathrm{mid}} = -\left(\frac{L^2}{8E_s I_s}\right) P_i e, \tag{3.3}$$

where L and E_s are the length of the member and the Young's modulus of the cold-formed steel respectively.

3.4.2 Stage II: Imposed vertical loading

As shown in Figure 3.8(a), Stage II involves the application of externally imposed vertical loading, in the form of a uniformly distributed load q, which induces a maximum sagging (positive) bending moment $M_{\mathrm{max}}=qL^2/8$ at the critical cross-section, *i.e.* at midspan. Note that, in the context of the present work, the term 'imposed vertical loading' refers to the total vertical load (*i.e.* dead load plus live load) carried by the member after the prestressing force has been applied.

Stage II: Imposed loading

(a) Loading configuration

(b) Deformed geometry

(c) Bending moment diagram
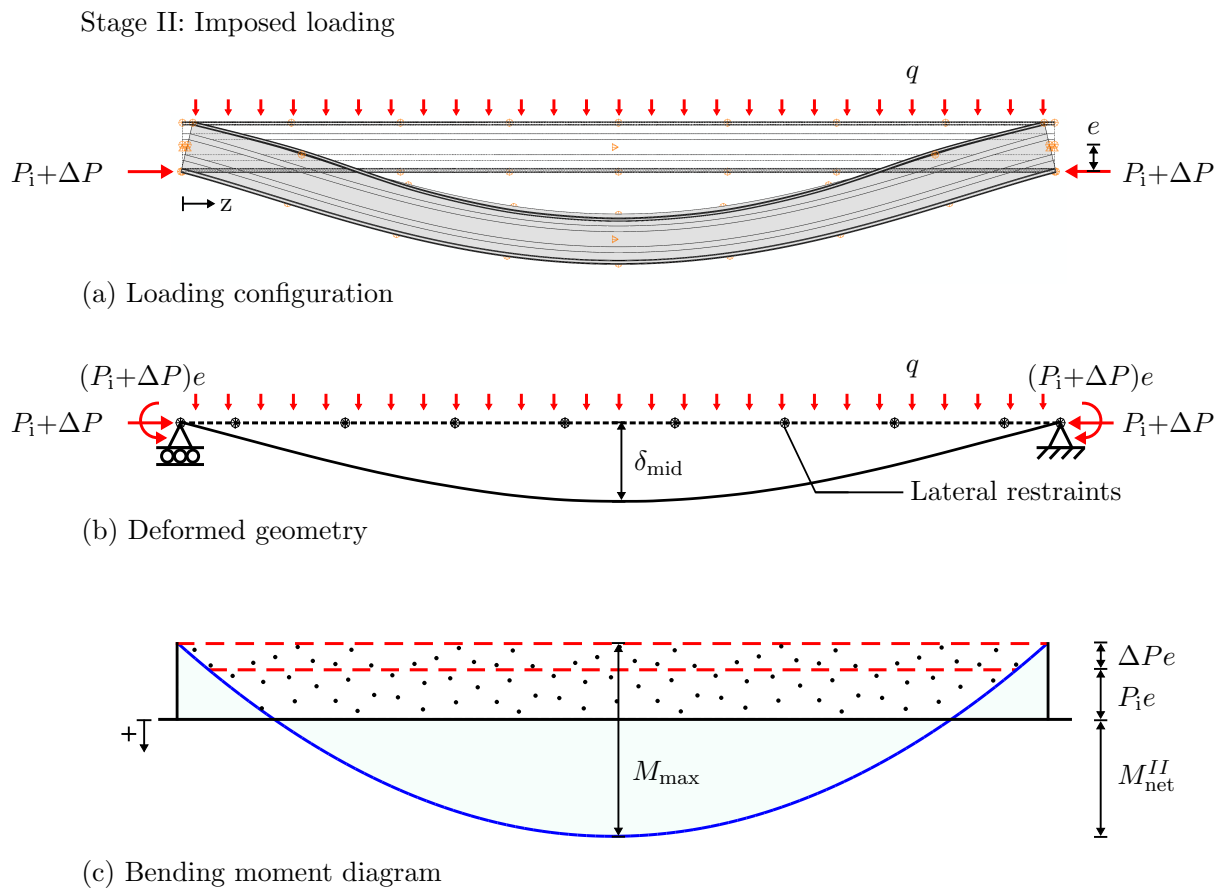
Figure 3.8: (a) Loading configuration, (b) deformed shape and (c) bending moment diagram at the end of Stage II.
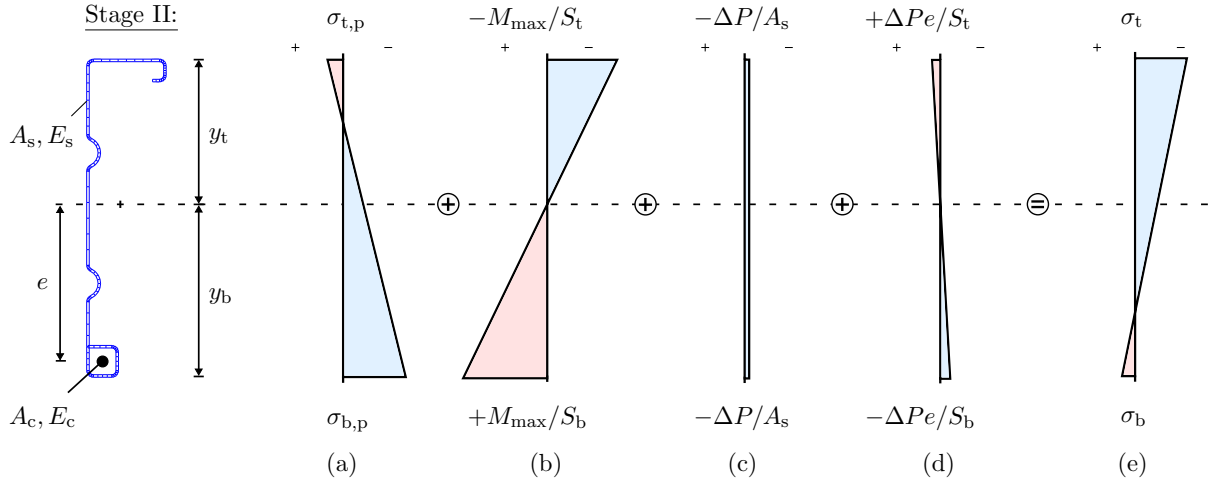
Figure 3.9: Axial stress distribution at the critical cross-section at the end of Stage II. (a) Stress distribution from Stage I, (b) bending component due to $M_{\max}$, (c) uniform compression component due to ΔP, (d) bending component due to the eccentricity of ΔP, and (e) net axial stress distribution.

As the beam deflects vertically, the cable is stretched further since it is located below the neutral axis of the cross-section and therefore an additional axial force is induced within the cable. This force is transferred back into the cold-formed steel beam at the end anchorages as an incremental prestressing force ΔP, which results in an additional uniform hogging moment equal to ΔPe, as shown in Figures 3.8(b) and (c). The method of determining ΔP is described in Section 3.4.3.

The bending moment diagram at the end of Stage II is shown in Figure 3.8(c), where the dotted area represents an approximation of the benefit obtained due to the prestressing process in terms of the partial cancellation of the applied bending moment. The effect of the prestressing may be seen to reduce the imposed moment at midspan from $M_{\max}$ to M_{net}^{II}, where M_{net}^{II} is the net bending moment at midspan at the end of Stage II.

As shown in Figure 3.9(e), the net stress distribution at the midspan of the beam at the end of Stage II comprises the stress distribution from the end of Stage I (Figure 3.9(a)), a linearly varying stress distribution about the centroid of the cross-section as a result of $M_{\max}$ (Figure 3.9(b)), as well as two stress distributions (compression and bending) due to ΔP (Figures 3.9(c) and (d)), which has the same effect as P_{i} during Stage I. Since the initial tensile stresses induced within the top flange during Stage I must first be overcome before detrimental compressive stresses are experienced, the occurrence of local and distortional buckling of the top flange is delayed and thus the moment capacity

of the member is enhanced. By superimposing the components shown in Figure 3.9 and utilising Equations (3.1)–(3.2), the expressions for the net stress levels at the top σ_t and bottom σ_b extreme fibres of the cold-formed steel cross-section at the end of Stage II can be obtained, thus:

$$\sigma_\mathrm{t} = (P_\mathrm{i} + \Delta P) \left(\frac{e}{S_\mathrm{t}} - \frac{1}{A_\mathrm{s}} \right) - \frac{M_\mathrm{max}}{S_\mathrm{t}}, \tag{3.4}$$

$$\sigma_\mathrm{b} = -(P_\mathrm{i} + \Delta P) \left(\frac{e}{S_\mathrm{b}} + \frac{1}{A_\mathrm{s}} \right) + \frac{M_\mathrm{max}}{S_\mathrm{b}}. \tag{3.5}$$

The capacity of the proposed prestressed member in Stage II is limited by either the ultimate capacity of the cold-formed steel beam when subjected to the loading configuration shown in Figure 3.8(b) or the tensile resistance of the cable when subjected to both P_i and ΔP. As shown in Figure 3.9(e), the capacity of the cold-formed steel cross-section in Stage II is limited by the level of compression within the top flange with failure occurring either by local/distortional buckling or yielding, depending on the cross-sectional slenderness.

The vertical deflections induced by the imposed vertical loading counteract the pre-camber induced during Stage I. The overall vertical deflection at midspan δ_mid^{II} at the end of Stage II is obtained by superposing the pre-camber induced in Stage I, as given in Equation (3.3), with the deflection due to the imposed vertical loading and incremental prestressing force from Stage II, such that:

$$\delta_\mathrm{mid}^{II} = \left(\frac{5L^2}{48 E_\mathrm{s} I_\mathrm{s}} \right) M_\mathrm{max} - \left(\frac{L^2}{8 E_\mathrm{s} I_\mathrm{s}} \right) (P_\mathrm{i} + \Delta P)e. \tag{3.6}$$

Note that the bending stiffness of the system, *i.e.* the gradient of the moment–deflection $(M_\mathrm{max} - \delta_\mathrm{mid}^{II})$ relationship, is independent of the initial prestressing force P_i.

3.4.3   Connection/bond between cable and steel cross-section

The behaviour of the prestressed system is influenced greatly by the connection/bond between the cable and the cold-formed steel beam, which complicates the calculation of ΔP. If grouting were introduced along the member, a fully bonded beam–cable connec-

tion would have been assumed. In the proposed beams, however, the cable is ungrouted and a connection is provided only at the end anchorages where the force-transfer mechanism takes place. Hence, the cable is considered to be unbonded, *i.e.* free to elongate along the entire length of the member. In this case, as the beam deflects vertically during the imposed loading stage, the axial strain in the cable, which is constant along the member length, is different from the axial strain in the steel cross-section at the level of the cable, which varies along the member length. Consequently, the contribution of the cable to the bending stiffness of the system varies with the form of the imposed vertical loading, and the cable elongation must be determined with consideration to the deformation of the entire member. The following approach is therefore taken to determine ΔP.

Since the system is statically determinate externally but statically indeterminate internally, the minimum potential energy principle (Thompson and Hunt, 1973) is employed, where, assuming a zero initial prestressing force, the strain energy due to axial shortening of the cold-formed steel beam U_{A1} and the cable U_{A2} can be taken as:

$$U_{\text{A1}} = \frac{1}{2} k_{\text{s}} z_{\text{p}}^2, \tag{3.7}$$

$$U_{\text{A2}} = \frac{1}{2} k_{\text{c}} z_{\text{p}}^2, \tag{3.8}$$

where z_{p} is the axial shortening or elongation of the beam and cable due to ΔP with $k_{\text{s}}=E_{\text{s}}A_{\text{s}}/L$ and $k_{\text{c}}=E_{\text{c}}A_{\text{c}}/L$ being the axial stiffnesses of the cold-formed steel beam and cable respectively; E_{c} and A_{c} are the Young's modulus and cross-sectional area of the cable respectively.

The strain energy from bending of the cold-formed steel beam to leading order, is:

$$U_{\text{B}} = \int_0^L \frac{1}{2} E_{\text{s}} I_{\text{s}} \left(\frac{\text{d}^2 w}{\text{d}z^2}\right)^2 \text{d}z, \tag{3.9}$$

where w is the vertical deflection of the beam. Utilising basic structural mechanics with sagging moments being positive, *i.e.*:

$$E_{\text{s}} I_{\text{s}} \left(\frac{\text{d}^2 w}{\text{d}z^2}\right) = M_{\text{net,x}}^{II}, \tag{3.10}$$

where $M^{II}_{\text{net,x}}$ is the net moment about the strong geometric axis of the cross-section during Stage II, Equation (3.9) may be expressed as:

$$U_{\text{B}} = \frac{1}{2} \int_0^L \frac{M^{II}_{\text{net,x}}{}^2}{E_{\text{s}} I_{\text{s}}} \mathrm{d}z. \tag{3.11}$$

Hence, assuming a zero initial prestressing force, the net moment along the member in Stage II is equivalent to $M_{\text{net,x}} = M_{\text{max}} - \Delta Pe$, such that:

$$U_{\text{B}} = \frac{1}{2} \int_0^L \frac{(M_{\text{max}} - \Delta Pe)^2}{E_{\text{s}} I_{\text{s}}} \mathrm{d}z, \tag{3.12}$$

where M_{max} is the bending moment imposed at the critical cross-section by the vertical loading. By superimposing Equations (3.7), (3.8) and (3.12) and using $\Delta P = k_{\text{s}} z_{\text{p}}$, the total strain energy U stored in the system is obtained:

$$U = \frac{1}{2} \int_0^L \frac{(M_{\text{max}} - k_{\text{s}} z_{\text{p}} e)^2}{E_{\text{s}} I_{\text{s}}} \mathrm{d}z + \frac{1}{2} k_{\text{s}} z_{\text{p}}^2 + \frac{1}{2} k_{\text{c}} z_{\text{p}}^2. \tag{3.13}$$

Differentiating Equation (3.13) with respect to the generalized coordinate z_{p}, setting it equal to zero for equilibrium, substituting in $\Delta P = k_{\text{s}} z_{\text{p}}$ and subsequently solving for ΔP, the relationship between ΔP and M_{max} is obtained:

$$\Delta P = \frac{\dfrac{e}{L} \int_0^L M_{\text{max}} \mathrm{d}z}{\left[e^2 + \dfrac{E_{\text{s}} I_{\text{s}}}{E_{\text{c}} A_{\text{c}}} + r^2 \right]}, \tag{3.14}$$

where $r = \sqrt{I_{\text{s}}/A_{\text{s}}}$ is the radius of gyration of the cold-formed steel cross-section.

The integral in Equation (3.14) is equivalent to the area under the applied bending moment diagram plotted with respect to the member length and hence, in the case of uniformly distributed loading, ΔP is proportional to M_{max} during the elastic response of the beam according to:

$$\Delta P = \frac{2 M_{\text{max}} e}{3 \left[e^2 + \dfrac{E_{\text{s}} I_{\text{s}}}{E_{\text{c}} A_{\text{c}}} + r^2 \right]}. \tag{3.15}$$

The additional tensile stress in the cable $\sigma_{c,p}$ induced in Stage II is thus:

$$\sigma_{c,p} = \frac{\Delta P}{A_c}. \tag{3.16}$$

For the determination of ΔP, the minimum potential energy approach has been used in a similar manner in previous works on prestressed composite girders (Hoadley, 1963; Ayyub et al., 1990b). An alternative approach is to apply the principle of virtual work, where compatibility of the cable and steel beam fibre elongations at the level of the cable is enforced (Hoadley, 1961; Troitsky, 1990; Troitsky et al., 1990; Tong and Saadatmanesh, 1992). Furthermore, ΔP can be also obtained from a method used to calculate the stress variation in unbonded tendons in prestressed concrete structures (Naaman et al., 2002). In that case, a strain-reduction coefficient is utilised to reduce the strain increment in the case of an equivalent fully bonded tendon to the average strain increment in the unbonded case (Naaman, 1990). The value of this coefficient is dependent on the loading case and the eccentricity profile; in the case of the proposed beams, this coefficient is equal to 2/3 owing to the parabolic profile of the bending moment diagram in the imposed vertical loading stage.

3.5 Failure criteria for design

As shown in Figures 3.6 and 3.8, prestressed cold-formed steel beams are subjected to combined axial compressive load and bending during both prestressing (Stage I) and under the application of external imposed loading (Stage II), and hence generally may be considered to be beam-column members. For this purpose, in the design of the proposed beams, linear interaction equations (see Section 2.3.6.4(a)) are adopted to check the capacity of the cold-formed steel member, as recommended in most current design standards, including the North American (AISI S100-16, 2016) and European (EN 1993-1-3, 2006) specifications. The tensile capacity of the prestressing cable is also checked during the two stages, as described below. Since the loading configuration is different in the two stages, design checks need to be performed in each stage by considering the respective net axial compressive force and bending moment.

3.5.1 Interaction equations

In the present work, the resistance functions and interaction equations from the North American (AISI S100-16, 2016) specification are employed as the basis for the design of the cold-formed steel member since, as discussed in Section 2.3.6, they facilitate the estimation of the capacity of geometrically complex cross-section profiles, such as those examined herein, through the Direct Strength Method (DSM) (Schafer, 2008). The basic interaction equation, as given by Equation H1.2-1 in AISI S100-16 (2016), is used for the design of cold-formed steel beam-columns:

$$\frac{\overline{P}}{P_{\mathrm{a}}} + \frac{\overline{M}_{\mathrm{x}}}{M_{\mathrm{ax}}} + \frac{\overline{M}_{\mathrm{y}}}{M_{\mathrm{ay}}} \leqslant 1.0, \tag{3.17}$$

where, in the numerator, $\overline{P}$ is the axial compressive force based on factored loads (*i.e.* the required axial compressive strength) with due allowance for any global second-order effects and $\overline{M}_{\mathrm{x}}$ and $\overline{M}_{\mathrm{y}}$ are the bending moments based on factored loads (*i.e.* the required flexural strengths) about the major and minor centroidal axes respectively, with due allowance for both global and member second-order effects. In the denominator, P_{a} is the factored axial compressive resistance (*i.e.* the available axial strength) of the member, but in the present study it needs only to allow for local and distortional buckling since global flexural buckling is restrained by the presence of the cable, as discussed in Section 3.3.3. Similarly, M_{ax} and M_{ay} are the factored bending resistances (*i.e.* the available flexural strengths) about the major and minor centroidal axes respectively, also allowing only for local and distortional buckling since the proposed beams are fully braced against lateral-torsional buckling, as discussed in Section 3.3.3. Note that, in the present work, $\overline{M}_{\mathrm{x}}$, $\overline{M}_{\mathrm{y}}$, M_{ax} and M_{ay} are taken with respect to the strong and weak geometric axes accordingly, with the difference between the bending moments about the major principal and strong geometric axes being less than 1% for the cross-sections studied herein. Finally, since no moment arises about the weak geometric axis of the cross-section, *i.e.* $\overline{M}_{\mathrm{y}}$=0, the third term in Equation (3.17) is eliminated hereafter. The determination of the aforementioned strengths in the case of prestressed cold-formed steel beams is described below.

3.5.1.1   Determination of cross-section forces and moments

In the studied system, there are no global sway P–Δ effects since the proposed beams are simply-supported and would not form part of the global stability system of the structure. Similarly, there are no member P–δ effects since the cable is housed within the cross-section and thus the lever arm of the prestressing force relative to the strong geometric axis remains constant during both loading stages, *i.e.* no second-order P–δ effects are generated as the member deforms. Moreover, lateral-torsional buckling is restrained by the lateral restraints that are present along the member, as discussed in Section 3.3.3.

The cross-section forces and moments $\overline{P}$ and $\overline{M}_{\mathrm{x}}$ (*i.e.* the required strengths) are thus simply taken as the net first-order axial compressive force P_{net} and bending moment $M_{\mathrm{net,x}}$ at the critical cross-section, *i.e.* at midspan, of the members respectively. The expressions for P_{net} and $M_{\mathrm{net,x}}$ in Stages I and II can be determined using Figures 3.6 and 3.8 respectively and are summarised in Table 3.2, where the superscripts denote the corresponding loading stage.

Table 3.2: Net first-order axial compressive force and bending moment at the critical cross-section in Stages I and II.

Stage I:	Stage II:
$P_{\mathrm{net}}^{I} = P_{\mathrm{i}}$	$P_{\mathrm{net}}^{II} = P_{\mathrm{i}} + \Delta P$
$M_{\mathrm{net,x}}^{I} = P_{\mathrm{net}}^{I} e$	$M_{\mathrm{net,x}}^{II} = M_{\mathrm{max}} - P_{\mathrm{net}}^{II} e$

The above considerations reduce the governing equation, *i.e.* Equation (3.17), for the design of the cold-formed steel beam to:

$$\frac{P_{\mathrm{net}}}{P_{\mathrm{a}}} + \frac{M_{\mathrm{net,x}}}{M_{\mathrm{ax}}} \leqslant 1.0, \tag{3.18}$$

where the expressions for P_{net} and $M_{\mathrm{net,x}}$ for each loading stage are listed in Table 3.2 and the factored axial P_{a} and bending M_{ax} resistances are determined using the DSM, as outlined below. This approach is similar to that followed in previous experimental and numerical works on cold-formed steel beam-columns (Torabian et al., 2014b, 2016b,c).

3.5.1.2   Determination of factored cross-section resistances

The factored resistances (*i.e.* the available strengths) are given by $P_a = \phi_c P_n$ and $M_{ax} = \phi_b M_{nx}$, where ϕ_c and ϕ_b are the resistance factors for axial compression and bending respectively. To determine the nominal axial P_n and bending M_{nx} resistances of the examined members, the DSM (see Section 2.3.6), which is a recently developed alternative to the more classical Effective Width Method (EWM), is employed.

The EWM, first proposed by von Kármán *et al.* (1932), requires the reduction of the gross properties of the cross-section to effective properties to account for the development of local instabilities in the compressed regions of the cross-section. The calculation of the effective properties can be an iterative and inefficient process, especially in the case of geometrically complex cross-section profiles, such as those employed in the proposed concept (see Figure 3.3).

In contrast, in the DSM, the stability of the entire cross-section is taken into consideration without the use of effective widths. The interaction between the different elements of the cross-section, as well as the effect of stiffeners, are considered directly by utilising advanced elastic buckling analysis tools (see Section 2.3.5) to determine the elastic critical buckling loads and moments of the member; the DSM design strength equations are then used to estimate the nominal axial and bending resistances of the member, as described below.

As discussed in Section 2.3.6, the DSM expressions are a function of the yield load or moment alongside the global, local and distortional elastic critical buckling loads (P_y, P_{cre}, P_{crl} and P_{crd} respectively) or moments (M_y, M_{cre}, M_{crl} and M_{crd} respectively) of the member. The elastic buckling loads and moments can be readily determined using the software CUFSM (Li and Schafer, 2010b), as described in Section 2.3.5.2, which employs the semi-analytical finite strip method (FSM) to assess the stability of the entire cross-section under any combination of axial and bending stresses. The CUFSM software provides the so-called signature curve of the member, as shown in Figure 3.10, where the minimum points indicate the critical local and distortional buckling moments and the corresponding critical half-wavelengths. Note that the signature curve in Figure 3.10 cor-
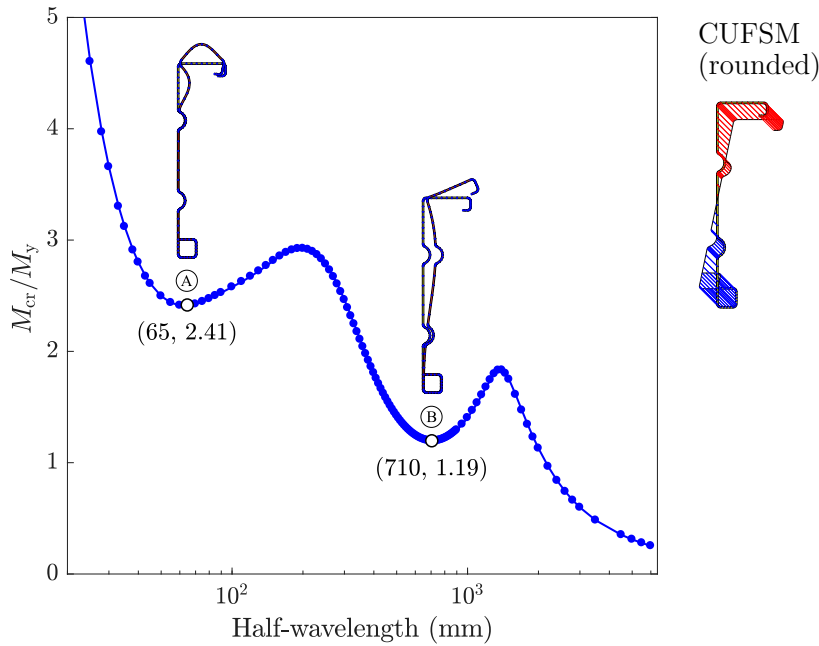
Figure 3.10: Signature curve for purely positive bending (M_y=34.5 kNm) for the reference geometry: points (A) and (B) are the local and distortional critical buckling points respectively for positive bending. The numbers in the parentheses denote the coordinates of the labelled points.

responds to the reference geometry utilised in the present chapter, as shown in Figure 3.3, when subjected to purely positive bending.

Since the conventional FSM considers the coupling effects between the local, distortional and global buckling modes (Ádány and Beregszászi, 2008), CUFSM in some cases fails to identify the minimum points on the signature curve (Li and Schafer, 2010b). In such cases the constrained Finite Strip Method (cFSM) (Li et al., 2014), which enables modal decomposition and identification by determining the pure local and distortional modes, may be employed, as discussed in Section 2.3.5.3. The cFSM is used in the form of the "FSM@cFSM-L_{cr}" method (Li and Schafer, 2010a) herein, where, as demonstrated in Figure 3.11(a) for the case of the reference cross-section under pure compression, an equivalent cross-section with sharp corners is analysed and the critical distortional L_{crd} half-wavelength is determined from the minimum point of the obtained curve. Subsequently, the critical buckling load is identified from the signature curve of the original cross-section. The FSM@cFSM-L_{cr} method is also used in the same manner to identify the elastic critical distortional buckling strength M_{crd}^- of the cold-formed steel beam under negative bending, as demonstrated in Figure 3.11(b). Note that this mode is similar
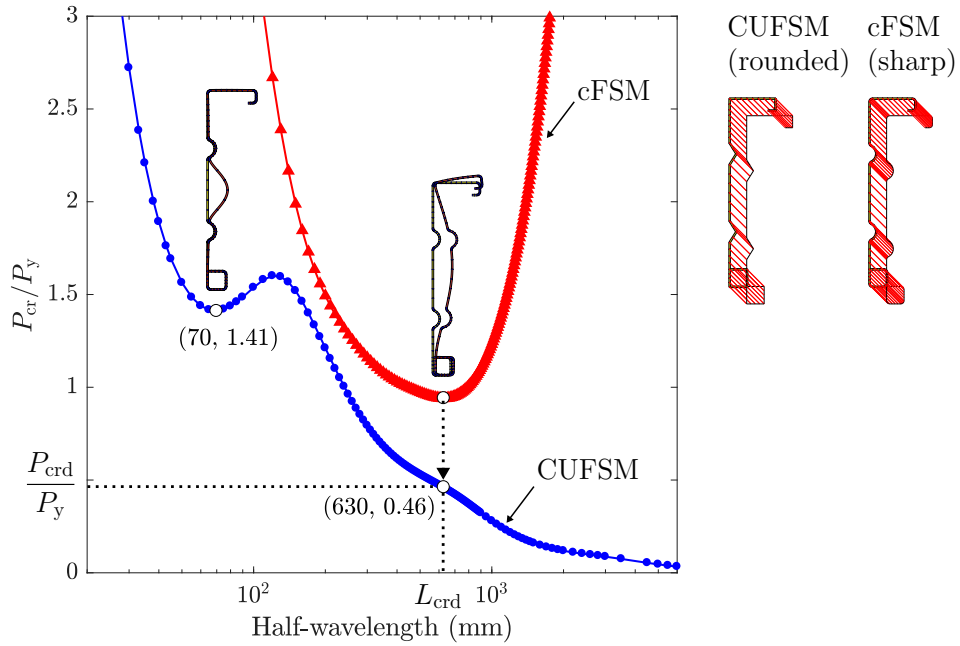
(a) Pure compression
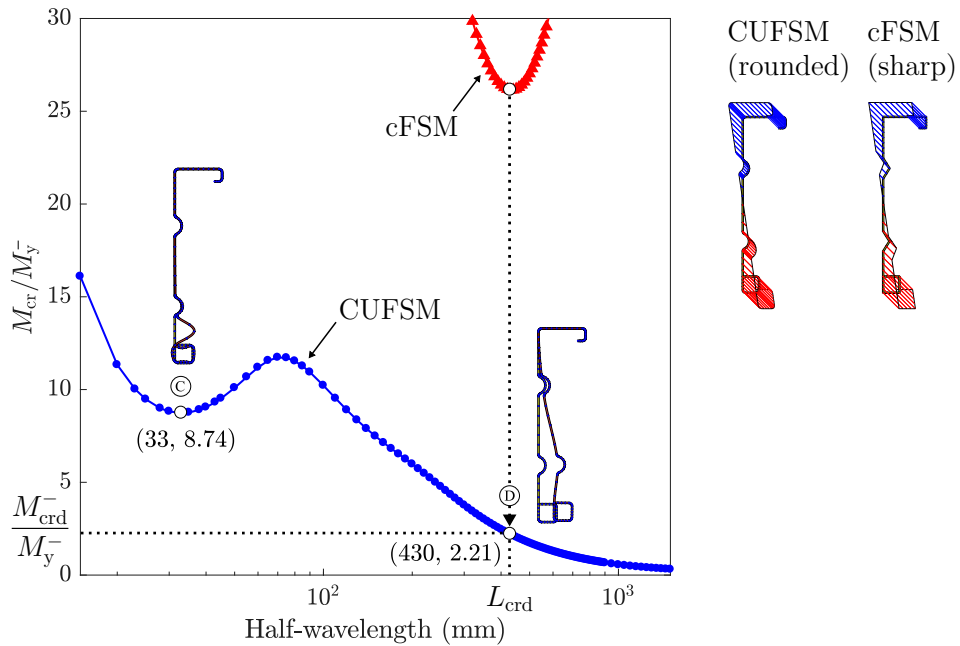
(b) Purely negative bending

Figure 3.11: Signature curves for (a) pure compression (P_y=502.1 kN) and (b) purely negative bending (M_y^-=34.5 kNm) for the reference geometry, as obtained using CUFSM and cFSM. Illustration of the application of the FSM@cFSM-L_{cr} method: points (C) and (D) are the local and distortional critical buckling points respectively for negative bending.

to that referred to as lateral distortional buckling in previous studies on LiteSteel Beams (Anapayan and Mahendran, 2012).

Once the elastic critical buckling loads/moments of the member have been obtained, the DSM expressions are used to estimate the nominal axial and bending resistances of the member, as discussed in Sections 2.3.6.2 and 2.3.6.3. The DSM equations for the global, local and distortional buckling of members in compression and bending are defined in Chapters E and F in AISI-S100-16 (2016) respectively.

It should be emphasised that, in the present work, the load-carrying capacities of both structural components of the proposed prestressed members need to be checked independently for Stages I and II. For this purpose, failure criteria are developed in the following sub-sections to check the capacity of the cold-formed steel beam and cable when subjected to the net axial forces and moments corresponding to Stages I and II.

3.5.2 Stage I: Prestressing

The failure criteria for Stage I ensure that the load-carrying capacities of the cold-formed steel beam and prestressing cable are greater than the required strengths, based on the net axial force and bending moment in Stage I.

3.5.2.1 Failure criterion I–A: Capacity of cold-formed steel beam

The failure criterion for the capacity of the cold-formed steel beam in Stage I is based on Equation (3.18) with the net axial force and bending moment at the critical cross-section during Stage I being obtained from Table 3.2. The nominal axial and negative bending resistances (*i.e.* P_{n} and M_{nx}^{-} respectively) are determined using the DSM. The nominal axial resistance is a function of the squash (yield) and elastic buckling loads, *i.e.* $P_{\mathrm{n}}=f(P_{\mathrm{y}}, P_{\mathrm{cre}}, P_{\mathrm{crl}}, P_{\mathrm{crd}})$, which are determined by applying a purely compressive axial stress distribution in CUFSM. The nominal negative bending resistance is a function of the yield and elastic buckling moments due to negative bending, *i.e.* $M_{\mathrm{nx}}^{-}=f(M_{\mathrm{y}}^{-}, M_{\mathrm{cre}}^{-}, M_{\mathrm{crl}}^{-}, M_{\mathrm{crd}}^{-})$, which are obtained by applying a purely negative bending stress distribution in CUFSM. Note that, in the studied system, global flexural buckling

and distortional buckling due to negative bending are restrained due to the presence of the cable and the lateral restraints; hence, $P_{cre}=P_y$ and $M^-_{cre}=M^-_{crd}=M^-_y$. As illustrated by the net stress distribution in Figure 3.7(c), the capacity of the cold-formed steel beam in Stage I is limited by the compression level at the bottom extreme fibres of the cross-section.

Depending on the local and distortional slendernesses ($\lambda_l=\sqrt{M_y/M_{crl}}$ and $\lambda_d=\sqrt{M_y/M_{crd}}$ respectively), the capacity of the cold-formed steel beam is governed by either of the following:

(i) Local/distortional buckling:

If λ_l and λ_d are sufficiently high such that, according to the DSM, $P_n<P_y$ and/or $M^-_{nx}<M^-_y$, the capacity of the beam needs to take account of local or distortional buckling and thus it is limited by P_n and/or M^-_{nx}. Hence, this failure criterion can be stated as:

$$\frac{P^I_{net}}{\phi_c P_n} + \frac{M^I_{net,x}}{\phi_b M^-_{nx}} \leqslant 1.0. \tag{3.19}$$

(ii) Material yielding:

If the cross-section is sufficiently stocky (compact) such that, according to the DSM, $P_n=P_y$ and $M^-_{nx}=M^-_y$, local/distortional buckling can be neglected. Hence, P_n and M^-_{nx} in Equation (3.19) can simply be replaced by P_y and M^-_y respectively.

3.5.2.2 Failure criterion I–B: Tensile capacity of prestressing cable

The failure criterion for the cable is defined as the point at which the initial prestressing force causes yielding of the cable, *i.e.*:

$$P^I_{net} \leqslant \phi_t F_{y,c} A_c, \tag{3.20}$$

where ϕ_t is the resistance factor for tension and $F_{y,c}$ is the yield stress of the cable.

Assuming that the maximum allowable initial prestressing force P_{max} that can be applied

in Stage I is limited by the capacity of the cold-formed steel beam (*i.e.* failure criterion I–A), *i.e.* assuming that the failure criterion I–B is satisfied by using a sufficiently large cable that can carry this force (*i.e.* $P_{\max} \leqslant \phi_t F_{y,c} A_c$), then $P_{\max}$ (utilising Equation (3.19), the net actions from Table 3.2 and rearranging for $P_{\max}$) is determined from the following expression:

$$P_{\max} = \frac{1}{\left[\dfrac{1}{\phi_c P_n} + \dfrac{e}{\phi_b M_{nx}^-}\right]}. \tag{3.21}$$

3.5.3 Stage II: Imposed vertical loading

The failure criteria for Stage II ensure that the cold-formed steel beam and prestressing cable can carry the net axial force and bending moment in Stage II.

3.5.3.1 Failure criterion II–A: Capacity of cold-formed steel beam

Using the same approach as for failure criterion I–A, the capacity of the cold-formed steel beam in Stage II is assessed using Equation (3.18) with the net axial force and bending moment being taken from Table 3.2. The nominal axial resistance P_n is the same as from Stage I, while the bending strength is now the resistance of the member under sagging moments M_{nx}^+. The latter is obtained using the DSM, where $M_{nx}^+ = f(M_y, M_{cre}^+, M_{crl}^+, M_{crd}^+)$, while the elastic critical buckling moments are determined by applying a purely positive bending stress distribution in CUFSM. Note that, since lateral-torsional buckling is prevented in the studied system, $M_{cre}^+ = M_y$. As is typically the case in cold-formed steel beams, the capacity of the cross-section under imposed loading is limited by the compressive stress level at the top fibres of the beam, as shown in Figure 3.9(e).

Depending on the local and distortional slendernesses, the capacity of the cold-formed steel beam is governed by either of the following:

(i) Local/distortional buckling:

If the cross-section is sufficiently slender such that, according to the DSM, $P_n < P_y$ and/or $M_{nx}^+ < M_y$, local/distortional buckling need to be considered. Therefore, the capacity of

the beam is limited by P_n and/or M_{nx}^+, thus:

$$\frac{P_{net}^{II}}{\phi_c P_n} + \frac{M_{net,x}^{II}}{\phi_b M_{nx}^+} \leqslant 1.0. \qquad (3.22)$$

(ii) Material yielding:

If the slenderness of the cross-section is sufficiently low such that, according to the DSM, $P_n = P_y$ and $M_{nx}^+ = M_y$, local/distortional buckilng can be neglected and thus P_n and M_{nx}^+ in Equation (3.22) can be replaced by P_y and M_y respectively.

3.5.3.2   Failure criterion II–B: Tensile capacity of prestressing cable

The tensile force in the cable during Stage II is equal to P_{net}^{II} and is limited by the yielding of the cable according to:

$$P_{net}^{II} \leqslant \phi_t F_{y,c} A_c. \qquad (3.23)$$

3.5.4   Summary of failure criteria

The failure criteria that have been developed in the present section ensure that the load-carrying capacities of the two structural components (*i.e.* the cold-formed steel beam and the cable) of the system are not exceeded during the two different loading stages (*i.e.* prestressing and imposed vertical loading); the criteria for Stages I and II are summarised in Tables 3.3 and 3.4 respectively.

Table 3.3: Failure criteria for Stage I.

Stage I: Prestressing

Eccentric axial compression

(a) Failure criterion I–A: Cold-formed steel beam

(i) Local/distortional buckling – if $P_n < P_y$ and/or $M_{nx}^- < M_y^-$:

$$\frac{P_{net}^I}{\phi_c P_n} + \frac{M_{net,x}^I}{\phi_b M_{nx}^-} \leqslant 1.0. \qquad (3.24)$$

(ii) Material yielding – if $P_n = P_y$ and $M_{nx}^- = M_y^-$:

$$\frac{P_{net}^I}{\phi_c P_y} + \frac{M_{net,x}^I}{\phi_b M_y^-} \leqslant 1.0. \qquad (3.25)$$

(b) Failure criterion I–B: Prestressing cable

(i) Material yielding:

$$P_{net}^I \leqslant \phi_t F_{y,c} A_c. \qquad (3.26)$$

Note: See Table 3.2 for the expressions for P_{net}^I and $M_{net,x}^I$.

Table 3.4: Failure criteria for Stage II.

Stage II: Imposed loading

Eccentric axial compression + vertical loading

(a) Failure criterion II–A: Cold-formed steel beam

(i) Local/distortional buckling – if $P_\mathrm{n} < P_\mathrm{y}$ and/or $M_\mathrm{nx}^+ < M_\mathrm{y}$:

$$\frac{P_\mathrm{net}^{II}}{\phi_\mathrm{c} P_\mathrm{n}} + \frac{M_\mathrm{net,x}^{II}}{\phi_\mathrm{b} M_\mathrm{nx}^+} \leqslant 1.0. \tag{3.27}$$

(ii) Material yielding – if $P_\mathrm{n} = P_\mathrm{y}$ and $M_\mathrm{nx}^+ = M_\mathrm{y}$:

$$\frac{P_\mathrm{net}^{II}}{\phi_\mathrm{c} P_\mathrm{y}} + \frac{M_\mathrm{net,x}^{II}}{\phi_\mathrm{b} M_\mathrm{y}} \leqslant 1.0. \tag{3.28}$$

(b) Failure criterion II–B: Prestressing cable

(i) Material yielding:

$$P_\mathrm{net}^{II} \leqslant \phi_\mathrm{t} F_\mathrm{y,c} A_\mathrm{c}. \tag{3.29}$$

Note: See Table 3.2 for the expressions for P_net^{II} and $M_\mathrm{net,x}^{II}$.

3.6   Concluding remarks

The conceptual development of prestressed cold-formed steel beams has been presented in the current chapter. In the proposed structural system, a prestressed cable is housed within the bottom hollow flange of a cold-formed steel beam at an eccentric location with respect to its strong geometric axis. The cable is anchored at the two member ends and is free to elongate along the member. Owing to the presence of floor sheeting and sag bars at the top and bottom flanges of the member respectively, it is assumed that the cold-formed steel beam is restrained against lateral-torsional buckling. These restraints also prevent any asymmetric and minor axis bending effects.

Loading is applied in two different stages; in Stage I, prestressing is applied while, in Stage II, vertical loading is imposed along the member. Following the description of the principal characteristics of the proposed beams, linear elastic analytical expressions have been developed to describe the mechanical behaviour of prestressed cold-formed steel beams during the two loading stages. For this purpose, the axial stress distribution at the critical cross-section of the prestressed members was studied. The connection between the prestressed cable and the cold-formed steel cross-section was analysed using the principle of minimum potential energy to develop a relationship between the bending moment induced at the critical cross-section and the incremental increase in the prestressing force.

Failure criteria for the design of prestressed cold-formed steel beams have been defined. These are essentially a set of expressions that limit the applied loading during the prestressing and imposed vertical loading stages, based on the predicted load-carrying capacities of the two structural components (*i.e.* the cold-formed steel beam and the cable) of the system. The applied loading for both loading stages can be expressed in terms of the net axial load and bending moment at the critical cross-section of the member. Since the proposed prestressed members can be treated as beam-columns, the load-carrying capacity of the cold-formed steel beam can be predicted using linear inter-action equations in conjunction with the Direct Strength Method (DSM). The resistance of the cable is equivalent to its tensile capacity.

The developed analytical expressions and failure criteria are utilised in Chapters 5–6, where the results obtained from numerical simulations are compared with the corresponding analytical results and capacity predictions.

CHAPTER 4

FINITE ELEMENT MODELLING AND VALIDATION

4.1 Introduction

Finite element (FE) modelling has been employed to simulate the mechanical behaviour of prestressed cold-formed steel beams during the prestressing and imposed vertical loading stages. In the present chapter, the principal features of the developed FE models, which idealise the material response, the beam–cable connection alongside the boundary and loading conditions, are presented. Subsequently, a review of previous experimental investigations on cold-formed steel beams is presented and the FE modelling approach is validated against the results of similar experimental studies on cold-formed steel beams to ensure that the behaviour of the proposed members is simulated accurately.

The developed FE models are utilised in subsequent chapters to study the behaviour of the proposed beams during the different loading stages, to investigate the effect of the key controlling parameters and to assess the suitability of the developed design recommendations. As discussed in Section 1.4, the FE modelling process, including the elastic buckling analysis, creation of the input files, simulation, data extraction, data analysis and post-processing, has been fully parametrised with the aim of automating the overall modelling process and thus making it more efficient. The development and validation of

the FE modelling approach presented in this chapter has been published by Hadjipantelis *et al.* (2019b; 2018c).

4.2 Development of finite element models

The commercial FE analysis package ABAQUS (2014), which has been widely used in previous research for the modelling of cold-formed steel members (Young and Yan, 2004; Dinis et al., 2007; Yu and Schafer, 2007; Keerthan and Mahendran, 2011; Kyvelou et al., 2018), is employed. Geometrically and materially nonlinear analysis with imperfections is performed, aiming to understand the mechanical behaviour of the prestressed cold-formed steel beams and to provide an insight to the scale of the potential benefits that can be derived from prestressing. The key features of the FE modelling approach are presented below.

4.2.1 Element types

Shell elements are typically used to model thin-walled structures, where one dimension (*i.e.* the thickness) is significantly smaller than the other dimensions, since they can capture local instability phenomena such as local and distortional buckling accurately (Sarawit et al., 2003; Dinis et al., 2007; Schafer et al., 2010). The 4-noded linear S4R shell element with reduced integration and hourglass control (ABAQUS, 2014) was used for the modelling of the cold-formed steel beam. The default ABAQUS (2014) value, *i.e.* five for Simpson's rule, was utilised for the number of section integration points through the element thickness, as demonstrated in Figure 4.1(a). As demonstrated in previous research studies, the chosen S4R elements can replicate accurately the local and distortional buckling that typically occur in cold-formed steel members subjected to bending (Yu and Schafer, 2007; Natário et al., 2014; Kyvelou et al., 2018).

The reduced integration S4R elements, shown in Figure 4.1(b), are computationally more efficient than the equivalent full integration S4 elements, shown in Figure 4.1(c). This is because, in the former case, only one in-plane integration point is present per element,

(a) 3-D view of shell element

(b) S4R element   (c) S4 element
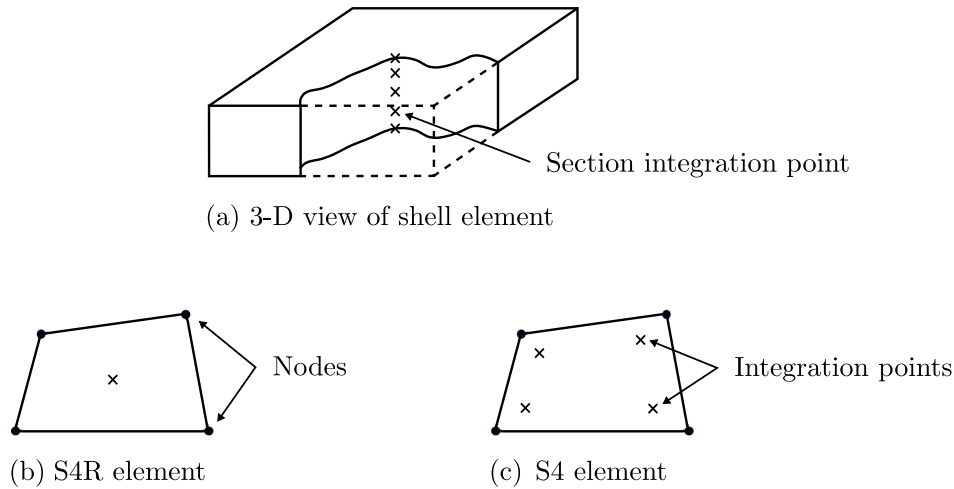
Figure 4.1: (a) Section integration points through the thickness of a shell element; 4-noded (b) reduced integration and (c) full integration shell elements. Adapted from ABAQUS (2014).

while, in the latter case, four integration points exist (ABAQUS, 2014). The location of the section integration points through the thickness are illustrated in Figure 4.1(a). However, note that reduced integration can result in a mesh instability, commonly known as 'hourglassing' (ABAQUS, 2014), whereby zero strains, and thus numerical convergence issues, may arise at the sole integration point of the elements experiencing distortion. To avoid this, the S4R elements require the use of hourglass control. The utilisation of a fine mesh and distributed loading to avoid excessive stress concentrations is also recommended (ABAQUS, 2014).

The prestressing cable was modelled using 2-noded three-dimensional T3D2 truss elements (ABAQUS, 2014), which are often employed to model slender structural members that can transmit axial forces only, *i.e.* they do not transmit any moments. The T3D2 elements have been employed successfully in previous research to simulate the mechanical response of cables in prestressed steel tubular members (Gosaye et al., 2014) and under-deck cable-stayed bridges (Madrazo-Aguirre et al., 2015a). The 2-noded truss elements have a straight profile with one integration point in the centre and use linear interpolation between the two edge nodes to determine the displacement field. The axial stress along the element is constant.

4.2.2 Meshing scheme

Mesh density can have a significant impact on the ultimate load and collapse response of cold-formed steel members experiencing local, distortional and/or global buckling (Schafer et al., 2010). Hence, a mesh sensitivity analysis was conducted to determine an appropriate cross-sectional discretisation that would be both computationally inexpensive and sufficiently fine to capture the local instabilities with good accuracy. The mesh chosen for the cold-formed steel cross-section is shown in Figure 4.2; in total, 105
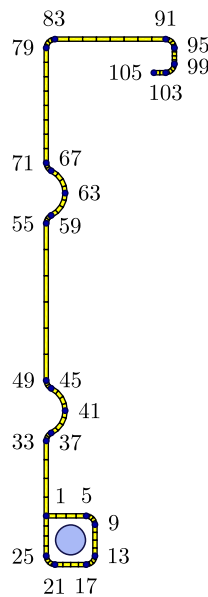
Figure 4.2: Cross-sectional discretisation and node numbering scheme.

nodes were utilised.

The chosen mesh density is similar to the one utilised in the works of Kyvelou *et al.* (2018) and Hui (2014), where good agreement was demonstrated between the FE and test results. In comparison with the flat regions, a finer mesh was employed in the corner and stiffener regions where stress concentrations occur. In the flat regions, the number of elements was chosen with the aim of maintaining a 1:1 aspect ratio, while, in the corner and stiffener regions, four and sixteen elements were utilised respectively. The longitudinal element size for both the cold-formed steel beam and the cable was 10 mm.

4.2.3 Material modelling

The material behaviour of the cold-formed steel beam and high-strength steel cable was modelled in ABAQUS using the approach described below. In both material models, to account for changes in the cross-sectional area due to straining, the engineering constitutive responses were converted into true stress σ_{true} and logarithmic plastic strain $\epsilon_{\text{ln}}^{\text{pl}}$ using the expressions:

$$\sigma_{\text{true}} = \sigma(1 + \epsilon), \tag{4.1}$$

$$\epsilon_{\text{ln}}^{\text{pl}} = \ln(1 + \epsilon) - \frac{\sigma_{\text{true}}}{E}, \tag{4.2}$$

where σ and ϵ are the engineering stress and strain respectively, and E is the Young's modulus of the material.

In the case of the cable, the above conversion was required since, by default, truss elements in ABAQUS (2014) have an effective Poisson's ratio v_{eff} equal to 0.5 and thus are assumed to be made from an incompressible material (*i.e.* their volume does not change under straining). Therefore, the change of the cross-sectional area of truss elements is accounted in the analysis and thus the conversion from engineering to true stresses is required.

4.2.3.1 Cold-formed steel

The principal material characteristics of cold-formed steel have been discussed in Section 2.3.2. For the purposes of the present work, two different material models were utilised for the cold-formed steel, as described below.

(a) Elastic, perfectly–plastic

Cold-formed steel typically features a rounded nonlinear material constitutive response with strain hardening and no distinct yielding point, as shown in Figure 2.13(a). However, to enable direct comparisons of the FE models with the linear elastic analytical expressions derived in Section 3.4, the material behaviour was idealised using an elastic,

perfectly-plastic material model with no strain hardening, as shown in Figure 4.3. A yield stress of $F_{y,s}$=491 N/mm^2 and Young's modulus of E_s=201 kN/mm^2 were chosen for the cold-formed steel, based on the experimental work conducted by Kyvelou *et al.* (2018). Note that residual stresses and strength enhancement in the corner regions of the cold-formed steel beam, which arise from the plastic deformations induced during the cold-forming process, as discussed in Sections 2.3.2.2 and 2.3.2.3 respectively, were not modelled in conjunction with this material model.
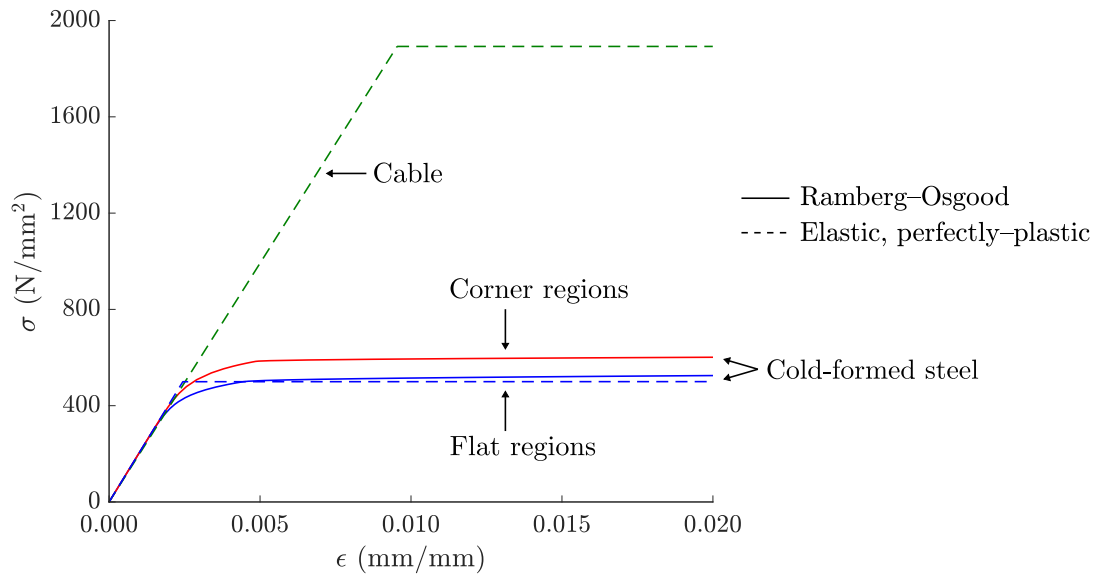
Figure 4.3: Initial part of the material constitutive curves for the flat and corner regions of the cold-formed steel beam and the equivalent for the high-strength steel cable.

(b) Ramberg–Osgood

To model the more realistic rounded material constitutive behaviour of cold-formed steel, shown in Figure 2.13(b), the modified two-stage Ramberg–Osgood model was employed. In this manner, direct comparisons of the FE results with the capacity predictions, which are based on the empirical Direct Strength Method, were enabled. Originally developed by Ramberg and Osgood (1943) to capture the nonlinear response of metallic materials, such as aluminium and stainless steel, this model was subsequently modified by several researchers (Hill, 1944; Mirambell and Real, 2000; Rasmussen, 2003), until Gardner and

Ashraf (2006) proposed the following expressions:

$$\epsilon = \frac{\sigma}{E_s} + 0.002 \left(\frac{\sigma}{\sigma_{0.2}}\right)^n \qquad \text{for} \quad \sigma \leqslant \sigma_{0.2}, \tag{4.3}$$

$$\epsilon = \frac{\sigma - \sigma_{0.2}}{E_{0.2}} + \left(\epsilon_{t1.0} - \epsilon_{t0.2} - \frac{\sigma_{1.0} - \sigma_{0.2}}{E_{0.2}}\right) \left(\frac{\sigma - \sigma_{0.2}}{\sigma_{1.0} - \sigma_{0.2}}\right)^{n'_{0.2,1.0}} + \epsilon_{t0.2} \qquad \text{for} \quad \sigma > \sigma_{0.2}, \tag{4.4}$$

where $E_{0.2}$ is the tangent modulus at the 0.2% proof stress $\sigma_{0.2}$, which is typically taken as the equivalent yield point for design. Moreover, $\epsilon_{t0.2}$ and $\epsilon_{t1.0}$ are the total strains at 0.2% proof stress $\sigma_{0.2}$ and 1.0% proof stress $\sigma_{1.0}$ respectively. The roundedness of the first and second stages of the constitutive relationship is defined by the strain hardening exponents n and $n'_{0.2,1.0}$ respectively. Regarding the determination of the 1.0% proof stress, Haidarali and Nethercot (2011) utilised experimental data from the tensile coupon tests conducted by Yu and Schafer (2003; 2006) to propose the following expression, where $\sigma_{0.2}$ and $\sigma_{1.0}$ are in N/mm²:

$$\frac{\sigma_{1.0}}{\sigma_{0.2}} = 1.8656\sigma_{0.2}^{-0.0948}. \tag{4.5}$$

The modified two-stage Ramberg–Osgood model has been utilised in previous research (Haidarali and Nethercot, 2011; Hui, 2014; Kyvelou et al., 2018) to replicate the nonlinear material response of cold-formed steel members accurately. Recently, Gardner and Yun (2018) analysed an extensive set of material strain data collected from literature to provide predictive expressions for the key input parameters in Equations (4.3) and (4.4), thus enabling the determination of the full constitutive response of cold-formed steels.

As discussed in Section 2.3.2.2, owing to the development of plastic deformations during the cold-forming process, the corner regions of cold-formed steel members exhibit higher yield and ultimate strengths, as well as lower ductility, than the flat regions. In the present study, when the modified Ramberg–Osgood material model was used, this effect was included by increasing the 0.2% proof stress of the material within the corner regions $\sigma_{0.2,\text{corner}}$ of the beam, according to $\sigma_{0.2,\text{corner}}=1.17\,\sigma_{0.2,\text{flat}}$, as determined experimentally by Kyvelou et al. (2018); $\sigma_{0.2,\text{flat}}$ being the 0.2% proof stress within the flat regions.

Following the same approach as Kyvelou *et al.* (2018), residual stresses through the thickness of the cold-formed steel section were not introduced into the FE models of the present study since their effect is assumed to be inherently included in the constitutive relationships obtained from the tensile coupon tests, as discussed in Section 2.3.2.3. It is worth noting that, as reported in the case of the LiteSteel beams (Anapayan et al., 2011), the combined cold-forming and electric welding resistance process, as recommended in Section 3.3.2.1, can have considerable effects on the constitutive response of the cold-formed steel and on the distributions of the residual stresses and initial geometric imperfections. In the future, these effects will need to be considered explicitly following the fabrication of the proposed cold-formed steel cross-sections.

The following material parameters, determined experimentally by Kyvelou *et al.* (2018) for cold-formed steel beams similar to those studied in the present work (see Figure 3.2), were adopted in the case of the modified Ramberg–Osgood material model: E_s=201 kN/mm^2, $\sigma_{0.2,\text{flat}}$=491 N/mm^2, n=11.2, $n'_{0.2,1.0}$=2.1. The resulting constitutive response of the cold-formed steel is shown in Figure 4.3 alongside the idealised elastic, perfectly–plastic material model introduced in Section 4.2.3.1(a).

4.2.3.2   High-strength steel cable

The high-strength steel cable was modelled as elastic, perfectly–plastic, as shown in Figure 4.3. The plastic part of the material curve was included to enable the identification of cable failure; the FE simulation terminated when the yield stress of the cable was reached. The yield stress of the cable was taken as $F_{y,c}$=1860 N/mm^2 following Gosaye *et al.* (2014), while the Young's modulus was taken to be E_c=195 kN/mm^2 based on Clause 3.3.6(3) in EN-1992-1-1 (2004) and the research by Madrazo-Aguirre *et al.* (2015b). The coefficient of thermal expansion of the cable α_{th} was taken to be 1.2×10^{-5} K^{-1} according to Clause 3.3(1) of EN-1993-1-11 (2006). As discussed in Section 4.2.7, this coefficient was needed since in the developed FE models the prestressing force within the cable was applied by means of restrained thermal contraction.

4.2.4 Initial geometric imperfections

As discussed in Section 2.3.4, the buckling behaviour and ultimate load-carrying capacity of cold-formed steel members are strongly influenced by the shape, distribution and magnitude of initial geometric imperfections (Schafer and Peköz, 1998a). Hence, in the present work, perturbations were imposed on the initially perfect geometry of the cold-formed steel members. As described below, the characteristics of these perturbations were based on the critical local and distortional buckling modes of the cold-formed steel cross-section, which can be obtained using the finite strip software CUFSM (Li and Schafer, 2010b). The CUFSM analysis and the extraction, scaling, distribution and superposition of the initial geometric imperfections were automated to improve the efficiency of the modelling process, as discussed in Section 1.4.

To account for the loading configurations of Stages I and II, *i.e.* compression plus negative and positive bending respectively, the imperfection shapes were obtained by applying negative and positive bending stress distributions in CUFSM respectively. The resulting signature curves, shown in Figures 3.10 and 3.11(b) for positive and negative bending respectively, were then utilised to determine the shapes and distributions of the initial imperfections, as described below. Note that, since, as discussed in Section 3.3.3, the studied members are fully braced against lateral-torsional buckling (during both loading stages) and negative bending distortional buckling (during the prestressing stage), initial imperfections corresponding to these modes were not introduced in the developed FE models.

Firstly, the cross-sectional deformations corresponding to the critical local buckling mode for negative bending, shown in Figure 4.4(C), as well as the local and distortional critical buckling modes for positive bending, shown in Figures 4.4(A) and (B) respectively, were extracted. The distortional mode for negative bending, shown in Figure 4.4(D), was not imposed since this mode is restrained by both the presence of the cable and by the lateral restraints that are present along the bottom flange of the member.

Subsequently, the buckling shapes were scaled according to the corresponding maximum imperfection magnitudes. Since no measured data were available for the purpose of the
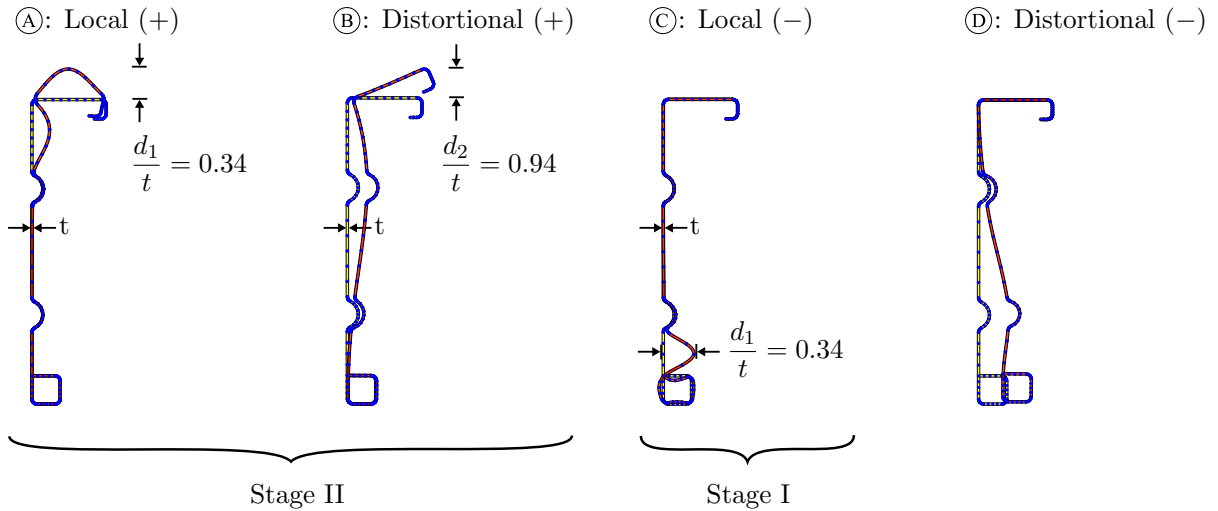
Figure 4.4: Deformed shapes and magnitudes of initial geometric imperfections corresponding to the signature curves in Figures 3.10 (points A–B) and 3.11(b) (points C–D) for positive and negative bending respectively.

present work, the imperfection magnitudes were based on the cumulative distribution functions (CDFs) proposed by Schafer and Peköz (1998a). As discussed in Section 2.3.4, the CDFs were derived from measured imperfection magnitudes and represent the probability of a magnitude being exceeded. As often adopted in the literature (Yu and Schafer, 2007; Haidarali and Nethercot, 2011; Shifferaw and Schafer, 2012; Torabian et al., 2014a; Ma et al., 2015; Ye et al., 2016b), initial geometric imperfections consistent with a CDF value of 50% were employed herein, corresponding to values of d_1/t=0.34 and d_2/t=0.94 for the local and distortional buckling modes respectively, as illustrated in Figures 4.4(A)–(C). The suitability of this assumption is verified in Section 4.3, where the validation of the FE modelling approach is presented.

The amplified cross-sectional imperfection shapes were distributed along the member using sinusoidal functions with half-wavelengths corresponding to the critical local and distortional modes, as determined using CUFSM (see Figures 3.10 and 3.11(b)). An example of the distribution of the critical local L_{crl}^+ and distortional L_{crd}^+ buckling half-wavelengths corresponding to the modes shown in Figures 4.4(A) and (B) respectively, is demonstrated in Figure 4.5. In the developed FE models, the distribution of the half-wavelengths was adjusted slightly to ensure that the peaks of the local and distortional modes were aligned at midspan, as shown in Figure 4.5, while an inward top flange–lip motion at midspan was also imposed (Shifferaw and Schafer, 2012; Hui et al., 2016).

Finally, the three imperfection distributions were superposed and then introduced to the initially perfect geometry of the cold-formed steel member, as illustrated in Figure 4.6.
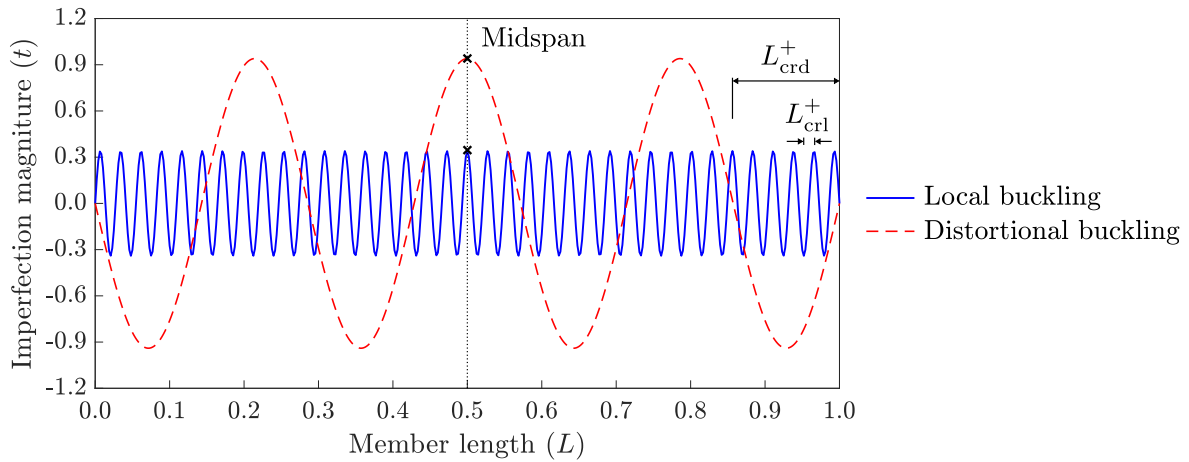
Figure 4.5: Distribution of the local and distortional buckling modes in the case of the reference cross-section profile under positive bending.
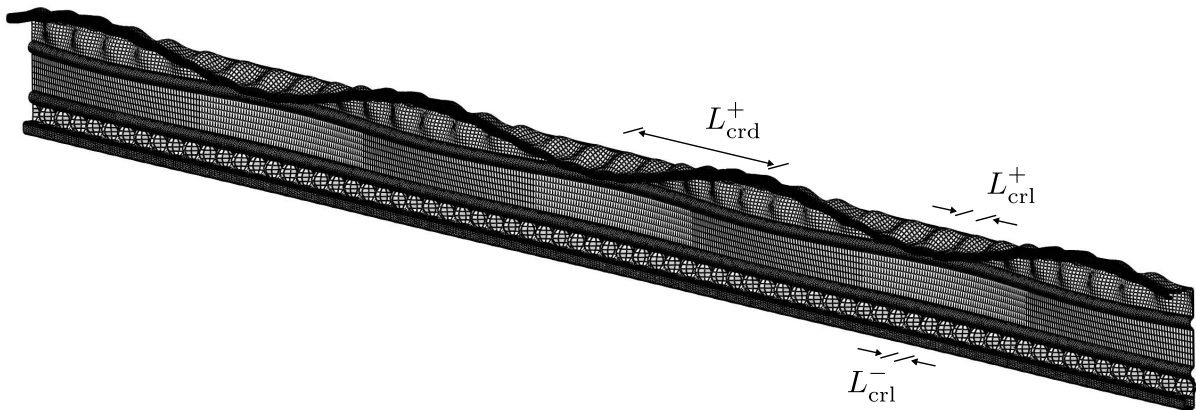
Figure 4.6: 3-D FE representation of the superposed initial geometric imperfections; L_{crl}^- is the critical half-wavelength to distortional buckling due to negative bending, shown in Figure 4.4(C). For illustration purposes the imperfections have been magnified by a factor of 20.

4.2.5   Beam–cable connection

An idealised connection between the cold-formed steel beam and the cable was modelled by making the following assumptions:

(i) The cable is unbonded and concentric with respect to the bottom hollow flange of the cross-section along the entire span of the member.

(ii) The end anchorages are the only locations where a physical (fully tied) connection between the beam and the cable is present.

(iii) No loss of prestress occurs within the cable or at the anchorages.

To achieve a good representation of the idealised beam–cable connection, two types of constraints were imposed to the degrees of freedom (DOFs) of the cable nodes, as shown in Figures 4.7(a)–(b).

(a) Bottom flange   (b) Bottom flange   (c) End supports
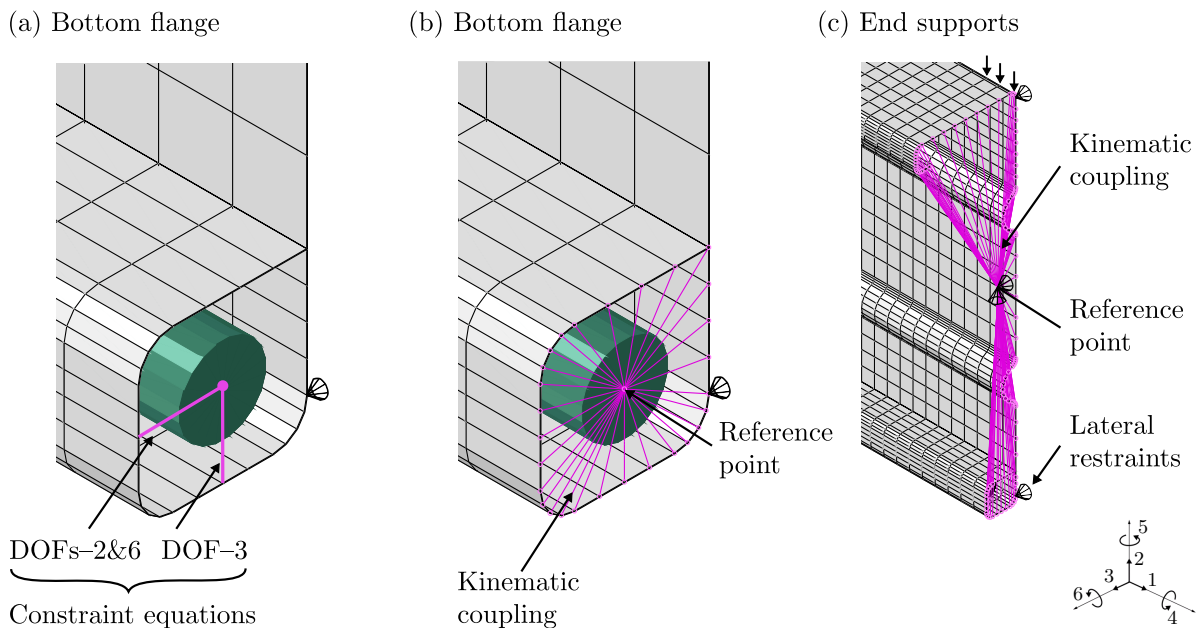
Figure 4.7: Modelling of the (a) beam–cable connection at every cross-section along the member, (b) anchorages at the two beam ends and (c) simply-supported boundary conditions.

Firstly, two sets of linear constraint equations, modelled with the *Equation keyword in ABAQUS (2014), were introduced at every cross-section along the entire length of the member, as illustrated in Figure 4.7(a). One set of equations constrained the vertical translation (DOF–2) and in-plane rotation (DOF–6) of the cable nodes to the middle side node of the bottom flange of the beam, while a second set of equations constrained the out-of-plane translation (DOF–3) of the cable nodes to the middle bottom node of the bottom flange. In this manner, the cable was kept in the centre of the bottom flange, but it was allowed to elongate freely along the member since DOF–1 remained unconstrained. Note that, since the cable is free to elongate, the axial stress level within the cable is constant along the entire length.

Secondly, kinematic coupling constraints (ABAQUS, 2014) were utilised to model the anchorages. As illustrated in Figure 4.7(b), the cable end node is tied to a reference point to which the end nodes of the bottom hollow flange were also linked using kinematic coupling. This type of connection ensured the uniform transfer of the prestressing force into the entire bottom flange at the two ends of the beam and thus prevented any excessive stress concentrations and therefore localised failures. In practice, the uniform transfer of the prestressing force can be achieved by utilising stiff end-plates, as performed by Gosaye *et al.* (2014) and Wang *et al.* (2017).

4.2.6   Boundary conditions

To model the simply-supported boundary conditions at the two end supports, kinematic coupling constraints were employed to link the DOFs of the member end nodes to those of a single reference point, which was defined at the centroid of the cross-section, as demonstrated in Figure 4.7(c). Subsequently, the vertical (DOF–2) and out-of-plane (DOF–3) translations of the reference point were restrained and thus the effect of the boundary conditions applied at the reference point was uniformly distributed across the entire cross-section. Note that the kinematic coupling constraints result in warping-fixed conditions at both end supports.

Longitudinal rigid body motion of the member was prevented by restraining the longitudinal (DOF–1) translation of the middle node of the web at midspan, as shown in Figure 3.6(a). Furthermore, since, as discussed in Section 3.3.3, the member is assumed to be fully restrained against lateral-torsional buckling, the out-of-plane (DOF–3) translations of the top and bottom nodes of the web, as shown in Figure 4.7(c), were restrained at 600 mm intervals along the member length, as illustrated in Figure 3.6(b).

4.2.7   Loading conditions

To model the prestressing and imposed vertical loading conditions, two distinct loading steps were defined. In the first step (*i.e.* Stage I), the prestressing force was modelled by imposing a negative change in temperature in the cable elements using the *Tem-

perature keyword (ABAQUS, 2014). The restrained thermal contraction of the cable resulted in the development of a tensile force P_i, which was then transferred as the initial prestressing force at the anchorages of the member. The temperature difference ΔT required to induce the desired prestressing force can be back-calculated using the expression $P_i = -E_c A_c \alpha_{th} \Delta T$, where α_{th} is the thermal expansion coefficient of the cable, as defined in Section 4.2.3.2. The approach of introducing prestress using thermal loading has been successfully used in previous studies (Gosaye et al., 2014; Madrazo-Aguirre et al., 2015b). It is worth noting that, to account for the initial elastic shortening of the cold-formed steel beam and cable, the prestressing stage was iterated until the desired initial prestress level was achieved.

In the second step (*i.e.* Stage II), the uniformly distributed loading was modelled by applying concentrated point loads at the junction between the top flange and the web at each cross-section along the entire span of the member, as shown in Figure 4.7(c).

4.2.8 Solution scheme

The first loading stage was modelled using a geometrically nonlinear 'Static' analysis (ABAQUS, 2014); in this manner, termination of the analysis when reaching the pre-defined initial prestress level was ensured. The second loading step was performed using the modified Riks arc-length solver (Riks, 1979) by means of a geometrically nonlinear 'Static, Riks' analysis (ABAQUS, 2014), which is typically employed to analyse complex geometrically nonlinear responses in FE models, such as in the case of cold-formed steel members (Schafer et al., 2010).

4.3 Validation of finite element modelling approach

Since experimental investigations were not within the scope of the present thesis, to ensure that the behaviour of the prestressed cold-formed steel beams was simulated accurately by the FE models, a combination of validation techniques is employed herein. The adopted validation approach regarding the two structural components of the prestressed system,

i.e. the prestressed cable and the cold-formed steel beam, is described below.

4.3.1 Modelling of prestressed cable

The modelling approach for the prestressed cable is validated against analytical results in Chapter 5. Specifically, validation is presented both at member level, in terms of vertical deflections (see Section 5.2.2), and at cross-section level, in terms of the axial stress distributions within the cold-formed steel beam and cable (see Section 5.2.3). This is performed for three different models, namely bare steel beams, non-prestressed beams (*i.e.* bare steel beams with a cable but no prestress) and prestressed beams. Furthermore, the FE modelling techniques employed to model the anchorages, the prestressing force and the connection/bond between the steel member and the cable have been successfully utilised by Gosaye *et al.* (2016) and Wang *et al.* (2017) to simulate prestressing in prestressed steel tubular members. The numerical models in the aforementioned studies were themselves successfully validated against experimental results.

4.3.2 Modelling of cold-formed steel beam

The performance of cold-formed steel beams with the same cross-section profile as that of the proposed beams (see Figure 3.3) has not been studied experimentally in the past. Hence, the FE modelling approach adopted to model the cold-formed steel beam is validated against experiments on cross-sections that are as similar as possible to those of the proposed beams. Specifically, the experimental investigations of Yu and Schafer (2006) and Wang and Zhang (2009), in which lipped channel cross-sections were tested in bending, have been chosen. Although the tested cross-sections are not identical to those modelled herein, the sizes, proportions, material properties and failure modes (*i.e.* local and distortional buckling) are similar. Further validation of the general approach to the modelling of the cold-formed steel cross-sections adopted herein is presented in Kyvelou *et al.* (2017). The experimental loading arrangement adopted by Yu and Schafer (2006) and Wang and Zhang (2009) was four-point bending; this arrangement is commonly employed in physical laboratory testing due to the convenience of the experimental setup (*i.e.* two

loading jacks or one loading jack and a spreader beam) and broadly reflects the parabolic bending moment distribution arising under uniform gravity loading, as modelled herein.

Comparisons against the results of the aforementioned experimental studies are presented in Sections 4.3.2.2 and 4.3.2.3.

4.3.2.1 Previous experimental studies on cold-formed steel beams

In this sub-section, previous experimental investigations on cold-formed steel beams are presented, with the aim of identifying the most suitable studies for the purposes of validating the FE modelling approach employed in the current work. The experiments conducted on lipped channel cross-sections, which have the closest geometry to that of the proposed beams, are considered. These studies are listed chronologically in Table 4.1.

Table 4.1: Summary of experimental studies on simply-supported cold-formed steel beams with a lipped channel cross-section profile.

Experimental study	Cross-section type	Loading configuration	No. of tests
LaBoube and Yu (1975) [*]	Lipped C	4-point bending	22
Nguyen and Yu (1980) [*]	Lipped C with web stiffener	4-point bending	30
Willis and Wallace (1990) [*]	Lipped C	Uniform loading	4
Moreyra and Peköz (1994) [*]	Lipped C	Uniform loading	9
Rogers (1995) [*,**]	Lipped C	4-point bending	49
Rogers (1995) [*,**]	Unlipped C	4-point bending	10
Yu and Schafer (2003) [*]	Lipped C	4-point bending	12
Javaroni and Gonçalves (2006) [**]	Lipped C	4-point bending	24
Yu and Schafer (2006) [**,ø]	Lipped C	4-point bending	15
Wang and Zhang (2009) [**,ø]	Lipped C	4-point and 3-point bending	6
Wang and Zhang (2009) [**,ø]	Lipped C with edge stiffeners	4-point and 3-point bending	6
Pham and Hancock (2013) [*,**,†]	Lipped C	4-point bending	12
Pham and Hancock (2013) [*,**,†]	Lipped C with edge stiffeners (SupaCee)	4-point bending	12
Kyvelou et al. (2017) [*]	Lipped C with web and edge stiffeners	4-point bending	2

[*] Bracing used to connect the top flanges of the two beams along the entire span.
[**] No bracing used between the top flanges in the constant moment region.
[ø] Experimental studies chosen for validation purposes in the current work.
[†] Involved the use of high strength steel.

In the listed studies, each test comprised a pair of cold-formed steel beams, which were inter-connected by means of steel decking, as shown in Figure 4.8(a), or angles, as shown in Figure 4.8(b), at the top and/or bottom flanges to prevent lateral buckling of each

individual beam. However, the presence of bracing at the top of the beams imposes a restraining effect on the vertical deformations of the flanges when distortional buckling takes place. Consequently, the bracing enhances the distortional buckling strength of the beams. Since, in the current work, both local and distortional buckling are allowed to take place freely, the experiments that involved the bracing of the top flanges (indicated with a single asterisk in Table 4.1) were not considered for validation purposes.
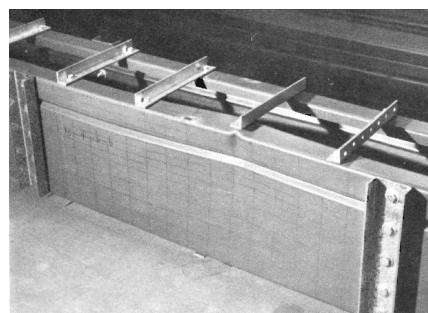
(a) Yu and Schafer (2007)   (b) Nguyen and Yu (1980)

Figure 4.8: Bracing inter-connecting the top/bottom flanges of the two tested cold-formed steel beams; (a) steel sheeting and (b) angle bracing.

(a) Young and Schafer (2005)   (b) Wang and Zhang (2009)

Figure 4.9: Test setups where both local and distortional buckling are allowed to take place freely within the constant moment region.

Fortunately, a few studies investigating the distortional buckling strength of cold-formed steel beams took the aforementioned effect into consideration by removing the bracing within the constant moment (*i.e.* the middle) span, as shown in Figure 4.9. Instead, bracing was used only along the shear (*i.e.* the first and third) spans to restrain lateral buckling. These studies are indicated with a double asterisk in Table 4.1. Specifically, the experimental investigations of Yu and Schafer (2006) and Wang and Zhang (2009),

whereby lipped channel cross-sections were tested in bending, have been chosen.

As discussed below, for the purposes of the validation, the FE modelling techniques presented in Section 4.2 were adjusted to match the conditions of the chosen experiments.

4.3.2.2 Yu and Schafer (2006) distortional buckling tests

Following a series of local buckling tests (Yu and Schafer, 2003), a series of fifteen tests was conducted by Yu and Schafer (2006) to investigate the failure of cold-formed steel lipped channel beams by distortional buckling. As shown in Figure 4.10, the beams in
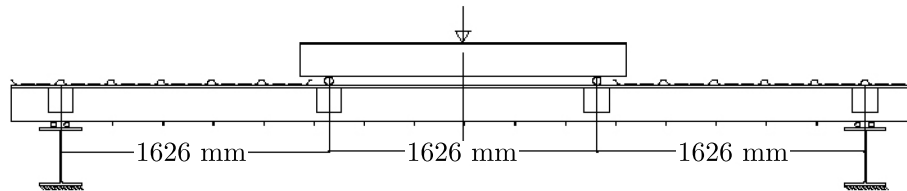
Figure 4.10: Test setup of the distortional buckling tests conducted by Yu and Schafer (2006).

the distortional buckling tests were simply-supported and tested in pairs under four-point bending. In contrast with the local buckling tests, shown in Figure 4.8(a), where the top flanges of the beams were braced along the entire span, in the distortional buckling tests, the top flanges were not braced within the constant moment region, as shown in Figure 4.9(a), thus allowing both local and distortional buckling to take place freely. Note that the bottom flanges were connected along the entire span using angles. By comparing nine identical tests, Yu and Schafer (2006) demonstrated that the presence of the bracing within the constant moment region increased the capacity of the beams by an average of 17%. Overall, the test results verified that the DSM approach for distortional buckling provides reliable predictions regarding the ultimate capacity of cold-formed steel beams undergoing distortional buckling failures (Yu and Schafer, 2006).

For the purposes of validation, only one of the cold-formed steel beams from each tested pair was modelled since the set up was symmetrical. The features of the FE models, which simulate the tests conducted by Yu and Schafer (2006), are illustrated in Figure 4.11. The material response of each specimen was extracted from the reported stress–strain curves (Yu and Schafer, 2005) and was utilised as the material model in the

128
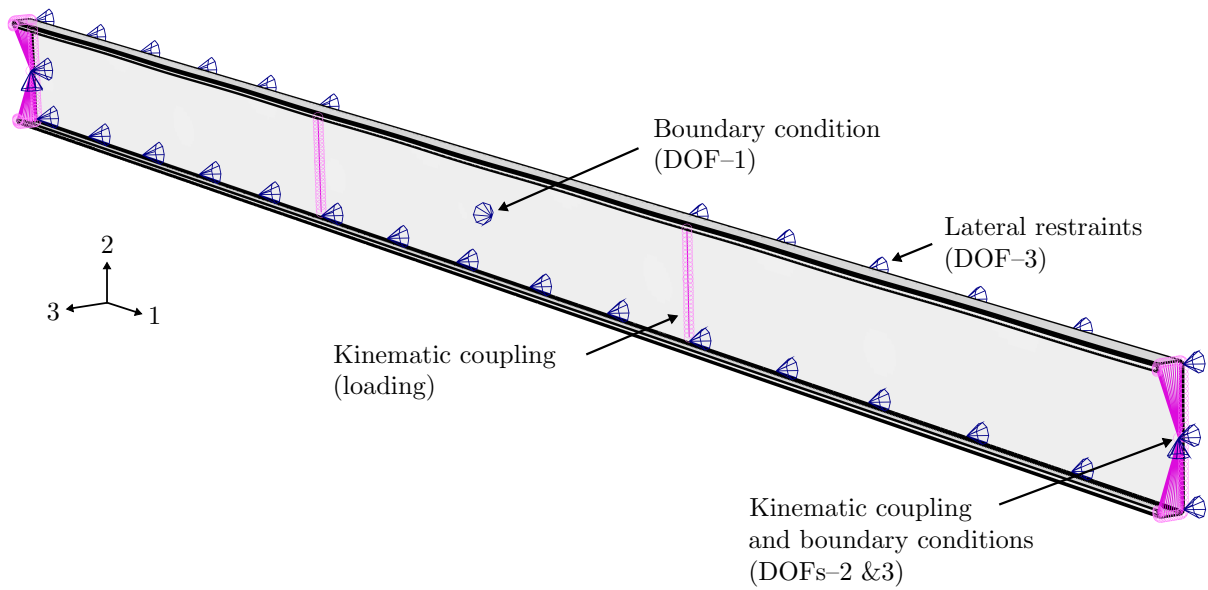
Figure 4.11: FE model simulating the four-point bending tests by Yu and Schafer (2006).
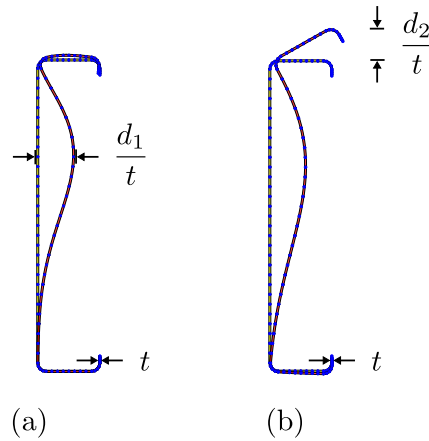
Figure 4.12: Cross-sectional imperfection shapes corresponding to the critical (a) local and (b) distortional buckling modes of the beams tested by Yu and Schafer (2006).

Table 4.2: Imperfection magnitudes corresponding to the studied CDF values; d_1 and d_2 are defined in Figure 4.12.

	25% CDF	50% CDF	75% CDF
d_1/t	0.14	0.34	0.66
d_2/t	0.64	0.94	1.55

Table 4.3: Summary of the validation results for the Yu and Schafer (2006) experiments. Comparisons of the FE results with the test results and DSM predictions.

Model no.	Test label	λ_l or λ_d	M_{FE}/M_{test}	M_{FE}/M_{DSM}	M_{test}/M_{DSM}	Failure mode
1	D8C097-7E6W	0.93	1.00	0.99	0.99	Distortional buckling
2	D8C097-5E4W	–	–	–	–	Lateral-torsional buckling
3	D8C085-2E1W	0.79	0.91	0.99	1.09	Distortional buckling
4	D8C068-6E7W	1.08	1.02	0.91	0.89	Distortional buckling
5	D8C054-7E6W	0.97	1.00	1.00	1.00	Distortional buckling
6	D8C045-1E2W	1.14	1.08	1.05	0.97	Local buckling
7	D8C043-4E2W	1.12	1.05	1.04	0.99	Distortional buckling
8	D8C033-1E2W	1.16	1.07	1.12	1.05	Local buckling
9	D12C068-10E11W *	1.09	0.83	0.98	1.18	Distortional buckling
10	D12C068-1E2W **	–	–	–	–	
11	D10C068-4E3W	0.78	0.93	0.94	1.01	Distortional buckling
12	D10C056-3E4W **	–	–	–	–	
13	D10C048-1E2W	1.26	1.08	1.10	1.02	Distortional buckling
14	D6C063-2E1W	0.91	1.00	1.02	1.02	Distortional buckling
15	D3.62C054-3E4W	0.72	0.84	0.90	1.07	Material yielding
		Mean	0.99	1.00	1.02	
		c.o.v.	0.09	0.07	0.07	

  *   Unexpected sharp drop in test result during loading.

 **   Beam damaged prior to testing, hence the test was not modelled.

corresponding FE simulation. The initial geometric imperfections were modelled using the approach described in the Section 4.2.4. For this purpose, the CUFSM software was used to obtain the cross-sectional imperfection level shapes corresponding to the local and distortional buckling modes for each specimen, as shown in Figure 4.12. Three different imperfections magnitudes corresponding to the CDF values of 25%, 50% and 75% (see Section 2.3.4) were used, as listed in Table 4.2. Modelling different magnitudes resulted in the imperfection sensitivity study that is presented in Section 4.3.2.4.

The validation results are summarised in Table 4.3, where the ultimate moment at the midspan of the FE models M_{FE} is compared with the test results M_{test} and the DSM predictions M_{DSM}. Note that the listed values of the local $\lambda_l = \sqrt{M_y/M_{crl}}$ and distortional $\lambda_d = \sqrt{M_y/M_{crd}}$ cross-sectional slendernesses were based on the elastic critical local M_{crl} and distortional M_{crd} buckling moments, as determined by Yu and Schafer (2006) using CUFSM. Overall, excellent agreement is observed between the FE and test results, with a mean M_{FE}/M_{test} value of 0.99. The FE models also show excellent agreement with the DSM predictions, with a mean M_{FE}/M_{DSM} value of 1.00 being achieved. The low coefficient of variation (c.o.v.) values indicate that there is a low degree of scatter in

the results. Note that Test 2 was not included in the comparisons since, during testing, the beam failed due to lateral-torsional buckling (Yu and Schafer, 2006). Similarly, tests 10 and 12 were not modelled since these beams were damaged prior to testing (Yu and Schafer, 2005, 2006).

4.3.2.3 Wang and Zhang (2009) four-point and three-point bending tests

Wang and Zhang (2009) conducted an experimental and numerical investigation into the behaviour of cold-formed steel beams subjected to four-point and three-point bending. In total, twelve tests were conducted, whereby beams with lipped channel cross-sections with different types of edge stiffeners, as shown in Figure 4.13(a), were tested in pairs.
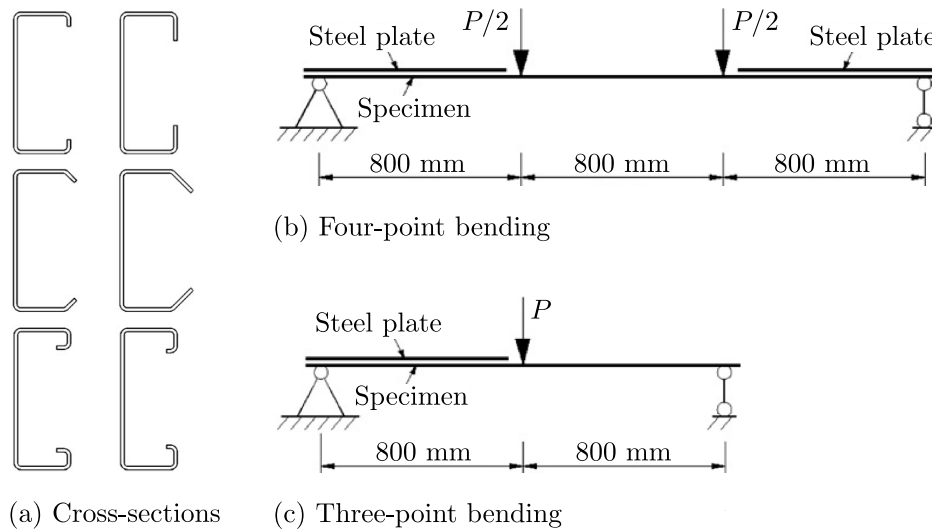
Figure 4.13: (a) Cross-sectional geometry and (b)–(c) loading configurations of the tests conducted by Wang and Zhang (2009).

As shown in Figures 4.9(b) and 4.13(b), in the four-point bending tests, the two beams were not braced within the constant moment region to allow distortional buckling to take place freely. In the three-point bending tests, steel plating was used as bracing only along one half of the beam length, as shown in Figure 4.13(c). The tests demonstrated that the governing buckling mode and the characteristics of the edge stiffeners can have a significant influence on the ultimate capacity of cold-formed steel beams (Wang and Zhang, 2009).

For the purposes of validation, eight of the beam tests were modelled herein; four in

four-point bending and four in three-point bending. The same FE modelling features as in the case of the Yu and Schafer experiments, described in Section 4.3.2.2, were used. As recommended by Wang and Zhang (2009), a bilinear stress–strain curve was employed for the material model, with the reported average yield stress and Young's modulus values being used. Furthermore, the reported average values of the imperfection magnitudes were utilised (Wang and Zhang, 2009). The validation results are summarised in Table 4.4, where excellent agreement between the FE and test results may be seen.

Table 4.4: Summary of the validation results for the Wang and Zhang (2009) experiments. Comparisons of the FE with the corresponding test results.

Model no.	Test label	Cross-section profile	Loading configuration	λ_{d}	$M_{\mathrm{FE}}/M_{\mathrm{test}}$
1	L_CH200B8Od30a20	Lipped C with edge stiffeners	4-point bending	0.60	0.95
2	L_CH200B8Od35a15	Lipped C with edge stiffeners	4-point bending	0.60	0.94
3	L_UH200B80d20	Lipped C	4-point bending	0.74	0.91
4	L_UH200B80d40	Lipped C	4-point bending	0.61	0.95
5	S_CH200B8Od30a20	Lipped C with edge stiffeners	3-point bending	0.55	1.01
6	S_CH200B8Od35a15	Lipped C with edge stiffeners	3-point bending	0.60	1.00
7	S_UH200B80d20	Lipped C	3-point bending	0.75	0.98
8	S_UH200B80d40	Lipped C	3-point bending	0.61	0.99
				Mean	0.97
				c.o.v.	0.04

4.3.2.4 Overall validation results

The comparisons of the FE model failure moments with those obtained experimentally by Yu and Schafer (2006) and Wang and Zhang (2009) are illustrated graphically in Figure 4.14. Overall, good agreement between the results from the FE models and the tests is demonstrated, with a mean $M_{\mathrm{FE}}/M_{\mathrm{test}}$ value of 0.98 and a c.o.v. value of 0.07 being achieved. The imperfection sensitivity study is represented by the error bars in Figure 4.14; imperfection sensitivity was only assessed in the case of the Yu and Schafer tests since, in the tests by Wang and Zhang, the reported imperfection magnitudes were utilised. Note that the results with $M_{\mathrm{FE}}/M_{\mathrm{test}}$ values of 0.83 and 0.84 correspond to tests where an unexpected sharp drop in the readings was observed during the testing (Yu and Schafer, 2005), and where, owing to their low slenderness, the beams failed by material yielding (Yu and Schafer, 2006) respectively. The results from the imperfection

sensitivity study are summarised in Table 4.5, where it is observed that the FE models with imperfection magnitudes corresponding to a CDF value of 50% provide the most accurate results with respect to the experiments, confirming the suitability of using this imperfection magnitude in the FE models of the proposed prestressed beams, as described in Section 4.2.4. Note that, in their own simulations of these experiments, Yu and Schafer (2007) also concluded that the 50% CDF value is the most representative.
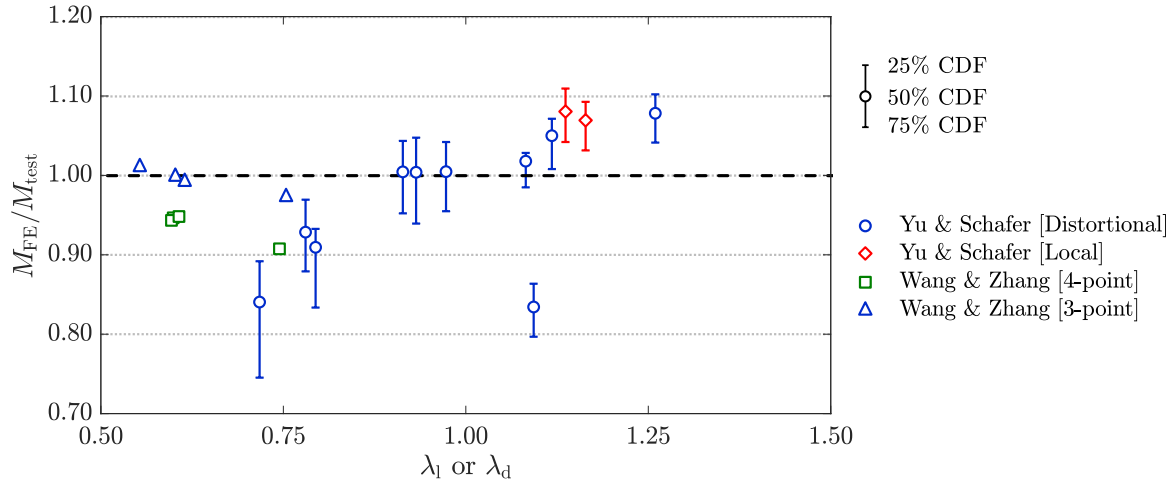
Figure 4.14: Comparison between the FE and test results for the validation purposes. Imperfection sensitivity study for the Yu and Schafer (2006) experiments.

Table 4.5: Summary of the results from the imperfection sensitivity study on the tests by Yu and Schafer (2006). The magnitudes corresponding to the CDF values are given in Table 4.2.

	25% CDF	50% CDF	75% CDF
$(M_{\mathrm{FE}}/M_{\mathrm{test}})_{\mathrm{mean}}$	1.02	0.99	0.93
c.o.v.	0.08	0.09	0.11

The FE results from the validation study are compared with the DSM capacity predictions in Figure 4.15, where the strength expressions for local and distortional buckling, which are obtained using Equations (2.8)–(2.9) and (2.10)–(2.11) respectively, are represented by the dashed and solid lines respectively. The comparison illustrates good agreement between the FE results and the design recommendations. Note that, since the inelastic reserve strength of the beams is not considered herein, the DSM predictions for the six beams of the Wang and Zhang study with $\lambda_{\mathrm{d}} \leqslant 0.673$ are slightly conservative.
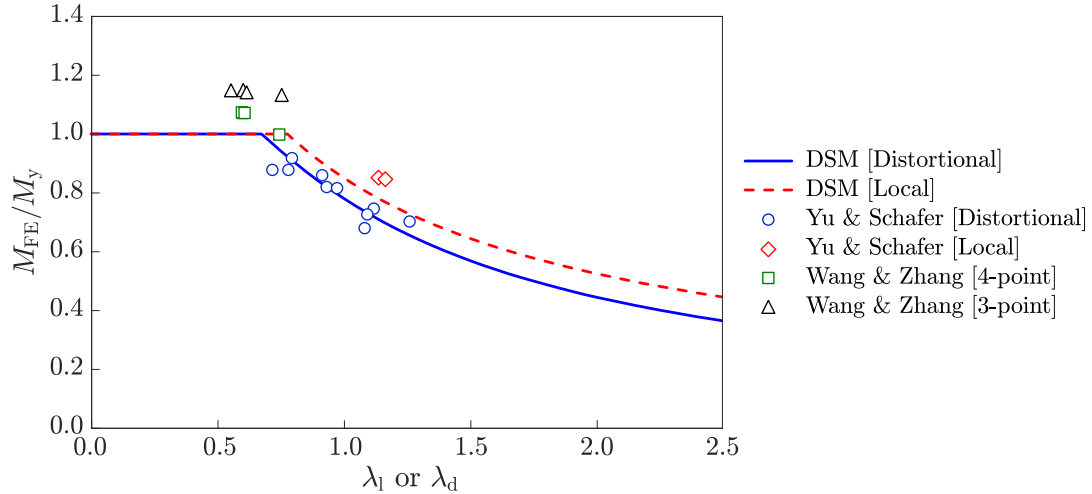
Figure 4.15: Comparison between the FE results from the validation study and the DSM curves, which correspond to local and distortional buckling for a beam fully braced against lateral-torsional buckling.

4.4 Concluding remarks

Geometrically and materially nonlinear finite element (FE) analysis has been employed in the present work to simulate the mechanical behaviour of the proposed prestressed cold-formed steel beams. In the current chapter, the principal features of the FE models have been presented first. In summary, shell and truss elements were employed to model the cold-formed steel and cable respectively, while a sufficiently fine mesh was utilised to ensure accurate results as well as computational efficiency. Two material models were used for the cold-formed steel. In particular, the elastic, perfectly–plastic and Ramberg–Osgood material models were used to enable comparisons of the FE results with the corresponding analytical results and design predictions respectively. The cable was modelled using an elastic, perfectly–plastic material model. Initial geometric imperfections were introduced on the initially perfect geometry of the cold-formed steel member. The characteristics of these perturbations were based on the critical buckling modes of the member, which were obtained using the CUFSM software. Kinematic coupling, equation constraints and lateral restraints were employed to model the beam–cable connection, boundary and loading conditions. Finally, the solution schemes corresponding to the two loading stages were described.

Subsequently, a brief summary regarding previous experimental investigations on cold-

formed steel beams has been conducted to identify the most suitable studies to be utilised for the purposes of validating the FE modelling approach. Overall, excellent agreement was achieved between the FE and test results, as well as between the FE results and DSM predictions, thus validating the suitability of the aforementioned FE modelling features to simulate the cold-formed steel beams in the proposed prestressed system accurately. Based on the validated FE modelling approach, sample FE results and a series of parametric studies are presented in the following chapter.

CHAPTER 5

MECHANICAL BEHAVIOUR
AND PARAMETRIC STUDIES

5.1 Introduction

The finite element (FE) models developed and validated in Chapter 4 are used to corroborate the analytical expressions and failure criteria developed in Chapter 3. The findings also serve to extend the understanding of the mechanical behaviour of prestressed cold-formed steel beams during the different loading stages and provide an insight into the potential benefits in terms of structural performance they may offer.

In the first section of the present chapter, sample FE results are presented and compared with the developed analytical expressions and failure criteria. To understand the effect of prestressing on the behaviour of the studied members, the moment–deflection and moment–stress responses, alongside the deformed shapes and axial stress distributions at the critical cross-section, are analysed in detail. In this manner, the origin of the obtained benefits in terms of the load-carrying capacity and serviceability performance of the prestressed members are demonstrated. Subsequently, the effect of the presence of the lateral restraints and the prestressed cable on the lateral stability of the member and on asymmetric bending is investigated. The sample FE results and their analysis presented in this chapter has been published by Hadjipantelis *et al.* (2018c).

A major advantage of numerical models over expensive experimental investigations is that, once the developed model has been validated against experimental data, many simulations can be processed in parallel, thus offering substantial cost and time benefits. This is exploited in the present chapter to investigate the effect of the key controlling parameters on the behaviour of the proposed prestressed system. A set of parametric studies is thus conducted, whereby in each case the studied controlling parameter is varied while maintaining the remaining parameters constant. The parametric results demonstrate the influence of the prestress level, cable size, section slenderness and centroid location on the structural benefits obtained from the addition of the prestressed cable. Finally, these results are utilised to determine how the obtained benefits can be maximised, demonstrating the significant enhancements in the structural performance of the cold-formed steel beam that can be achieved. The results from the parametric studies presented in this chapter has been published by Hadjipantelis *et al.* (2019b; 2018b).

5.2   Analysis of mechanical behaviour

Comparisons between sample FE results, analytical results and capacity predictions are presented below. The FE results were obtained using the modelling approach presented in Section 4.2. To enable direct comparisons of the FE results with the analytical results, the FE results were obtained using the elastic, perfectly–plastic material model presented in Section 4.2.3.1(a). The analytical results and capacity predictions were based on the developed analytical expressions from Section 3.4 and the failure criteria from Section 3.5 respectively. Note that the resistance factors (*i.e.* ϕ_c, ϕ_b and ϕ_t) in the failure criteria equations are set, together with the load factors, to be unity throughout the present section.

5.2.1   General

The sample FE results were based on the reference geometry, shown in Figure 3.3, with the dimensions listed in Table 3.1; additional geometric properties of the reference beam are given in Table 5.1.

Table 5.1: Properties of the reference cold-formed steel beam and cable.

$P_y = 502.1$ kN	$M_y = 34.5$ kNm	$A_s = 1022.6$ mm^2	$S_t = 7.80{\times}10^4$ mm^3
$P_n = 0.528 P_y$	$M_{nx}^+ = 0.830 M_y$	$I_s = 1.04{\times}10^7$ mm^4	$S_b = 7.04{\times}10^4$ mm^3
$P_{max} = 131.1$ kN	$M_{nx}^- = 1.0~M_y$	$A_c = 86.5$ mm^2	$e = 133.2$ mm

In the present section, the following cases are examined:

(i) Bare cold-formed steel beam

(ii) Non-prestressed beam with the cable present (P_i/P_{max}=0.0)

(iii) Fully prestressed beam (P_i/P_{max}=1.0)

The maximum allowable initial prestressing force that the cold-formed steel beam can carry in the prestressing stage P_{max} is defined in Equation (3.21) and is based on failure criterion I–A from Section 3.5.2.1. Hence, when P_i/P_{max}=1.0 the beam is considered to be fully prestressed. Based on the CUFSM and cFSM results, shown in Figures 3.10 and 3.11, and the nominal axial and bending resistances estimated using the Direct Strength Method (DSM), which are listed in Table 5.1, P_{max} can be calculated to be 131.1 kN in the case of the reference beam. Note that in the FE models of the present section, unless otherwise stated, the length of the member is 4800 mm.

5.2.2 Moment–deflection response

The applied loading in Stage II can be expressed in terms of M_{max} (*i.e.* the maximum moment due to the imposed loading only, as shown in Figure 3.8(c)), and in a normalised form, as M_{max}/M_y, where $M_y = F_{y,s} S_{fy}$ is the yield moment of the bare cold-formed steel cross-section, $F_{y,s}$ is the material yield stress and S_{fy} is the elastic section modulus corresponding to the extreme fibre in first yield. Meanwhile, the global response of the system can be measured in terms of the vertical deflection of the beam at midspan δ_{mid}, which can also be normalised by the midspan vertical deflection of the bare steel beam at the point of first yield $\delta_{mid,y}$.

The M_{max}/M_y versus $\delta_{mid}/\delta_{mid,y}$ response of the reference system considering the three cases listed above is plotted in Figure 5.1, where the analytical results (sloping part)
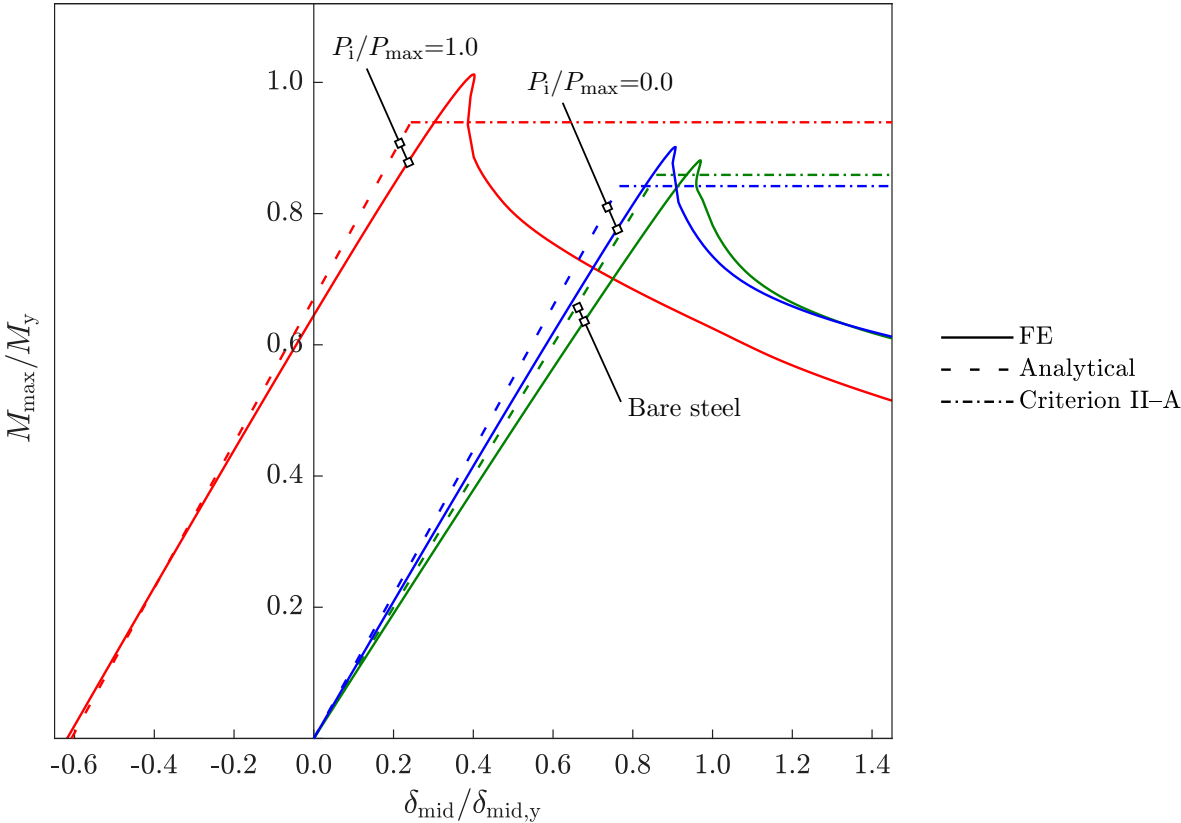
Figure 5.1: Comparison of the normalised moment–deflection response of the three sample FE models against the corresponding analytical results and failure criteria. The FE results correspond to the elastic, perfectly–plastic material model.

and failure criteria (horizontal part) are represented by the dashed lines. The analytical results were calculated using Equations (3.3) and (3.6) for Stages I and II respectively. The capacity prediction for the bare steel beam was simply taken as M_{nx}^{+}, *i.e.* the nominal bending resistance of the bare steel beam about the strong geometric axis under positive bending, as estimated using the DSM (see Section 3.5.1.2). The capacity predictions for the non-prestressed and fully prestressed beams are based on failure criterion II–A, as discussed in Section 3.5.3.1. More specifically, by substituting the expressions for P_{net}^{II} and $M_{net,x}^{II}$ from Table 3.2 and the equation for ΔP, as given in Equation (3.15), into Equation (3.22), the maximum moment M_{max} that can be carried by the cold-formed steel beam for a given initial prestressing force P_i can be estimated as:

$$M_{max} \leqslant \frac{\left[1.0 - \dfrac{P_i}{P_n} + \dfrac{P_i e}{M_{nx}^{+}} \right]}{\left[\dfrac{2e}{3P_n C} + \dfrac{1}{M_{nx}^{+}} - \dfrac{2e^2}{3M_{nx}^{+} C} \right]}, \tag{5.1}$$

where C is the denominator of the equation for ΔP, *i.e.*:

$$C = e^2 + \frac{E_s I_s}{E_c A_c} + r^2. \tag{5.2}$$

During the elastic response of the system in Figure 5.1, good agreement is observed between the FE and analytical results in all cases. The slight deviation of the FE results from the analytical results is attributed to the effect of the initial geometric imperfections, as illustrated in Figure 5.2, where the response of the bare steel and fully prestressed FE models with and without imperfections is shown. The influence of the imperfections is evident firstly by the gradual decrease in the bending stiffness and secondly by the reduced ultimate moment capacity of the beams. Both of these effects are attributed to the fact that, as discussed in Section 4.2.4, the presence of initial geometric imperfections induces the early development of local and/or distortional buckling during loading. Hence, as demonstrated by the fact that the ultimate points of the FE responses with imperfections (*i.e.* the dotted curves) in Figure 5.2 are closer to the DSM predictions (*i.e.* the horizontal dashed lines), the presence of initial geometric imperfections can provide more representative results in the FE simulations. The relatively high imperfection sens-
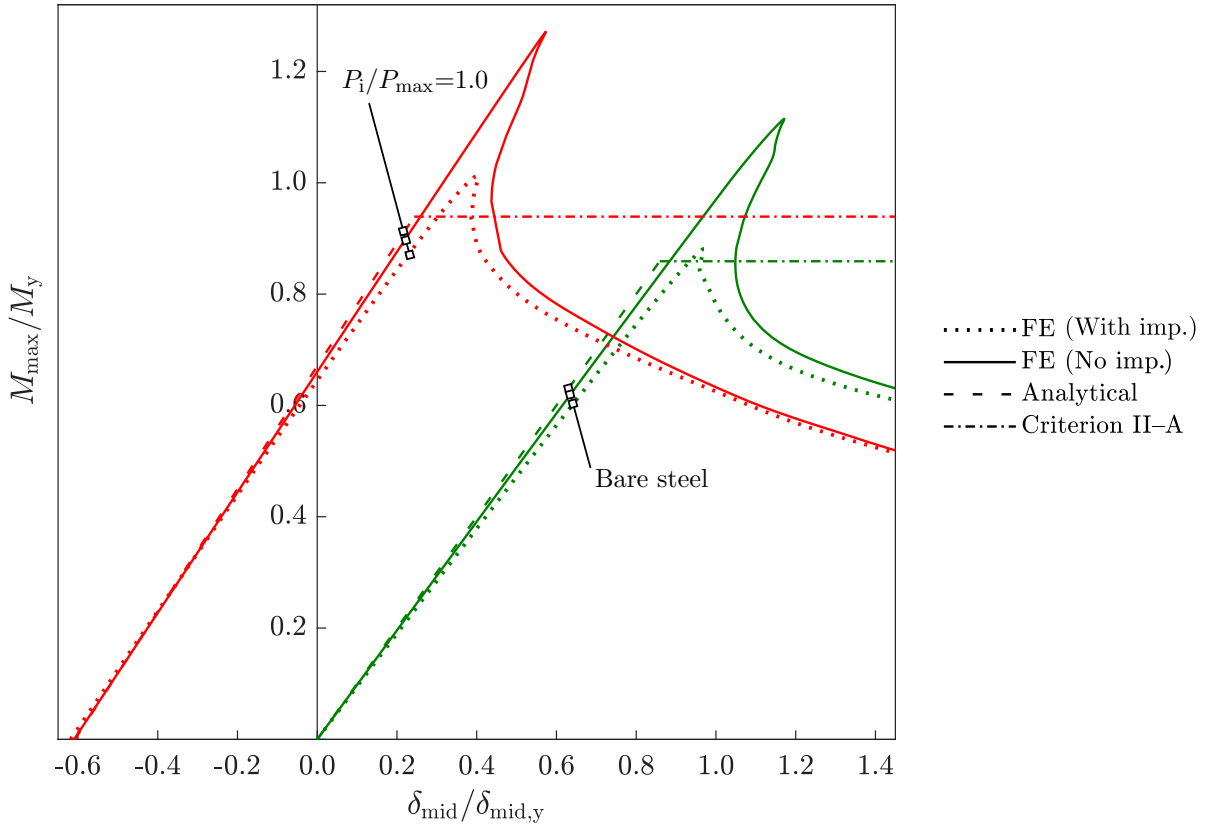
Figure 5.2: Normalised moment–deflection response of the bare steel and fully prestressed FE models with (solid) and without (dotted) initial geometric imperfections.

itivity can be attributed to the fact that the modelled cross-section has a distortional slenderness value λ_d of 0.92, which places the chosen cross-section within the slenderness region of high sensitivity to initial geometric imperfections and residual stresses; note that generally distortional buckling failures are considered to have higher imperfection sensitivity than local buckling failures (Schafer, 2002).

In Figure 5.1, good agreement is also exhibited between the FE results and the capacity predictions in all cases, demonstrating that the proposed design approach provides a suitable estimation of the load-carrying capacity of prestressed cold-formed steel beams. It is also observed that the ultimate moment capacity of the prestressed beam $M_{ult,p}$ is considerably higher than that of the bare steel beam M_{ult}. This increase represents the principal benefit from the prestressing process, as far as the load-carrying capacity of the beam is concerned. In the present example, an increase of 15% in the ultimate moment capacity of the bare steel beam was achieved as a result of the application of a 131.1 kN initial prestressing force using a cable of radius 5.25 mm (*i.e.* 8.5% more material, as

calculated using the A_c/A_s ratio). As discussed in Section 5.3, with further optimisation, an increase in the ultimate moment capacity of up to 40% can be achieved.

As shown in Figure 5.1, in terms of the vertical deflections of the beam, with the application of prestress, an initial pre-camber was induced at midspan, hence the shift of the moment–deflection response of the non-prestressed beam to the left. In the present example, a 60% decrease in the overall vertical deflections of the beam at midspan was accomplished. Comparing the gradients of the bare steel and non-prestressed responses, it can also be observed that the introduction of the cable increases the system bending stiffness, thus reducing the service load deflections of the member. Note that, as discussed in Section 3.4.3, owing to the unbonded nature of the beam–cable connection, the cable does not contribute fully to the bending stiffness of the system. Hence, the increase in the bending stiffness of the beam due to the presence of the cable was calculated by considering the effect of ΔP on the moment–deflection response, as given in Equation (3.6). Additionally, the fact that the non-prestressed and fully prestressed responses have the same gradient indicates that the bending stiffness of the system is independent of the applied initial prestressing force. This is also evident in Equation (3.6) which, if rearranged in the form $M_{max}=f(\delta_{mid})$, shows that P_i only determines the starting point of the moment–deflection response and does not affect the gradient.

Depending on the initial prestressing force and the slenderness of the cold-formed steel beam, the prestressing can delay local/distortional buckling in the Serviceability Limit State (SLS) and thus prolong the full utilisation of the bending stiffness of the cross-section. This is owing to the fact that the initial stresses introduced during prestressing must be overcome first before the elastic buckling stress of the cross-section is reached. As a result, the addition of the prestressed cable can potentially decrease the vertical deflections of the cold-formed steel beam during service. This effect is more profound in slender cross-sections, where elastic buckling may be initiated earlier during loading, and when local buckling within the top flange is the governing buckling mode.

5.2.3 Moment–stress responses

Owing to the different stages and combinations of loading acting on prestressed cold-formed steel beams, and since the stability of cold-formed steel cross-sections is generally highly dependent on the applied stress distribution (Torabian et al., 2015), the variations in stress at critical locations within the cross-section, namely the top flange, bottom flange and cable, are studied herein. The average membrane stress levels across the width of the top $\sigma_{t,av}$ and bottom $\sigma_{b,av}$ flanges of the critical cross-section of the beam are given. Furthermore, the axial stress level in the cable σ_c is uniform along its entire length due to the unbonded nature of the beam–cable connection, as discussed in Section 3.4.3. Note that, in the analytical results presented below, the axial stress levels are also calculated with respect to the centre line of the top and bottom flanges. The stress levels are normalised against the corresponding material yield strength (*i.e.* $F_{y,s}$ for the cold-formed steel or $F_{y,c}$ for the cable).

5.2.3.1 Stage I: Prestressing

In the case of the reference system, in Stage I, the axial stress levels at the aforementioned locations within the critical cross-section of the fully prestressed model (*i.e.* P_i/P_{max}=1.0) are shown in Figure 5.3, where a precise match between the FE and analytical results, evaluated using Equation (3.1) for the top flange and Equation (3.2) for the bottom flange, is achieved. The axial stress level within the cable at the end of the prestressing stage is approximately 80% of its yield strength, thus allowing for the subsequent increase in the prestressing force ΔP in Stage II. Furthermore, the stress levels within the top and bottom flanges are approximately 20% and 80% of the yield strength respectively. Note that, even though the maximum allowable force P_{max} has been applied in the reference FE model, the axial stress level within the bottom flange did not reach the material yield strength since the calculation of P_{max} in Equation (3.21) accounts for both the local and distortional buckling effects that may develop during prestressing.
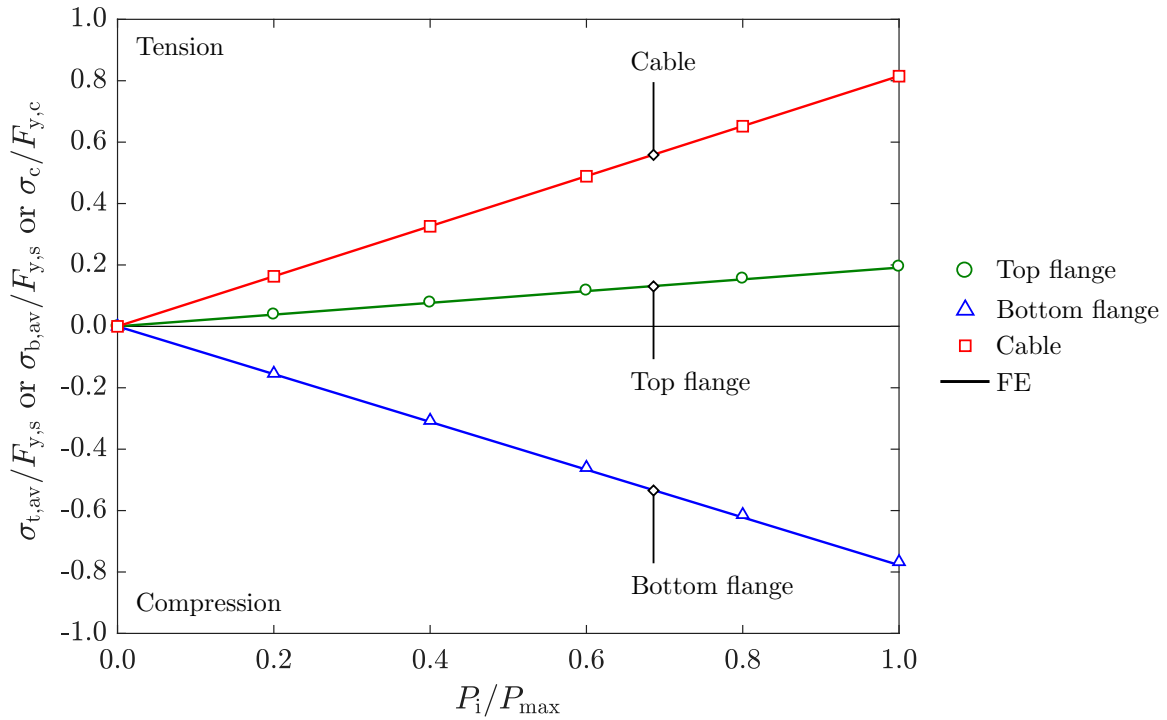
Figure 5.3: Normalised moment–stress responses for the top and bottom flanges and the cable at the critical cross-section of the fully prestressed FE model in Stage I.

5.2.3.2 Stage II: Imposed vertical loading

The axial stress levels at the end of Stage I define the starting points of the normalised moment–stress responses in Stage II, as shown in Figure 5.4, where again a good match between the FE and analytical results is generally achieved during the elastic response of the system. In the case of the top flange, the deviation of the FE results from the analytical results is attributed to the influence of the initial geometric imperfections, which induce the development of a non-uniform stress distribution across the flange from an early stage. The non-uniform shape means that, for a given applied moment, the $\sigma_{t,av}$ level in the FE model is higher than the analytical stress level, where a uniform stress distribution across the top flange is assumed. As shown in Figure 5.4, the deviation of the FE results from the analytical results grows as the buckling effects develop.

The influence of the imperfections can be verified by comparing the response of the FE models with and without imperfections, as shown in Figure 5.5. For both the bare steel and fully prestressed beams, excellent agreement can be observed between the results from the FE models without imperfections and the analytical results. This is because, owing to

(a) Top flange
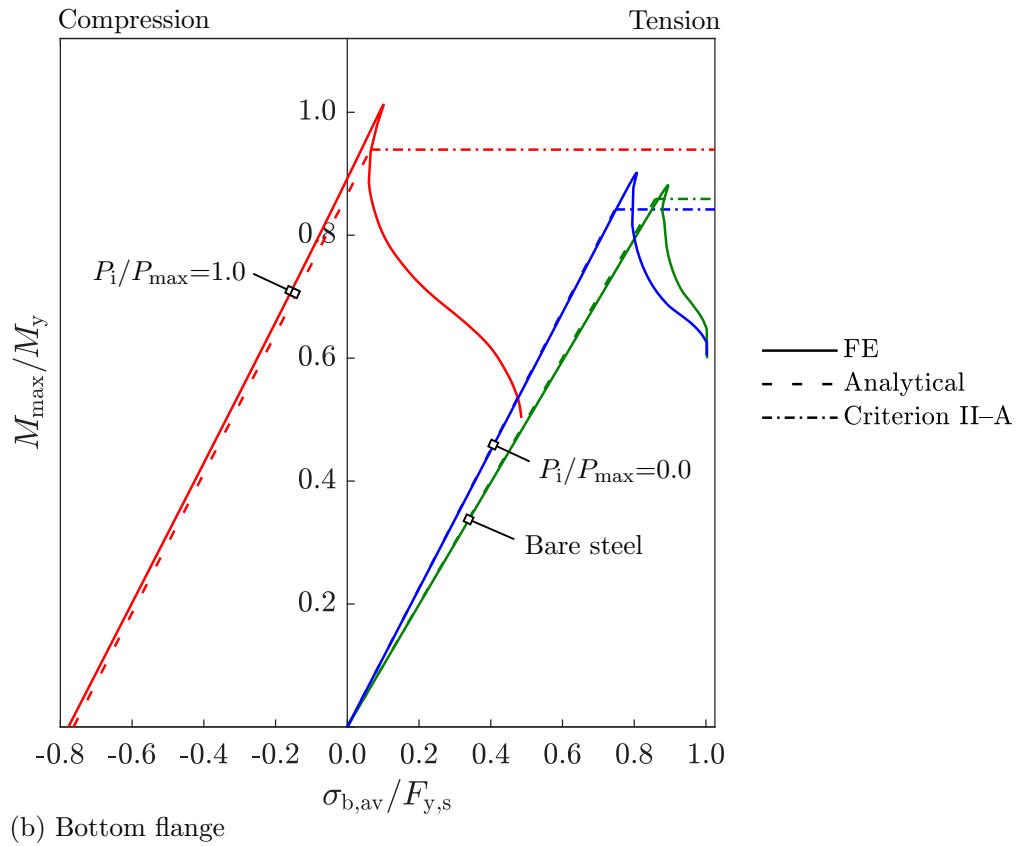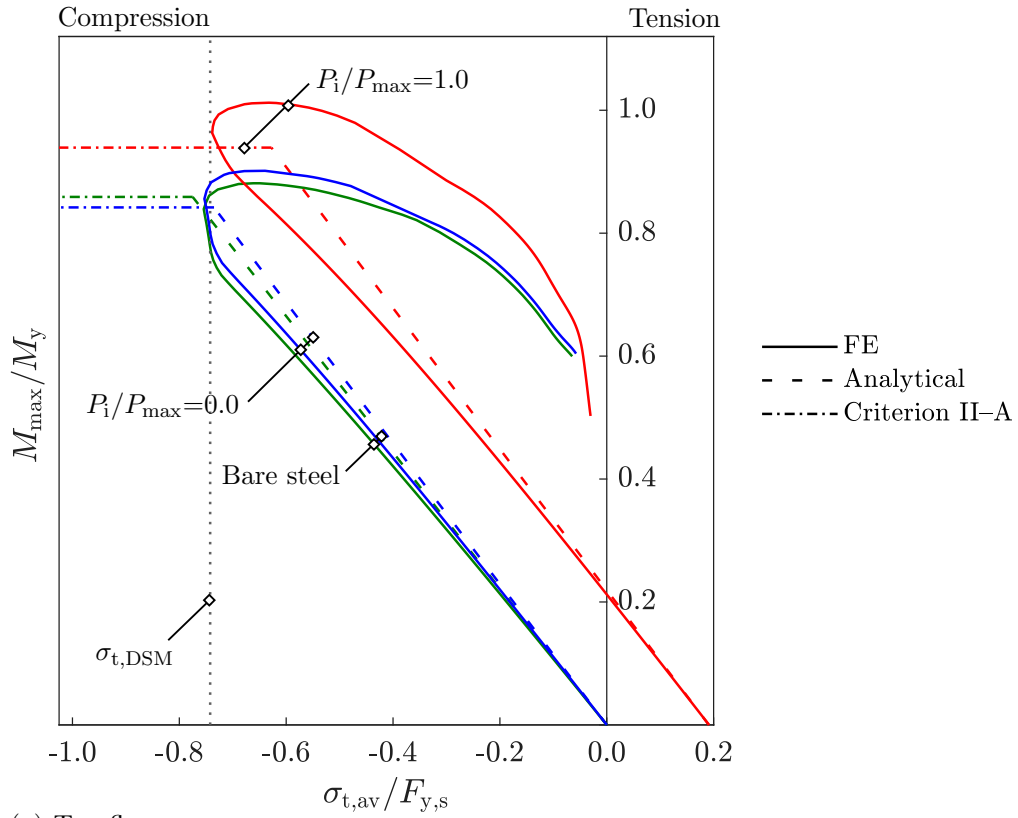
(b) Bottom flange

Figure 5.4: Normalised moment–stress responses for the (a) top and (b) bottom flanges at the critical cross-section of the three sample models during Stage II.
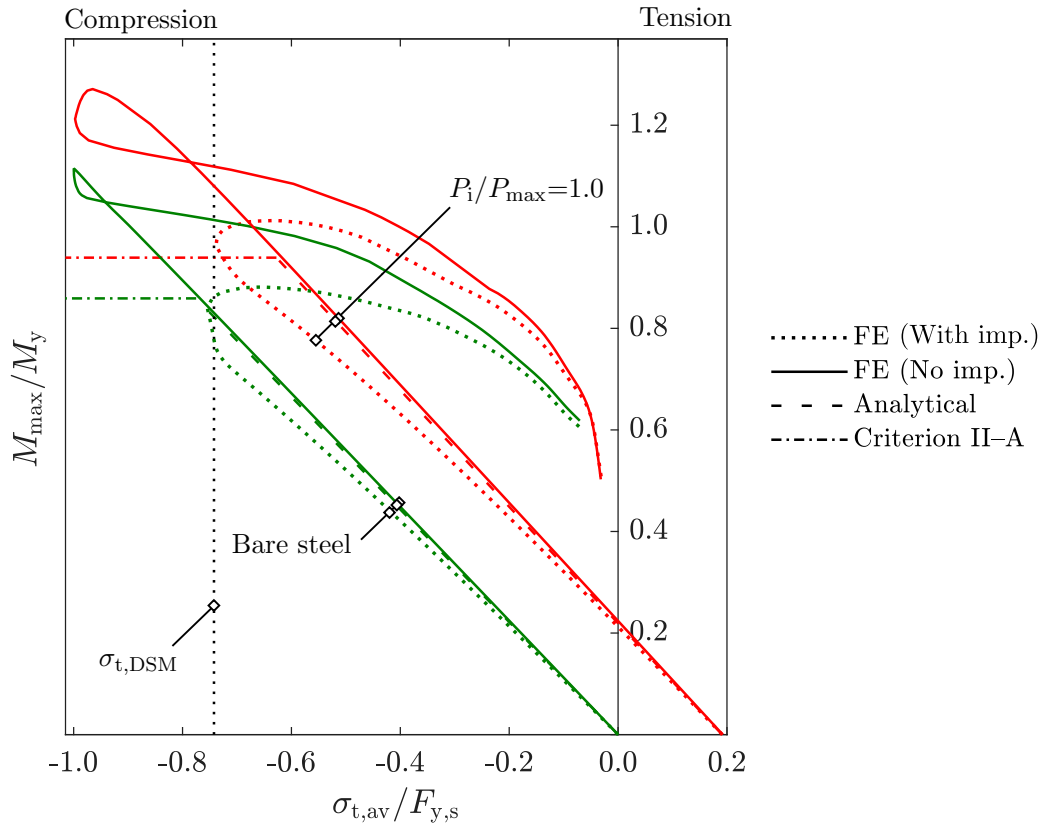
Figure 5.5: Normalised moment–stress response of the bare steel and fully prestressed FE models with (solid) and without (dashed) initial geometric imperfections.

the absence of the local buckling imperfection in the top flange, shown in Figure 4.4(A), the stress level within the top flange remains constant, thus matching the distribution assumed in the analytical expressions. When the material yield stress is reached within the top flange, failure of the cold-formed steel beam takes place. Note the substantial difference between the ultimate moment capacity achieved in the case of the FE models without imperfections and the failure criteria. In contrast, when the imperfections are included in the FE models, the ultimate points of the FE responses are closer to the design predictions.

In Figure 5.4, the effect of the application of prestress is evident from the shift of the starting points away from the non-prestressed case, towards the right for the top flange, *i.e.* towards tension, and towards the left for the bottom flange, *i.e.* towards compression. As shown in Figure 5.4(a), in all cases, irrespective of whether prestressing has been applied, the failure of the beam takes place once $\sigma_{t,av}$ reaches approximately the same stress level, which can be accurately predicted by the DSM, as indicated by the vertical dotted line. In the present work, this stress level is termed as the "DSM failure stress"
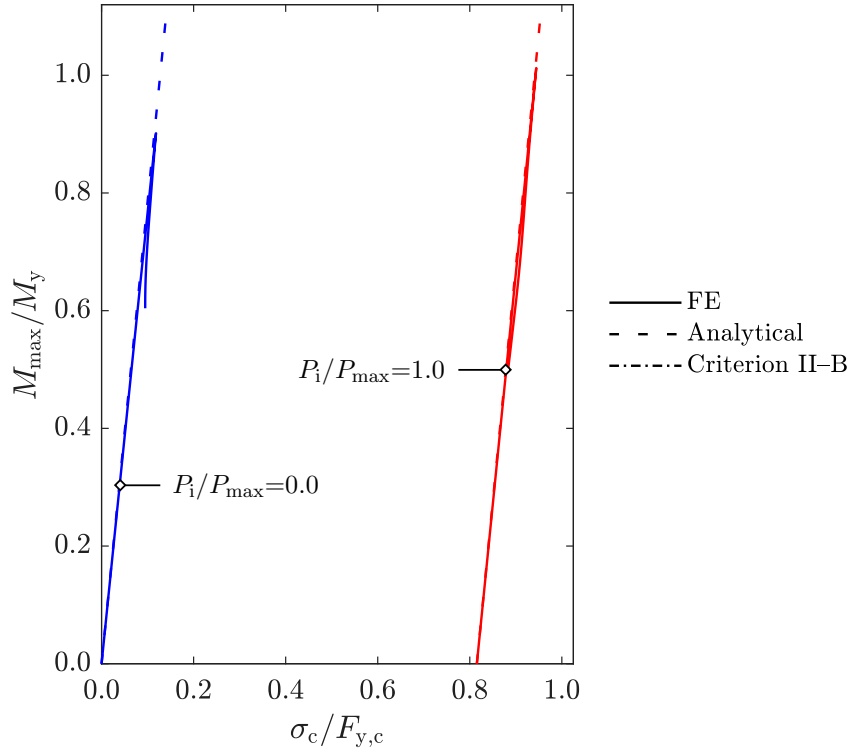
Figure 5.6: Normalised moment–stress responses for the cable in the cases of the non-prestressed and fully prestressed sample models.

$\sigma_{\text{t,DSM}} = M_{\text{nx}}^+ / S_{\text{t}}$, where M_{nx}^+ is the DSM prediction for the bending resistance of the bare steel beam when subjected to positive bending and S_{t} is the elastic section modulus corresponding to the top flange. The DSM failure stress is also shown in Figure 5.5, where it can be seen that the presence of the initial geometric imperfections has a significant influence on the accuracy of the $\sigma_{\text{t,DSM}}$ prediction.

As shown in Figure 5.4(a), when prestressing is applied, since the tensile stresses imposed within the top flange in Stage I need to be overcome first during Stage II, the entire response of the non-prestressed case is shifted to the right and thus the moment–stress path to reach $\sigma_{\text{t,DSM}}$ is extended. Consequently, failure of the cold-formed steel beam takes place at a higher applied moment, *i.e.* the ultimate moment capacity of the member is enhanced. This is where the benefits, in terms of load-carrying capacity, from the prestressing process originate.

Comparing the bare steel and $P_{\text{i}}/P_{\text{max}} = 0.0$ cases in Figure 5.4(b), it can be observed that the addition of the cable decreases the stress level within the bottom flange of the steel beam, for a given applied moment. This is because, as shown in Figure 5.6, part of the

applied load is now carried by the cable. Furthermore, as shown in Figure 5.4(b), when prestressing is applied, owing to the relatively high initial compressive stresses imposed in Stage I, the stress level within the bottom flange at failure is only at approximately 10% of the material yield stress, thus indicating that the bottom flange is not efficiently utilised. Hence, it may be concluded that, even though the maximum allowable prestressing force was applied in this case, the solution is sub-optimal for the given amount of material in the system. The aforementioned observation indicates that by optimising the solution, even greater benefits may be obtained. For this reason, the effect of various key parameters on the performance of the proposed beams is investigated through a set of parametric studies in Section 5.3.

The starting point of the normalised moment–stress response of the cable, shown in Figure 5.6, is equal to the initial prestressing force P_i applied in Stage I divided by the cross-sectional area of the cable A_c. The additional axial stress induced within the cable in Stage II is a function of the additional prestressing force ΔP, as defined in Equation (3.16). Note the excellent agreement between the FE results and the analytical results; this verifies the suitability of the FE modelling approach chosen to model the unbonded beam–cable connection, as discussed in Section 4.2.5. To check the capacity of the cable, failure criterion II–B can be used, as defined in Section 3.5.3.2. More specifically, by substituting the expressions for P_net^{II} from Table 3.2 and ΔP from Equation (3.15) into Equation (3.23), the maximum moment that can be applied at midspan before the cable yields in tension can be estimated as:

$$M_\mathrm{max} \leqslant \frac{3C}{2e}(F_\mathrm{y,c}A_\mathrm{c} - P_\mathrm{i}), \tag{5.3}$$

where C is given in Equation (5.2).

In the case of the fully prestressed sample model, the maximum moment corresponding to failure criterion II–B (capacity of cable) is equal to 1.47 M_y; this criterion is not within the range of Figure 5.6. For the same model, the maximum moment corresponding to failure criterion II–A (capacity of cold-formed steel beam) is 0.94 M_y, as shown in Figure 5.4, and thus this criterion governs the failure of the prestressed system.

5.2.4   Deformed shapes

The effect of prestressing is studied further by comparing the deformed shape of the fully prestressed beam (*i.e.* model P_i/P_{max}=1.0) at different stages of loading. The overall structural behaviour of the prestressed member is illustrated by the 3-D FE representations in Figure 5.8, where the indicated loading levels correspond to Points A–E on the moment–deflection response in Figure 5.7. Note the pre-camber along the member at Point A (*i.e.* the end of Stage I and the start of Stage II), as well as the fact that at this stage the top region of the beam is under tension. Furthermore, note the distortional buckling waves developing along the member at Points C–D.
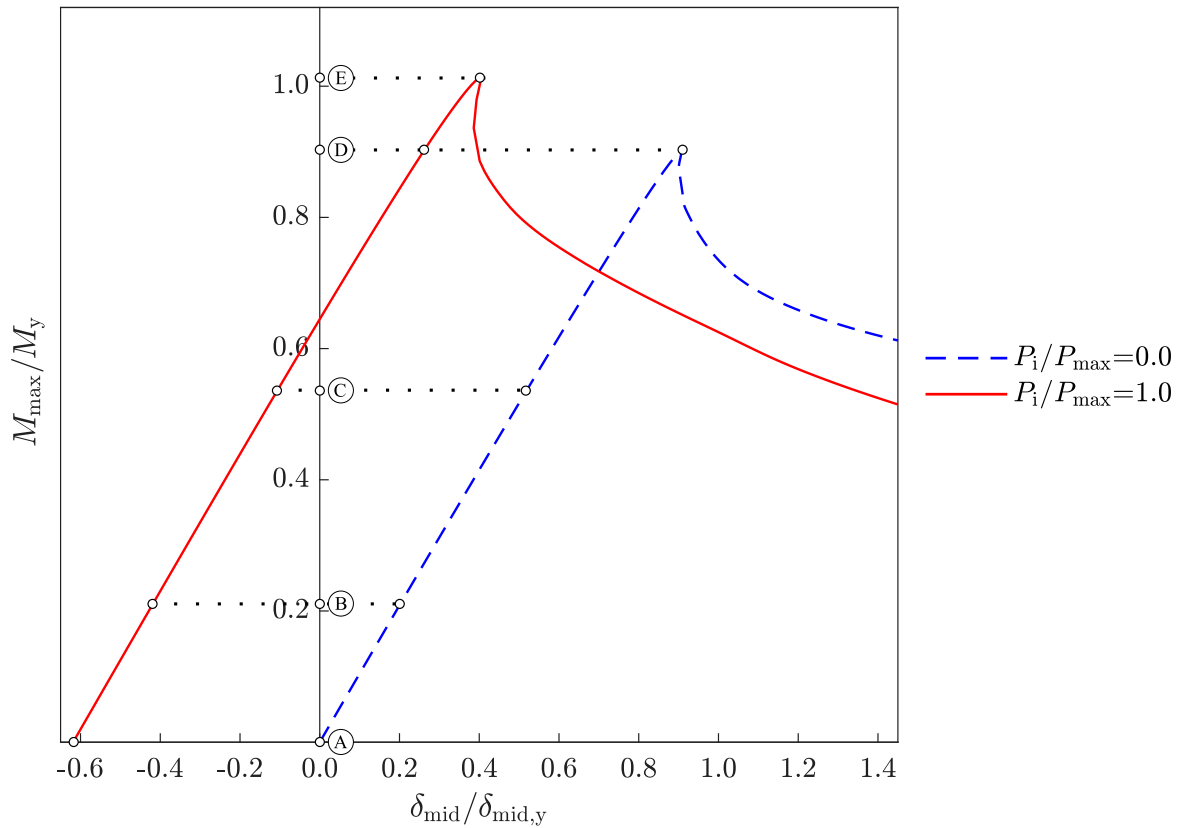
Figure 5.7: Normalised moment–deflection responses of the non-prestressed (dashed lines) and fully prestressed (solid lines) FE models. Points A–E correspond to the points in Figures 5.8, 5.9, 5.11 and 5.12.

The deformed shapes at the critical cross-section of the fully prestressed member at Points A–E are shown in Figure 5.9. The initial pre-camber at Point A decreases gradually with the application of vertical loading until the unloaded position is reached approximately
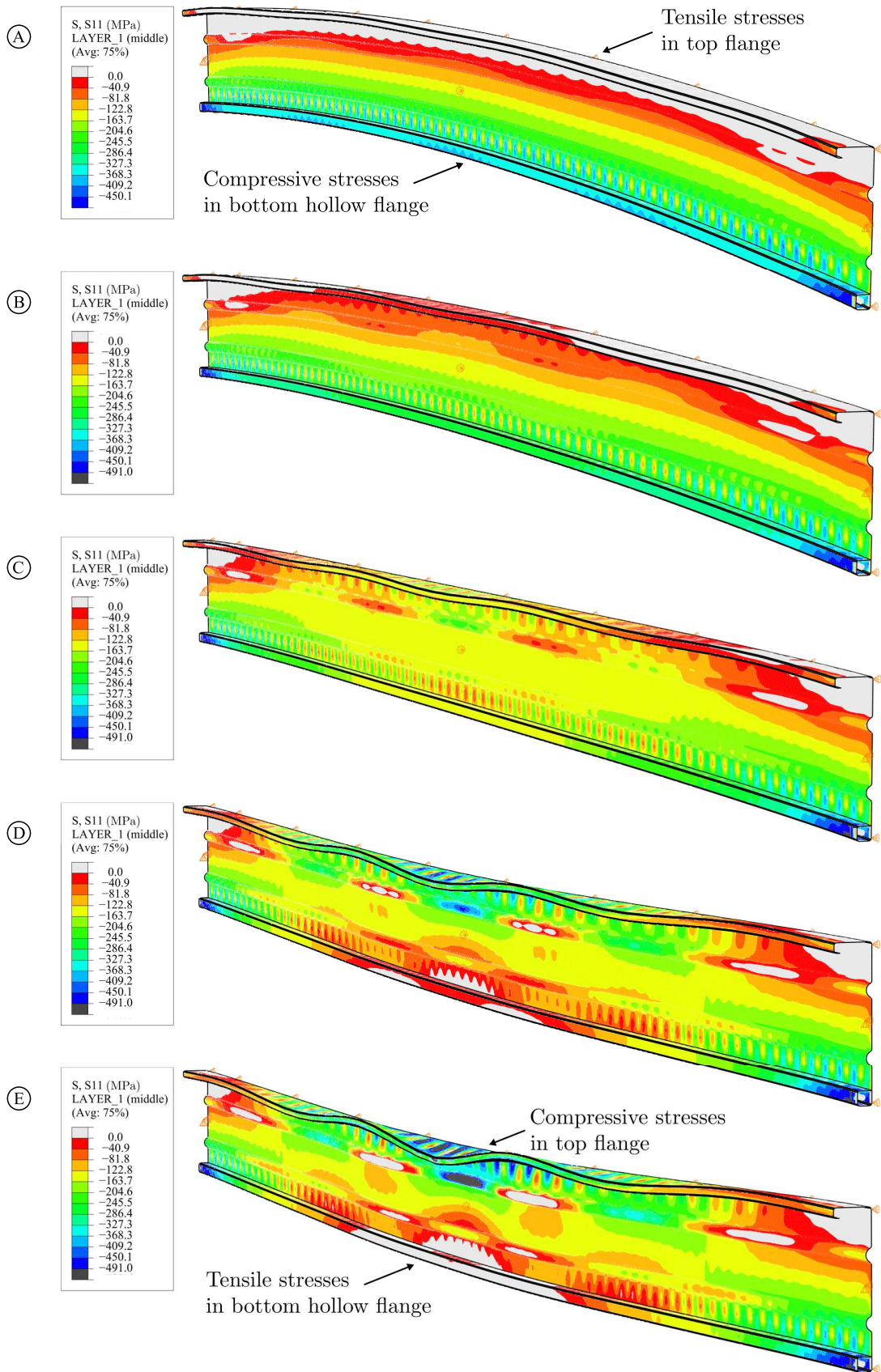
Figure 5.8: Structural behaviour of the fully prestressed beam at the loading levels corresponding to Points A–E in Figure 5.7. The contour map illustrates the axial compressive stresses in N/mm^2; tensile stresses are indicated by the light grey areas. For illustration purposes the vertical deformations are magnified by a factor of 3.
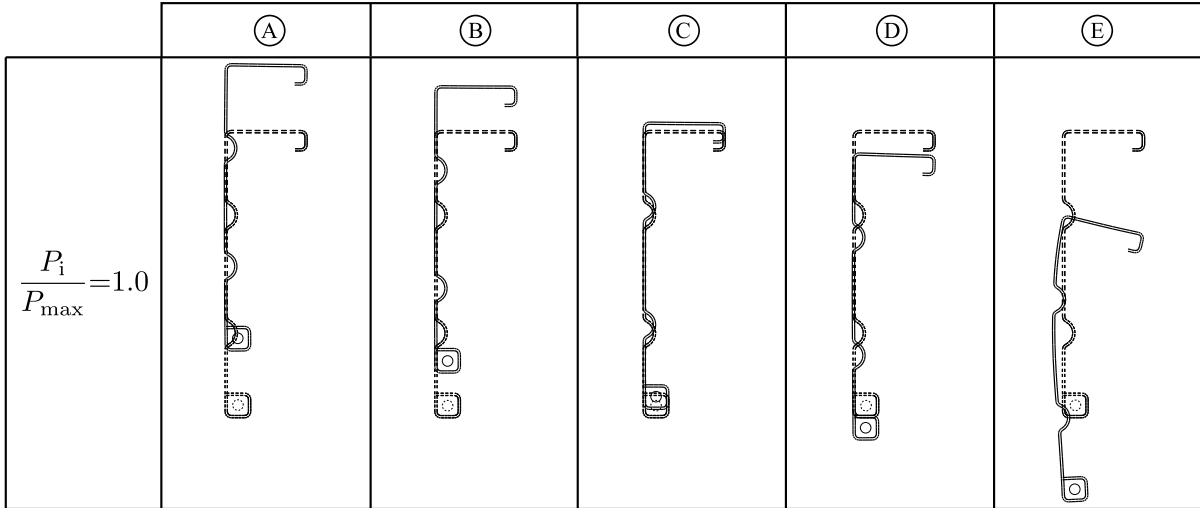
Figure 5.9: Deformed (solid lines) and undeformed (dashed lines) geometry of the critical cross-section of the fully prestressed model. Points A–E correspond to the levels indicated in Figures 5.7–5.8. For illustration purposes vertical deformations are magnified by a factor of 3.

at Point C. Eventually, at Point E, failure of the cold-formed steel beam takes place due to distortional buckling and subsequently the behaviour of the system becomes strongly unstable, as indicated by the sharp drop in capacity after Point E in Figure 5.7.

In general, it is observed that, owing to the initial pre-camber and the contribution of the cable to the bending stiffness of the system, the overall deflections of the beam are reduced significantly and thus the serviceability performance of the system is enhanced.

5.2.5 Failure modes

Failure of the proposed prestressed system takes place when the load-carrying capacity of either the cold-formed steel beam or the cable is exceeded, in either of the two loading stages. Generally, provided a sufficiently large cable is employed, failure of the prestressed member will be governed by the capacity of the cold-formed steel beam. In Stage I, compressive stresses arise in the bottom flange, but the geometry of the section is resistant to local/distortional buckling in this region. Meanwhile, the top region of the beam is subjected to tensile stresses, as shown in Figure 5.8 at Point A. The presence of the prestressed cable and the bottom lateral restraints prevent distortional, lateral-torsional and flexural buckling, as discussed in Section 3.3.3.

In Stage II, the stresses arising from the applied vertical loading counteract the initial

stresses induced due to the prestressing, and eventually the top region of the cold-formed steel beam is subjected to compressive stresses, as shown in Figure 5.8 at Point E. Failure is then triggered in this region by local buckling, distortional buckling or material yielding, depending on the cross-section proportions. In the case of the studied cross-section profiles, distortional buckling was the predominant mode of failure, as shown in Figure 5.8 at Point E.

The distortional buckling failure is also evident in Figure 5.10, where the material yielding (dark grey) within the top regions of the cold-formed steel beam just beyond the ultimate load is also shown.
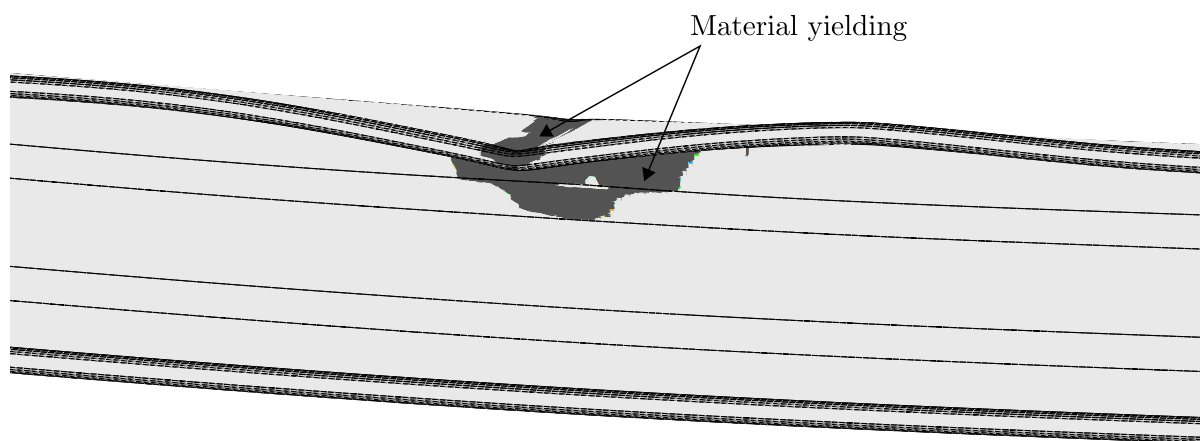
Figure 5.10: 3-D FE representation of the distortional buckling failure mode and yielded regions (dark grey) at the midspan of the fully prestressed beam just beyond the ultimate load. For illustration purposes the deformations have been magnified by a factor of 2.

5.2.6 Axial stress distributions at critical cross-section

The axial stress distributions at the critical cross-section (*i.e.* at midspan) of the non-prestressed and fully-prestressed models, at the loading levels corresponding to Points A–E in Figures 5.7 and 5.11, where the normalised moment–deflection and moment–stress responses are shown respectively, are compared in Figure 5.12, providing valuable insight into the effect of prestressing.

In the non-prestressed model, shown in Figure 5.12(a), as expected, the imposed vertical loading results in the axial stress distribution that is traditionally observed in beams
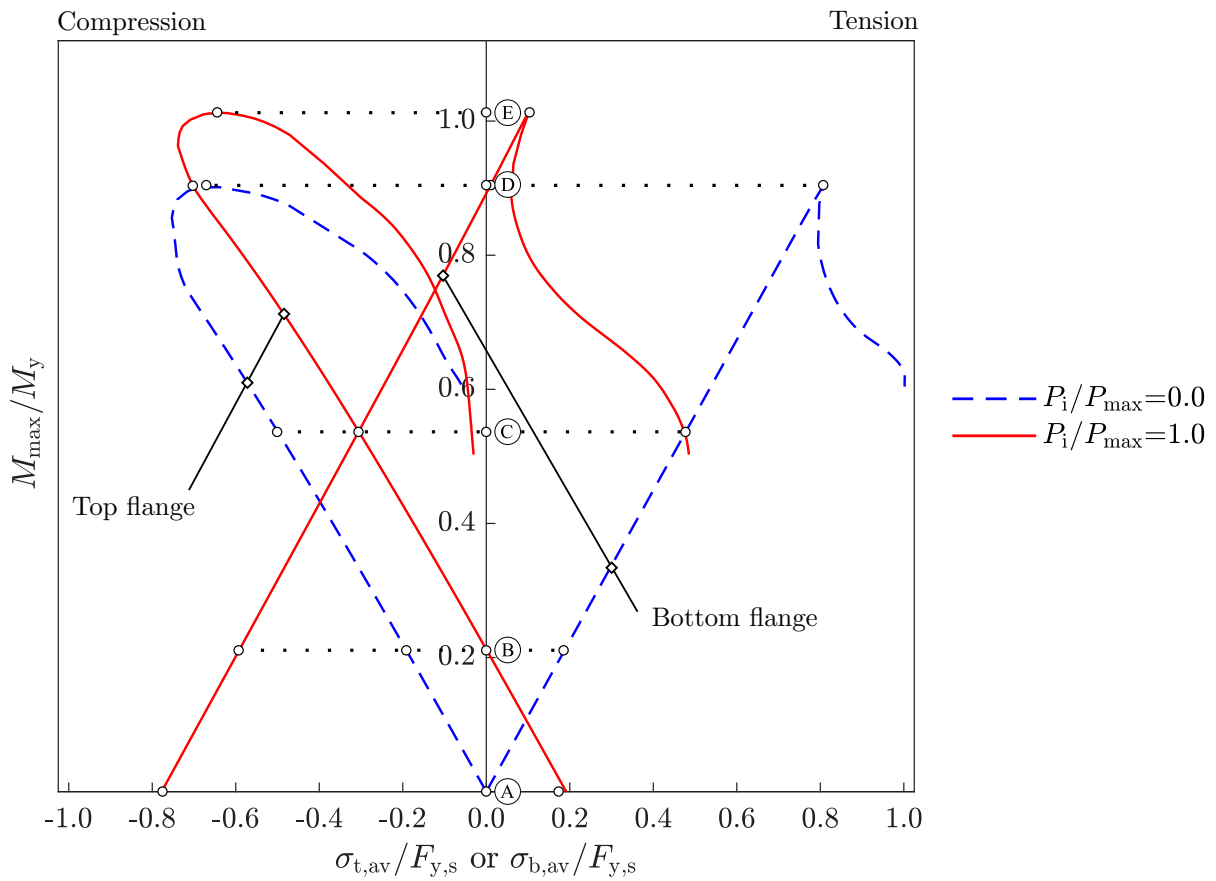
Figure 5.11: Normalised moment–stress responses corresponding to the top and bottom flanges of the non-prestressed (dashed lines) and fully prestressed (solid lines) FE models. Points A–E correspond to the points in Figures 5.7 and 5.12.
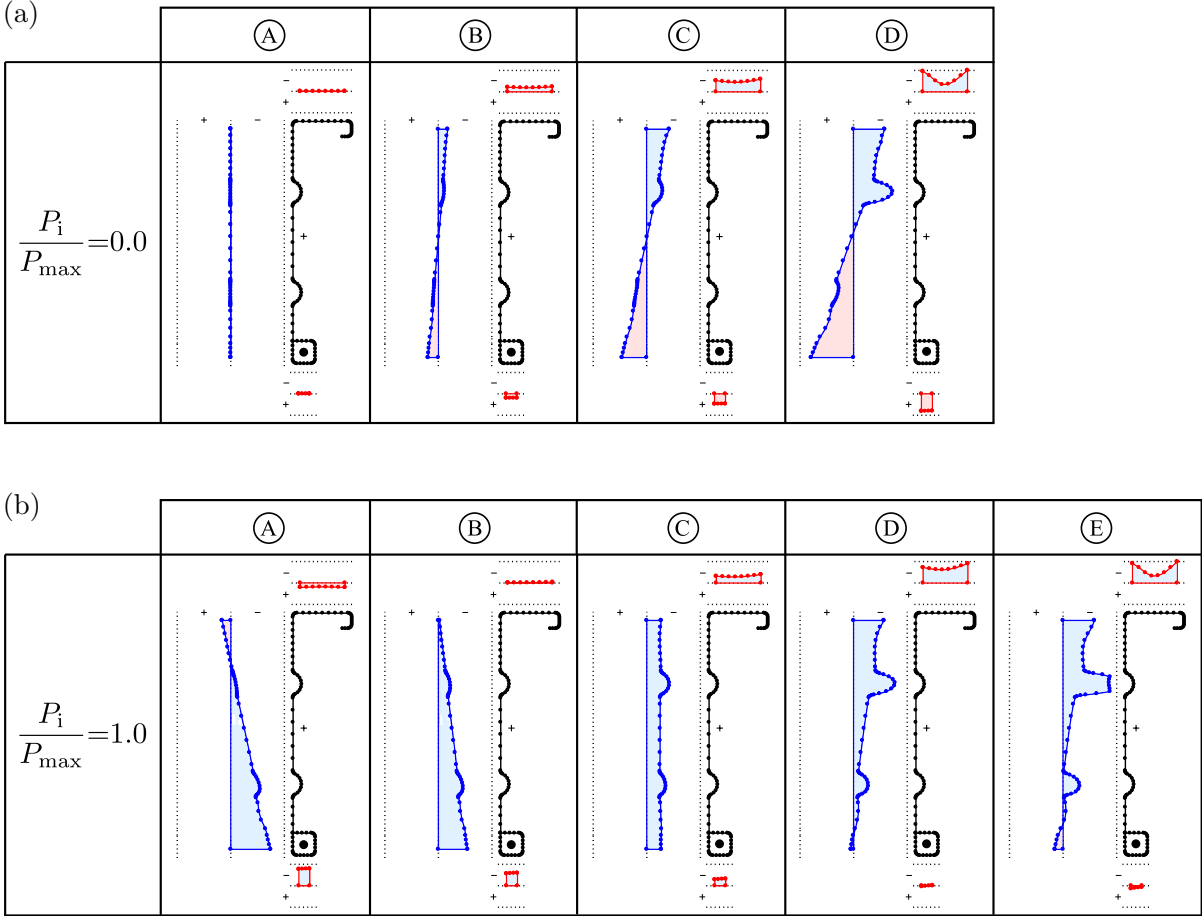
Figure 5.12: Axial stress distributions across the top flange, web and bottom flange of the critical cross-section of the (a) non-prestressed and (b) fully prestressed FE models. Points A–E correspond to the loading levels indicated in Figures 5.7 and 5.11. The dotted lines indicate the material yield strength of the cold-formed steel.

subjected to purely positive bending, *i.e.* compression above the centroidal axis and tension below. The stress levels increase with loading and the location of the neutral axis remains essentially unchanged, until the collapse of the beam that takes place at Point D, when the average membrane stress level within the top flange reaches the DSM failure stress $\sigma_{t,DSM}$, as discussed in Section 5.2.3.2. Note the development of the non-uniform stress distribution across the top flange, as discussed in Section 5.2.3.2. Also note that, as local and distortional buckling become more prominent, stress concentrations build up at the locations of the intermediate stiffeners in the web. This is attributed to the fact that the stiffeners retain their axial stiffness and attract a higher proportion of the applied load while the surrounding flat regions experience buckling, thus heralding a local loss in axial stiffness. Stress concentrations at the location of intermediate stiffeners have also been reported in previous research works (Schafer and Peköz, 1996; Schafer, 1997).

In the fully prestressed case shown in Figure 5.12(b), the top and bottom parts of the cross-section are initially under tension and compression respectively due to the prestressing applied in Stage I. As the imposed vertical loading is introduced and increased, a triangular stress distribution is reached at Point B, where the top flange is under no stress. Subsequently, a purely compressive distribution is reached across the entire section at Point C, where, as indicated in Figure 5.11, the stress levels at the top and bottom flanges are equal. An inverted triangular distribution is reached at approximately Point D. Eventually, at Point E, when the DSM failure stress is reached within the top flange, the collapse of the beam takes place due to distortional buckling.

Comparing the two models, it is observed that the application of prestressing decreases the overall compressive stress level within the top flange at any given stage and thus delays the development of local and distortional buckling and the subsequent collapse of the beam. Hence, a higher applied moment is needed to cause the failure of the cold-formed steel beam, *i.e.* the moment capacity of the member is enhanced.

5.2.7 Effect of member restraints

The assumptions regarding the effect of the presence of the lateral restraints and the prestressed cable, as stated in Section 3.3.3, on the behaviour of the proposed beams are verified in the present sub-section.

5.2.7.1 Asymmetric bending effects

In the present work, it is assumed that asymmetric bending effects are prevented by the lateral restraints present at the top and bottom flanges of the member. The aim of the present sub-section is to verify this assumption by studying the behaviour of the example cross-section profile, shown in Figure 5.13. Its dimensions are the same with the reference profile, as defined in Figure 3.3 and Table 3.3, but with a wider top flange (b_2=95.0 mm) and a narrower bottom flange (b_1=d_1=20.0 mm). In this manner, the asymmetry of the profile is increased, with the major (1–1) and minor (2–2) principal axes of the cross-section in this case being located at an angle θ of 8.54° with respect to the strong (x–x) and weak (y–y) geometric axes.

The nature of the axial stress distribution within the cross-section of the example profile when subjected to restrained and asymmetric bending is studied below. Subsequently, the effect of lateral restraints is examined to determine whether their presence prevents the occurrence of any asymmetric bending effects, as assumed in Section 3.3.3.

(a) Restrained bending

Restrained bending takes place when the decomposition of the bending moment applied about the geometric axis into the bending components about the principal axes is prevented. For instance, in the case of the example profile, when the applied bending moment M_x is restrained about the strong geometric axis of the cross-section, the axial stress distribution shown in Figure 5.13 is obtained since M_x is not allowed to decompose into the M_1 and M_2 components. In essence, the cross-section behaves in a symmetric manner, even though it is geometrically asymmetric, *i.e.* not symmetric about either an axis or
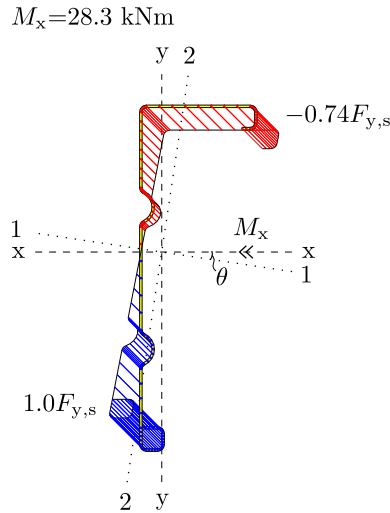
Figure 5.13: Axial stress distribution in the case of restrained bending about the strong geometric axis of the example profile; the magnitude of M_x corresponds to the yield moment. The designation of the bending moment (double arrows) follows the so-called 'right hand screw' rule.

a point. In this case, the yield moment is equal to M_x=28.3 kNm, with the yield stress $F_{y,s}$ being reached at the bottom extreme fibre first.

(b) Asymmetric bending

Asymmetric bending occurs when the decomposition of the bending moment applied about the geometric axis into the bending components about the principal axes is allowed. In the case of asymmetric bending in the example profile, as shown in Figure 5.14, owing to the asymmetry of the cross-section, M_x can resolve into the two components about the major M_1=$M_x\cos\theta$ and minor M_2=$M_x\sin\theta$ principal axes (*i.e.* into biaxial bending about the principal axes); M_1 and M_2 induce vertical and lateral deformations of the cross-section respectively. In this case, as shown by the overall stress distribution in Figure 5.14(a), the yield moment (M_x=21.1 kNm) is 25% lower than the yield moment due to restrained bending (M_x=28.3 kNm). This is because, as shown in Figure 5.14(c), the M_2 component induces tensile stresses in the bottom extreme fibres that are equal to approximately 30% of the yield stress; hence, overall, a smaller moment needs to be applied about the strong geometric axis to cause yielding of the bottom extreme fibres.

More importantly, as shown in Figure 5.14(c), the M_2 component induces tensile stresses within the right part of the top flange. Consequently, the overall compressive stress level

(a) Overall: (b) Major: (c) Minor:
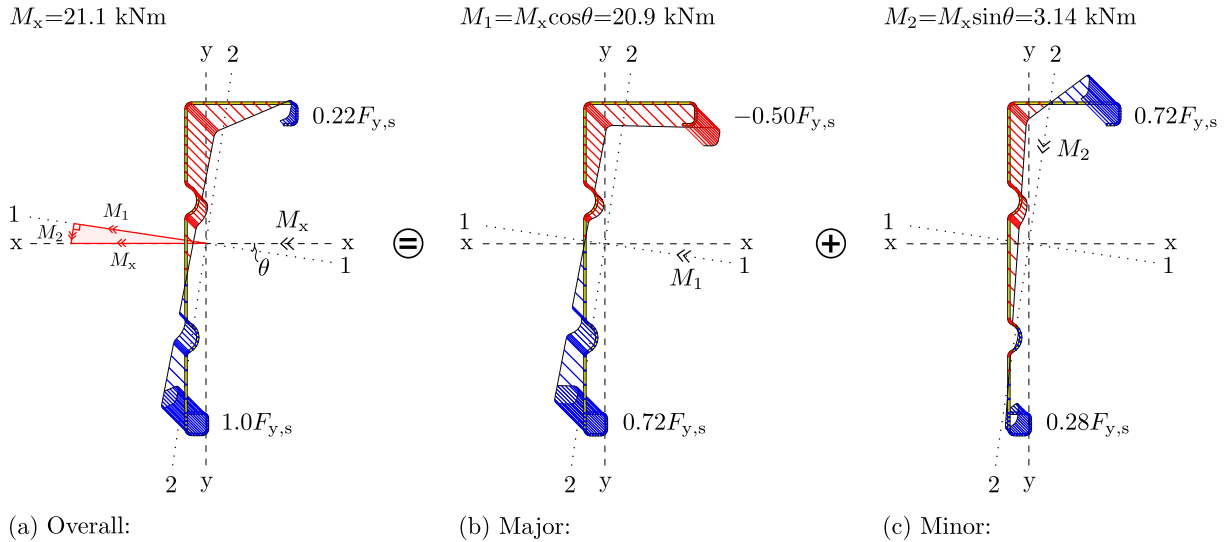
Figure 5.14: Axial stress distribution in the case of unrestrained asymmetric bending. The magnitude of the applied bending moment M_x corresponds to the point of first yield.

within the top flange is reduced significantly, as shown in Figure 5.14(a), with top flange lip being overall in tension. In this manner, the M_2 component acts as a stabilising moment for the cross-section.

Overall, by comparing Figures 5.14(a) and 5.13, it is concluded that asymmetric bending relieves the compressive stress levels at the lip of the top flange and, consequently, improves the distortional buckling strength of the cross-section; hence, counter-intuitively, the presence of asymmetric bending has a beneficial effect on the bending resistance of the cross-section. This can also be illustrated using the signature curves shown in Figure 5.15, where it is observed that asymmetric bending increases both the local and the distortional critical buckling strengths of the member, with the increase being more profound in the case of the latter. This increase, alongside the reduction of the yield moment, implies that asymmetric bending reduces the slenderness $\lambda = \sqrt{M_y/M_{cr}}$. It is worth noting that the critical half-wavelength for distortional buckling is almost halved when asymmetric bending effects are allowed, while the deformed shape at the critical distortional buckling point also changes substantially. In the FE models, these changes would alter the shape and distribution of the imposed initial geometric imperfections, thus affecting the ultimate moment capacity of the member.
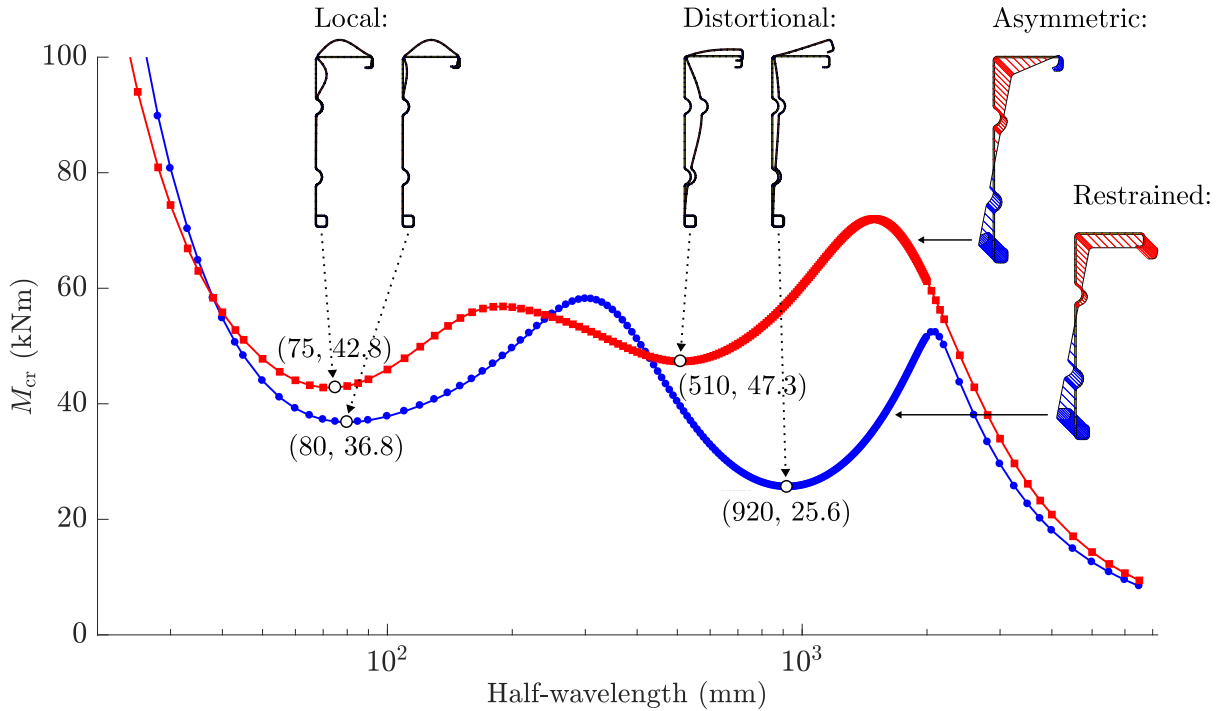
Figure 5.15: Signature curves for the cases of restrained and asymmetric bending. Deformed shapes at the critical local and distortional buckling points. The numbers in the brackets denote the elastic critical buckling moment M_{cr} and critical half-wavelength at the minimum points.

(c) Effect of lateral restraints in finite element models

In the present work, it is assumed that lateral restraints are present at the top and bottom flanges of the studied beams. At a cross-sectional level, these lateral restraints restrain any lateral deformations and therefore prevent the decomposition of the applied M_x into the M_1 and M_2 components; *i.e.* restrained bending is enforced. However, it is not clear whether, at a member level, asymmetric bending is allowed to take place between the lateral restraints, which are located at 600 mm intervals, as shown in Figure 3.6(b). To investigate this, two FE models with the example cross-section profile above, with elastic properties and no initial geometric imperfections, were created. In the first model, lateral restraints were placed only at the two member ends to allow lateral deformations to occur freely along the entire member. In the second model, the lateral restraints were maintained at 600 mm spacings.

The deformed shapes and axial stress distributions at the midspan (where, in both cases, no lateral restraints are present) of the two models are shown in Figure 5.16. In the first model, as shown in Figure 5.16(a), lateral deformations are not prevented and thus lateral-

(a) Asymmetric bending

(b) Restrained bending

Lateral restraints only
at the two beam ends

Lateral restraints
at 600 mm intervals
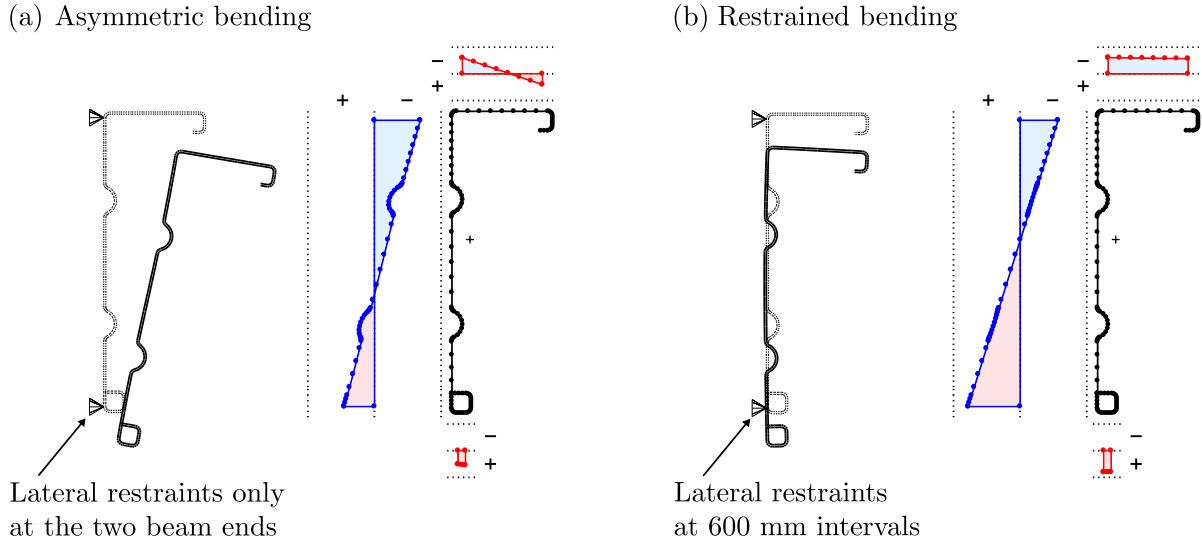
Figure 5.16: Deformed (solid) and undeformed (dashed) shapes, alongside the axial stress distribution, at the midspan of the two FE models utilised to investigate the effects of asymmetric bending. The results correspond to the same level of applied vertical loading.

torsional buckling occurs. Hence, as indicated by the fact that the extracted axial stress distribution matches the distribution for asymmetric bending shown in Figure 5.14(a), the absence of lateral restraints along the entire member allows asymmetric bending to occur without hindrance. In the second model, as shown in Figure 5.16(b), the 600 mm lateral restraints spacings are sufficiently small to prevent the lateral deformations within the cross-section; hence, the decomposition of M_x is prevented. For this reason, the applied bending is restrained about the strong geometric axis only, as indicated by the fact that the obtained stress distribution in this case matches the distribution for restrained bending, as shown in Figure 5.13.

In conclusion, the above observations demonstrate that the lateral restraints at 600 mm spacings prevent the lateral deformations within the cross-section of the proposed beams and thus prevent any asymmetric bending effects. It is worth noting that this conclusion is also supported by the discussion in Section 5.2.3.2, where it is demonstrated that the FE results without imperfections match perfectly the corresponding analytical predictions, which do not consider any asymmetric bending effects.

5.2.7.2 Lateral-torsional and distortional buckling due to negative bending

In the current research, as discussed in Section 3.3.3, it is assumed that both the bottom lateral restraints and the prestressed cable prevent lateral-torsional and distortional buckling due to negative bending, *i.e.* during the prestressing stage while the bottom part of the cross-section is under compression. The distortional buckling mode due to negative bending is shown in Figure 4.4(D). This assumption is verified below by investigating the effect of the prestressed cable on the lateral stability of the system during Stage I. The influence of the bottom lateral restraints has been studied in the previous sub-section.

For the purposes of this verification, the following three FE models were utilised:

(A) Bare steel beam, but with no bottom lateral restraints

(B) Cable present, but with no bottom lateral restraints

(C) Cable and bottom lateral restraints present.

In all models, only the prestressing stage was modelled. A nonlinear Riks analysis (see Section 4.2.8) was conducted with the applied internal prestressing force increased until member failure. In the bare steel case, *i.e.* Model A, the prestressing force was applied by means of two external notional loads at the two member ends, at the location where the cable would be present. The obtained FE results are presented in Figure 5.17 in terms of the initial prestressing force P_i versus the axial deformation at the member ends u_1. In the same figure, section cuts at the midspan of the members at the respective ultimate points are also shown. The ultimate prestressing force achieved in the FE models is compared with the initial prestressing force corresponding to first yield at the bottom extreme fibre $P_{i,y}$, which can be evaluated using Equation (3.2). The overall axial stress distribution during Stage I is shown in Figure 3.7(c).

In Model A, as indicated in Figure 5.17, lateral deformations occur at the bottom flange while member failure takes place at a low prestress level relative to $P_{i,y}$. This is because the absence of both the bottom lateral restraints and the cable allow lateral-torsional buckling to occur freely.

With the addition of the prestressed cable, *i.e.* comparing Model A with Model B, it is
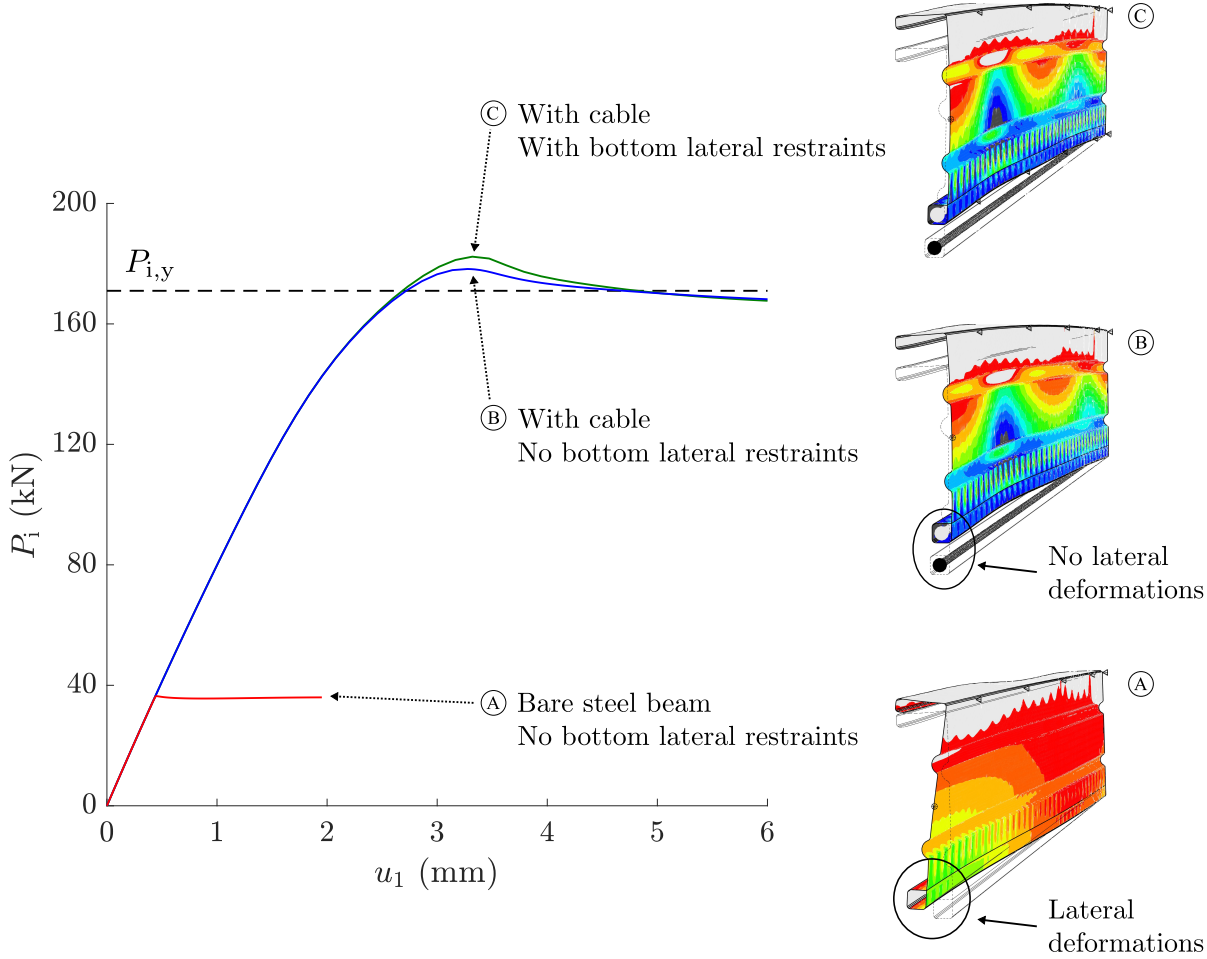
Figure 5.17: FE results in terms of the initial prestressing force P_i versus axial deformation u_1 responses of the studied members. 3–D midspan cross-section cuts at the ultimate points; tensile stresses are shown in light grey.

observed that the ultimate prestressing force is increased substantially, while no lateral deformations take place at the bottom flange. Therefore, it may be concluded that the presence of the cable prevents lateral-torsional and distortional buckling during prestressing and thus enhances the lateral stability of the member significantly.

It is worth noting that, with the addition of the bottom lateral restraints, *i.e.* comparing Model B with Model C, the ultimate prestressing force does not change considerably. Hence, it may be concluded that the presence of the prestressed cable is adequate in ensuring the lateral stability of the member during prestressing.

5.3 Parametric studies

The purpose of the parametric finite element (FE) studies presented in the current section is to investigate the influence of the key controlling parameters on the structural performance of prestressed cold-formed steel beams. Ultimately, the results indicate how these parameters may be optimised and thus how the benefits obtained from the addition of the prestressed cable may be maximised while minimising the required additional material.

5.3.1 Key controlling parameters

The parametric studies explore the effect of the prestress level, cable size, section slenderness and centroid location on the benefits obtained from the prestressing, with the respective controlling parameters being $P_\mathrm{i}/P_\mathrm{max}$, $A_\mathrm{c}/A_\mathrm{s}$, t and y_b/h, as indicated in Table 5.2.

In each study, the controlling parameter, indicated with an asterisk in Table 5.2, was varied while the remaining parameters were kept constant. In some cases, to keep a parameter constant, its numerator had to be adjusted due to the fact that its denominator is a function of the controlling (variable) parameter; these cases are indicated with the symbol "†" in Table 5.2. An example of the adopted notation is shown in Figure 5.18. The example corresponds to the parametric study regarding the effect of the centroid

Table 5.2: Summary of the variation of the controlling parameters in the parametric studies.

		Prestressing force: P_i/P_{max}	Area: A_c/A_s	Thickness: t	Profile: y_b/h
(i)	Effect of prestress level	*	−	−	−
(ii)	Effect of cable size	−	*	−	−
(iii)	Effect of section slenderness	†	†	*	−
(iv)	Effect of centroid location	†	−	−	*

* Controlling (variable) parameter.

− Constant parameter.

† Constant parameter; the denominator is a function of the controlling (variable) parameter and thus the numerator had to be adjusted accordingly to ensure the current parameter is constant.

location, whereby, the cross-section profile of the member was varied while maintaining constant values for both the thickness of the cold-formed steel beam and the size of the cable. However, since the value of P_{max} depends on the profile of the cold-formed steel beam, the initial prestressing force P_i was adjusted accordingly with the aim of keeping the relative prestress level P_i/P_{max} constant.

Thickness: 2.00 mm   Prestressing force: Variable (kN)

$$\text{Pr*–t200–c55–P}_i{}^\dagger$$

Profile: Controlling variable   Cable radius: 5.5 mm
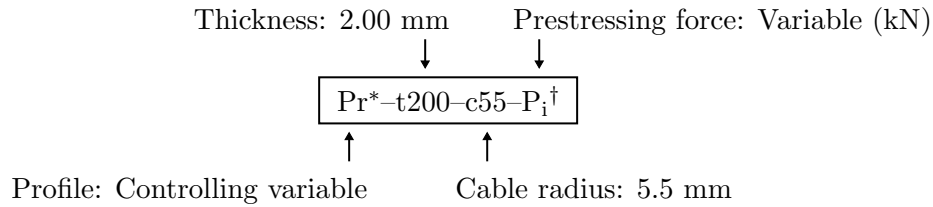
Figure 5.18: Example of the adopted notation.

In the present section, six cross-section profiles are utilised to study the effect of shifting the centroid location within the cold-formed steel cross-section upwards. The dimensions of the chosen profiles, as defined in Figure 3.3, are listed in Table 5.3. Essentially, the centroid location y_b/h was varied by changing the dimensions of the top and bottom flanges, while maintaining the total area of the cross-section, the height of the cross-section and the location of the web stiffeners all to be constant. The resulting profiles are illustrated in Figure 5.19.

It should be noted that, as discussed in Sections 3.3.3 and 5.2.7.1, the presence of lateral restraints at the junctions between the web and the top and bottom flanges confines
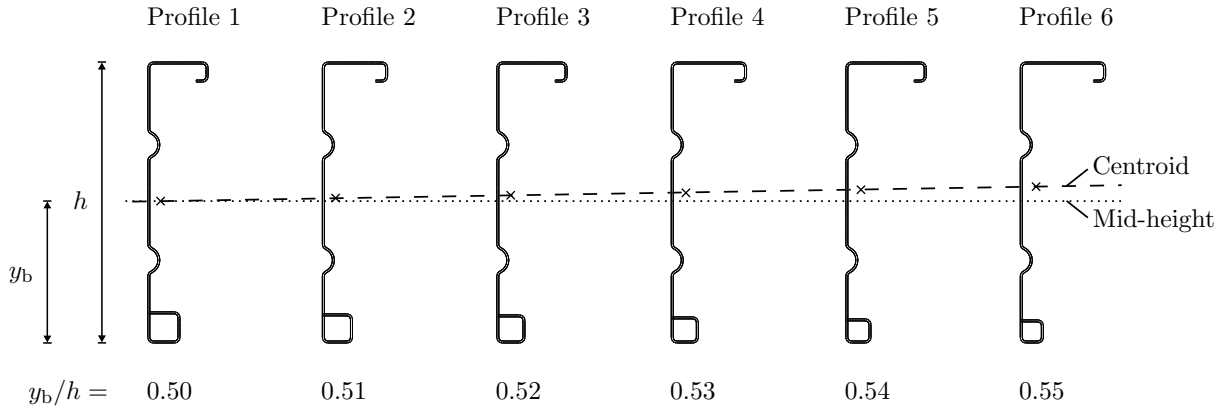
Figure 5.19: Cross-section profiles of the cold-formed steel beams used in the parametric studies.

Table 5.3: Dimensions of the top and bottom flanges of the chosen profiles.

Profile	b_1 (mm)	d_1 (mm)	b_2 (mm)	y_b/h
1	32.0	31.0	60.0	0.50
2	30.0	29.0	65.0	0.51
3	28.0	28.0	70.0	0.52
4	27.0	26.0	75.0	0.53
5	25.0	24.0	80.0	0.54
6	23.0	23.0	85.0	0.55

Note: For all the profiles h=280.0 mm, b_3=12.0 mm, d_2=20.0 mm, a_1=82.5 mm, a_2=115.0 mm, r_1=3.5 mm, r_2=12.0 mm.

bending about the strong geometric axis. In the present work, the maximum difference between the bending moments about the major principal and strong geometric axes of the cross-section is less than 2% and occurs in the case of Profile 6.

In the parametric models, the modified two-stage Ramberg–Osgood model was employed, as discussed in Section 4.2.3.1(b), to enable direct comparisons of the FE results with the design predictions. Furthermore, note that, unless otherwise stated, the length of the member was 4800 mm.

In the following sub-sections, the increase in the ultimate moment capacity of the cold-formed steel beams due to the addition of the prestressed cables is given by the ratio $M_{ult,p}/M_{ult}$, where $M_{ult,p}$ is the ultimate moment at the midspan of the prestressed beam and M_{ult} is the ultimate moment of the bare steel beam. The key properties of the studied beams are listed in Tables A.1–A.2 in Appendix A, alongside the corresponding FE results. The moment–deflection responses of the parametric FE models are presented in Figures B.1–B.3 in Appendix B. As discussed in Section 1.4, the entire parametric FE

modelling process was automated for the purposes of computational efficiency. A detailed analysis of the mechanical behaviour of prestressed cold-formed steel beams during the different loading stages has been presented in Section 5.2, while the FE modelling approach has been described in Section 4.2.

5.3.2   Effect of prestress level

The prestress level was controlled using the normalised parameter $P_\mathrm{i}/P_\mathrm{max}$, where, for a given beam geometry, P_i (*i.e.* the initial prestressing force) was variable and P_max, *i.e.* the maximum allowable prestressing force, as defined in Equation (3.21), was constant. As shown in Table 5.2, the geometry of the cold-formed steel member and the size of the cable were maintained to be constant. The results presented below correspond to model Pr4–t200–c55–P_i*, where P_max is equal to 109 kN and the contribution of the cable to the system is given by $A_\mathrm{c}/A_\mathrm{s}$=10.5%. In this parametric study, P_i was varied to give the following eleven levels of prestress:

$$P_\mathrm{i}/P_\mathrm{max} = \{0.0, 0.2, 0.4, 0.6, 0.8, 0.9, 1.0, 1.1, 1.2, 1.3, 1.4\} \,. \tag{5.4}$$

As discussed in Section 3.5.2.1, the value of P_max was determined by predicting the capacity of the cold-formed steel beam under the loading configuration of Stage I. To investigate whether higher prestress levels than P_max could actually be carried by the member, and whether these levels can offer greater benefits, prestress levels up to 1.4 times P_max were modelled; these results are shown with dashed lines in the figures below.

The normalised moment–deflection responses of the Pr4–t200–c55–P_i* models are shown in Figure 5.20, where M_y is the yield moment of the bare steel beam, δ_mid is the vertical deflection at the member midspan and $\delta_\mathrm{mid,y}$ is the midspan vertical deflection at the first yield point of the bare steel beam. Firstly, it is observed that as the prestress level is increased, the pre-camber (*i.e.* the starting point of the response) induced during Stage I also increases, and thus the overall vertical deflections of the member at failure decrease. Secondly, as the level of prestress is increased, the ultimate moment capacity of the beam is enhanced.
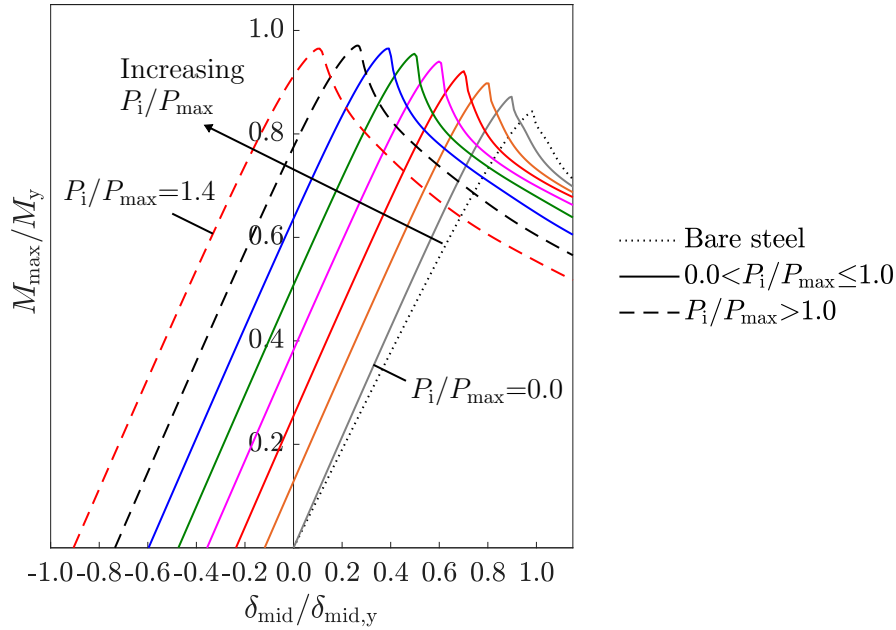
Figure 5.20: Normalised moment–deflection responses of the Pr4–t200–c55–P_i^* models for the relative prestress levels $P_i/P_{max}=\{0.0, 0.2, 0.4, 0.6, 0.8, 1.0, 1.2, 1.4\}$, alongside the response of the bare steel model.

To explain the increase in capacity, Figures 5.21(a)–(b) can be utilised, whereby the normalised moment–stress responses corresponding to the top and bottom flanges respectively of the above models are shown; $\sigma_{t,av}$ and $\sigma_{b,av}$ are the average membrane stress levels within the top and bottom flanges respectively, while $F_{y,s}$ is the yield stress of the cold-formed steel. As discussed in Section 5.2.3.2, failure of the cold-formed steel member can be predicted by the DSM failure stress $\sigma_{t,DSM}$, which is indicated by the vertical dotted line in Figure 5.21(a). The higher the prestress level, the greater the tensile stresses within the top flange at the start of Stage II, as shown in Figure 5.21(a). Since these initial stresses have to be first overcome before compressive stresses can develop and $\sigma_{t,DSM}$ is reached, a greater moment is required to cause failure of the beam. Hence, the higher the level of prestress, the more the occurrence of local/distortional buckling is delayed and thus the greater the capacity of the member is enhanced.

As shown in Figure 5.21(b), owing to the compressive stresses imposed within the bottom flange during prestressing, the utilisation of the bottom flange decreases with increasing prestress levels. For instance, when $P_i/P_{max}=1.0$, the average stress level within the bottom flange at the ultimate point is only 10% of the yield stress. Furthermore, as expected, a higher prestress level induces higher stresses within the cable, as shown in

(a) Top flange
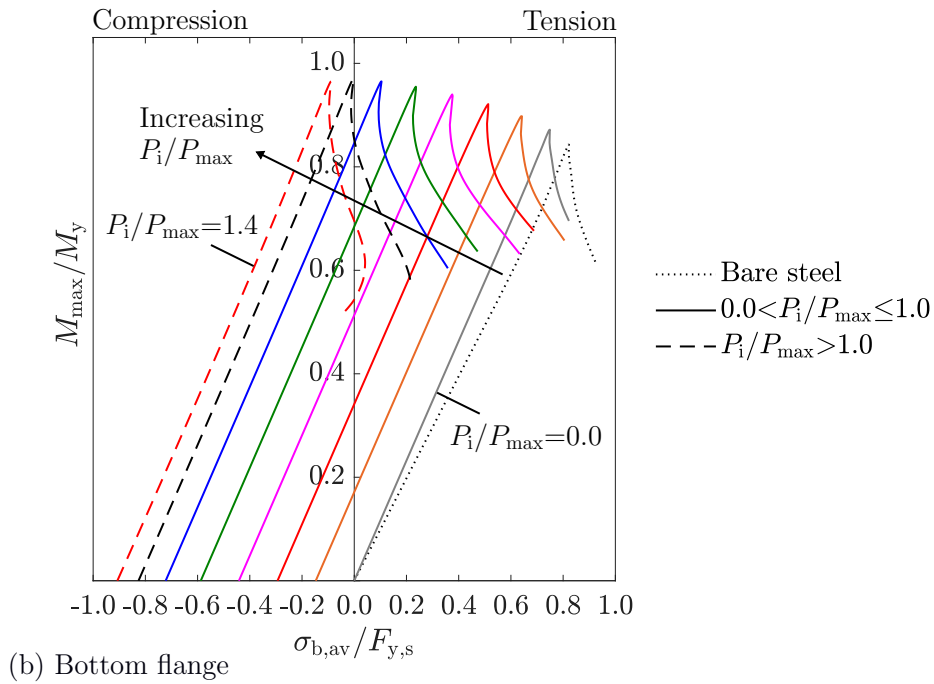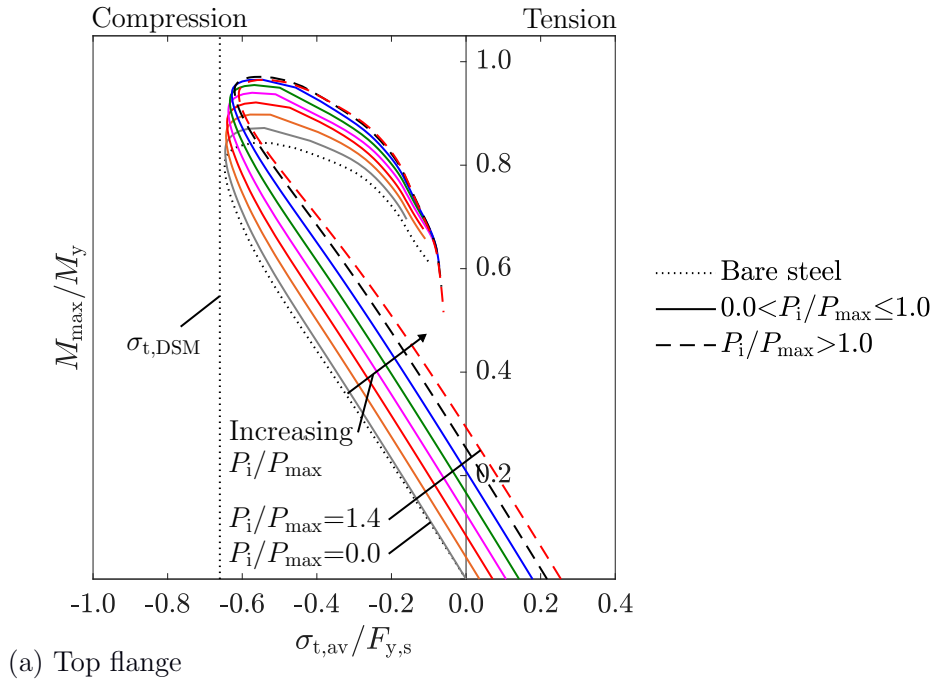
(b) Bottom flange

Figure 5.21: Normalised moment–stress responses for the (a) top and (b) bottom flanges of the Pr4–t200–c55–P$_i$* and bare steel models for the relative prestress levels P_i/P_{max}={0.0, 0.2, 0.4, 0.6, 0.8, 1.0, 1.2, 1.4}.
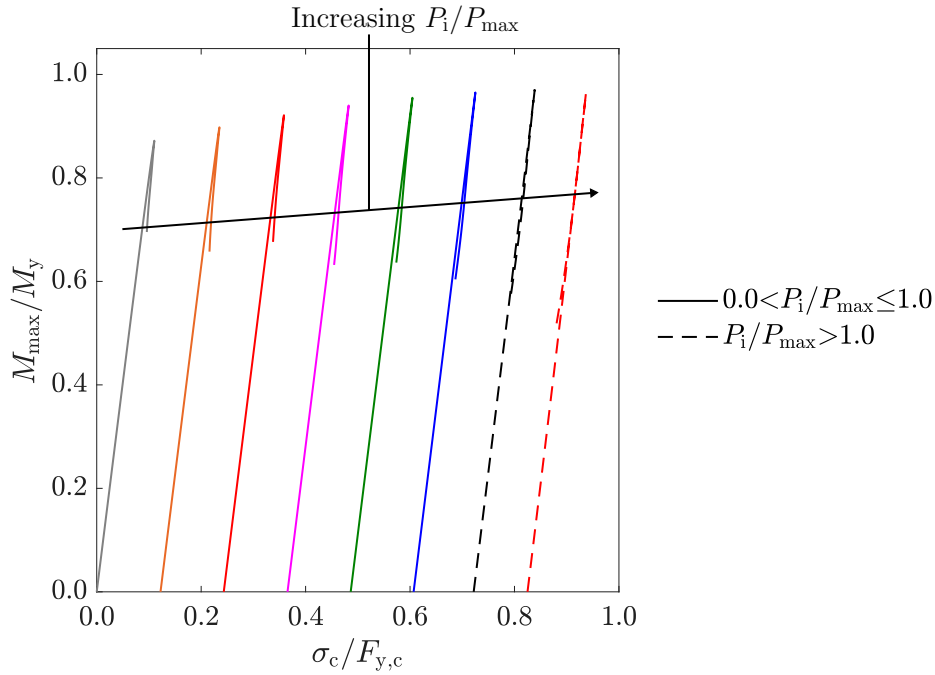
Figure 5.22: Normalised moment–stress responses for the cable of the Pr4–t200–c55–P$_\text{i}$* models for the relative prestress levels $P_\text{i}/P_\text{max}=\{0.0, 0.2, 0.4, 0.6, 0.8, 1.0, 1.2, 1.4\}$.

Figure 5.22, where σ_c and $F_\text{y,c}$ are the axial stress level and the material yield stress of the cable respectively.

The relationship between the increased moment capacity of the prestressed beam over the bare steel beam $M_\text{ult,p}/M_\text{ult}$ and the studied levels of prestress is demonstrated in Figure 5.23, where the results from two more combinations of beam geometries and cable sizes, namely Pr2–t250–c62–P$_\text{i}$* and P6–t150–c48–P$_\text{i}$*, are shown. In general, it may be concluded that P_max, as defined in Equation (3.21), is a representative approximation of the prestress level that maximises $M_\text{ult,p}/M_\text{ult}$ and thus, unless otherwise stated, is chosen as the default prestress level in the parametric studies. Note that, in the case of $P_\text{i}/P_\text{max}=1.4$ of model Pr2–t250–c62–P$_\text{i}$*, the cable failed in tension before the ultimate capacity of the cold-formed steel beam was reached; hence, the result is not within the range of the current figure.

At very high prestress levels, a descending trend in the moment capacity enhancement can be observed in Figure 5.23. This stems from the fact that the increasing prestress levels result in increasing negative bending, but also increasing compression of the cold-formed steel cross-section. While the net effect of prestress remains beneficial, beyond a certain level, the detrimental influence of the applied compression begins to outweigh the
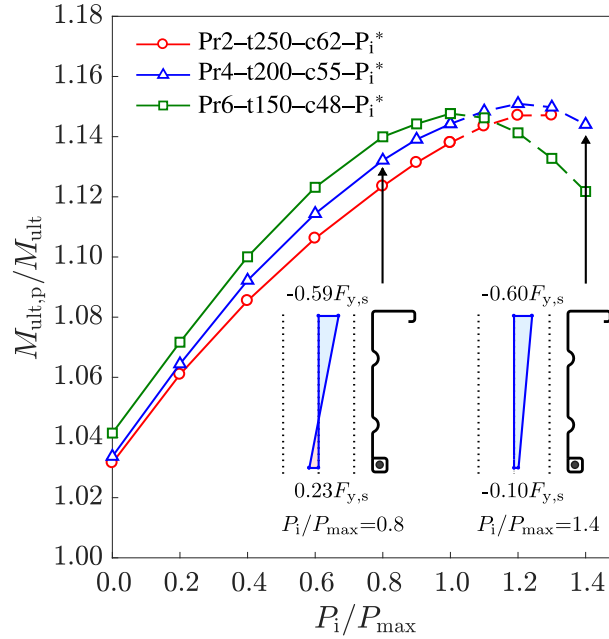
Figure 5.23: Variation of the increase in the ultimate moment capacity with respect to the studied levels of prestress for three different combinations of beam geometries and cable sizes.

advantage derived from the applied negative bending. This can be seen with reference to the midspan net axial stress distributions at failure shown, for model Pr4–t200–c55 with $P_i/P_{max}=0.8$ and $P_i/P_{max}=1.4$, in idealised form in Figure 5.23. For $P_i/P_{max}=0.8$, it can be seen that the top and bottom flanges are in compression and tension at failure, respectively. However, for $P_i/P_{max}=1.4$, the entire cross-section is under compressive stress at failure.

5.3.3   Effect of cable size

As shown in Table 5.2, the effect of the cable size was investigated by keeping the geometry of the cold-formed steel beam (*i.e.* Profile and thickness) and the initial prestressing force constant, while varying the size of the cable. The latter was controlled using the normalised parameter A_c/A_s. Seven cable sizes were considered according to:

$$A_c/A_s = \{7.0, 8.0, 10.0, 12.0, 14.0, 16.0, 18.0\}\%. \tag{5.5}$$

The normalised moment–deflection responses of the Pr4–t200–c*–P_i109 models, where P_i/P_{max} was kept to unity, are shown in Figure 5.24, alongside the response of the bare
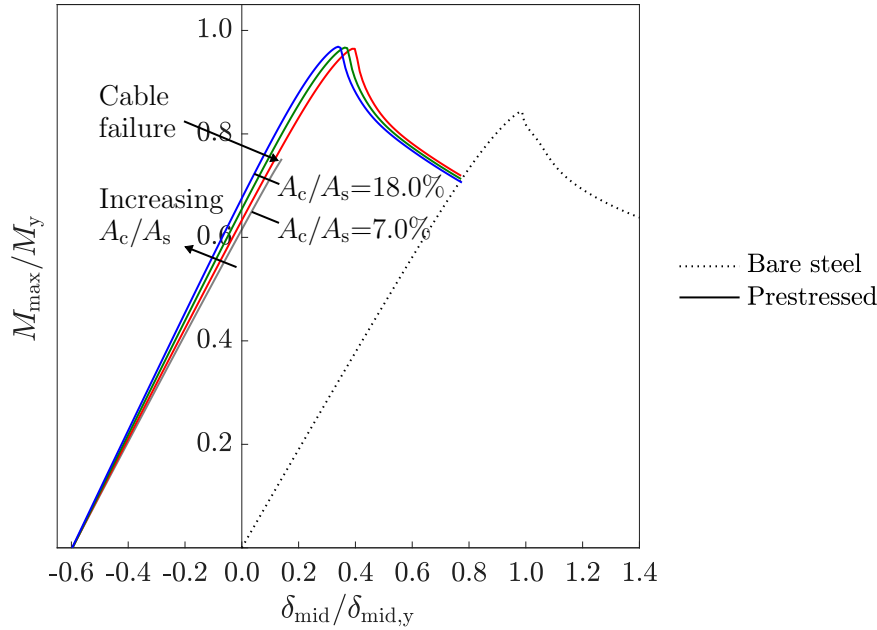
Figure 5.24: Normalised moment–deflection responses of the Pr4–t200–c*–P$_\mathrm{i}$109 models for the cable radii r_c={4.5, 5.4, 6.4, 7.2} mm (*i.e.* $A_\mathrm{c}/A_\mathrm{s}$={7.0, 10.0, 14.0, 18.0}%), alongside the response of the bare steel model.

steel beam. It is observed that the ultimate moment capacity of the members at the end of Stage II is not influenced greatly by the cable size. However, as illustrated in the case of $A_\mathrm{c}/A_\mathrm{s}$=7.0%, the use of an insufficiently large cable may result in failure of the cable in tension before the capacity of the cold-formed steel beam is reached, thus compromising the capacity of the system. In the aforementioned case, failure of the cable during Stage II is caused by the incremental increase in the prestressing force ΔP, demonstrating the requirement to check the capacity of the cable during both Stages I and II, as discussed in Section 3.5. Furthermore, as expected, the presence of the cable enhances the bending stiffness of the system, as indicated by the increased gradient of the normalised moment–deflection responses.

The normalised moment–stress responses corresponding to the top and bottom flanges of the Pr4–t200–c*–P$_\mathrm{i}$109 models are shown in Figure 5.25, where it is observed that as the cable size is increased, the stress level within the bottom flange decreases; this is owing to the fact that the larger the cable, the larger the proportion of the imposed loading it attracts, as shown in Figure 5.26, where it is also demonstrated that the utilisation of the cable is dependent on its size. For instance, the use of a cable with a radius of 7.2 mm was not efficient in this case since only 45% of its tensile capacity was utilised at failure.
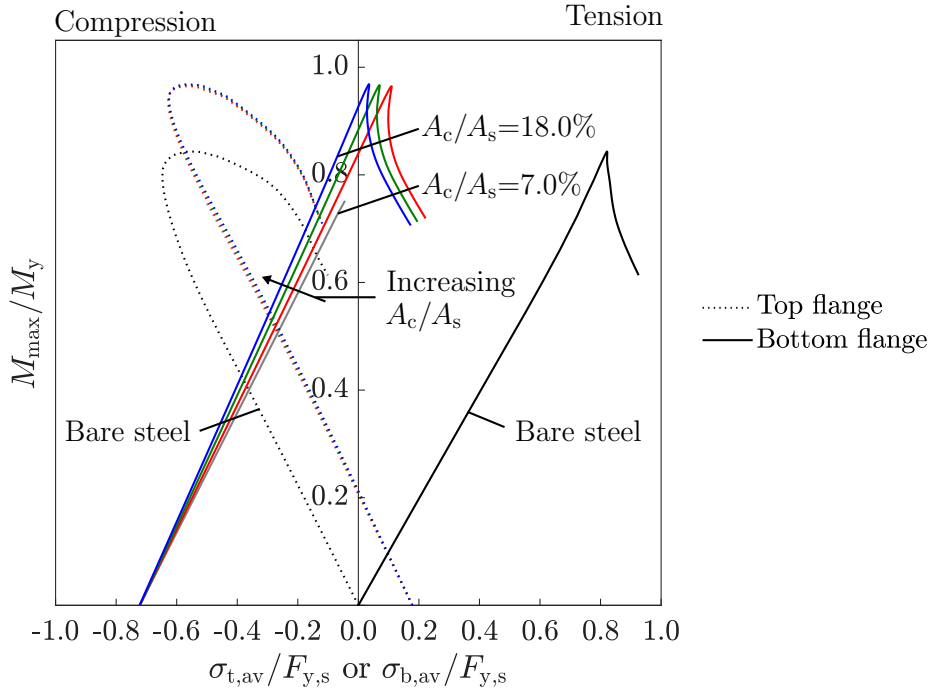
Figure 5.25: Normalised moment–stress responses corresponding to the top and bottom flanges of the Pr4–t200–c*–P$_i$109 models for for the cable radii $r_c=\{4.5, 5.4, 6.4, 7.2\}$ mm (*i.e.* $A_c/A_s=\{7.0, 10.0, 14.0, 18.0\}$%), alongside the bare steel beam responses.
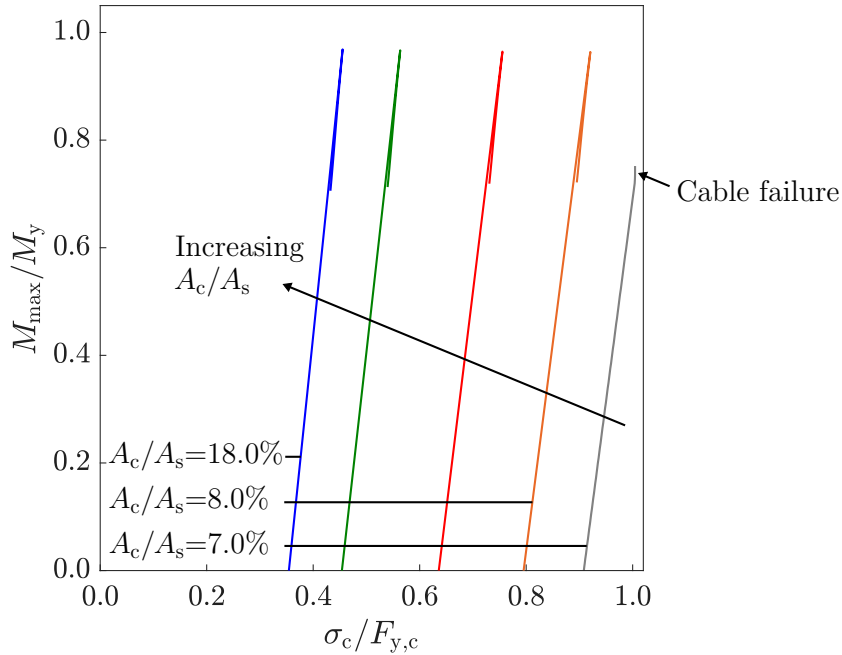
Figure 5.26: Normalised moment–stress responses corresponding to the cable of the Pr4–t200–c*–P$_i$109 models for the cable radii $r_c=\{4.5, 5.4, 6.4, 7.2\}$ mm.

On the other hand, as illustrated by the use of a cable with a radius of 4.5 mm, the use of an insufficiently large cable results in its premature failure. The optimal scenario is the one where the steel beam and the cable fail simultaneously, thus fully utilising the load-carrying capacity of both structural components of the system. In the current example, the most efficient cable size was the one with a radius of 4.8 mm (corresponding to A_c/A_s=8.0% in Figure 5.26) since at failure σ_c=0.92$F_{y,c}$. Note that, as discussed in Section 3.5, in design calculations, suitable safety factors would of course be applied to the resistances of both the cold-formed steel beam and the cable.

5.3.4   Effect of section slenderness

As shown in Table 5.2, the effect of the cross-sectional slenderness was investigated by varying the thickness of the cold-formed steel beam. To keep the contribution of the cable to the bending stiffness of the system (*i.e.* the ratio A_c/A_s) constant, the size of the cable was adjusted accordingly. Furthermore, since by changing the thickness, the maximum prestress level P_{max} that the beam can carry also changed, the initial prestressing force P_i was also adjusted to keep the ratio P_i/P_{max} constant. The profile of the cold-formed steel beam was also kept constant.

Table 5.4: Properties of the Pr4–t*–c†–P$_i$† models, where t is the controlling parameter.

t (mm)	1.00	1.25	1.50	1.75	2.00	2.25	2.50	2.75	3.00
λ_d	1.43	1.27	1.16	1.06	0.99	0.93	0.88	0.83	0.79
r_c (mm)	4.0	4.4	4.8	5.2	5.5	5.9	6.2	6.4	6.7
P_i (kN)	46	61	77	93	109	126	143	159	176

The models utilised in the present study are defined by the notation Pr4–t*–c†–P$_i$†, with the thickness being varied according to Table 5.4, where the corresponding section slenderness values, cable radii and initial prestressing forces are also listed. Note that the distortional slenderness λ_d corresponds to positive bending, the cable radii were chosen with the aim of maintaining A_c/A_s=10.5% and the initial prestressing forces were varied to keep P_i/P_{max}=1.0. The key properties of the studied beams are listed in Tables A.1–A.2 in Appendix A, alongside the corresponding FE results. The moment–deflection
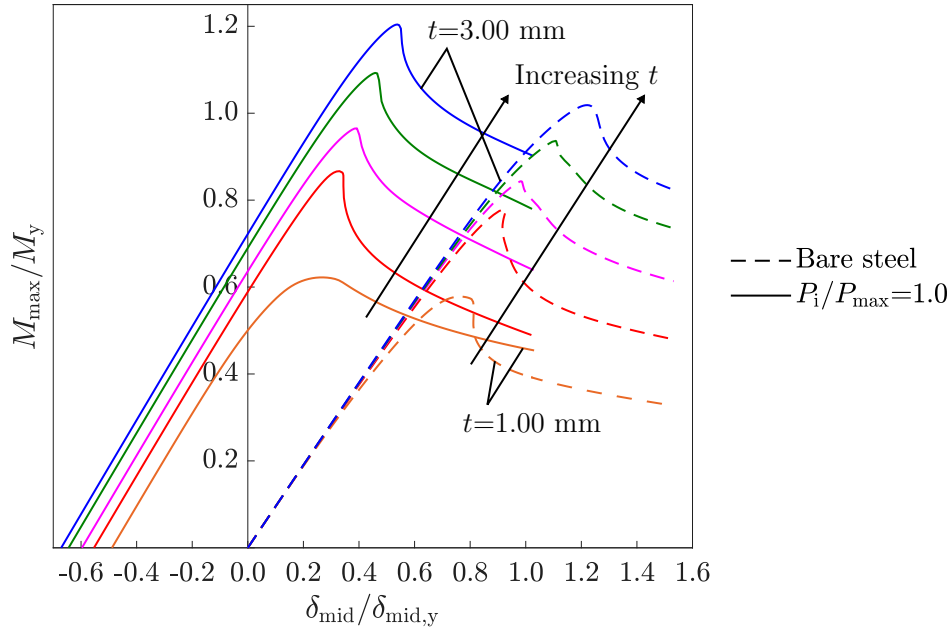
Figure 5.27: Normalised moment–deflection responses of the Pr4–t*–c†–P$_i^†$ models for the thicknesses $t=\{1.00, 1.50, 2.00, 2.50, 3.00\}$ mm, alongside the responses of the corresponding bare steel models; the value of $\delta_{mid,y}$ is the same for all models.

responses are presented in Figures B.1–B.3 in Appendix B.

The normalised moment–deflection responses of the Pr4–t*–c†–P$_i^†$ models, alongside the corresponding bare steel models, for five section thicknesses, are shown in Figure 5.27. In the case of the bare steel beams, as expected, the ultimate capacity is enhanced with increasing thickness. In the case of the prestressed beams, as the thickness is increased, the axial compressive resistance P_n and thus the predicted capacity of the member for Stage I (*i.e.* P_{max}) also increase, as shown in Figure 5.28; hence, a greater initial prestressing force was applied to keep the relative prestress level P_i/P_{max} to be unity. For this reason, as shown in Figure 5.27, a larger pre-camber and a greater enhancement in the ultimate moment capacity of the beams were achieved with increasing thickness. Note that the responses of the bare steel models in Figure 5.27 have the same gradient since, for each response, M_{max} is normalised by the corresponding yield moment M_y. Also, since the contribution of the cable to the system bending stiffness (*i.e.* the ratio A_c/A_s) was kept constant, the responses of the prestressed models also have the same gradient.

The parametric study presented above was repeated for the six section profiles presented in Figure 5.19. The variation of the enhancement of the ultimate moment capacity of the bare steel beams, *i.e.* $M_{ult,p}/M_{ult}$, with respect to the thickness of the beams, for
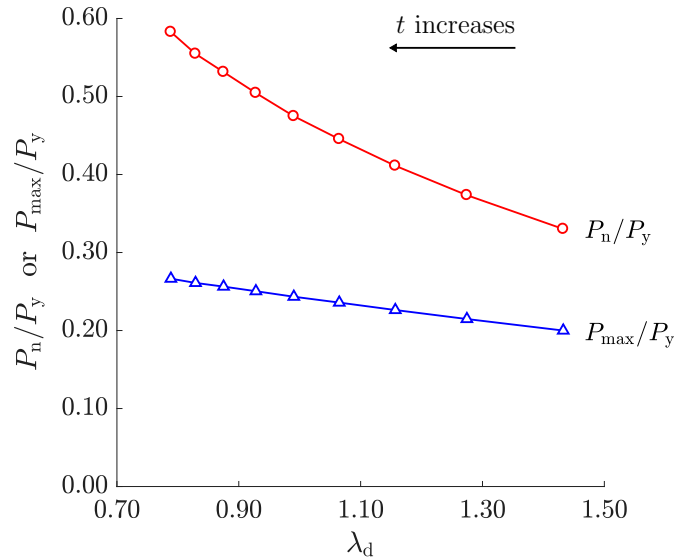
Figure 5.28: Variation of the axial compressive resistance P_n and maximum allowable prestressing force P_max, both being normalised by the corresponding squash load P_y, for the Pr4–t*–c†–Pi† models.

the six different profiles, is shown in Figure 5.29. Overall, it can be concluded that the thicker the section, the greater the prestressing force the member can carry and thus the greater the moment capacity enhancement. It can also be observed that the profile (*i.e.* the centroid location) of the steel beam also influences the benefits obtained from the addition of the prestressed cable. This effect is examined in the next sub-section.
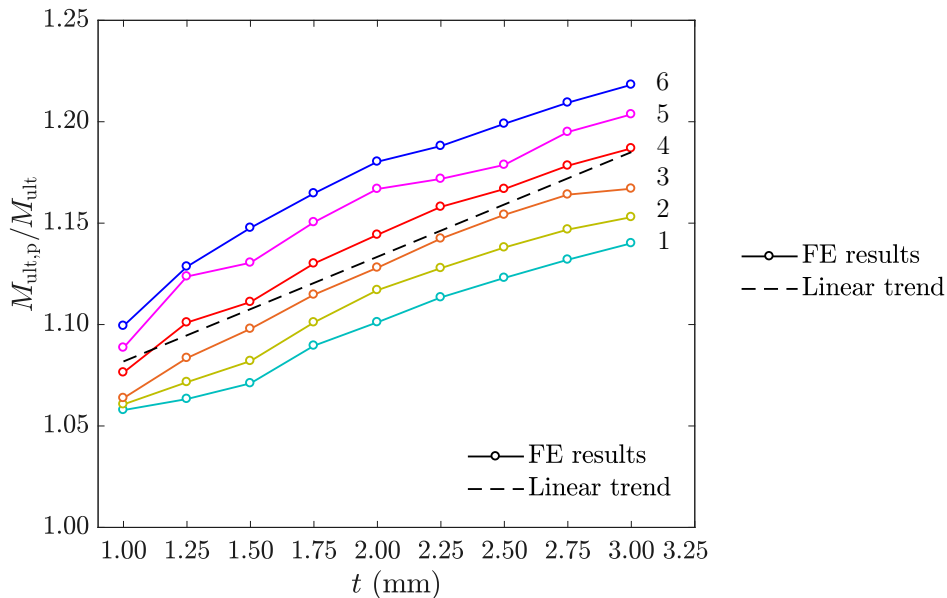
Figure 5.29: Increase in the ultimate moment capacity of the bare steel beam for the nine studied thicknesses and for Profiles 1–6 (inclusive).

5.3.5 Effect of centroid location

As discussed in Section 5.3.1, to investigate the effect of the centroid location within the cross-section of the steel beam, six different profiles were utilised. In the present subsection, the origin of the benefits obtained due to the shift of the centroid location are demonstrated first and, subsequently, the parametric FE results are presented.

5.3.5.1 Origin of obtained benefits

As discussed in Section 2.2.4, in a prestressed system, the cross-sectional geometry of the prestressed member plays a significant role in the effectiveness of prestressing. Potentially, a well-proportioned cross-section can provide increased structural benefits and thus a more economical solution.

To illustrate the influence of the centroid location on the behaviour of the proposed beams, an example is presented in Figure 5.30, whereby the components of the axial stress distribution at the midspan of a prestressed beam with Profile 1 (model Pr1–t200–c55–P$_i$123) and a beam with Profile 6 (model Pr6–t200–c55–P$_i$123) are explored. The centroid of the former is located at the mid-height of the section (*i.e.* y_b/h=0.50), while the centroid of the latter is located at a higher location corresponding to y_b/h=0.55. The components of the axial stress distributions were determined using the linear elastic expressions that have been developed in Section 3.4. Note that, for illustration purposes, the stress components induced by ΔP are not shown but still have been considered in the evaluation of the overall stress levels. The values shown correspond to the average membrane stress levels within the top and bottom flanges, after being normalised by the material yield stress. In both models, the same prestressing force was applied in Stage I, with the P_{max} value corresponding to Profile 1 (*i.e.* P_{max}=123 kN) being chosen. In Stage II, a bending moment corresponding to the yield moment of Profile 1 (*i.e.* M_y=32.1 kNm) was applied.

The shift of the centroid upwards has two principal effects. Firstly, the application of prestressing in Stage I becomes more effective due to the larger lever arm of the prestress-
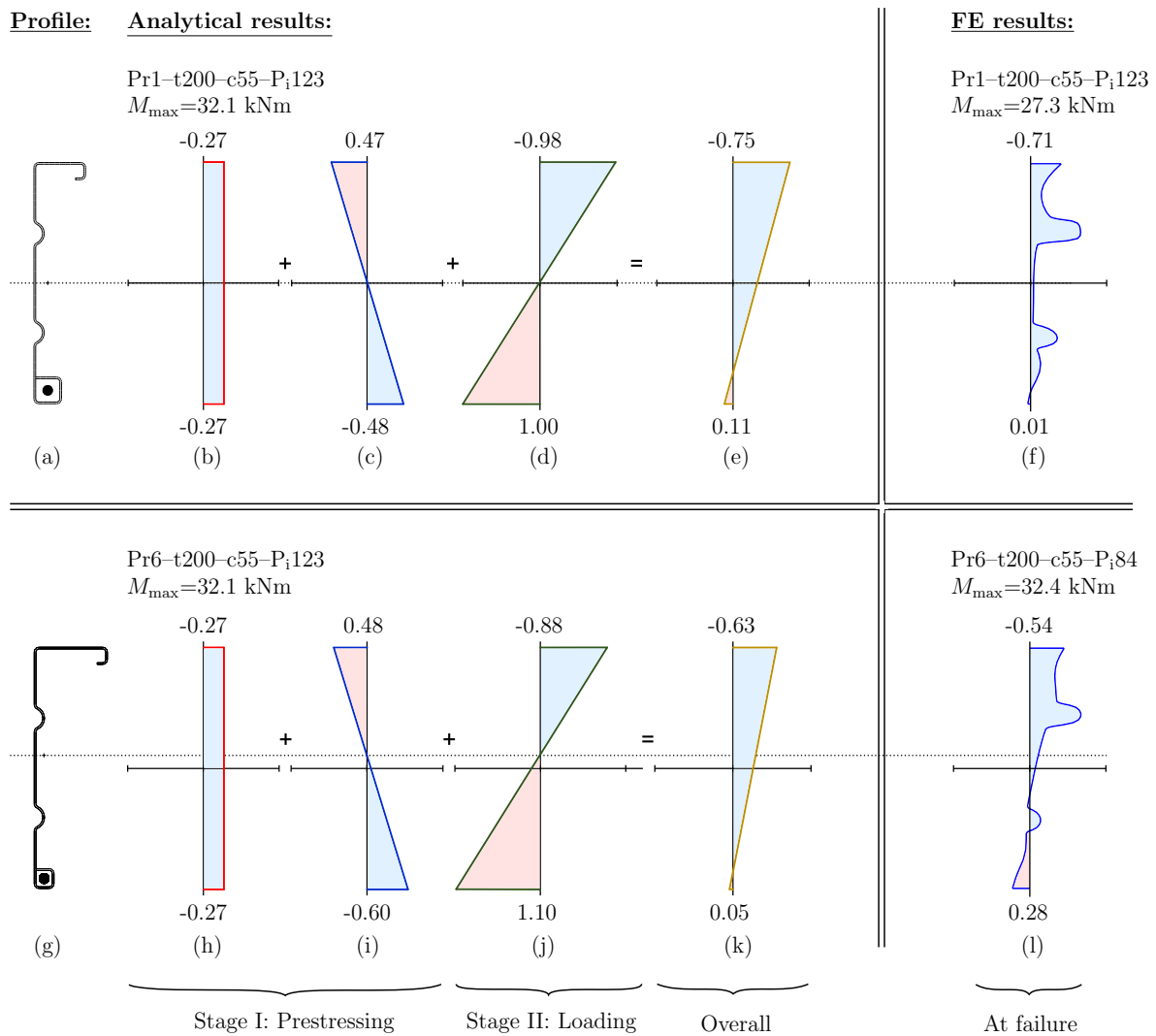
Figure 5.30: Examination of the effect of the centroid location on the axial stress distribution at the critical cross-section using the linear elastic expressions developed in Section 3.4. Axial stress distributions from the FE models at failure.

ing force from the strong geometric axis (compare Figures 5.30(c) and (i)). Secondly, and most importantly, the application of vertical loading in Stage II imposes smaller compressive stress levels within the top flange of the beam with a higher centroid (compare Figures 5.30(d) and (j)). Hence, the overall compressive stress level within the top flange at the end of Stage II is reduced (compare Figures 5.30(e) and (k)). Consequently, the susceptibility of the member to local/distortional buckling during loading is reduced, and thus an even greater moment is required to cause beam failure, *i.e.* the capacity of the beam is enhanced further.

It should be noted that the reduced compressive stress levels within the top flange during Stage II comes at the expense of increased tensile stress levels within the bottom flange. However, in the proposed prestressed beams, this increase is counteracted by the compressive stresses that are induced within the bottom flange during Stage I. As a consequence, as shown in Figure 5.30(i), the proposed system can in fact carry bending moments that are greater than the yield moment of the bare steel section.

5.3.5.2   Results from parametric study

To investigate the effect of the centroid location y_b/h within the cross-section of the cold-formed steel beam, the six cross-section profiles presented in Figure 5.19 were utilised. As shown in Table 5.2, the thickness of the profile was kept constant. Since all the chosen profiles have the same cross-sectional area, the size of the cable, and thus the ratio A_c/A_s, were also maintained to be constant. Furthermore, since the maximum allowable prestressing force P_{max} for each profile is different, the initial prestressing force P_i was adjusted accordingly, with the aim of keeping the ratio P_i/P_{max} constant. Note that the key properties of the studied beams are listed in Tables A.1–A.2 in Appendix A, alongside the corresponding FE results. The moment–deflection responses are presented in Figures B.1–B.3 in Appendix B.

It is worth noting that, even though by widening the top flange the local slenderness λ_l of the cross-section increases, the distortional slenderness λ_d does not vary considerably since the web dimensions remain unchanged. Meanwhile, the distortional buckling mode remains the dominant mode (*i.e.* $\lambda_d > \lambda_l$) in all the chosen geometries. This has enabled
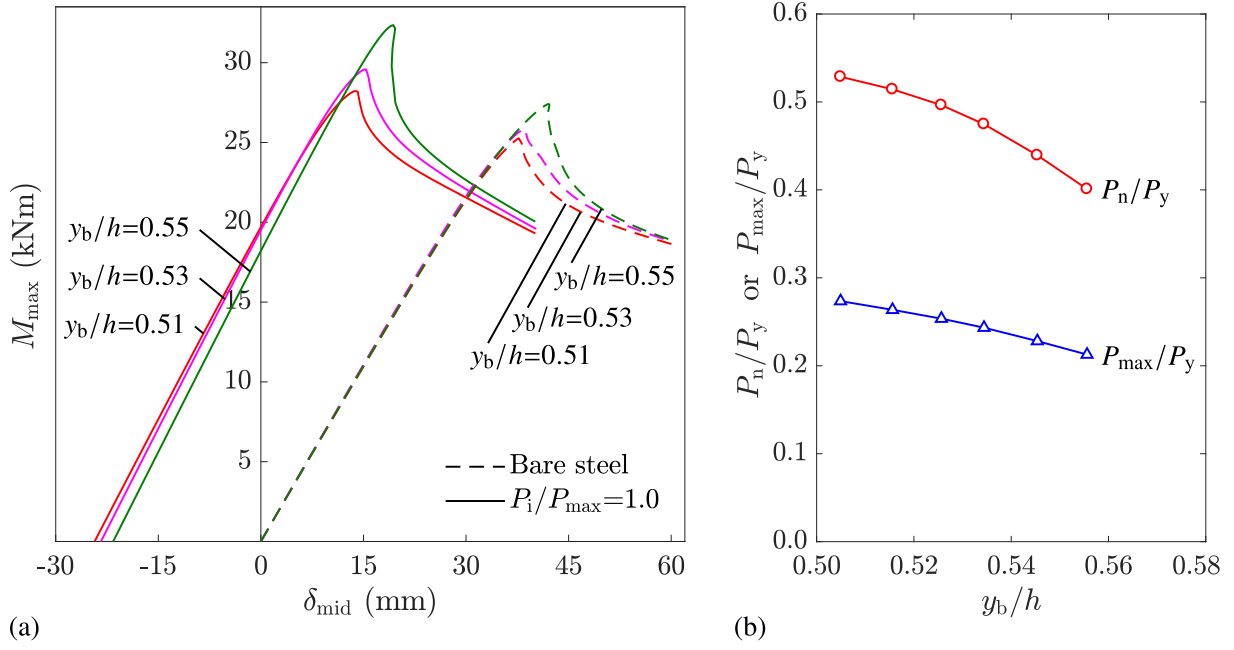
Figure 5.31: (a) Moment–deflection responses for the Pr*–t200–c55–$P_i^\dagger$ and bare steel models for Profiles 2, 4 and 6, *i.e* y_b/h={0.51, 0.53, 0.55}. (b) Variation of the normalised axial compressive resistance P_n/P_y and maximum allowable prestressing force P_{max}/P_y with increasing centroid location, where P_y is the squash load.

the author to study the effect of shifting the centroid location independently from the effect of the section slenderness.

The FE results from models Pr*–t200–c55–$P_i^\dagger$ are presented below for the following cross-section profiles:

$$\mathrm{Pr} = \{1, 2, 3, 4, 5, 6\}, \tag{5.6}$$

with the prestressing levels required to maintain the ratio P_i/P_{max}=1.0 being:

$$\mathrm{P_i} = \{123, 118, 114, 109, 102, 95\} \text{ kN}, \tag{5.7}$$

and with the ratio A_c/A_s being kept constant at 10.5%. The centroid locations y_b/h of the above profiles are given in Table 5.3. The normalised moment–deflection responses of the aforementioned models alongside the responses of the corresponding bare steel models are shown in Figure 5.31(a), where it is observed that, with increasing y_b/h, a smaller pre-camber is induced along the member during the prestressing stage. This is because, by widening the top flange of the cross-section to shift the centroid upwards the axial compressive resistance P_n of the cold-formed steel beam is decreased, as shown in

179

Figure 5.31(b). Consequently, the maximum allowable prestressing force P_{max} decreases and thus a lower initial prestressing force is applied to maintain $P_{\text{i}}/P_{\text{max}}$ to be unity; hence a smaller pre-camber is induced along the member.

In Figure 5.31(a), it is also observed that the higher the location of the centroid within the cross-section, the greater the enhancement of the ultimate capacity of the bare steel beam due to the addition of the prestressed cable. This is attributed to the effect of the centroid location, as discussed in Section 5.3.5.1. This can be examined further by studying the normalised moment–stress response of the Pr^*–t200–c55–$\text{P}_{\text{i}}{}^{\dagger}$ models in Figure 5.32(a), where the variations of the average membrane stress levels at the top ($\sigma_{\text{t,av}}$) and bottom ($\sigma_{\text{b,av}}$) flanges with respect to the applied moment are shown. Firstly, it is observed that the failure of the members with higher centroids occurs at lower levels of $\sigma_{\text{t,av}}$. This is owing to the fact that these members have cross-sections that are more slender, thus having a lower DSM failure stress level $\sigma_{\text{t,DSM}}$ (see Section 5.2.3.2). Despite that, owing to the higher centroid location, the slope of the moment–stress response of these members is greater and hence a larger moment is required to reach $\sigma_{\text{t,DSM}}$ and cause failure.

Comparing the $\sigma_{\text{b,av}}$ levels in Figure 5.32(a), it is observed that by shifting the centroid upwards, the utilisation of the bottom flange is increased substantially, for instance, from approximately 5% in the case of Profile 2 to 30% in the case of Profile 6. As a result, since the bottom flange is able to carry greater proportion of the applied loading, the stress level within the cable is decreased, as shown in Figure 5.32(b). Hence, an even smaller cable can be used to carry the prestressing force. This effect is also attributed to the fact that a lower prestress level is applied to the members with higher centroids.

The above observations are also illustrated in Figures 5.30(f) and (l), where the axial stress distributions at the critical cross-section of the models Pr1–t200–c55–P_{i}123 and Pr6–t200–c55–P_{i}84 at failure respectively are shown. It should be noted though that the stress distributions from the FE models exhibit nonlinearity due to the occurrence of local/distortional buckling, with higher stresses observed at the locations of the intermediate stiffeners in the web. This is because, as discussed in Section 5.2.6, while the flat regions experience local out-of-plane deformations (*i.e.* buckling), the stiffeners retain their axial stiffness, thus attracting a higher proportion of the applied load. It is worth

(a) Top and bottom flanges (b) Cable
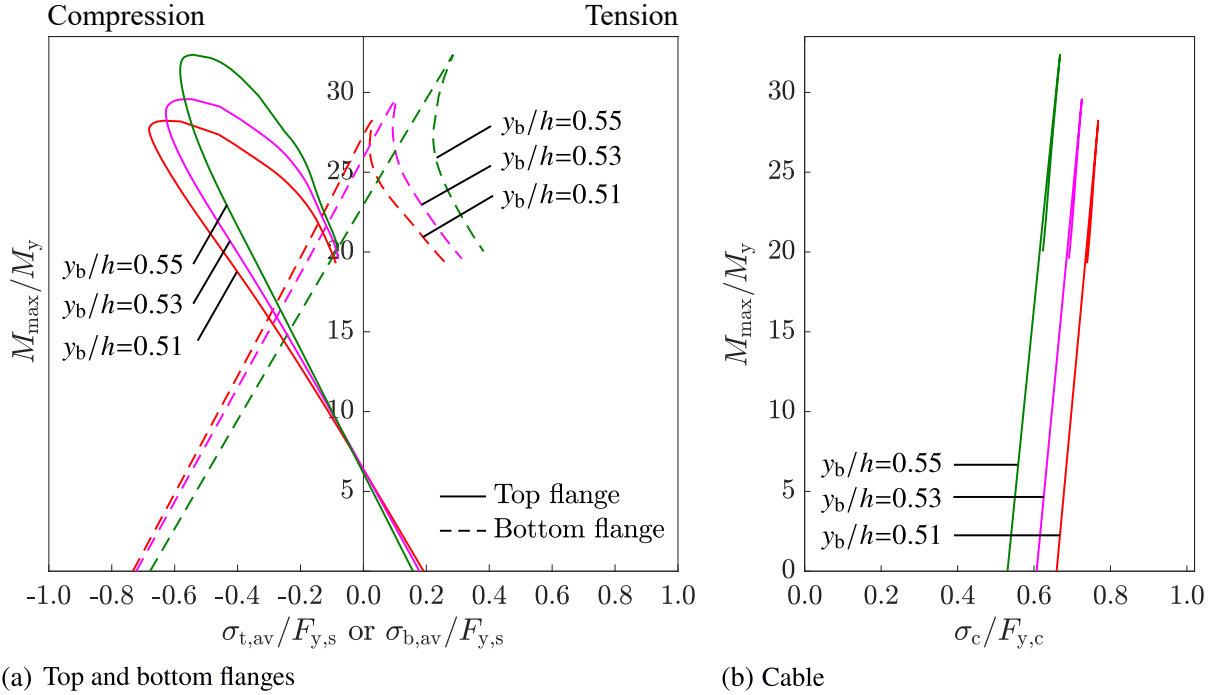
Figure 5.32: Normalised moment–stress responses for the (a) top and bottom flanges and the (b) cable of the Pr*–t200–c55–P$_i^\dagger$ models for profiles Pr=$\{2, 4, 6\}$, which correspond to *i.e.* $y_b/h=\{0.51, 0.53, 0.55\}$, alongside the corresponding bare steel models.

noting that, in the case of Profile 6, a smaller part of the cross-section is subjected to compression than in the case of Profile 1 at failure.

In the present example, while using the same amount of material for both the cold-formed steel beam and the cable, the ultimate capacity was increased by 18% simply by relocating some of the material of the steel beam from the bottom flange to the top flange and thus increasing y_b/h by 5%. This shift even reduces the applied prestressing force by approximately 25%, which is also beneficial.

The ultimate moment capacities achieved by the bare steel M_{ult} and prestressed $M_{ult,p}$ models with Profiles 1–6 are shown in Figure 5.33(a) for three different thicknesses. It is observed that, in general, as discussed in Section 5.3.4, the thicker the steel beam, the greater the increase in the capacity of the bare steel beams due to the addition of the prestressed cable. The effect of the centroid location is investigated using the ratio $M_{ult,p}/M_{ult}$ (*i.e.* comparing the prestressed and bare steel models having the same profile) in Figure 5.33(b), where it is shown that the higher the location of the centroid within the cross-section, the greater the obtained benefits. However, as discussed in Section 5.3.1, all the studied profiles have the same cross-sectional area; therefore, as

181
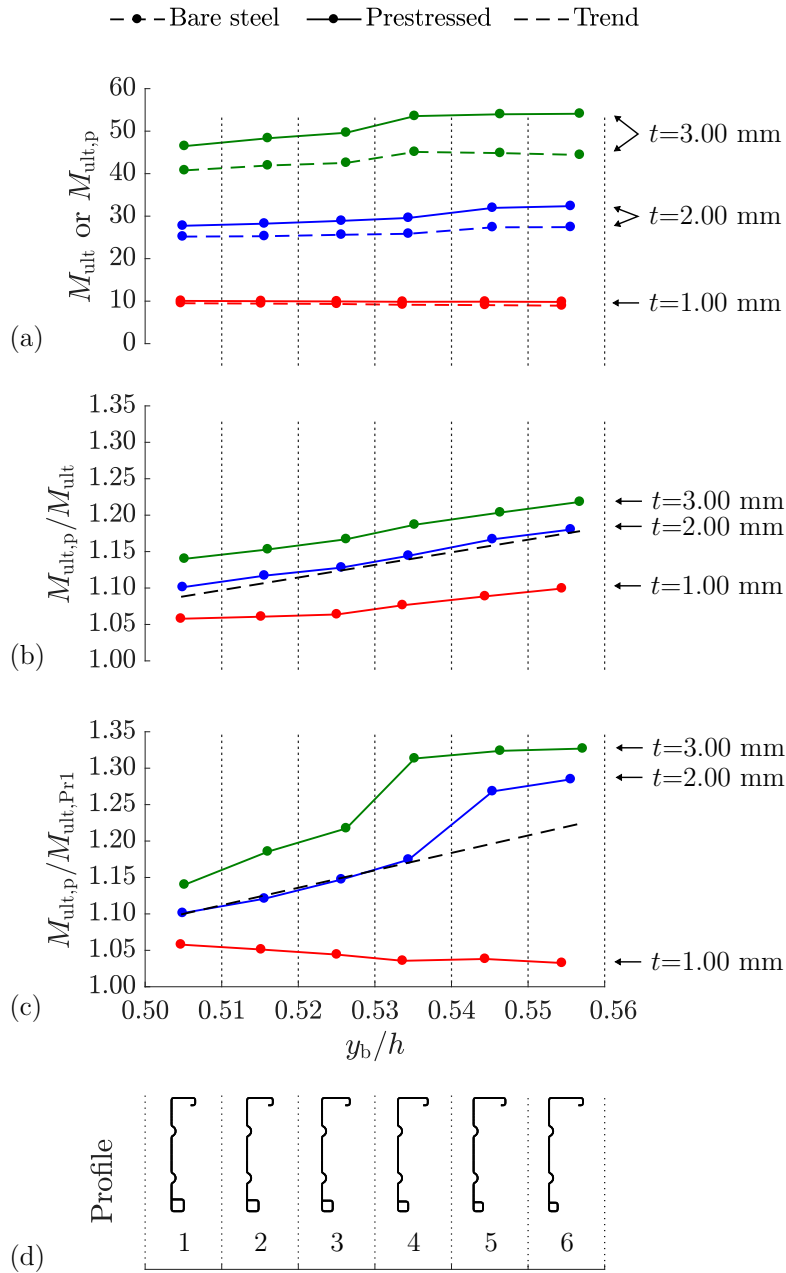
Figure 5.33: (a) FE results for the bare steel and prestressed models with Profiles 1–6 for three different thicknesses. (b) Variation of the ultimate moment capacity of the prestressed beams, normalised by the capacities of the corresponding bare steel beams, with respect to the centroid location. (c) Variation of the ultimate moment capacity of the prestressed beams, normalised by the capacities of the original bare steel beam with Profile 1, with respect to the centroid location.

shown in Figure 5.33(c), the effect of the centroid location can also be studied by comparing the capacities of the prestressed models with the capacity of the original bare steel beam (*i.e.* the bare steel beam with Profile 1), $M_{\mathrm{ult,Pr1}}$, where the centroid is located at the mid-height of the cross-section. Hence, as shown in Figure 5.33(c), the ratio $M_{\mathrm{ult,p}}/M_{\mathrm{ult,Pr1}}$ represents the benefits offered by the proposed concept due to both the addition of the prestressed cable and the shift of the centroid upwards. In the case of Profile 6 and t=3.00 mm, benefits of approximately 35% are demonstrated. Note that the linear trends shown as dashed lines in Figures 5.33(b) and (c) were obtained by utilising the results from the models of all nine section thicknesses.

5.3.6   Maximising the obtained benefits

From the parametric studies presented in the Sections 5.3.2–5.3.5, it was concluded that the benefits obtained from prestressing cold-formed steel beams can be maximised by increasing: (i) the prestress level, (ii) the size of the cable, (iii) the thickness of the cold-formed steel beam, and (iv) the height at which the centroid is located within the cross-section of the cold-formed steel beam.

In the present sub-section, the aforementioned conclusions are utilised to determine the maximum benefits that the prestressing process can offer in the proposed concept. For this purpose, a prestressed member with the properties listed in Table 5.5 was modelled; this model is thus named Pr7–t400–c70–P_i*. The contribution of the cable to the system is given by the ratio A_c/A_s=8.5%, while the initial prestressing force was varied with the aim of determining the prestress level that provides the greatest increase in the capacity

Table 5.5: Properties of the Pr7–t400–c70–P_i* model. The dimensions not listed in the present table are the same with those given in Table 5.3.

Geometric properties:	$b_1 = 22.0$ mm	$d_1 = 22.0$ mm	$b_2 = 90.0$ mm
	$t = 4.00$ mm	$e = 147.5$ mm	$r_c = 7.0$ mm
Section properties:	$y_b/h = 0.57$	$\lambda = 0.70$	$A_s = 1768$ mm^2
Prestressing:	$P_{\max} = 205$ kN	$P_n = 0.535 P_y$	$M_{\mathrm{nx}}^- = 1.0 M_y$
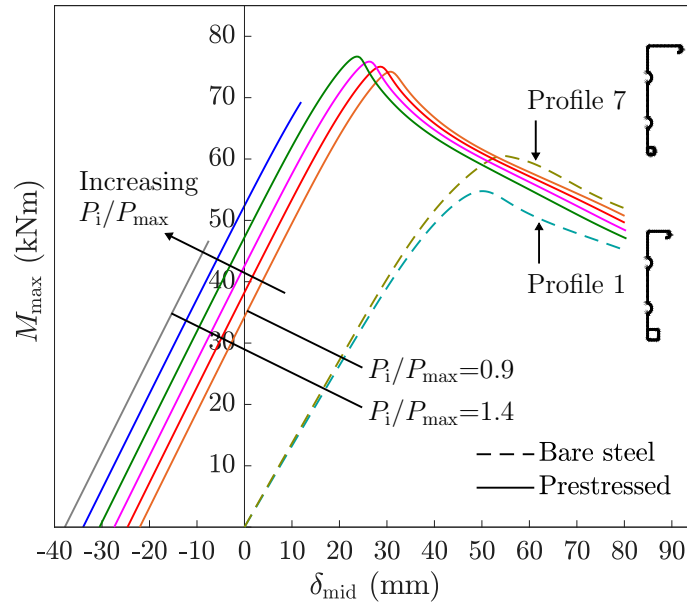
Figure 5.34: Moment–deflection responses of the Pr7–t400–c70–P_i^* models for the prestress levels P_i/P_{max}={0.9, 1.0, 1.1, 1.2, 1.3, 1.4}, alongside the responses of the corresponding bare steel beam with Profile 7 and the original bare steel beam with Profile 1.

of the beam. This was performed according to the following relative prestress levels:

$$P_i/P_{max} = \{0.9, 1.0, 1.1, 1.2, 1.3, 1.4\}. \tag{5.8}$$

The moment–deflection responses of the Pr7–t400–c70–P_i^* models are shown in Figure 5.34, alongside the responses of the corresponding bare steel model (*i.e.* with Profile 7) and the bare steel model with the original cross-section profile (*i.e.* Profile 1), where the centroid is located at the mid-height of the cross-section. As discussed in Section 5.3.5, by comparing the prestressed models with the bare steel model with Profile 1, the benefits from both the effect of the addition of the prestressed cable and the effect of shifting the centroid upwards are considered. As demonstrated in Figure 5.34, the greatest benefit is achieved when P_i/P_{max} is equal to 1.2; hence, this is considered to be the optimised case herein. At higher prestress levels, the cable yields before the ultimate capacity of the cold-formed steel beam is reached.

In the optimised case, the addition of the prestressed cable increases the ultimate capacity of the original bare steel section with Profile 1 by 40% while also decreasing the deflections at the ultimate point by 53%. By comparing the prestressed beam with the

corresponding bare steel section with Profile 7, the aforementioned benefits become 27% and 57% respectively. It is worth noting that, in the optimised case, the axial stress level in the cable at the ultimate point is equal to $\sigma_c=0.96F_{y,c}$, demonstrating that the capacity of both structural components has been utilised effectively.

5.4   Concluding remarks

The benefits and potential of prestressing cold-formed steel beams, in terms of enhanced structural performance at both serviceability and ultimate limit states have been demonstrated in the present chapter. The proposed structural system comprises two structural components, namely the cold-formed steel beam and the cable, and is subjected to combined axial compression and bending in two different loading stages. Furthermore, the cold-formed steel beam has an asymmetric cross-section profile, while, owing to its thin-walled geometry, it is highly susceptible to local instabilities, such as local and distortional buckling. The aforementioned features complicate the structural behaviour of the proposed prestressed cold-formed steel beams, thus, in the present chapter, the mechanical response of the proposed members during the different loading stages has been analysed in detail.

Sample finite element (FE) results for three reference models, namely the bare cold-formed steel beam, the non-prestressed beam but with the cable present and the fully prestressed beam, have been presented. The sample FE results were analysed in terms of the moment–deflection and moment–stress responses. Good agreement between the FE results and the corresponding analytical results and proposed failure criteria was demonstrated. The impact of the presence of the initial geometric imperfections on the ultimate capacity of the cold-formed steel member was also presented. The deformed shape and axial stress distribution at the critical cross-section of the beam at different loading stages were shown to be a valuable tool for understanding the mechanical behaviour and failure mechanism of prestressed cold-formed steel beams. Subsequently, it was verified that presence of lateral restraints at regular intervals along the member prevents any asymmetric bending effects and that the presence of the prestressed cable prevents lateral-torsional and distortional

buckling during the prestressing stage.

The analysis has demonstrated that the addition of the prestressed cable offers two principal benefits, both originating from the eccentric location at which the prestressed cable is located with respect to the strong geometric axis of the cold-formed steel beam. Firstly, the ultimate moment capacity of the cold-formed steel beam is enhanced. This benefit originates from the fact that, during prestressing, tensile stresses are induced within the top region of the beam. Since these initial stresses need to be overcome during the subsequent imposed loading stage before the detrimental compressive stresses develop leading to local/distortional buckling, greater loading is required to cause failure of the beam. Secondly, owing to the pre-camber induced during the prestressing stage and the contribution of the cable to the system bending stiffness, the overall vertical deflections of the member are reduced; hence, the serviceability performance of the beam is enhanced.

In the second section of the present chapter, the results from a set of parametric FE studies, in which the influence of the key controlling parameters has been investigated, were presented. A total number of 120 FE models have been utilised for this purpose. In each study, one key controlling parameter was varied while maintaining the remaining parameters constant. The effect of each parameter on the behaviour of the proposed beams was analysed in detail using the normalised moment–deflection and moment–stress responses obtained from the FE models, with the origin of the obtained benefits being demonstrated in each case.

Firstly, it was concluded that the higher the prestress level, the further the occurrence of local/distortional buckling is delayed and thus the greater the moment capacity enhancement. Secondly, it was demonstrated that an insufficiently large cable can compromise the capacity of the prestressed member and that, in the optimal scenario, the cold-formed steel beam and the cable fail simultaneously, thus utilising the capacity of both structural components in full. Furthermore, it has been shown that a greater enhancement in the ultimate moment capacity of the steel beams can be achieved with increasing section thickness. Finally, it was concluded that a well-proportioned cross-section can provide increased structural benefits and thus a more economical solution. In the case of the proposed beams, this can be achieved by shifting the centroid of the cold-formed steel beam

upwards. The above conclusions have been utilised to demonstrate that enhancements of up to 40% in the load-carrying capacity of cold-formed steel beams and reductions of approaching 60% in their overall deflections can be achieved. The parametric FE results are extended in Chapter 6 and are utilised for the purposes of assessing suitability of the developed design recommendations.

CHAPTER 6

DESIGN OF PRESTRESSED COLD-FORMED STEEL BEAMS

6.1 Introduction

Structural design rules for prestressed cold-formed steel beams, considering both the prestressing and imposed vertical loading stages, are presented in the current chapter. In the proposed approach, the cold-formed steel member is designed as a beam-column using linear interaction equations in conjunction with the Direct Strength Method (DSM), while the prestressed cable is designed by ensuring that its tensile capacity is not violated during the two loading stages. Essentially, in the design recommendations, the net axial force and net bending moment at the critical cross-section of the member are compared with the predicted load-carrying capacities of the two structural components of the system. This comparison has to be performed for both loading stages independently. Furthermore, to ensure that excessive vertical deflections of the member during service are limited, a serviceability check is also required.

In the present chapter, the failure criteria developed in Chapter 3 are also utilised to define the permissible design zone for the prestressed system, which can facilitate the selection of the initial prestressing force and imposed vertical loading for a given beam geometry and cable size. Subsequently, the suitability of the design recommendations is assessed

by comparing the parametric finite element (FE) results presented in Chapter 5 with the corresponding design predictions. In the case of the prestressed beams, this comparison is achieved using an axial force versus bending moment (P–M) interaction diagram. Furthermore, the reliability of the design recommendations is evaluated by means of statistical analysis and, finally, the implementation of the design recommendations is illustrated through a practical worked example.

In the current chapter, the principal characteristics, including the loading configurations, net actions and failure criteria, corresponding to the two loading stages are briefly revisited to facilitate the development of the design recommendations. The design recommendations for prestressed cold-formed steel beams and their assessment presented in this chapter has been published by Hadjipantelis *et al.* (2019a; 2018b).

6.2   Loading stages

The behaviour of prestressed cold-formed steel beams during the prestressing and imposed vertical loading stages (*i.e.* Stages I and II respectively) has been described analytically in Section 3.4.

6.2.1   Stage I: Prestressing

In Stage I, owing to the eccentricity e at which the prestressed cable is located relative to the strong geometric axis of the steel cross-section, the initial prestressing force P_i is transmitted into the cold-formed steel beam as eccentric compression. As illustrated in Figure 6.1(a), this is equivalent to pure axial compression plus negative (*i.e.* hogging) bending equal to $P_i e$ at the two beam ends. The axial force and bending moment diagrams at the end of Stage I are both uniform, as shown in Figures 6.1(b) and (c) respectively.

6.2.2   Stage II: Imposed vertical loading

In Stage II, as shown in Figure 6.2(a), a uniformly distributed load q is imposed along

Stage I: Prestressing

(a) Loading configuration

(b) Axial force diagram

(c) Bending moment diagram
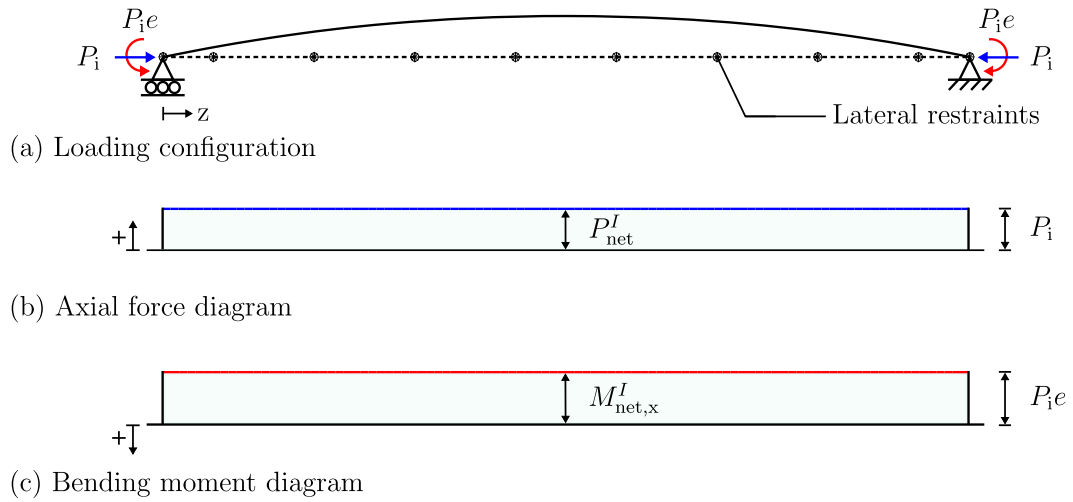
Figure 6.1: (a) Loading configuration alongside the (b) axial force and (c) bending moment diagrams for Stage I.

Stage II: Imposed vertical loading

(a) Loading configuration

(b) Axial force diagram

(c) Bending moment diagram
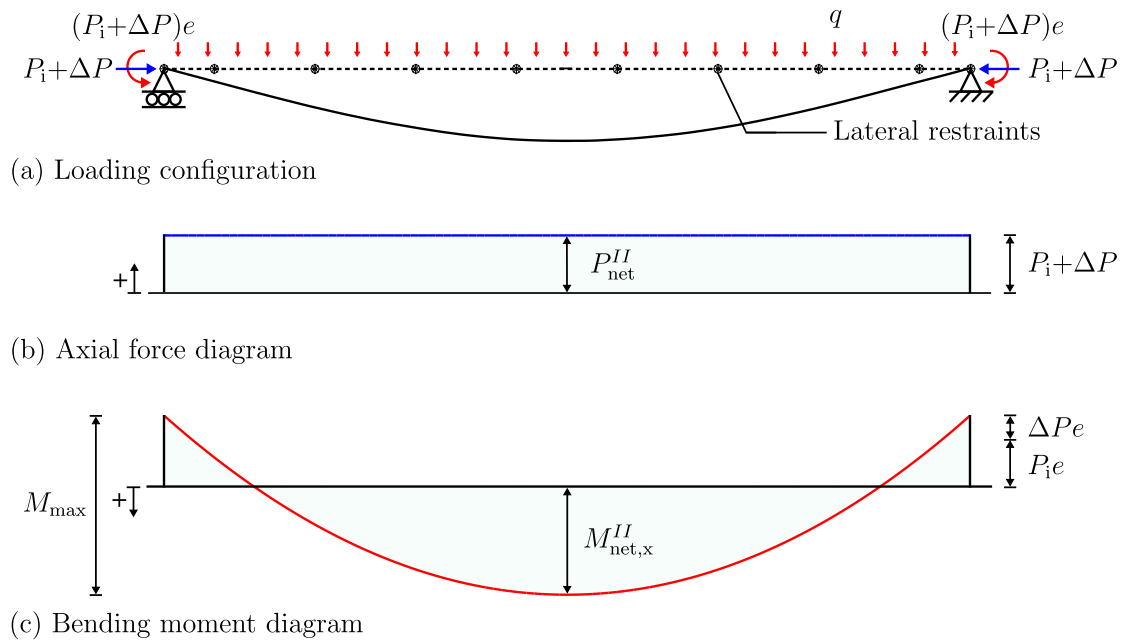
Figure 6.2: (a) Loading configuration alongside the (b) axial force and (c) bending moment diagrams for Stage II.

the member length L; hence, a maximum bending moment $M_{\max}=qL^2/8$ is applied at midspan. Note that, in the context of the present work, the term 'imposed vertical loading' refers to the total vertical load (*i.e.* dead load plus live load) carried by the member after the prestressing force has been applied.

As the member deflects downwards, the cable is stretched further since it is located within the tension zone of the cross-section; hence, an increase in the prestressing force ΔP is induced. As shown in Figure 6.2(a), ΔP has the same effect as P_{i} during Stage I; *i.e.* it induces additional axial compression and bending moment at the two beam ends. As discussed in Section 3.4.3, in the case of uniformly distributed loading, ΔP is directly proportional to $M_{\max}$ according to the following expression:

$$\Delta P = \frac{2M_{\max}e}{3\left[e^2 + \dfrac{E_{\mathrm{s}}I_{\mathrm{s}}}{E_{\mathrm{c}}A_{\mathrm{c}}} + r^2\right]}, \tag{6.1}$$

where all the symbols have been defined in previous chapters.

In Stage II, the axial force diagram remains uniform, as shown in Figure 6.2(b), with an increased magnitude compared to Stage I owing to ΔP. Concurrently, as shown in Figure 6.2(c), the negative bending due to the total prestressing force (*i.e.* $P_{\mathrm{i}}+\Delta P$) causes the partial cancellation of the applied bending moment.

6.3 Design recommendations

Prestressed cold-formed steel beams can be designed by adapting existing design methods, as discussed below. In the proposed design method, the load-carrying capacities of both structural components of the system, *i.e.* the cold-formed steel beam and prestressed cable, must be checked at each loading stage, *i.e.* prestressing and imposed vertical loading, independently. As outlined below, in the case of the cold-formed steel member, these checks are conducted by comparing the net axial force and bending moment at the critical cross-section, *i.e.* at midspan, with the axial and bending resistances respectively. In the case of the prestressed cable, the design checks are required to ensure that the net axial force does not exceed the design tensile resistance of the cable.

6.3.1 Net axial force and bending moment at midspan

As illustrated in Sections 6.2.1–6.2.2, prestressed cold-formed steel beams are subjected to combinations of axial forces and bending moments during both loading stages. The net axial force P_{net} and bending moment about the strong geometric axis $M_{\text{net,x}}$ at the critical cross-section in Stages I and II can be determined with reference to Figures 6.1–6.2 respectively. Typically, the critical cross-section is located at midspan, where, according to Figure 6.2(c), a net bending moment $M_{\text{net,x}}^{II}$ arises in Stage II. Nevertheless, it should be noted that the capacity of the end cross-sections must also be checked against the hogging moment $(P_{\text{i}} + \Delta P)e$.

Assuming that the critical cross-section is located at midspan, the expressions for P_{net} and $M_{\text{net,x}}$ are given in Table 6.1, where the superscripts (I or II) denote the corresponding loading stage.

Table 6.1: Net first-order axial force and bending moment at midspan in Stages I and II.

	Net axial force	Net bending moment
Stage I:	$P_{\text{net}}^{I} = P_{\text{i}}$	$M_{\text{net,x}}^{I} = P_{\text{net}}^{I} e$
Stage II:	$P_{\text{net}}^{II} = P_{\text{i}} + \Delta P$	$M_{\text{net,x}}^{II} = M_{\text{max}} - P_{\text{net}}^{II} e$

In the Load and Resistance Factor Design (LRFD) or limit states design concept, partial factors are applied to the loading and resistance to achieve the required level of structural reliability. Prestressing forces P_{net} are typically treated as permanent (dead) actions, with a load factor of 1.0 being adopted; this approach is followed in the case of prestressed concrete in both the American (ACI 318-14, 2014) and the European (EN 1990:2002+A1, 2005; EN 1992-1-1, 2004) design specifications. The applied vertical loading leading to the bending moment $M_{\text{net,x}}$, would typically comprise dead and imposed loading components, attracting different load factors from different Standards, *e.g.* a vertical load combination of 1.2D + 1.6L, where D is the dead load and L is the live load, is generally adopted in North America (ASCE/SEI 7-16, 2016), while 1.35D + 1.5L is generally adopted in Europe (EN 1990:2002+A1, 2005).

It should be noted that, since the proposed beams are simply-supported and would not form part of the global stability system of the structure, no global sway P–Δ effects need to be considered. Similarly, since the cable is located at a constant eccentricity from the centroid, the lever arm of the prestressing force remains constant as the member deforms and thus no P–δ effects are generated either. Hence, no frame or member second-order effects need to be considered herein. Also note that, as discussed in Section 3.3.3, the lateral restraints at the top and bottom parts of the cross-section prevent lateral-torsional buckling, while, as discussed in Section 5.2.7.1, they also confine bending about the strong geometric axis, thus preventing any asymmetric bending effects. Finally, as discussed in Section 3.3.4, prestress losses are not directly considered in the present work; hence, P_i is taken simply as the effective prestressing force, *i.e.* the force after account has been taken of the prestress losses.

6.3.2   Design of cold-formed steel beam

Since the cold-formed steel beam is subjected to combined axial loading and bending, it can be designed as a beam-column member. For this purpose, linear interaction equations in conjunction with the Direct Strength Method (DSM) (Schafer, 2008; Camotim et al., 2016) are utilised herein, as proposed in the North American Specification (AISI-S100-16) (2016).

As demonstrated in Section 3.5.1, to check the capacity of the cold-formed steel beam, Equation H1.2-1 in AISI-S100-16 (2016), which is used for the design of cold-formed steel beam-columns, can be adapted into the following form:

$$\frac{P_\mathrm{net}}{\phi_\mathrm{c} P_\mathrm{n}} + \frac{M_\mathrm{net,x}}{\phi_\mathrm{b} M_\mathrm{nx}} \leqslant 1.0, \tag{6.2}$$

where, in the numerators, P_net and $M_\mathrm{net,x}$ are the net first-order axial compressive force and bending moment at the critical cross-section respectively, as discussed in Section 6.3.1, based on factored loads. In the denominators, P_n is the nominal axial compressive resistance of the cold-formed steel beam and M_nx is the nominal bending resistance about its strong geometric axis. It should be noted that both P_n and M_nx are cross-section

resistances. This is because, as discussed in Section 3.3.3, the presence of the cable and the lateral restraints prevents global flexural and lateral-torsional buckling during both loading stages; hence, only local and distortional buckling need to be considered. The determination of P_n and M_{nx} using the DSM is discussed below. Lastly, ϕ_c and ϕ_b are the resistance factors for compression and bending respectively.

It is important to emphasise that Equation (6.2) needs to be employed for each loading stage independently, with the appropriate expressions for P_{net} and $M_{net,x}$, as given in Table 6.1, being used in each case. Furthermore, in Stages I and II, M_{nx} is equal to M_{nx}^- and M_{nx}^+ respectively, where the superscript (positive or negative) denotes the sign of the bending moment component.

As discussed in Section 2.3.6.4(b), the current AISI-S100-16 beam-column design approach can be overly conservative since a linear interaction between the pure axial and pure bending resistance end points is assumed. However, as demonstrated by Torabian *et al.* (2015; 2016c; 2016b; 2014a; 2016a), substantial increases in the load-carrying capacity of cold-formed steel beam-columns can be obtained by considering the actual stress distribution arising from the combined axial loading and bending. A new extension to the DSM has been proposed recently to account for these potential strength increases (Torabian and Schafer, 2018; Schafer, 2018).

6.3.2.1 Determination of axial compressive and bending resistances

In the present work, the DSM is employed to determine the nominal axial compressive P_n and bending M_{nx} resistances of the cold-formed steel member. The principal characteristics of the DSM have been described in Section 2.3.6, while the reason for using the DSM, instead of the more classical Effective Width Method (EWM), has been discussed in Sections 2.3.6.5 and 3.5.1.2.

In summary, the DSM allows the use of advanced elastic buckling analysis to determine the elastic critical buckling loads/moments of the cold-formed steel member, from which the resistances can be directly determined, as opposed to the lengthy and iterative calculations required in applying the EWM. As described in Sections 2.3.5.2, 2.3.5.3

and 3.5.1.2, in the present work, the elastic buckling analyses are performed using the CUFSM software (Li and Schafer, 2010b), while utilisation of the constrained Finite Strip Method (cFSM) (Li et al., 2014), following the "FSM@cFSM-L_{cr}" (Li and Schafer, 2010a) approach, is also required in certain cases. The obtained elastic critical buckling loads/moments are subsequently used to determine the values of P_n and M_{nx} through the DSM expressions, which are given in Sections 2.3.6.2 and 2.3.6.3 respectively. Implementation of the above processes is illustrated in Sections 6.5.4 and 6.5.5.

6.3.3 Design of prestressed cable

The prestressed cable is designed simply by checking that, in each stage, the prestressing force (*i.e.* the net axial force P_{net}, as given in Table 6.1) does not exceed the tensile capacity $P_{y,c}$, such that:

$$P_{net} \leqslant P_{y,c}, \tag{6.3}$$

$$\text{where} \quad P_{y,c} = \phi_t F_{y,c} A_c, \tag{6.4}$$

with ϕ_t being the resistance factor in tension and $F_{y,c}$ being the yield stress of the cable.

6.3.4 Failure criteria for design

The design approach presented above defines a set of two failure criteria for each loading stage as demonstrated in Sections 3.5.2 and 3.5.3. These criteria limit the applied loading in each stage according to the predicted load-carrying capacities of the cold-formed steel beam and cable, and can be employed to define the permissible design zone for the prestressed system, as shown below.

6.3.4.1 Cold-formed steel beam criteria

To obtain the failure criteria limiting the applied initial prestressing force P_i and bending moment at midspan M_{max} that can be carried by the cold-formed steel beam in Stages

I and II respectively, the expressions for P_{net} and $M_{\text{net,x}}$ from Table 6.1 can be substituted into Equation (6.2), which can then be rearranged for P_{i} and M_{max} accordingly, as discussed below.

For Stage I, the initial prestressing force is limited by:

$$P_{\text{i}} \leqslant \frac{1}{\dfrac{1}{\phi_{\text{c}} P_{\text{n}}} + \dfrac{e}{\phi_{\text{b}} M_{\text{nx}}^{-}}}, \tag{6.5}$$

where P_{n} is the nominal axial compressive resistance of the beam and M_{nx}^{-} is the nominal negative bending resistance of the beam. It is worth noting that, in the present work, as discussed in Section 3.5.2.1, assuming that a sufficiently large cable is used, Equation (6.5) defines the maximum allowable prestressing force P_{max} that the prestressed cold-formed steel beam can carry.

The failure criterion for Stage II also requires the use of the expression for ΔP (*i.e.* Equation (6.1)), such that the applied bending moment at midspan M_{max} is limited by:

$$M_{\text{max}} \leqslant \frac{\left[1.0 - \dfrac{P_{\text{i}}}{\phi_{\text{c}} P_{\text{n}}} + \dfrac{P_{\text{i}} e}{\phi_{\text{b}} M_{\text{nx}}^{+}} \right]}{\left[\dfrac{2e}{3\phi_{\text{c}} P_{\text{n}} C} + \dfrac{1}{\phi_{\text{b}} M_{\text{nx}}^{+}} - \dfrac{2e^2}{3\phi_{\text{b}} M_{\text{nx}}^{+} C} \right]}, \tag{6.6}$$

where M_{nx}^{+} is the nominal positive bending resistance of the beam and C, which is included in the denominator of Equation (6.1), is thus:

$$C = e^2 + \frac{E_{\text{s}} I_{\text{s}}}{E_{\text{c}} A_{\text{c}}} + r^2. \tag{6.7}$$

When yielding controls the behaviour, *i.e.* for cross-sections of sufficiently low slenderness, P_{n}, M_{nx}^{-} and M_{nx}^{+} in Equations (6.5) and (6.6) are simply substituted by the squash (yield) load P_{y} and yield moment M_{y} of the cross-section accordingly.

6.3.4.2 Cable criteria

The failure criteria for the prestressed cable are obtained by substituting the expressions for P_{net}^{I} and P_{net}^{II} from Table 6.1 into Equation (6.3) and rearranging for P_{i}. Hence, the

failure criterion for Stage I is:

$$P_{\mathrm{i}} \leqslant \phi_{\mathrm{t}} F_{\mathrm{y,c}} A_{\mathrm{c}}, \tag{6.8}$$

while, for Stage II, it becomes:

$$P_{\mathrm{i}} \leqslant \phi_{\mathrm{t}} F_{\mathrm{y,c}} A_{\mathrm{c}} - \frac{2e}{3C} M_{\mathrm{max}}. \tag{6.9}$$

6.3.5   Permissible design zone for prestressed system

The failure criteria presented above can be represented graphically in terms of P_{i} and M_{max}, as shown in Figure 6.3, where the inequalities given by Equations (6.5)–(6.6) and (6.8)–(6.9) are plotted for the case of the prestressed cold-formed steel beam with notation Pr3–t300–c58, as defined in Figure 5.18. Note that the same member is utilised in the worked example in Section 6.5. The structural component and loading stage associated with each criterion in Figure 6.3 are listed in Table 6.2, alongside the corresponding failure mode and limiting equation.

The area enclosed by the critical limiting criteria defines the permissible design zone, as demonstrated in Figure 6.3. Inspired by the so-called Magnel diagram, developed in the 1940s for the design of prestressed concrete beams (Magnel, 1948), the permissible design zone designates the acceptable combinations of P_{i} and M_{max} for a given beam geometry and cable size. Essentially, provided that the initial prestressing force applied in Stage I and the maximum bending moment imposed in Stage II are located within this zone, it is ensured that the load-carrying capacities of the selected cold-formed steel beam and cable will not be exceeded in either of the two loading stages. Note that the increase in the prestressing force due to the imposed vertical loading, *i.e.* ΔP, is accounted by the Stage II criteria, *i.e.* lines 'd'–'f'.

The critical limiting criteria depend on the section slenderness of the cold-formed steel beam and on the cable size. For instance, in the example shown in Figure 6.3, the limiting criterion due to cable yielding in Stage II, *i.e.* line 'f', can be converted into a non-critical limiting criterion by using a larger cable. In this manner, line 'f' can be shifted upwards, until the design zone is defined only by the lines 'a' and 'd', *i.e.* the buckling capacity
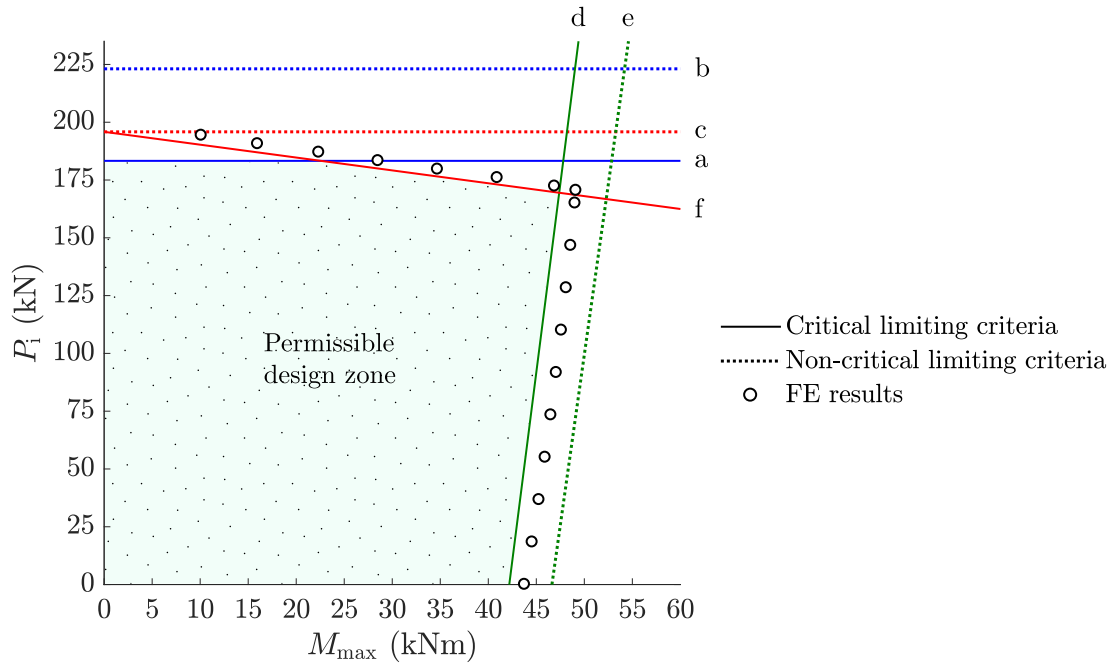
Figure 6.3:   Typical graphical representation of the failure criteria for the design of the prestressed system and illustration of the permissible design zone alongside a series of parametric FE results for different prestress levels; lines 'a'–'f' are defined in Table 6.2.

Table 6.2: Definition of the failure criteria lines in Figure 6.3.

Line:	Structural component:	Loading stage:	Failure mode:	Limiting equation:
a	Beam	Stage I	Buckling	Equation (6.5)
b	Beam	Stage I	Yielding	Equation (6.5)*
c	Cable	Stage I	Yielding	Equation (6.8)
d	Beam	Stage II	Buckling	Equation (6.6)
e	Beam	Stage II	Yielding	Equation (6.6)*
f	Cable	Stage II	Yielding	Equation (6.9)

* When yielding controls the behaviour, P_{n}, M_{nx}^{-} and M_{nx}^{+} in Equations (6.5) and (6.6) are replaced by the respective yield resistances.

of the cold-formed steel beam in Stages I and II respectively. In consequence, a higher initial prestressing force can be introduced to the system.

A parametric finite element (FE) study on the prestressed cold-formed steel beam utilised to obtain the permissible design zone shown in Figure 6.3 has been conducted. In this study, the level of prestress P_i was varied while maintaining the remaining parameters constant. The obtained results, corresponding to the ultimate capacity of the FE models, are plotted alongside the design zone in Figure 6.3. Note that the characteristics of the modelled prestressed member are provided in Section 6.5.2. In all cases, as indicated by the fact that the FE results are located outside the permissible design zone, the FE models achieved a higher ultimate capacity than the failure criteria predictions; hence, the design zone is on the safe-side.

6.3.6 Serviceability check

The purpose of the serviceability check is to limit excessive vertical deflections of the member during service, *i.e.* in Stage II. Note that in Stage I the beam is not under service loads, therefore the deflection check is not required.

The midspan vertical deflections at different loading stages are defined in Figure 6.4, where δ_{mid}^{I} is the pre-camber at the end of Stage I, δ_{mid}^{II} is the overall vertical deflection at the end of Stage II, δ_{perm} is the deflection due to permanent loads and δ_{serv} is the deflection due to service loads. The analytical expression for δ_{mid}^{II}, which has been developed in Section 3.4.2, is:

$$\delta_{\text{mid}}^{II} = \left(\frac{5L^2}{48E_s I_{\text{eff}}} \right) M_{\max} - \left(\frac{L^2}{8E_s I_{\text{eff}}} \right) (P_i + \Delta P)e, \tag{6.10}$$

where I_{eff} is the effective second moment of area of the cold-formed steel section, as defined below.

Figure 6.4: Midspan vertical deflection at different loading stages.

Since the initial prestressing force is treated as a permanent (dead) action herein, for the purposes of the serviceability check, only the live loading components of the bending moment induced in Stage II need to be considered; hence, δ_{serv} can be calculated using the following expression:

$$\delta_{\text{serv}} = \left(\frac{5L^2}{48E_{\text{s}}I_{\text{eff}}}\right) M_{\text{max}}^{\text{L}} - \left(\frac{L^2}{8E_{\text{s}}I_{\text{eff}}}\right) \Delta P^{\text{L}} e, \tag{6.11}$$

where $M_{\text{max}}^{\text{L}}$ is the sagging moment due to the live load and ΔP^{L} is the increase in the prestressing force, as defined by Equation (6.1), due to $M_{\text{max}}^{\text{L}}$.

According to Chapter L in AISI-S100-16 (2016), service load deflections in cold-formed steel beams may be determined by reducing the gross second moment of area, *i.e.* I_{s} herein, to an effective second moment of area I_{eff} using the following expression:

$$I_{\text{eff}} = I_{\text{s}} \left(\frac{M_{\text{d}}}{M_{\text{serv}}}\right) \leqslant I_{\text{s}}, \tag{6.12}$$

where M_{d} is the nominal bending resistance, but with the yield moment M_{y} in all the DSM expressions (see Section 6.3.2.1) replaced by the moment due to unfactored service loads M_{serv}, as given by:

$$M_{\text{serv}} = M_{\text{max}}^{\text{L}} - \Delta P^{\text{L}} e. \tag{6.13}$$

6.4 Assessment of design recommendations

The suitability of the developed design recommendations is assessed in the present section by comparing the results obtained using FE modelling with the corresponding design predictions. The FE modelling approach and its validation against the results from similar experimental studies has been presented in Chapter 4.

6.4.1 Parametric FE results versus design predictions

To assess the adequacy of the design recommendations, the parametric FE results presented in Section 5.3 are compared with the corresponding design predictions. The para-

metric studies investigated the effect of the prestress level, cable size, section slenderness and centroid location on the mechanical behaviour of prestressed cold-formed steel beams and, for this purpose, several combinations of cold-formed steel beam geometries, cable sizes and prestress levels were modelled.

6.4.1.1   Bare steel beams

As discussed in Sections 5.3.4 and 5.3.5, 54 different beam geometries have been modelled (Profiles 1–6, as defined in Section 5.3.1, for 9 different section thicknesses, as given in Table 5.4) to investigate the effect of the centroid location and section slenderness of the cold-formed steel beam. In the present sub-section, the ultimate capacities of the bare steel beam models M_{ult} are compared with the corresponding nominal DSM bending resistances under purely positive bending M_{nx}^+. According to the DSM procedure in AISI-S100-16 (2016), M_{nx}^+ is limited by the minimum of the bending resistances for yielding M_{y}, lateral-torsional M_{ne}^+, local M_{nl}^+ and distortional M_{nd}^+ buckling. Since, currently, the proposed beams are fully braced against lateral-torsional buckling, $M_{\text{nx}}^+=\min\{M_{\text{y}}, M_{\text{nl}}^+, M_{\text{nd}}^+\}$.

The design predictions for the bending resistances of the bare steel beams are represented by the DSM curve in Figure 6.5, where the 54 FE results are also plotted. Note that distortional buckling is the controlling buckling mode (*i.e.* $M_{\text{nd}}^+<M_{\text{nl}}^+$) for all the beam geometries studied in the present work; hence all the FE results (markers) in Figure 6.5 are given in terms of λ_{d} and M_{nd}^+. This is because the presence of the intermediate stiffeners within the web enhances the elastic critical local buckling strength of the cold-formed steel beam and thus distortional buckling becomes the critical mode. The fact that the majority of the results of the FE models (markers) are located above the DSM distortional curve indicates that, in general, the FE models were able to achieve greater ultimate moment capacities than the design predictions. Hence, overall, the DSM predictions are on the safe-side, with a mean value $(M_{\text{ult}}/M_{\text{nx}}^+)_{\text{mean}}$ of 1.08 and a coefficient of variation (c.o.v.) of 0.07. It should be noted that, as indicated in Figure 6.5, the DSM becomes increasingly conservative when the centroid of the cold-formed steel cross-section is shifted upwards. Note that, in Section 5.3.5, the centroid location, as represented by the normalised parameter y_{b}/h, where y_{b} is the distance of the centroid from the bottom
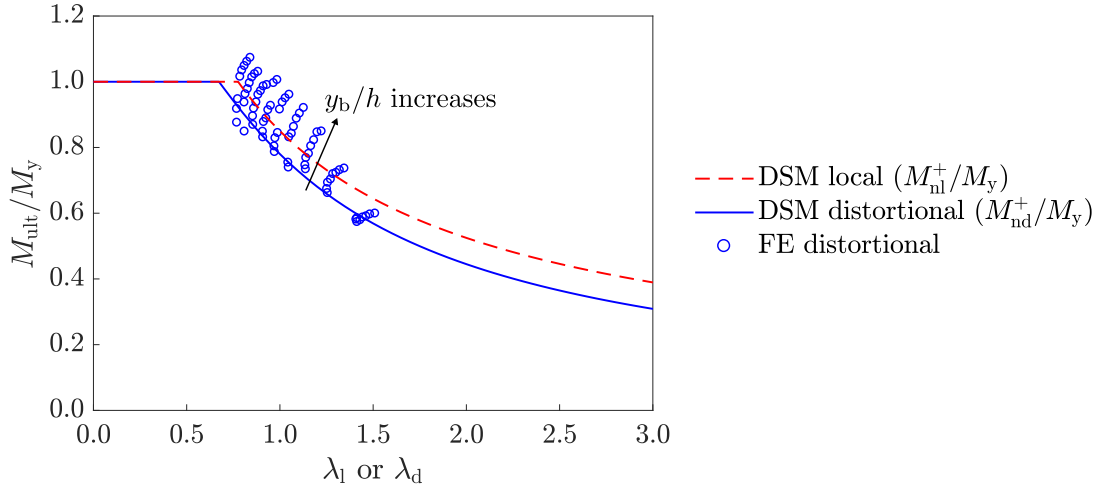
Figure 6.5: Comparison between the FE results of the bare steel beam models with the DSM moment capacity predictions.

extreme fibre and h is the total height of the cross-section, was varied by widening and narrowing the top and bottom flanges of the cold-formed steel beam respectively.

6.4.1.2 Prestressed beams

In the case of the prestressed beams, to compare the parametric FE results with the design predictions, an axial force versus bending moment (P–M) interaction diagram is employed. The main features of the P–M diagram, as demonstrated in Figure 6.6, are the following:

(i) The vertical and horizontal axes represent the net prestressing P_{net} and bending moment $M_{\mathrm{net,x}}$ components of the applied loading, as defined in Table 6.1, respectively.

(ii) The axial compressive (*i.e.* P_{n}) and bending (*i.e.* M_{nx}^{-} and M_{nx}^{+}) resistances of the cold-formed steel beam act as anchor points for the design envelope, which represents graphically the design expression for the cold-formed steel beam, *i.e.* Equation (6.2).

(iii) The equilibrium path of the FE model is plotted in terms of P_{net} and $M_{\mathrm{net,x}}$, with Stages I and II being indicated by the $P_{\mathrm{I}}-M_{\mathrm{I}}$ and $P_{\mathrm{II}}-M_{\mathrm{II}}$ coordinate systems respectively.

(iv) When $P_{\mathrm{i}}/P_{\mathrm{max}}=1.0$, the Stage II origin is located on the left side of the design envelope since $P_{\mathrm{max}}=f(P_{\mathrm{n}}, M_{\mathrm{nx}}^{-})$.
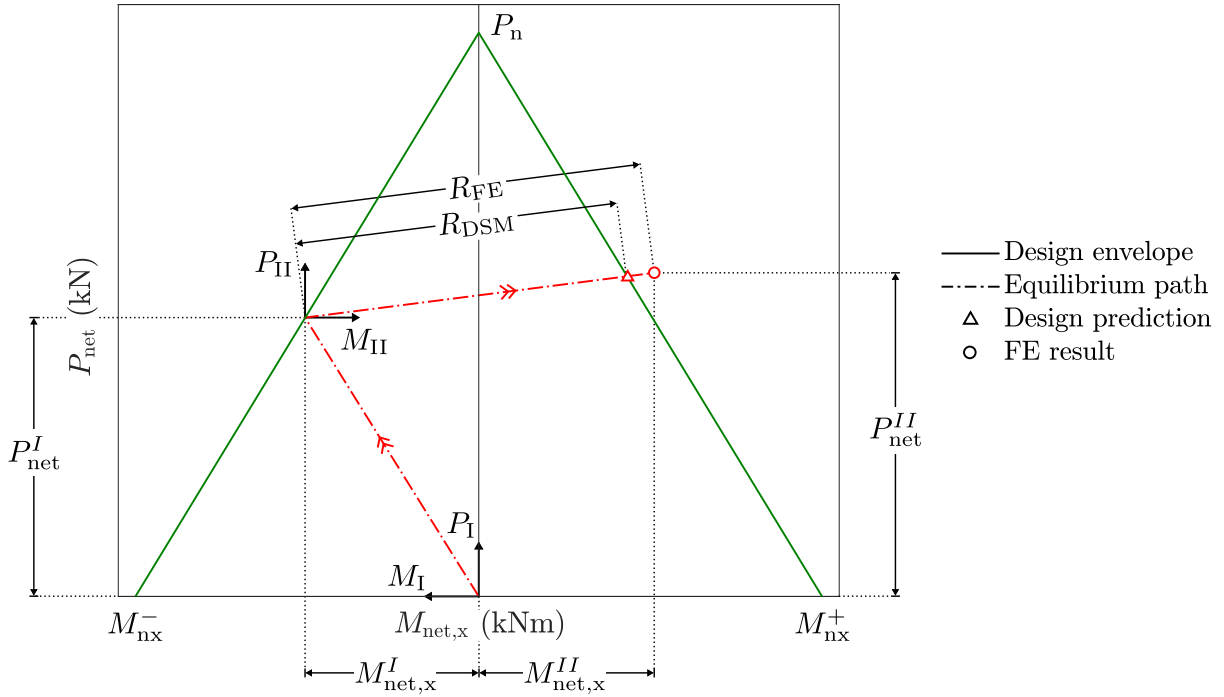
Figure 6.6: Axial force versus bending moment (P–M) interaction diagram for the design of prestressed cold-formed steel beams.

(v) The FE result corresponds to the ultimate point in the analysis.

(vi) The design prediction is calculated with respect to the Stage II origin; for this purpose, Equation (6.6) is used to determine the allowable value of M_{max} for the applied initial prestressing force P_i.

(vii) The accuracy of the design prediction is evaluated using the ratio R_{FE}/R_{DSM}, where R_{FE} and R_{DSM} are the distances of the FE and design points respectively from the Stage II origin. The fact that the FE result shown in Figure 6.6 is located outside the design envelope indicates that the FE model achieved a higher ultimate capacity than the design prediction; hence, when $R_{FE}/R_{DSM} > 1.0$, the design prediction is on the safe-side and *vice versa*.

In the parametric studies, 27 different combinations of beam geometries (Profiles 2, 4 and 6, as defined in Section 5.3.1, for 9 different section thicknesses, as given in Table 5.4) and cable sizes (according to $A_c/A_s = 10.5\%$) were subjected to 11 levels of prestress corresponding to:

$$P_i/P_{max} = \{0.0, 0.2, 0.4, 0.6, 0.8, 0.9, 1.0, 1.1, 1.2, 1.3, 1.4\}. \tag{6.14}$$
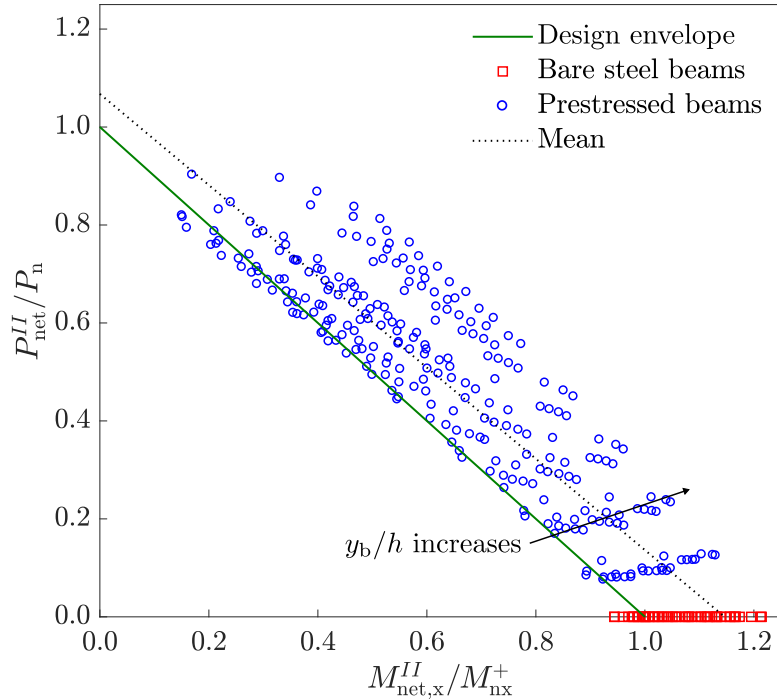
Figure 6.7: Normalised P–M diagram comparing the parametric FE results (markers) with the design recommendations (solid line). In 31 cases, the cable failed before the ultimate capacity of the cold-formed steel beam was reached, thus these results are not shown.

Note that, as discussed in Section 5.3.2, the beams have been subjected to prestressing forces larger than P_{max} to investigate whether higher benefits can be obtained when $P_i/P_{max}>1.0$.

The P–M diagram introduced in Figure 6.6 is utilised to compare the obtained parametric FE results with the design predictions. As demonstrated in Figure 6.7, for illustration purposes, only the right hand side of the P–M diagram is shown. Furthermore, the vertical and horizontal axes are normalised by the axial and bending resistances of the beam respectively, such that each axis corresponds to one of the components of Equation (6.2); in this manner, the results from several models can be plotted on a single P–M diagram. Generally, as indicated by the fact that the majority of the FE results are located outside the design envelope, it is observed that the design recommendations are on the safe-side. As demonstrated in Figure 6.6, the accuracy of the design predictions can be represented by the ratio R_{FE}/R_{DSM}; in the case of the 297 prestressed beams modelled in the parametric studies, a mean value of 1.13 and a c.o.v. value of 0.09 is achieved.

It should be noted that, as indicated in Figure 6.7, the design predictions become increasingly conservative as the centroid of the cross-section is shifted upwards, *i.e.* as y_b/h

increases. This is attributed to the fact that the conservatism of the DSM predictions for the bending resistance of bare steel beams with high centroid locations, as discussed in Section 6.4.1.1, is carried forward into the interaction equation, *i.e.* Equation (6.2), governing the design of the prestressed beams.

6.4.2 Reliability analysis

The reliability of the design recommendations is evaluated by means of statistical analysis in the present sub-section. This is achieved by comparing the two sets of parametric FE results (one set for bare steel beams and the other for prestressed beams) with the capacity predictions obtained using the proposed design method. The reliability analysis is conducted following the procedure outlined in Section K2 in AISI-S100-16 (2016) and according to the LRFD method, which is based on the following expression:

$$\Sigma \gamma_i Q_i \leqslant \phi R_n, \tag{6.15}$$

where the left hand side represents the required strength of the structural member based on the most critical load combination, while the right hand side is the predicted available resistance; Q_i are the load effects, *i.e.* the forces on the cross-section determined by structural analysis, and R_n is the predicted nominal resistance, *i.e.* the strength of the member for a given limit state; γ_i and ϕ are the load and resistance factors respectively, accounting for uncertainties and variabilities in Q_i and R_n.

To obtain a relative measure of the design safety level, the reliability index β is employed, which, as demonstrated in Figure 6.8, essentially accounts for the probability of violating Equation (6.15) and can be calculated using:

$$\beta = \frac{\ln(R_m/Q_m)}{\sqrt{V_R^2 + V_Q^2}}, \tag{6.16}$$

where Q_m and R_m are the mean values of the load effects and nominal resistance respectively, with V_Q and V_R being the respective coefficients of variation. The mean nominal
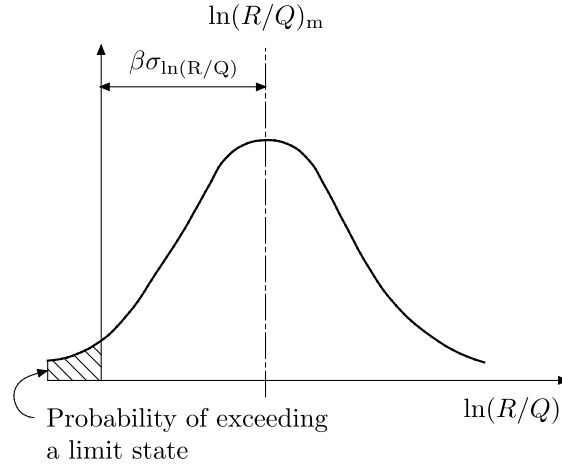
Figure 6.8: Definition of the reliability index β; σ is the standard deviation.

resistance R_m can be calculated using the following formula:

$$\frac{R_\mathrm{m}}{R_\mathrm{n}} = M_\mathrm{m} F_\mathrm{m} P_\mathrm{m}, \tag{6.17}$$

where M_m, F_m are the mean values of the material and fabrication factors respectively, while P_m is the mean ratio of the experimental/numerical ultimate loads to the predicted nominal resistances. The coefficient of variation of the nominal resistance V_R can be determined using:

$$V_\mathrm{R} = \sqrt{V_\mathrm{M}^2 + V_\mathrm{F}^2 + C_\mathrm{P} V_\mathrm{P}^2}, \tag{6.18}$$

where V_M, V_F are the coefficients of variation of the material and fabrication factors respectively. Furthermore, V_P is the coefficient of variation of P_m, while C_P is the correction factor for a given sample size (*i.e.* number of tests/models) n, as given by:

$$C_\mathrm{P} = \frac{n^2 - 1}{n^2 - 3n} = \frac{(n+1)(n-1)}{n(n-3)}. \tag{6.19}$$

Re-arranging Equation (6.15) and accounting for the appropriate load intensities and loading combinations, an expression relating R_m and Q_m can be obtained:

$$\frac{R_\mathrm{m}}{Q_\mathrm{m}} = \frac{C_\phi}{\phi} \left(\frac{R_\mathrm{m}}{R_\mathrm{n}} \right), \tag{6.20}$$

where C_ϕ is the calibration coefficient that is dependent on the critical loading combination and the dead-to-live load ratio D/L (AISI S100-16, 2016). Assuming $1.2D + 1.6L$

and D/L=1/5, it can be shown that C_ϕ is equal to 1.521 (Hsiao et al., 1990). Furthermore, for the aforementioned loading conditions, V_Q can be taken to be equal to 0.21 (AISI S100-16, 2016). For other loading conditions, Meimand and Schafer (2014) have provided revised values for C_ϕ and V_Q.

Combining Equations (6.17), (6.18) and (6.20) with Equation (6.16), an expression relating the target reliability index β_0 to the resistance factor ϕ can be obtained:

$$\phi = C_\phi M_m F_m P_m e^{-\beta_0 \sqrt{V_M^2 + V_F^2 + C_P V_P^2 + V_Q^2}}. \tag{6.21}$$

The reliability analysis approach presented above has been utilised to assess the suitability of the design recommendations developed for prestressed cold-formed steel beams. The key adopted parameters include M_m=1.05, V_M=0.10, F_m=1.00 and V_F=0.05, as specified in Table K2.1.1-1 in AISI S100-16 (2016) for cold-formed steel structural members subjected to combined axial loading and bending. Furthermore, as discussed above, the values of C_ϕ=1.521 and V_Q=0.21 have been utilised. In the present study, P_m is the mean ratio of the ultimate capacity achieved by the FE models (for a given initial prestressing force, if prestressing is applied) over the corresponding design prediction; *i.e.* $(M_{ult}/M_{nx}^+)_{mean}$ for the bare steel beams and $(R_{FE}/R_{DSM})_{mean}$ for the prestressed beams. Finally, V_P is the coefficient of variation of the aforementioned FE-to-predicted ratios.

In the present work, a target reliability index β_0=2.5 is adopted, as recommended in AISI S100-16 (2016) for cold-formed steel structural members subjected to gravity loads. Furthermore, since all the 54 beam geometries modelled in the current work satisfy the dimensional limitations outlined in Table B4.1-1 of AISI-S100-16 (2016), the modelled cross-sections can be considered as "prequalified"; hence, the compression ϕ_c=0.85 and bending ϕ_b=0.90 resistance factors, as given in Chapters E and F in AISI-S100-16 (2016) respectively, are adopted.

As performed in similar studies (Bock et al., 2015; Afshan et al., 2019), to account for the fact that the reliability analysis is based on numerical results, an additional term $C_{FEM} V_{FEM}^2$ was included in the determination of the combined coefficient of variation of the required resistance V_R; *i.e.* the square root term in Equation (6.21). The V_{FEM} term

Table 6.3: Reliability analysis results.

Dataset	n	P_{m}	V_{P}	$\beta(\phi{=}0.85)$	$\beta(\phi{=}0.90)$
Bare steel beams ($M_{\mathrm{ult}}/M_{\mathrm{nx}}^{+}$)	54	1.08	0.07	–	2.51
Prestressed beams ($R_{\mathrm{FE}}/R_{\mathrm{DSM}}$)	297	1.13	0.09	2.94	2.71

describes the variability in the validation results, which are reported in Sections 4.3.2.2–4.3.2.4, and compare the obtained FE results with available experimental results. This comparison was performed only for the bare steel beams, with a V_{FEM} value of 0.07 being obtained, as reported in Section 4.3.2.4. As discussed above, C_{FEM} is the correction factor for the sample size n, which in the case of the validation results is equal to 20.

The reliability analysis results are presented in Table 6.3, where the reliability index β is provided for both of the resistance factors ϕ_{c} and ϕ_{b}; this is because a resistance factor for cold-formed steel beam-columns is not available in AISI S100-16 (Torabian et al., 2016c). Note that the resistance factor for compression is not applicable in the case of the bare steel beams since they are subjected to purely positive bending. As shown in Table 6.3, for all cases, the obtained β is greater than the target reliability index of 2.5; this demonstrates the reliability of the proposed design method. Hence, it may be concluded that the utilisation of the $\phi_{\mathrm{c}}{=}0.85$ and $\phi_{\mathrm{b}}{=}0.90$ factors recommended in AISI S100-16 (2016) in the proposed design method is suitable.

6.5 Implementation of design recommendations

The design recommendations outlined in Section 6.3 are implemented in the present section through a detailed worked example.

6.5.1 Problem statement

A thin slab flooring system comprises a 6.2 metre long prestressed cold-formed steel beams at 600 mm spacings. The beams are simply-supported and subjected to the loading configuration shown in Figure 6.9(b). In Stage I, an initial prestressing force P_{i}

of 70 kN is applied using a cable of radius 5.8 mm. In Stage II, the flooring system is subjected to a dead load of 1.6 kN/m^2 and a live load of 4.2 kN/m^2, which is equivalent to a uniformly distributed load along the beams comprising a dead load q_D of 1.0 kN/m and a live load q_L of 2.5 kN/m.
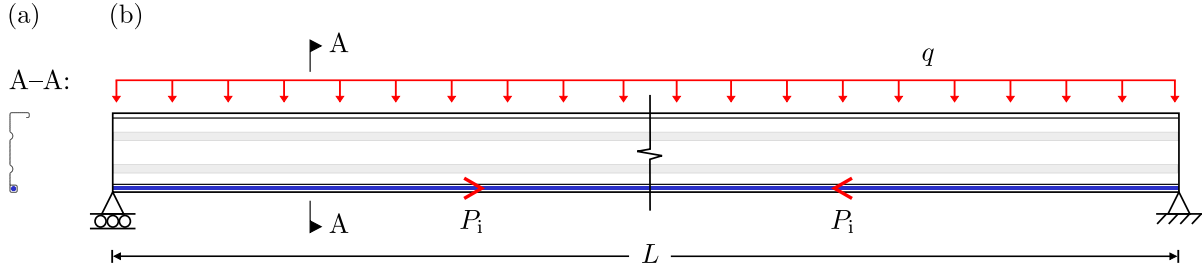
Figure 6.9: (a) Cross-section profile and (b) loading configuration of the prestressed cold-formed steel beam in the worked example.

The dimensions of the cross-section profile of the cold-formed steel beam and cable, alongside the relevant geometric and material properties, are given below. The beam is fully restrained against lateral-torsional buckling due to the presence of the flooring and sag bars at regular intervals along the top and bottom parts of the beam respectively. Furthermore, the presence of the cable restrains global flexural buckling during both loading stages and distortional buckling due to negative bending in Stage I. It is assumed that no loss of prestress takes place.

Evaluate the load-carrying capacity and serviceability performance of the prestressed cold-formed steel beam in Stages I and II. The deflection limits of $L/360$ and $L/240$ are to be assumed for the service load and overall vertical deflections respectively.

6.5.2 Member characteristics

The cross-section profile of the prestressed member is shown in Figure 6.10, its dimensions are listed in Table 6.4 and its geometric and material properties in Table 6.5. Note that the section slenderness of the cold-formed steel beam λ is equal to the maximum of the local $\lambda_l = \sqrt{M_{ne}^+/M_{crl}^+}$ and distortional $\lambda_d = \sqrt{M_y/M_{crd}^+}$ slenderness values for positive bending, where M_{crl}^+ and M_{crd}^+ are the respective elastic critical buckling moments, as determined by applying a purely positive bending stress distribution in CUFSM; M_{ne}^+ and

M_y are the nominal bending resistance for lateral-torsional buckling and the yield moment respectively. The maximum allowable prestressing force P_{max}, defined in Section 6.3.4.1, for the prestressed member is equal to 183 kN; the contribution of the cable to the system can be represented by the A_c/A_s ratio, which is equal to 7.8% in the present example.
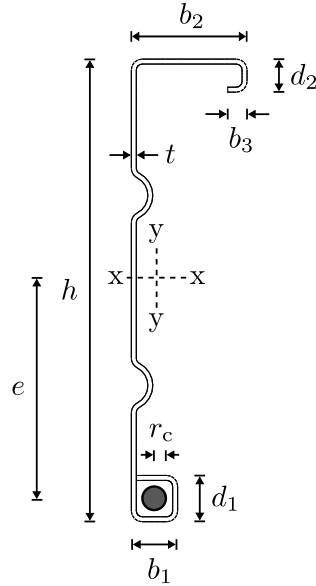
Figure 6.10: Cross-section of the prestressed member; the dimensions are given in Table 6.4.

Table 6.4: Dimensions of the prestressed member; the cross-section is shown in Figure 6.10.

$h = 280$ mm	$b_1 = 28$ mm	$t = 3.00$ mm
$d_1 = 28$ mm	$b_2 = 70$ mm	$e = 133$ mm
$d_2 = 20$ mm	$b_3 = 12$ mm	$r_c = 5.8$ mm

Table 6.5: Geometric and material properties of the prestressed member; P_y and M_y are the squash load and yield moment of the cold-formed steel cross-section respectively.

$E_s = 2.01{\times}10^5$ N/mm^2	$\lambda_d = 0.776$	$E_c = 1.95{\times}10^5$ N/mm^2
$A_s = 1345$ mm^2	$M_y = 44.9$ kNm	$A_c = 105$ mm^2
$I_s = 1.35{\times}10^7$ mm^4	$P_y = 660.3$ kN	$F_{y,c} = 1860$ N/mm^2

6.5.3 Summary of design process

Step 1: Determine the elastic critical local and distortional buckling loads/moments of the cold-formed steel beam when subjected to: (i) purely positive bending, (ii) purely negative bending and (iii) pure compression (see Section 6.3.2.1).

Step 2: Determine the positive bending, negative bending and axial compressive resistances of the cold-formed steel beam using the DSM (see Section 6.3.2.1).

Step 3: Determine the factored net axial force and bending moment at the critical cross-section of the prestressed member for Stages I and II (see Section 6.3.1).

Step 4: Design the prestressed system for Stage I; *i.e.* check the load-carrying capacity of the cold-formed steel beam (see Section 6.3.2) and the tensile capacity of the cable (see Section 6.3.3) under the loading configuration of Stage I.

Step 5: Repeat Step 4, but for the Stage II loading.

Step 6: Check that the vertical deflections satisfy the serviceability criteria.

6.5.4 Determination of critical buckling loads and moments

The local (P_{crl} and M_{crl}) and distortional (P_{crd} and M_{crd}) critical buckling loads and moments of the steel beam are listed in Table 6.6. As shown in Figure 6.11, the critical loads and moments correspond to the minimum points of the signature curves, which are obtained using CUFSM, as discussed in Section 6.3.2.1, by applying purely positive bending, purely negative bending and axial compressive stress distributions accordingly.

Table 6.6: Elastic critical buckling loads and moments as functions of the squash load P_{y} and the yield moment M_{y} respectively; '+' and '−' indicate positive and negative bending respectively.

Positive bending	Negative bending	Axial compression
$M_{\mathrm{crl}}^{+} = 3.99\ M_{\mathrm{y}}$	$M_{\mathrm{crl}}^{-} = 14.50\ M_{\mathrm{y}}$	$P_{\mathrm{crl}} = 2.44\ P_{\mathrm{y}}$
$M_{\mathrm{crd}}^{+} = 1.66\ M_{\mathrm{y}}$	$M_{\mathrm{crd}}^{-} = 2.66\ M_{\mathrm{y}}$	$P_{\mathrm{crd}} = 0.62\ P_{\mathrm{y}}$

(a) Positive bending

(b) Negative bending
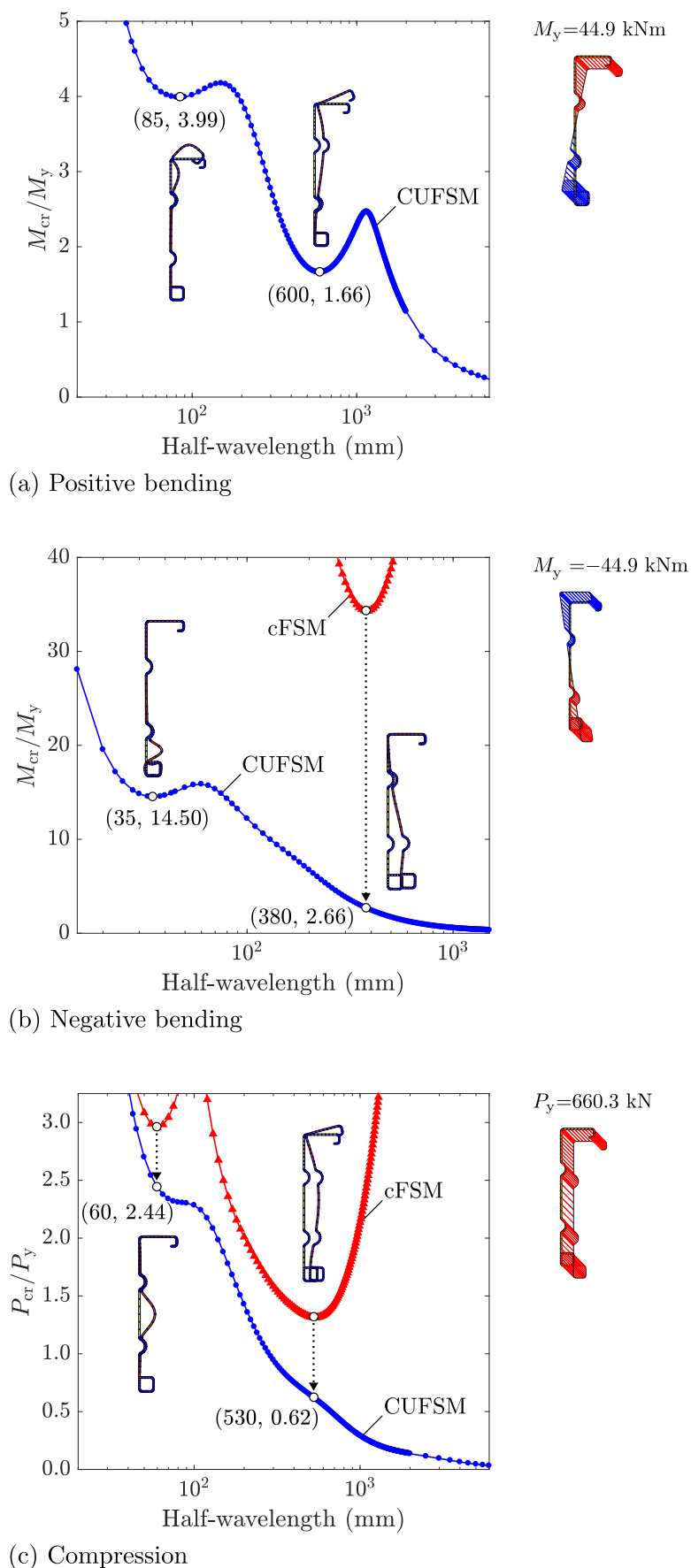
(c) Compression

Figure 6.11: Signature curves corresponding to (a) purely positive bending, (b) purely negative bending and (c) axial compression.

6.5.5 Determination of bending and compressive resistances

To determine the bending M_{nx} and compressive P_{n} resistances of the cold-formed steel beam, the DSM equations given in Sections 2.3.6.3 and 2.3.6.2 are employed respectively. The DSM expressions are functions of the elastic critical buckling loads/moments of the beam, as determined above.

6.5.5.1 Positive bending resistance

The positive bending resistance M_{nx}^{+} of the cold-formed steel beam is equal to the minimum resistance to yielding M_{y}, lateral-torsional M_{ne}^{+}, local M_{nl}^{+} and distortional M_{nd}^{+} buckling.

(i) Yielding and global (lateral-torsional) buckling

Since the beam is fully braced against lateral-torsional buckling:

$$M_{\mathrm{ne}}^{+} = M_{\mathrm{y}} = 44.9 \text{ kNm},$$

where $M_{\mathrm{y}} = S_{\mathrm{fy}} F_{\mathrm{y,s}}$ is the yield moment and S_{fy} is the elastic section modulus relative to the extreme fibre in first yield.

(ii) Local buckling interacting with yielding and global buckling

$$\lambda_{\mathrm{l}} = \sqrt{M_{\mathrm{ne}}^{+}/M_{\mathrm{crl}}^{+}} = 0.501.$$

$$\text{For} \quad \lambda_{\mathrm{l}} \leqslant 0.776, \quad M_{\mathrm{nl}}^{+} = M_{\mathrm{ne}}^{+},$$

$$\text{for} \quad \lambda_{\mathrm{l}} > 0.776, \quad M_{\mathrm{nl}}^{+} = \left[1 - 0.15 \left(\frac{M_{\mathrm{crl}}^{+}}{M_{\mathrm{ne}}^{+}} \right)^{0.4} \right] \left(\frac{M_{\mathrm{crl}}^{+}}{M_{\mathrm{ne}}^{+}} \right)^{0.4} M_{\mathrm{ne}}^{+},$$

$$\text{thus} \quad M_{\mathrm{nl}}^{+} = M_{\mathrm{ne}}^{+} = 44.9 \text{ kNm}.$$

(iii) Distortional buckling

$$\lambda_{\mathrm{d}} = \sqrt{M_{\mathrm{y}}/M_{\mathrm{crd}}^{+}} = 0.776.$$

For $\quad \lambda_\mathrm{d} \leqslant 0.673, \quad M_\mathrm{nd}^+ = M_\mathrm{y},$

for $\quad \lambda_\mathrm{d} > 0.673, \quad M_\mathrm{nd}^+ = \left[1 - 0.22 \left(\dfrac{M_\mathrm{crd}^+}{M_\mathrm{y}}\right)^{0.5}\right] \left(\dfrac{M_\mathrm{crd}^+}{M_\mathrm{y}}\right)^{0.5} M_\mathrm{y},$

thus $\quad M_\mathrm{nd}^+ = (1 - 0.22 \times 1.66^{0.5}) \times 1.66^{0.5} \times 44.9 = 41.5 \ \mathrm{kNm}.$

(iv) Positive bending resistance

$$M_\mathrm{nx}^+ = \min\{M_\mathrm{y}, M_\mathrm{ne}^+, M_\mathrm{nl}^+, M_\mathrm{nd}^+\} = 41.5 \ \mathrm{kNm}.$$

6.5.5.2 Negative bending resistance

The negative bending resistance M_nx^- of the cold-formed steel beam is equal to the minimum resistance to yielding M_y, lateral-torsional M_ne^-, local M_nl^- and distortional M_nd^- buckling. The DSM expressions are the same as in Section 6.5.5.1.

(i) Yielding and global (lateral-torsional) buckling

Since the beam is fully braced against lateral-torsional buckling:

$$M_\mathrm{ne}^- = M_\mathrm{y} = 44.9 \ \mathrm{kNm}.$$

(ii) Local buckling interacting with yielding and global buckling

$$\lambda_\mathrm{l} = \sqrt{M_\mathrm{ne}^-/M_\mathrm{crl}^-} = 0.263,$$

thus $\quad M_\mathrm{nl}^- = M_\mathrm{ne}^- = 44.9 \ \mathrm{kNm}.$

(iii) Distortional buckling

Since the presence of the cable restrains distortional buckling due to negative bending:

$$M_\mathrm{nd}^- = M_\mathrm{ne}^- = 44.9 \ \mathrm{kNm}.$$

(iv) Negative bending resistance

$$M_\mathrm{nx}^- = \min\{M_\mathrm{y}, M_\mathrm{ne}^-, M_\mathrm{nl}^-, M_\mathrm{nd}^-\} = 44.9 \ \mathrm{kNm}.$$

6.5.5.3 Axial compressive resistance

The axial compressive resistance P_n of the cold-formed steel beam is equal to the minimum resistance to yielding P_y, global flexural P_{ne}, local P_{nl} and distortional P_{nd} buckling.

(i) Yielding and global (flexural) buckling

Since the presence of the cable restrains the global flexural buckling mode:

$$P_{ne} = P_y = 660.3 \text{ kN},$$

with $P_y = A_s F_{y,s}$ being the squash load.

(ii) Local buckling interacting with yielding and global buckling

$$\lambda_l = \sqrt{P_{ne}/P_{crl}} = 0.640.$$

For $\quad \lambda_l \leqslant 0.776, \quad P_{nl} = P_{ne},$

for $\quad \lambda_l > 0.776, \quad P_{nl} = \left[1 - 0.15\left(\dfrac{P_{crl}}{P_{ne}}\right)^{0.4}\right]\left(\dfrac{P_{crl}}{P_{ne}}\right)^{0.4} P_{ne},$

thus $\quad P_{nl} = P_{ne} = 660.3 \text{ kN}.$

(iii) Distortional buckling

$$\lambda_d = \sqrt{P_y/P_{crd}} = 1.270.$$

For $\quad \lambda_d \leqslant 0.561, \quad P_{nd} = P_y,$

for $\quad \lambda_d > 0.561, \quad P_{nd} = \left[1 - 0.25\left(\dfrac{P_{crd}}{P_y}\right)^{0.6}\right]\left(\dfrac{P_{crd}}{P_y}\right)^{0.6} P_y,$

thus $\quad P_{nd} = (1 - 0.25 \times 0.62^{0.6}) \times 0.62^{0.6} \times 660.3 = 402.6 \text{ kN}.$

(iv) Compressive resistance

$$P_n = \min\{P_y, P_{ne}, P_{nl}, P_{nd}\} = 402.6 \text{ kN}.$$

6.5.6 Determination of net axial force and bending moment

The expressions for the net axial force P_{net} and bending moment $M_{net,x}$ at the critical cross-section during Stages I and II are reported in Table 6.1. As discussed in Section 6.3.1, the prestressing force is taken as a dead load, with a load factor of 1.0 being used, while the load combination of $1.2D + 1.6L$ is used for the applied bending moment.

6.5.6.1 Stage I: Prestressing

The initial prestressing force P_i is considered as a dead load herein, thus:

$$P_{net}^{I} = 1.0P_i = 1.0 \times 70 = 70.0 \text{ kN,}$$

$$M_{net,x}^{I} = 1.0P_i e = 1.0 \times 70 \times 0.133 = 9.3 \text{ kNm.}$$

6.5.6.2 Stage II: Imposed vertical loading

The bending moment at midspan due to the unfactored dead load M_{max}^{D} is:

$$M_{max}^{D} = 1.0 \times 6.2^2/8 = 4.8 \text{ kNm,}$$

while the bending moment due to the unfactored live load M_{max}^{L} is:

$$M_{max}^{L} = 2.5 \times 6.2^2/8 = 12.0 \text{ kNm.}$$

The dead load ΔP^{D} and live load ΔP^{L} components of the increase in the prestressing force, as defined by Equation (6.1), are a function of M_{max}^{D} and M_{max}^{L} respectively, thus:

$$\Delta P^{D} = \frac{2M_{max}^{D}e}{3\left[e^2 + \dfrac{E_s I_s}{E_c A_c} + r^2\right]} = 2.7 \text{ kN,}$$

$$\Delta P^{L} = \frac{2M_{max}^{L}e}{3\left[e^2 + \dfrac{E_s I_s}{E_c A_c} + r^2\right]} = 6.6 \text{ kN.}$$

Assuming that the critical cross-section is located at midspan, the net factored axial force P_{net}^{II} and bending moment $M_{\text{net,x}}^{II}$ are calculated as follows:

$$P_{\text{net}}^{II} = 1.0P_{\text{i}} + 1.2\Delta P^{\text{D}} + 1.6\Delta P^{\text{L}}$$

$$= 1.0 \times 70 + 1.2 \times 2.7 + 1.6 \times 6.6$$

$$= 83.8 \text{ kN},$$

$$M_{\text{net,x}}^{II} = (1.2M_{\text{max}}^{\text{D}} + 1.6M_{\text{max}}^{\text{L}}) - P_{\text{net}}^{II}e$$

$$= (1.2 \times 4.8 + 1.6 \times 12.0) - 83.3 \times 0.133 = 13.9 \text{ kNm.}$$

To verify the assumption that the critical cross-section is located at midspan, the net factored (hogging) bending moment at the end sections in Stage II, $M_{\text{end,x}}^{II}$, is calculated by utilising Figure 6.2(c), thus:

$$M_{\text{end,x}}^{II} = P_{\text{net}}^{II}e = 83.8 \times 0.133 = 11.1 \text{ kNm.}$$

Given that $M_{\text{end,x}}^{II} < M_{\text{net,x}}^{II}$ and $M_{\text{nx}}^{-} > M_{\text{nx}}^{+}$, the assumption that the critical cross-section is located at midspan is verified.

6.5.7 Design of cold-formed steel beam

To check the load-carrying capacity of the cold-formed steel beam in Stages I and II, Equation (3.17) is employed. For this purpose, the net axial force and bending moment, as determined in Section 6.5.6, are compared with their respective resistances, as calculated in Section 6.5.5. As discussed in Section 6.4.2, since the cross-sectional geometry of the cold-formed steel beam satisfies the dimensional limitations of (AISI S100-16, 2016), *i.e.* the cross-section is prequalified, the compression ϕ_{c} and bending ϕ_{b} resistance factors are taken to be 0.85 and 0.90 respectively.

6.5.7.1   Capacity check for Stage I

In Stage I, $P_{\text{net}} = P^I_{\text{net}}$, $M_{\text{net,x}} = M^I_{\text{net,x}}$ and $M_{\text{nx}} = M^-_{\text{nx}}$, such that:

$$\frac{P^I_{\text{net}}}{\phi_{\text{c}} P_{\text{n}}} + \frac{M^I_{\text{net,x}}}{\phi_{\text{b}} M^-_{\text{nx}}} = \frac{70.0}{0.85 \times 402.6} + \frac{9.3}{0.90 \times 44.9} = 0.44 \leqslant 1.0 \qquad \therefore \text{O.K.}$$

6.5.7.2   Capacity check for Stage II

In Stage II, $P_{\text{net}} = P^{II}_{\text{net}}$, $M_{\text{net,x}} = M^{II}_{\text{net,x}}$ and $M_{\text{nx}} = M^+_{\text{nx}}$, such that:

$$\frac{P^{II}_{\text{net}}}{\phi_{\text{c}} P_{\text{n}}} + \frac{M^{II}_{\text{net,x}}}{\phi_{\text{b}} M^+_{\text{nx}}} = \frac{83.8}{0.85 \times 402.6} + \frac{13.9}{0.90 \times 41.5} = 0.62 \leqslant 1.0 \qquad \therefore \text{O.K.}$$

Hence, the chosen cold-formed steel beam is able to carry the applied combined loading during both stages.

6.5.8   Design of prestressed cable

To check the capacity of the prestressed cable in Stages I and II, Equation (6.3) is employed. For this purpose, the net axial force, as determined in Section 6.5.6, is compared with the tensile capacity of the cable, as defined by Equation (6.4). According to (ASCE/SEI 19-16, 2016), an amplification factor of 2.2 must be applied to the overall prestressing force to safeguard against accidentally overstressing the cable, deviations in the material properties and fabrication tolerances; hence the resistance factor in tension ϕ_{t} is taken equal to $1/2.2 = 0.45$ herein, such that:

$$P_{\text{y,c}} = \phi_{\text{t}} F_{\text{y,c}} A_{\text{c}} = 0.45 \times 1860 \times 105 = 87.9 \text{ kN}.$$

6.5.8.1   Capacity check for Stage I

In Stage I, $P_{\text{net}} = P^I_{\text{net}}$, thus:

$$P^I_{\text{net}} = 70.0 \text{ kN} \leqslant 87.9 \text{ kN} \qquad \therefore \text{O.K.}$$

6.5.8.2   Capacity check for Stage II

In Stage II, $P_{\text{net}} = P_{\text{net}}^{II}$, thus:

$$P_{\text{net}}^{II} = 83.8 \text{ kN} \leqslant 87.9 \text{ kN} \qquad \therefore \text{O.K.}$$

Hence, the chosen cable is able to carry the prestressing force in both stages.

6.5.9   Serviceability check

As discussed in Section 6.3.6, to perform the serviceability check for Stage II, the effective second moment of area of the cold-formed steel beam I_{eff} is required. This can be determined using Equation (6.12), with the moment due to service loads M_{serv} being calculated using Equation (6.13), thus:

$$M_{\text{serv}} = M_{\text{max}}^{\text{L}} - \Delta P^{\text{L}} e = 12.0 - 6.6 \times 0.133 = 11.1 \text{ kNm}.$$

Subsequently, to determine the (positive) bending resistance of the member at the service stress level M_{d}, the procedure outlined in Section 6.5.5.1 must be repeated, but with M_{y} in all the DSM equations replaced by M_{serv}. In this example, this procedure gives $M_{\text{d}} = M_{\text{serv}}$ and thus $I_{\text{eff}} = I_{\text{s}}$. Hence, at service, the cross-section is fully effective and thus the bending stiffness for Stage II is not reduced. This is due to the fact that a significant part of the applied bending moment at midspan M_{max} is counteracted by the eccentric prestressing force and therefore M_{serv} has a low value relative to M_{y}.

Utilising Equation (6.11), the midspan vertical deflection due to service loads δ_{serv} is calculated as:

$$\delta_{\text{serv}} = \left(\frac{5L^2}{48 E_{\text{s}} I_{\text{eff}}} \right) M_{\text{max}}^{\text{L}} - \left(\frac{L^2}{8 E_{\text{s}} I_{\text{eff}}} \right) \Delta P^{\text{L}} e$$

$$= 16.2 \text{ mm} \leqslant L/360 = 17.2 \text{ mm} \qquad \therefore \text{O.K.}$$

Hence, the serviceability criterion is satisfied herein.

Finally, utilising Equation (6.10), the overall midspan vertical deflection at the end of Stage II, $\delta_{\mathrm{mid}}^{II}$, can be calculated as:

$$\delta_{\mathrm{mid}}^{II} = 6.1 \text{ mm} \leqslant L/240 = 25.8 \text{ mm} \qquad \therefore \text{O.K.}$$

Hence, the serviceability criterion is satisfied herein.

6.6 Concluding remarks

Prestressed cold-formed steel beams can be designed by checking the load-carrying capacities of the two structural components of the prestressed system, *i.e.* the cold-formed steel beam and the cable, during both the prestressing and the imposed vertical loading stages. In the proposed approach, the cold-formed steel beam can be designed as a beam-column member since it is subjected to combined axial compression and bending during both loading stages. For this purpose, linear interaction equations together with the Direct Strength Method (DSM), as given in AISI-S100-16, can be employed. The prestressed cable is designed simply by ensuring that its design tensile resistance is not exceeded by the prestressing force during the two loading stages. The aforementioned design checks are based on the comparison between the net axial force and bending moment at the critical cross-section of the member with the predicted resistances of the cold-formed steel beam and cable accordingly.

In the present chapter, recommendations for the design of the cold-formed steel beam and cable have been presented, alongside a set of failure criteria that limit the applied loading in each stage according to the load-carrying capacities of the two structural components of the system. These criteria were subsequently utilised to define the permissible design zone for the prestressed system, which facilitates the selection of the applied initial prestressing force and imposed vertical loading for a given beam geometry and cable size. A serviceability criterion was also provided to limit the excessive vertical deflections of the prestressed member during service. The suitability of the design recommendations

was subsequently assessed by comparing 351 finite element (FE) results (for the cases of bare steel and prestressed beams) with the corresponding design predictions using an axial force versus bending moment (P–M) interaction diagram. Reliability analysis was also conducted to demonstrate that the developed recommendations can be used safely to design the studied prestressed cold-formed steel beams. Finally, to illustrate the implementation of the design recommendations, a detailed worked example has been presented, whereby the steps required for the design of prestressed cold-formed steel beams were outlined.

Chapter 7

CONCLUSIONS

AND FURTHER RESEARCH

In the current chapter, a summary of the research presented in this thesis is provided and the principal conclusions from each chapter are outlined. Furthermore, potential applications of prestressed cold-formed steel beams in practice are provided and, finally, recommendations for further research are given.

7.1 Summary and conclusions

Owing to their high strength-to-weight ratio, cold-formed steel members provide light-weight solutions in construction, offering economies in transportation and efficiency in handling, erection and installation. However, cold-formed steel members are highly vulnerable to local instability phenomena owing to their thin-walled geometry. These instabilities may occur at stress levels lower than the material yield strength, thus preventing the full utilisation of the cross-sectional capacity. In the current research, a simple yet novel concept is proposed, whereby the occurrence of these instabilities in cold-formed steel beams is delayed by means of prestressing; consequently, the load-carrying capacity of the steel beams is enhanced. The focus of the present thesis has been the conceptual development of the proposed prestressed cold-formed steel beams, which structural

engineers will be able to employ as a structurally efficient solution in design. The motivation, objectives and methodology employed in the current research have been described in Chapter 1.

To determine the state-of-the-art with regards to the two driving principles of the proposed concept, namely prestressing technologies and cold-formed steel members, a literature review has been conducted and the main findings have been presented in Chapter 2. The concept of enhancing the performance of structural members by means of prestressing, whereby initial stresses are introduced within the members to counteract the stresses induced during subsequent loading stages, has been demonstrated first. Subsequently, the practical applications and principal characteristics of cold-formed steel members have been presented, while the utilisation of elastic buckling analysis and the Direct Strength Method (DSM) for the purposes of designing cold-formed steel members has been discussed.

In the proposed beams, the prestressing force is applied by means of a high-strength steel cable that is housed within the cross-section profile of the cold-formed steel beam. The cross-sectional geometry of the cold-formed steel beam is that of a lipped channel section with two longitudinal stiffeners in the web and with the bottom flange being bent back towards the web to form the tubular region of the section, where the prestressing cable is located. Owing to the eccentric location of the cable with respect to the strong geometric axis of the member, the prestressing force introduces initial tensile stresses within the top region of the cold-formed steel beam, thus cancelling part of the compressive stresses induced during the subsequent imposed vertical loading stage. Consequently, the occurrence of local instabilities is delayed and thus the cold-formed steel member can carry greater loading before failure, *i.e.* its load-carrying capacity is enhanced. Additionally, owing to the pre-camber induced during prestressing and the contribution of the cable to the system bending stiffness, the overall vertical deflections of the member are reduced significantly; hence, its serviceability performance is also enhanced. The above concept has been presented in Chapter 3, where the principal characteristics of the proposed system have also been described.

Prestressed cold-formed steel beams are subjected to two loading stages. In Stage I,

the prestressing force is transferred into the cold-formed steel member and, in Stage II, uniformly distributed loading is applied along the member. To capture the linear elastic response of the beams during these two stages, analytical expressions have been developed in Chapter 3. The analytical work considered the components of the axial stress distribution at the critical cross-section and demonstrated the origins of the enhancement in the moment capacity of the member. Subsequently, the unbonded nature of the connection between the cable and the steel cross-section was studied using the minimum potential energy principle. Thus, an expression for the incremental increase in the prestressing force, which is induced since the cable is located below the neutral axis of the member, was obtained. The developed analytical expressions have been utilised in subsequent chapters to verify the behaviour of the studied members within the elastic pre-buckling stage.

Failure criteria, based on linear interaction equations in conjunction with the DSM, have also been developed in Chapter 3. These criteria are a function of the net axial force and bending moment at the critical cross-section of the member alongside the predicted capacities of the cold-formed steel beam and the prestressing cable. For this to be achieved, the cold-formed steel member was treated as a beam-column since it is subjected to combined axial loading and bending during both loading stages. In the case of the cable, the criteria simply ensure that its tensile capacity is not violated. The method of determining the net axial forces and bending moments, as well as the axial compressive and bending resistances of the cold-formed steel member, was described in detail.

Geometrically and materially nonlinear finite element (FE) analysis with imperfections has been employed to simulate the behaviour of prestressed cold-formed steel beams during the different loading stages. In the developed FE models, which have been described in Chapter 4, shell and truss elements were employed to model the cold-formed steel member and cable respectively, while a sufficiently fine mesh was used to discretise the member. To model the cold-formed steel member, two material models, namely the elastic, perfectly–plastic and the modified two-stage Ramberg–Osgood models, were utilised. In this manner, direct comparisons of the obtained FE results with the analytical and DSM capacity predictions respectively were enabled. The cable was modelled

using an elastic, perfectly–plastic model. Subsequently, the method of introducing initial geometric imperfections into the cold-formed steel members was outlined. The shape, distribution and magnitude of these imperfections were obtained by means of elastic buckling analysis. Furthermore, simulations of the unbonded beam–cable connection alongside the idealised boundary and loading conditions have been discussed and, finally, the solution schemes employed in each loading stage have been reported.

The validation of the FE modelling approach against available experimental data has also been presented in Chapter 4. For the purposes of the validation, two previous experimental studies, which investigated the failure of cold-formed steel lipped channel beams by distortional buckling, were considered. Overall, excellent agreement between the FE and test results has been demonstrated, thus validating the suitability of the FE modelling approach.

The mechanical behaviour of prestressed cold-formed steel beams during the prestressing and imposed vertical loading stages has been analysed in detail in Chapter 5. For this purpose, the FE results from three sample models were compared with the corresponding analytical results and failure criteria. The effect of prestressing was investigated by analysing the moment–deflection and moment–stress responses of these models, while the effect of initial geometric imperfections was also explored. Substantial benefits from the addition of the prestressed cable, in terms of enhanced structural performance at both serviceability and ultimate limit states, have been demonstrated. In the case of the studied reference prestressed beam, an enhancement of 15% in the ultimate moment capacity, as well as a reduction of 60% in the overall vertical deflections at failure, was observed. The deformed shape and axial stress distribution at the critical cross-section at different loading stages were shown to be a valuable tool for understanding the failure mechanism and the origin of the obtained benefits. The effect of the lateral restraints and the prestressed cable on asymmetric bending and the lateral stability of the member respectively has also been discussed.

The results from a set of parametric FE studies, where the influence of the key controlling parameters was investigated, have been presented in Chapter 5. The results were analysed in detail in order to demonstrate the origin of the obtained benefits in each case.

Firstly, it was shown that the occurrence of local/distortional buckling can be delayed by applying higher prestress levels. In this manner, a greater moment capacity enhancement can be achieved. Secondly, it was concluded that, optimally, the cold-formed steel beam and the cable must fail simultaneously, thus fully utilising the capacity of both structural components of the system. Thirdly, it has been demonstrated that the increase in the ultimate moment capacity of the steel beam can be extended further by increasing its section thickness. Finally, it was concluded that by shifting the centroid of the cold-formed steel beam upwards, increased structural benefits and thus a more economical solution can be obtained. The aforementioned conclusions have been utilised to demonstrate that enhancements of up to 40% in the load-carrying capacity of cold-formed steel beams and reductions approaching 60% in their overall deflections can be achieved.

Prestressed cold-formed steel beams can be designed by adapting existing design methods, as discussed in Chapter 6, where rules for the structural design of the studied beams have been developed. Since the cold-formed steel beam is subjected to a combination of axial force and bending moment during both loading stages, it can be designed as a beam-column using linear interaction equations, as set out in the North American Specification. The cable is designed by checking that the prestressing force does not exceed its tensile capacity. In the proposed design method, the capacities of both structural components of the system are compared with the net axial force and the net bending moment at the critical cross-section of the member. The design checks need to be performed for both the prestressing and the imposed loading stages by considering the appropriate loading configuration. In Chapter 6, the developed failure criteria have also been utilised to define the permissible design zone for the prestressed system at both loading stages. The suitability of the design recommendations was subsequently assessed against the parametric FE results using an axial force versus bending moment $(P\text{--}M)$ interaction diagram. This assessment, alongside the conducted reliability analysis, demonstrated that the developed provisions can be used safely to design the proposed prestressed cold-formed steel beams. Finally, implementation of the design recommendations has been demonstrated through a practical worked example.

7.2 Potential applications in practice

Owing to their enhanced load-carrying capacity and serviceability performance, prestressed cold-formed steel beams can provide highly-efficient structural solutions and, potentially, can open up new applications for cold-formed steel in construction. The application of the studied beams in practice is facilitated by the fact that they can be designed by adapting existing design methods.

The enhanced structural performance of the proposed beams implies that, for a given demand in capacity and span length, a smaller cold-formed steel cross-section is required; hence, material and therefore self-weight savings, relative to conventional non-prestressed beams, are achieved. This can enable the utilisation of the proposed concept in the development of thin-slab composite floor systems, as discussed in the following section.

Potentially, the proposed beams may be employed more widely as primary structural elements in the construction of buildings and other structures. For this purpose, the studied beams can also be arranged in a 'back-to-back' configuration to enhance the lateral stability of the prestressed system and avoid asymmetries in the cross-sectional shape. Potentially, in this configuration, the addition of prestressed cables can offer even greater enhancements in the ultimate moment capacity of the cold-formed steel members.

Certainly, the prestressing procedure incurs higher installation costs, while the costs of the cable and anchorage system should also be considered when estimating the net benefits that prestressed cold-formed steel beams can offer. Emphasis also needs to be given to other important practical considerations, such as vibrations, durability and maintenance.

7.3 Further research

With the aim of encouraging further developments on the currently proposed concept, recommendations for further research and the qualitative time scales required for these to be completed are provided below.

Short-term

Prestressed cold-formed steel beams can be arranged in the back-to-back configuration to enhance the load-carrying capacity and to improve the lateral stability of the member substantially and thus avoid the requirement for lateral restraints along the member. A pilot study regarding the behaviour of prestressed built-up cold-formed steel beams has been conducted by the author. In this study, the contact between the two cold-formed steel members, as well as the connection between them along the member length, was considered. It has been concluded that the built-up configuration can provide even higher benefits from the addition of the prestressed cables; enhancements of up to 60% in the ultimate moment capacity of the cold-formed steel beams and reductions approaching 70% in their overall deflections have been achieved. Recent research on cold-formed steel built-up members includes the work of Fratamico *et al.* (2018) and Ye *et al.* (2018).

A recently conducted experimental investigation into cold-formed steel composite flooring systems has demonstrated that the mobilisation of composite action within these systems is feasible, bringing substantial performance benefits both at serviceability and ultimate limit states (Kyvelou et al., 2017, 2018). The shear connection in the flooring system can be achieved by making simple alterations to the fastening arrangements between the steel section and the boards currently used in practice (Kyvelou et al., 2017). Currently, as indicated in Section 1.7, the concept of combining the proposed prestressed cold-formed steel beams with the aforementioned composite flooring systems is being explored. Ultimately, the development of a novel and highly-efficient prestressed composite flooring system comprising cold-formed steel joists and wood-based floorboards is feasible.

Medium-to-long term

Experimental studies on prestressed cold-formed steel beams, whereby the two loading stages are investigated independently, could be conducted. In this manner, the validation of the developed numerical models could be extended. Note that, in this case, the simluation of the anchorage system used in the experiments would be required. In the present work, the anchorage system has been idealised as being fully effective in transferring the

prestressing force into the cold-formed steel member. Furthermore, the effects of the combined cold-forming and electric welding resistance process on the material response, residual stresses and initial geometric imperfections will need to be considered. The experimental investigations could test the beam geometries and cable sizes that have been considered in the present thesis. Note that, to provide lateral stability during testing, the studied beams would need to be tested in pairs. Previous experimental investigations with similar arrangements include those of Kyvelou *et al.* (2017) and Yu and Schafer (2003; 2006).

To maximise the structural benefits obtained from the addition of the prestressed cable, optimisation techniques could be employed to optimise the cross-sectional geometry of the cold-formed steel member. For this purpose, the various loading configurations to which the proposed beams are subjected during the two loading stages would need to be considered. The optimisation study could explore various controlling parameters, such as the form of the cross-sectional profile, the location of the cable within the cross-section (*i.e.* its eccentricity with respect to both the strong and the weak bending axes of the cross-section) and the location of the intermediate stiffeners. For this purpose, shape optimisation frameworks, such as the Particle Swarm Optimisation algorithm (PSO), could be employed. This particular algorithm has been utilised in previous research to optimise the cross-sectional geometry of cold-formed steel members, demonstrating substantial increases in their load-carrying capacities (Ma et al., 2015; Ye et al., 2016a, 2018).

Further work could also include the investigation of the behaviour of prestressed cold-formed steel beams when subjected to uplift forces. In this case, the axial stress distribution due to the imposed vertical loading is reversed and thus the uplift forces could have a detrimental effect on the capacity of the beams. Similarly, to study the concept of continuous prestressed cold-formed steel beams, the effect of the hogging moments at the intermediate supports would need to be considered carefully.

In addition, the effect of prestressing on the shear capacity of the cold-formed steel beam could be explored. Since the maximum shear force due to the uniformly distributed loading is located at the supports, and since the prestressing force induces a hogging moment,

which would otherwise be absent, at the supports, the prestressing could potentially have a negative effect on the shear capacity of the cold-formed steel beam. Experimental and numerical investigations on cold-formed steel sections subjected to combined bending and shear include the works of Pham and Hancock (2012) and Pham *et al.* (2014; 2015).

Finally, the parametric FE results presented in the current thesis could be compared with the recently proposed DSM provisions for the design of cold-formed steel beam-columns (Torabian and Schafer, 2018) to determine whether the new DSM provisions could also be utilised for the design prestressed cold-formed steel beams.

References

ABAQUS (2014). *Version 6.14-2 Analysis User's Guide - Online Documentation.* Dassault Systemes Simulia Corp.

ACI 318-14 (2014). *Building code requirements for structural concrete.* American Concrete Institute, Michigan.

Ádány, S. and Beregszászi, Z. (2008). Local and distortional buckling of thin-walled members - Numerical study to compare conventional and constrained finite strip methods. In *Proceedings of the Fifth International Conference on Thin-Walled Structures*, Brisbane, Australia, June 18–20, 2008.

Ádány, S., Silvestre, N., Schafer, B. W., and Camotim, D. (2009). GBT and cFSM: Two modal approaches to the buckling analysis of unbranched thin-walled members. *Advanced Steel Construction*, 5(2):195–223.

Afshan, S., Rossi, B., and Gardner, L. (2013). Strength enhancements in cold-formed structural sections – Part I: Material testing. *Journal of Constructional Steel Research*, 83:177–188.

Afshan, S., Zhao, O., and Gardner, L. (2019). Standardised material properties for numerical parametric studies of stainless steel structures and buckling curves for tubular columns. *Journal of Constructional Steel Research*, 152:2–11.

AISI S100-12 (2012). *North American specification for the design of cold-formed steel structural members.* Washington, D.C.

AISI S100-16 (2016). *North American specification for the design of cold-formed steel structural members.* Washington, D.C.

Allen, H. G. and Bulson, P. S. (1980). *Background to buckling.* McGraw-Hill, New York.

Anapayan, T. and Mahendran, M. (2012). Numerical modelling and design of LiteSteel Beams subject to lateral buckling. *Journal of Constructional Steel Research*, 70:51–64.

Anapayan, T., Mahendran, M., and Mahaarachchi, D. (2011). Section moment capacity tests of LiteSteel beams. *Thin-Walled Structures*, 49(4):502–512.

ArcelorMittal WireSolutions (2018). Prestressed concrete: wire and strands specification. http://www.constructalia.com/repository/Products/CivilEngineering/ Wire_Strands_EN.pdf (accessed August 2018).

ASCE/SEI 19-16 (2016). *Structural applications of steel cables for buildings.* American Society of Civil Engineers.

ASCE/SEI 7-16 (2016). *Minimum design loads for buildings and other structures.* American Society of Civil Engineers.

ASTM standard A416/A416M (2012). *Standard specification for steel strand, uncoated seven-wire for prestressed concrete.* ASTM International, West Conshohocken, PA.

ASTM standard A421/A421M (2015). *Standard specification for stress-relieved steel wire for prestressed concrete.* ASTM International, West Conshohocken, PA.

Ayyub, B. M., Ibrahim, A., and Schelling, D. (1990a). Posttensioned trusses: analysis and design. *Journal of Structural Engineering, ASCE*, 116(6):1491–1506.

Ayyub, B. M., Sohn, Y. G., and Saadatmanesh, H. (1990b). Prestressed composite girders under positive moment. *Journal of Structural Engineering, ASCE*, 116(11):2931–2951.

Basaglia, C., Camotim, D., and Silvestre, N. (2011). Non-linear GBT formulation for open-section thin-walled members with arbitrary support conditions. *Computers and Structures*, 89(21–22):1906–1919.

Belletti, B. and Gasperi, A. (2010). Behaviour of prestressed steel beams. *Journal of Structural Engineering, ASCE*, 136(9):1131–1139.

Beregszászi, Z. and Ádány, S. (2011). Application of the constrained finite strip method for the buckling design of cold-formed steel columns and beams via the direct strength method. *Computers and Structures*, 89(21-22):2020–2027.

Bleich, F. (1952). *Buckling strength of metal structures.* McGraw-Hill, New York.

Bock, M., Mirada, F. X., and Real, E. (2015). Statistical evaluation of a new resistance model for cold-formed stainless steel cross-sections subjected to web crippling. *International Journal of Steel Structures*, 15(1):227–244.

Bulson, P. S. (1970). *The stability of flat plates.* Chatto and Windus, London.

Camotim, D., Dinis, P. B., and Martins, A. D. (2016). Direct strength method - a general approach to the design of cold-formed steel structures. In Yu, C., editor, *Recent trends in cold-formed steel construction,* Chapter 4. Woodhead Publishing.

Camotim, D., Silvestre, N., Basaglia, C., and Bebiano, R. (2008). GBT-based buckling analysis of thin-walled members with non-standard support conditions. *Thin-Walled Structures*, 46(7–9):800–815.

Casson, L. (1971). *Ships and seamanship in the ancient world.* Princeton University Press, Princeton.

Chajes, A., Britvec, S. J., and Winter, G. (1963). Effects of cold-straining on structural sheet steels. *Journal of the Structural Division, ASCE*, 89(ST2):1–32.

Chen, S. and Gu, P. (2005). Load carrying capacity of composite beams prestressed with external tendons under positive moment. *Journal of Constructional Steel Research*, 61(4):515–530.

Chen, S. and Jia, Y. (2010). Numerical investigation of inelastic buckling of steel-concrete composite beams prestressed with external tendons. *Thin-Walled Structures*, 48(3):233–242.

Chen, S., Wang, X., and Jia, Y. (2009). A comparative study of continuous steel-concrete composite beams prestressed with external tendons: Experimental investigation. *Journal of Constructional Steel Research*, 65(7):1480–1489.

Cheung, Y. K. and Tham, L. G. (1997). *The Finite Strip Method.* CRC Press, first edition.

Clarke, M. J. and Hancock, G. J. (1991). Finite-element nonlinear analysis of stressed-arch frames. *Journal of Structural Engineering, ASCE*, 117(10):2819–2837.

Cruise, R. B. and Gardner, L. (2008). Residual stress analysis of structural stainless steel sections. *Journal of Constructional Steel Research*, 64(3):352–366.

CSC Building Systems (2018). Cold-formed steel in construction. https://www.cscbuildingsystems.com (accessed August 2018).

Davison, B. and Owens, G. W., editors (2012). *Steel designers' manual.* Wiley-Blackwell, seventh edition.

Dinis, P. B., Camotim, D., and Silvestre, N. (2007). FEM-based analysis of the local-plate/distortional mode interaction in cold-formed steel lipped channel columns. *Computers and Structures*, 85(19–20):1461–1474.

Dischinger, F. (1949). Stahlbrucken im verbundmit stahlebeton druckplatten bei gleichzeitiger vorspannung durch hochwertige seite (in German). *Der Bavingerniever*, 11:321–332.

Dubina, D., Ungureanu, V., and Landolfo, R. (2012). *Design of cold-formed steel structures: Eurocode 3: Design of steel structures. Part 1-3: Design of cold-formed steel structures.* European Convention for Constructional Steelwork (ECCS), first edition.

El-Zohairy, A., Salim, H., Shaaban, H., Mustafa, S., and El-Shihy, A. (2015). Finite-element modeling of externally posttensioned composite beams. *Journal of Bridge Engineering*, 20(12):04015018.

Ellen, M. E., Gosaye, J., Gardner, L., and Wadee, M. A. (2012). Design and construction of long-span post-tensioned tubular steel structures. In *Tubular Structures XIV - Fourteenth International Symposium on Tubular Structures*, pages 687–693.

Ellen, P. E. (1987). *U.S. Patent No. 4,676,045.* Washington, DC: U.S. Patent and Trademark Office.

EN 10138 (2000). *European standard - Prestressing steels*. Brussels: European Committee for Standardization (CEN).

EN 1990:2002+A1 (2005). *Eurocode 0 - Basis of structural design*. Brussels: European Committee for Standardization (CEN).

EN 1992-1-1 (2004). *Eurocode 2 - Design of concrete structures - Part 1-1: General rules and rules for buildings*. Brussels: European Committee for Standardization (CEN).

EN 1993-1-11 (2006). *Eurocode 3 - Design of steel structures - Part 1-11: Design of structures with tension components*. Brussels: European Committee for Standardization (CEN).

EN 1993-1-3 (2006). *Eurocode 3: Design of steel structures - Part 1-3: General rules - Supplementary rules for cold-formed members and sheeting*. Brussels: European Committee for Standardization (CEN).

Fratamico, D. C., Torabian, S., Zhao, X., Rasmussen, K. J. R., and Schafer, B. W. (2018). Experimental study on the composite action in sheathed and bare built-up cold-formed steel columns. *Thin-Walled Structures*, 127:290–305.

Gardner, L. and Ashraf, M. (2006). Structural design for non-linear metallic materials. *Engineering Structures*, 28(6):926–934.

Gardner, L. and Yun, X. (2018). Description of stress–strain curves for cold-formed steels. *Construction and Building Materials*.

Gosaye, J. (2015). *Behaviour and design of prestressed steel structures*. PhD thesis, Imperial College London, London.

Gosaye, J., Gardner, L., Wadee, M. A., and Ellen, M. E. (2014). Tensile performance of prestressed steel elements. *Engineering Structures*, 79:234–243.

Gosaye, J., Gardner, L., Wadee, M. A., and Ellen, M. E. (2016). Compressive behaviour and design of prestressed steel elements. *Structures*, 5:76–87.

Grubb, P. J., Gorgolewski, M. T., and Lawson, R. M. (2001). *Light steel framing in residential construction*. Steel Construction Institute, SCI P301.

Grubb, P. J. and Lawson, R. M. (1997). *Building design using cold formed steel sections: construction detailing and practice*. Steel Construction Institute, SCI P165.

Hadjipantelis, N., Gardner, L., and Wadee, M. A. (2018a). Prestressed cold-formed steel beams – conceptual development. In *Proceedings of the Eighth International Conference on Thin-Walled Structures*, Lisbon, Portugal, July 24–27, 2018.

Hadjipantelis, N., Gardner, L., and Wadee, M. A. (2018b). Prestressed cold-formed steel beams – parametric studies and design recommendations. In *Proceedings of the Ninth International Conference on Advances in Steel Structures*, Hong-Kong, China, December 5–7, 2018.

Hadjipantelis, N., Gardner, L., and Wadee, M. A. (2018c). Prestressed cold-formed steel beams: Concept and mechanical behaviour. *Engineering Structures*, 172:1057–72.

Hadjipantelis, N., Gardner, L., and Wadee, M. A. (2019a). Design of prestressed cold-formed steel beams. *Thin-Walled Structures*, (Accepted).

Hadjipantelis, N., Gardner, L., and Wadee, M. A. (2019b). Finite element modeling of prestressed cold-formed steel beams. *Journal of Structural Engineering, ASCE*, (Accepted).

Haidarali, M. R. and Nethercot, D. A. (2011). Finite element modelling of cold-formed steel beams under local buckling or combined local/distortional buckling. *Thin-Walled Structures*, 49(12):1554–1562.

Hancock, G. J. (1978). Local, distortional and lateral buckling of I-beams. *Journal of the Structural Division, ASCE*, 104(11):1787–1798.

Hancock, G. J. (2016). Cold-formed steel structures: Research review 2013–2014. *Advances in Structural Engineering*, 19(3):393–408.

Hancock, G. J., Kwon, Y. B., and Bernard, E. S. (1994). Strength design curves for thin-walled sections undergoing distortional buckling. *Journal of Constructional Steel Research*, 31(2-3):169–186.

Hancock, G. J., Murray, T. M., and Ellifritt, D. S. (2001). *Cold-formed steel structures to the AISI specification*. Marcel Dekker, Inc.

Hill, H. N. (1944). Determination of stress–strain relations from offset yield strength values. *National Advisory Committee for Aeronautics; Technical Note No. 927.*

Hoadley, P. G. (1961). *An analytical study of the behavior of prestressed steel beams.* PhD thesis, University of Illinois Urbana-Champaign, Illinois.

Hoadley, P. G. (1963). Behavior of prestressed composite steel beams. *Journal of the Structural Division, ASCE*, 89:21–34.

Hoadley, P. G. (1968). Development and use of prestressed steel flexural members: Part 2 - Prestressing by means of high strength steel wires or bars. *Subcommittee 3 on Prestressed Steel of Joint ASCE-AASHO Committee on Steel Flexural Members, Journal of the Structural Division, ASCE*, 94(9):2035–2042.

Hsiao, L. E., Yu, W. W., and Galambos, T. V. (1990). AISI LRFD method for cold-formed steel structural members. *Journal of Structural Engineering, ASCE*, 116(2):500–517.

Hui, C. (2014). *Moment redistribution in cold-formed steel purlin systems.* PhD thesis, Imperial College London, London.

Hui, C., Gardner, L., and Nethercot, D. A. (2016). Moment redistribution in cold-formed steel continuous beams. *Thin-Walled Structures*, 98:465–477.

Jandera, M., Gardner, L., and Machacek, J. (2008). Residual stresses in cold-rolled stainless steel hollow sections. *Journal of Constructional Steel Research*, 64(11):1255–1263.

Javaroni, C. E. and Gonçalves, R. M. (2006). Distortional buckling of simple lipped channel in bending – results of the experimental analysis versus direct strength methods. In *Proceedings of the Eighteenth International Specialty Conference on Cold-Formed Steel Structures*, pages 133–146, Orlando, Florida, USA, October 26–27, 2006.

Kambal, M. E. M. and Jia, Y. (2018). Theoretical and experimental study on flexural behavior of prestressed steel plate girders. *Journal of Constructional Steel Research*, 142:5–16.

Karren, K. W. (1967). Corner properties of cold-formed shapes. *Journal of the Structural Division, ASCE*, 93(1):401–433.

Karren, K. W. and Winter, G. (1967). Effects of cold-forming on light-gage steel members. *Journal of the Structural Division, ASCE*, 93(1):433–469.

Keerthan, P. and Mahendran, M. (2010). Experimental studies on the shear behaviour and strength of LiteSteel beams. *Engineering Structures*, 32(10):3235–3247.

Keerthan, P. and Mahendran, M. (2011). Numerical modeling of LiteSteel beams subject to shear. *Journal of Structural Engineering, ASCE*, 137(12):1428–1439.

Kyvelou, P., Gardner, L., and Nethercot, D. A. (2017). Testing and analysis of composite cold-formed steel and wood-based flooring systems. *Journal of Structural Engineering, ASCE*, 143(11):04017146.

Kyvelou, P., Gardner, L., and Nethercot, D. A. (2018). Finite element modelling of composite cold-formed steel flooring systems. *Engineering Structures*, 158:28–42.

LaBoube, R. A. and Yu, W. W. (1975). Study of cold-formed steel beam webs subjected to bending stress. In *Proceedings of the Third International Specialty Conference on Cold-Formed Steel Structures*, pages 315–335, St. Louis, Missouri, USA, November 24–25, 1975.

Lau, S. C. W. and Hancock, G. J. (1987). Distortional buckling formulas for channel columns. *Journal of Structural Engineering, ASCE*, 113(5):1063–1078.

Li, Z. (2016). Advanced computational tools for elastic buckling analysis of cold-formed steel structures. In Yu, C., editor, *Recent trends in cold-formed steel construction*, Chapter 5. Woodhead Publishing.

Li, Z., Ádány, S., and Schafer, B. W. (2013). Modal identification for shell finite element models of thin-walled members in nonlinear collapse analysis. *Thin-Walled Structures*, 67:15–24.

Li, Z., Batista Abreu, J. C., Leng, J., Ádány, S., and Schafer, B. W. (2014). Review: Constrained finite strip method developments and applications in cold-formed steel design. *Thin-Walled Structures*, 81:2–18.

Li, Z. and Schafer, B. W. (2010a). Application of the finite strip method in cold-formed steel member design. *Journal of Constructional Steel Research*, 66(8–9):971–980.

Li, Z. and Schafer, B. W. (2010b). Buckling analysis of cold-formed steel members with general boundary conditions using CUFSM: Conventional and constrained finite strip methods. In *Proceedings of the Twentieth International Specialty Conference on Cold-Formed Steel Structures*, Missouri, USA, November 3–4, 2010.

Lorenc, W. and Kubica, E. (2006). Behavior of composite beams prestressed with external tendons: Experimental study. *Journal of Constructional Steel Research*, 62(12):1353–1366.

Lou, T., Lopes, S. M. R., and Lopes, A. V. (2016). Numerical modeling of externally prestressed steel–concrete composite beams. *Journal of Constructional Steel Research*, 121:229–236.

Ma, W., Becque, J., Hajirasouliha, I., and Ye, J. (2015). Cross-sectional optimization of cold-formed steel channels to Eurocode 3. *Engineering Structures*, 101:641–651.

Madrazo-Aguirre, F., Ruiz-Teran, A. M., and Wadee, M. A. (2015a). Dynamic behaviour of steel-concrete composite under-deck cable-stayed bridges under the action of moving loads. *Engineering Structures*, 103:260–274.

Madrazo-Aguirre, F., Wadee, M. A., and Ruiz-Teran, A. M. (2015b). Non-linear stability of under-deck cable-stayed bridge decks. *International Journal of Non-Linear Mechanics*, 77:28–40.

Magnel, G. (1948). *Prestressed concrete.* Concrete Publications Ltd, London.

Magnel, G. (1950). Prestressed steel structures. *The Structural Engineer*, 28:285–295.

Meimand, V. Z. and Schafer, B. W. (2014). Impact of load combinations on structural reliability determined from testing cold-formed steel components. *Structural Safety*, 48:25–32.

Mirambell, E. and Real, E. (2000). On the calculation of deflections in structural stainless steel beams: an experimental and numerical investigation. *Journal of Constructional Steel Research*, 54(1):109–133.

Moen, C. D., Igusa, T., and Schafer, B. W. (2008). Prediction of residual stresses and strains in cold-formed steel members. *Thin-Walled Structures*, 46(11):1274–1289.

Moen, C. D. and Schafer, B. W. (2009a). Elastic buckling of cold-formed steel columns and beams with holes. *Engineering Structures*, 31(12):2812–2824.

Moen, C. D. and Schafer, B. W. (2009b). Elastic buckling of thin plates with holes in compression or bending. *Thin-Walled Structures*, 47(12):1597–1607.

Moreyra, M. E. and Peköz, T. (1994). Experiments on lipped channel flexural members. In *Proceedings of the Twelfth International Specialty Conference on Cold-Formed Steel Structures*, St. Louis, Missouri, USA, October 18–19, 1994.

Naaman, A. E. (1990). A new methodology for the analysis of beams prestressed with external or unbonded tendons. *External Prestressing in Bridges*, SP-120:339–354.

Naaman, A. E., Burns, N., French, C., Gamble, W. L., and Mattock, A. H. (2002). Stresses in unbonded prestressing tendons at ultimate: recommendation. *ACI Structural Journal*, 99(4):518–529.

Natário, P., Silvestre, N., and Camotim, D. (2014). Computational modelling of flange crushing in cold-formed steel sections. *Thin-Walled Structures*, 84:393–405.

Nguyen, P. and Yu, W. W. (1980). Bending strength of cold-formed steel longitudinally reinforced beam webs. In *Proceedings of the Fifth International Specialty Conference on Cold-Formed Steel Structures*, pages 201–224, St. Louis, Missouri, USA, November 18–19, 1980.

Osofero, A. I., Wadee, M. A., and Gardner, L. (2012). Experimental study of critical and post-buckling behaviour of prestressed stayed columns. *Journal of Constructional Steel Research*, 79:226–241.

Pham, C. H., Bruneau, L. A., and Hancock, G. J. (2015). Experimental study of longitudinally stiffened web channels subjected to combined bending and shear. *Journal of Structural Engineering, ASCE*, 141(11):04015018.

Pham, C. H., Davis, A. F., and Emmett, B. R. (2014). Numerical investigation of cold-formed lapped Z purlins under combined bending and shear. *Journal of Constructional Steel Research*, 95:116–125.

Pham, C. H. and Hancock, G. J. (2012). Direct strength design of cold-formed c-sections for shear and combined actions. *Journal of Structural Engineering, ASCE*, 138(6):759–768.

Pham, C. H. and Hancock, G. J. (2013). Experimental investigation and direct strength design of high-strength, complex c-sections in pure bending. *Journal of Structural Engineering, ASCE*, 139(11):1842–1852.

Ramberg, W. and Osgood, W. R. (1943). Description of stress–strain curves by three parameters. *National Advisory Committee for Aeronautics; Technical Note No. 902;*.

Rasmussen, K. J. R. (2003). Full-range stress–strain curves for stainless steel alloys. *Journal of Constructional Steel Research*, 59(1):47–61.

Rhodes, J. and Lawson, R. M. (1992). *Design of structures using cold formed steel sections: section properties and member capacities*. Steel Construction Institute, SCI P089.

Riks, E. (1979). An incremental approach to the solution of snapping and buckling problems. *International Journal of Solids and Structures*, 15(7):529–551.

Rogers, C. A. and Schuster, R. M. (1995). *Interaction buckling of flange, edge stiffener and web of C-sections in bending*. PhD thesis, University of Waterloo, Waterloo, Ontario.

Rossi, B., Afshan, S., and Gardner, L. (2013). Strength enhancements in cold-formed structural sections – Part II: Predictive models. *Journal of Constructional Steel Research*, 83:189–196.

Saadatmanesh, H., Albrecht, P., and Ayyub, B. M. (1989a). Analytical study of prestressed composite beams. *Journal of Structural Engineering, ASCE*, 115(9):2364–2381.

Saadatmanesh, H., Albrecht, P., and Ayyub, B. M. (1989b). Experimental study of prestressed composite beams. *Journal of Structural Engineering, ASCE*, 115(9):2348–2363.

Saadatmanesh, H., Albrecht, P., and Ayyub, B. M. (1989c). Guidelines for flexural design of prestressed composite beams. *Journal of Structural Engineering, ASCE*, 115(11):2944–2961.

Saito, D. and Wadee, M. A. (2008). Post-buckling behaviour of prestressed steel stayed columns. *Engineering Structures*, 30:1224–1239.

Saito, D. and Wadee, M. A. (2009). Buckling behaviour of prestressed steel stayed columns with imperfections and stress limitation. *Engineering Structures*, 31:1–15.

Saito, D. and Wadee, M. A. (2010). Optimal prestressing and configuration of stayed columns. *Structures and Buildings, Proceedings of the Institution of Civil Engineers*, 163(SB5):343–355.

Sarawit, A. T., Kim, Y., Bakker, M. C. M., and Peköz, T. (2003). The finite element method for thin-walled members-applications. *Thin-Walled Structures*, 41(2-3):191–206.

Schafer, B. W. (1997). *Cold-formed steel behavior and design: Analytical and numerical modeling of elements and members with longitudinal stiffeners*. PhD thesis, Cornell University, Ithaca, New York.

Schafer, B. W. (2002). Local, distortional, and Euler buckling of thin-walled columns. *Journal of Structural Engineering, ASCE*, 128(3):289–299.

Schafer, B. W. (2006). *Direct Strength Method design guide*. American Iron and Steel Institute (AISI), Washington, D.C.

Schafer, B. W. (2008). Review: The Direct Strength Method of cold-formed steel member design. *Journal of Constructional Steel Research*, 64(7–8):766–778.

Schafer, B. W. (2017). Developments in research and assessment of steel structures: Highlights from the perspective of an American researcher. In *Proceedings of the Eight European Conference on Steel and Composite Structures, Eurosteel*, Copenhagen, Denmark, September 13–15, 2017.

Schafer, B. W. (2018). Advances in the Direct Strength Method of thin-walled steel design. In *Proceedings of the Eighth International Conference on Thin-Walled Structures*, Lisbon, Portugal, July 24–27, 2018.

Schafer, B. W. and Ádány, S. (2006). Buckling analysis of cold-formed steel members with general boundary conditions using CUFSM: Conventional and constrained finite strip methods. In *Proceedings of the Eighteenth International Specialty Conference on Cold-Formed Steel Structures*, pages 39–54, Orlando, Florida, USA, October 26–27, 2006.

Schafer, B. W., Li, Z., and Moen, C. D. (2010). Computational modeling of cold-formed steel. *Thin-Walled Structures*, 48(10–11):752–762.

Schafer, B. W. and Peköz, T. (1996). Design of cold-formed steel stiffened elements with multiple longitudinal intermediate stiffeners. In *Proceedings of the Thirteenth International Specialty Conference on Cold-Formed Steel Structures*, St. Louis, Missouri, USA, October 17–18, 1996.

Schafer, B. W. and Peköz, T. (1998a). Computational modeling of cold-formed steel: characterizing geometric imperfections and residual stresses. *Journal of Constructional Steel Research*, 47(3):193–210.

Schafer, B. W. and Peköz, T. (1998b). Direct strength prediction of cold-formed steel members using numerical elastic buckling solutions. In *Proceedings of the Fourteenth International Specialty Conference on Cold-Formed Steel Structures*, St. Louis, Missouri, USA, October 15–16, 1998.

Schafer, B. W. and Peköz, T. (1999). Laterally braced cold-formed steel flexural members with edge stiffened flanges. *Journal of Structural Engineering, ASCE*, 125(2):118–127.

Schardt, R. (1989). *Verallgemeinerte Technische Biegetheorie (in German)*. Springer Verlag, Berlin.

SFIA (2018). Steel Framing Industry Association. https://www.cfsteel.org/ (accessed August 2018).

Shifferaw, Y. and Schafer, B. W. (2012). Inelastic bending capacity of cold-formed steel members. *Journal of Structural Engineering, ASCE*, 138(4):468–480.

Silvestre, N. and Camotim, D. (2002a). First-order generalised beam theory for arbitrary orthotropic materials. *Thin-Walled Structures*, 40(9):755–789.

Silvestre, N. and Camotim, D. (2002b). Second-order generalised beam theory for arbitrary orthotropic materials. *Thin-Walled Structures*, 40(9):791–820.

Standards Australia (2018). *Cold-formed steel structures*. AS/NZS 4600:2018, Sydney, Australia.

Subcommittee 3 on Prestressed Steel of Joint ASCE-AASHO Committee on Steel Flexural Members (1968). Development and use of prestressed steel flexural members. *Journal of the Structural Division, ASCE*, 94(9):2033–2060.

Thompson, J. M. T. and Hunt, G. W. (1973). *A general theory of elastic stability*. Wiley, London.

Timoshenko, S. and Gere, J. M. (1961). *Theory of elastic stability*. McGraw-Hill, New York.

Tong, W. and Saadatmanesh, H. (1992). Parametric study of continuous prestressed composite girders. *Journal of Structural Engineering, ASCE*, 118(1):186–206.

Torabian, S., Amouzegar, H., Tootkaboni, M., and Schafer, B. W. (2016a). Finite element modeling protocols and parametric analyses for short cold-formed steel zee-section beam-columns. In *Proceedings of the Annual Stability Conference, Structural Stability Research Council*, pages 1–12, Orlando, Florida, USA, April 12–15, 2016.

Torabian, S., Fratamico, D. C., and Schafer, B. W. (2016b). Experimental response of cold-formed steel Zee-section beam-columns. *Thin-Walled Structures*, 98:496–517.

Torabian, S. and Schafer, B. W. (2018). Development and experimental validation of the Direct Strength Method for cold-formed steel beam-columns. *Journal of Structural Engineering, ASCE*, 144(10):04018175.

Torabian, S., Zheng, B., and Schafer, B. W. (2014a). Development of a new beam-column design method for cold formed steel lipped channel members. In *Proceedings of the Twenty-second International Specialty Conference on Cold-Formed Steel Structures*, St. Louis, Missouri, USA, November 5–6, 2014.

Torabian, S., Zheng, B., and Schafer, B. W. (2014b). Experimental study and modeling of cold-formed steel lipped channel stub beam-columns. In *Proceedings of the Annual Stability Conference, Structural Stability Research Council*, pages 366–387, Toronto, Canada, March 25–28, 2014.

Torabian, S., Zheng, B., and Schafer, B. W. (2015). Experimental response of cold-formed steel lipped channel beam-columns. *Thin-Walled Structures*, 89:152–168.

Torabian, S., Zheng, B., Shifferaw, Y., and Schafer, B. W. (2016c). Direct strength prediction of cold-formed steel beam-columns. *AISI Committee on Specifications for the Design of Cold-Formed Steel Structural Members*, RP16-3.

Trebilcock, P. J. (1994). *Building design using cold formed steel sections: an architect's guide.* Steel Construction Institute, SCI P130.

Troitsky, M. S. (1990). *Prestressed steel bridges: theory and design.* Van Nostrand Reinhold, New York.

Troitsky, M. S., Zielinski, Z. A., and Nouraeyan, A. (1990). Pre-tensioned and posttensioned composite girders. *Journal of Structural Engineering, ASCE*, 115(12):3142–3153.

Troitsky, M. S., Zielinski, Z. A., and Rabbani, N. F. (1989). Prestressed-steel continuous-span girders. *Journal of Structural Engineering, ASCE*, 115(6):1357–1370.

UN General Assembly (2015). Transforming our world: The 2030 agenda for sustainable development (A/RES/70/1).

Von Kármán, T., Sechler, E. E., and Donnell, L. H. (1932). The strength of thin plates in compression. *Transactions of the American Society of Mechanical Engineers*, 54:53–57.

Wadee, M. A., Gardner, L., and Osofero, A. I. (2013). Design of prestressed stayed columns. *Journal of Constructional Steel Research*, 80:287–298.

Wang, H. and Zhang, Y. (2009). Experimental and numerical investigation on cold-formed steel C-section flexural members. *Journal of Constructional Steel Research*, 65(5):1225–1235.

Wang, J., Afshan, S., and Gardner, L. (2017). Axial behaviour of prestressed high strength steel tubular members. *Journal of Constructional Steel Research*, 133:547–563.

Williams, L. W. (2016). Introduction to recent trends in cold-formed steel construction. In Yu, C., editor, *Recent trends in cold-formed steel construction,* Chapter 1. Woodhead Publishing.

Willis, C. T. and Wallace, B. (1990). Behavior of cold-formed steel purlins under gravity loading. *Journal of Structural Engineering, ASCE*, 116(8):2061–2069.

Winter, G. (1947). Strength of thin steel compression flanges. *Transactions of the American Society of Civil Engineers*, 112(1):527–554.

Ye, J., Becque, J., Hajirasouliha, I., Mojtabaei, S. M., and Lim, J. B. P. (2018). Development of optimum cold-formed steel sections for maximum energy dissipation in uniaxial bending. *Engineering Structures*, 161:55–67.

Ye, J., Hajirasouliha, I., Becque, J., and Eslami, A. (2016a). Optimum design of cold-formed steel beams using Particle Swarm Optimisation method. *Journal of Constructional Steel Research*, 122:80–93.

Ye, J., Hajirasouliha, I., Becque, J., and Pilakoutas, K. (2016b). Development of more efficient cold-formed steel channel sections in bending. *Thin-Walled Structures*, 101:1–13.

Young, B. and Yan, J. (2004). Numerical investigation of channel columns with complex stiffeners - part II: parametric study and design. *Thin-Walled Structures*, 42(6):895–909.

Yu, C., editor (2016). *Recent trends in cold-formed steel construction*. Woodhead Publishing, first edition.

Yu, C. and Schafer, B. W. (2003). Local buckling tests on cold-formed steel beams. *Journal of Structural Engineering, ASCE*, 129(12):1596–1606.

Yu, C. and Schafer, B. W. (2005). Distortional buckling of cold-formed steel members in bending. *AISI Committee on Specifications for the Design of Cold-Formed Steel Structural Members*, RP05-1, 77.

Yu, C. and Schafer, B. W. (2006). Distortional buckling tests on cold-formed steel beams. *Journal of Structural Engineering, ASCE*, 132(4):515–528.

Yu, C. and Schafer, B. W. (2007). Simulation of cold-formed steel beams in local and distortional buckling with applications to the direct strength method. *Journal of Constructional Steel Research*, 63(5):581–590.

Yu, J. and Wadee, M. A. (2017). Mode interaction in triple-bay prestressed stayed columns. *International Journal of Non-Linear Mechanics*, 88:47–66.

Yu, W. W. and LaBoube, R. A. (2010). *Cold-formed steel design*. John Wiley & Sons, Inc., fourth edition.

Yun, X. and Gardner, L. (2017). Stress–strain curves for hot-rolled steels. *Journal of Constructional Steel Research*, 133:36–46.

Zeinoddini, V. M. and Schafer, B. W. (2012). Simulation of geometric imperfections in cold-formed steel members using spectral representation approach. *Thin-Walled Structures*, 60:105–117.

Appendix A

Key properties and results for parametric studies

In the present appendix, the key properties and FE results of the bare steel and prestressed models corresponding to the parametric studies investigating the effect of the section slenderness (*i.e.* Section 5.3.4) and centroid location (*i.e.* Section 5.3.5) are presented. Tables A.1 and A.2 correspond to Profiles 1–3 and 4–6 respectively. The moment–deflection responses are presented in Figures B.1–B.3 in Appendix B. In all models, $P_\mathrm{i}/P_\mathrm{max}$ and $A_\mathrm{c}/A_\mathrm{s}$ are equal to 1.0 and 10.5% respectively, while $\sigma_\mathrm{ult,p}$ is the normalised axial stress in the cable at the ultimate point.

Table A.1: FE results for the prestressed and bare steel beams with the cross-sectional geometries corresponding to Profiles 1–3, as defined in Table 5.3, and the nine section thicknesses listed in Table 5.4.

Profile	Geometry			Section properties			Prestressing	FE results		
	t (mm)	e (mm)	r_c (mm)	λ_d	A_s (mm^2)	M_y (kNm)	P_{max} (kN)	M_{ult} (kNm)	$M_{ult,p}$ (kNm)	$\sigma_{ult,p}/F_{y,c}$
1	1.00	126	3.95	1.42	466	16.5	51	9.5	10.2	0.63
	1.25	126	4.40	1.26	580	20.5	68	13.5	14.4	0.68
	1.50	126	4.81	1.14	693	24.4	86	17.9	19.2	0.73
	1.75	126	5.19	1.05	804	28.3	104	20.9	22.7	0.75
	2.00	126	5.53	0.97	915	32.1	123	25.2	27.7	0.79
	2.25	126	5.85	0.91	1025	35.8	142	29.7	33.1	0.82
	2.50	126	6.16	0.86	1134	39.5	161	34.3	38.5	0.84
	2.75	126	6.44	0.81	1241	43.1	179	36.5	41.3	0.85
	3.00	126	6.71	0.77	1348	46.6	198	40.8	46.5	0.87
2	1.00	130	3.94	1.41	465	16.2	49	9.4	10.0	0.61
	1.25	130	4.40	1.25	578	20.2	66	13.6	14.5	0.67
	1.50	130	4.81	1.14	691	24.0	83	17.9	19.3	0.71
	1.75	130	5.18	1.05	802	27.8	101	20.9	23.0	0.75
	2.00	130	5.52	0.97	913	31.5	118	25.3	28.2	0.77
	2.25	130	5.85	0.91	1022	35.1	136	29.8	33.6	0.79
	2.50	130	6.15	0.86	1131	38.7	154	34.6	39.4	0.82
	2.75	130	6.43	0.81	1238	42.3	172	39.6	45.4	0.84
	3.00	130	6.70	0.77	1344	45.7	191	41.9	48.3	0.85
3	1.00	133	3.94	1.43	465	16.0	48	9.3	9.9	0.61
	1.25	133	4.40	1.26	579	19.8	64	13.7	14.9	0.66
	1.50	133	4.81	1.14	691	23.6	80	18.1	19.9	0.69
	1.75	133	5.18	1.05	803	27.3	97	22.7	25.3	0.73
	2.00	133	5.52	0.98	913	31.0	114	25.6	28.9	0.75
	2.25	133	5.85	0.92	1023	34.5	131	30.3	34.6	0.77
	2.50	133	6.15	0.86	1131	38.1	149	34.9	40.3	0.80
	2.75	133	6.43	0.82	1238	41.5	166	39.9	46.5	0.82
	3.00	133	6.70	0.78	1345	44.9	183	42.5	49.6	0.83

Table A.2: FE results for the prestressed and bare steel beams with the cross-sectional geometries corresponding to Profiles 4–6, as defined in Table 5.3, and the nine section thicknesses listed in Table 5.4.

Profile	Geometry			Section properties			Prestressing	FE results		
	t (mm)	e (mm)	r_c (mm)	λ_d	A_s (mm^2)	M_y (kNm)	P_max (kN)	M_ult (kNm)	$M_\mathrm{ult,p}$ (kNm)	$\sigma_\mathrm{ult,p}/F_\mathrm{y,c}$
4	1.00	136	3.95	1.50	466	15.8	46	9.2	9.8	0.58
	1.25	136	4.40	1.27	580	19.6	61	13.8	15.2	0.63
	1.50	137	4.81	1.16	693	23.4	77	18.2	20.2	0.68
	1.75	137	5.19	1.06	804	27.0	93	22.7	25.7	0.71
	2.00	137	5.53	0.99	915	30.6	109	25.8	29.6	0.73
	2.25	137	5.85	0.93	1025	34.2	126	30.4	35.2	0.75
	2.50	137	6.16	0.88	1134	37.7	143	35.3	41.2	0.78
	2.75	137	6.44	0.83	1241	41.1	159	40.2	47.3	0.79
	3.00	137	6.71	0.79	1348	44.5	176	45.1	53.5	0.81
5	1.00	140	3.94	1.55	465	15.5	42	9.1	9.9	0.54
	1.25	141	4.40	1.29	579	19.2	57	13.8	15.5	0.61
	1.50	141	4.81	1.17	691	22.8	72	18.3	20.7	0.65
	1.75	141	5.18	1.08	803	26.4	87	22.8	26.2	0.68
	2.00	141	5.52	1.00	913	29.9	102	27.4	31.9	0.70
	2.25	141	5.85	0.94	1023	33.4	118	30.5	35.7	0.72
	2.50	141	6.15	0.89	1131	36.8	133	35.3	41.6	0.74
	2.75	141	6.43	0.84	1238	40.1	149	39.9	47.7	0.76
	3.00	141	6.70	0.80	1345	43.4	165	44.8	54.0	0.78
6	1.00	144	3.94	1.62	465	15.1	39	8.9	9.8	0.51
	1.25	144	4.40	1.30	579	18.8	53	13.6	15.3	0.57
	1.50	144	4.81	1.18	691	22.3	67	18.3	21.1	0.61
	1.75	144	5.18	1.09	803	25.8	81	22.9	26.7	0.64
	2.00	144	5.52	1.02	913	29.3	95	27.4	32.4	0.67
	2.25	144	5.85	0.95	1023	32.6	110	30.2	35.9	0.68
	2.50	144	6.15	0.90	1131	36.0	125	34.9	41.9	0.71
	2.75	144	6.43	0.85	1238	39.2	140	39.7	48.0	0.73
	3.00	144	6.70	0.81	1345	42.4	154	44.4	54.1	0.74

Appendix B

Moment–deflection responses for parametric studies

In the present appendix, the moment–deflection responses of the bare steel and prestressed FE models corresponding to the parametric studies investigating the effect of the section slenderness (*i.e.* Section 5.3.4) and centroid location (*i.e.* Section 5.3.5) are presented. The key properties and results are listed in Tables A.1 and A.2 in Appendix A for Profiles 1–3 and 4–6 respectively. In all models, P_i/P_{max} and A_c/A_s are equal to 1.0 and 10.5% respectively.
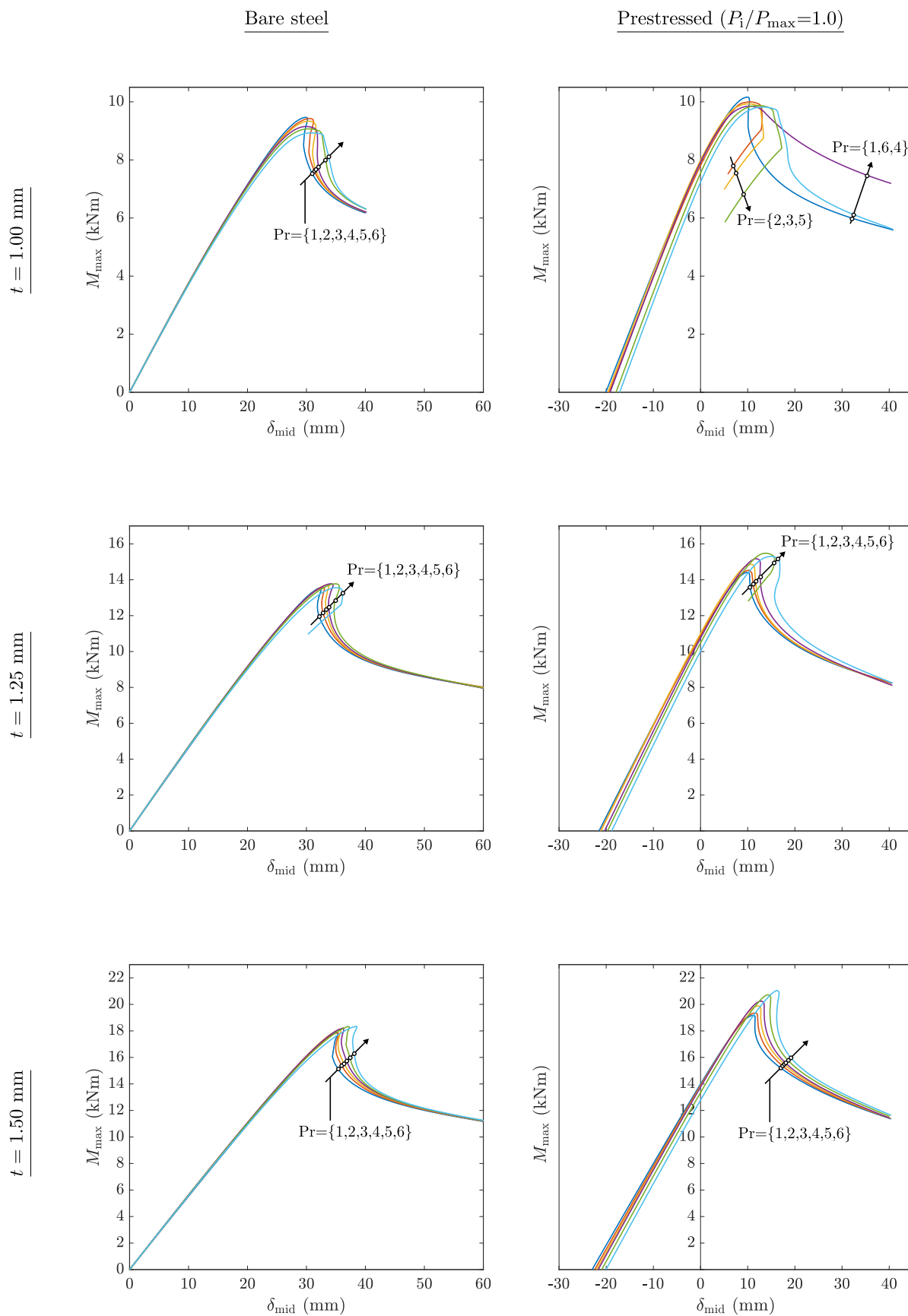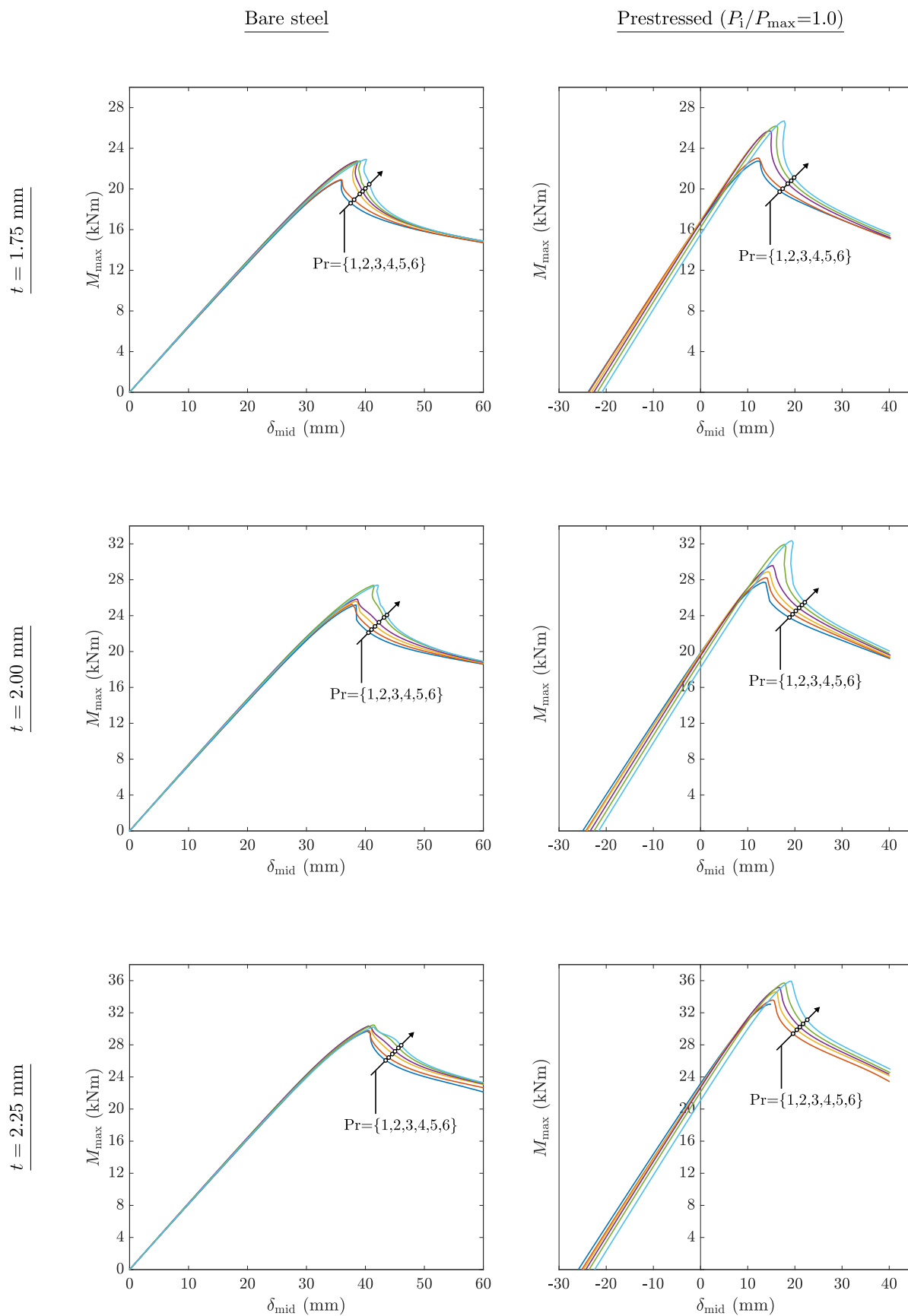
Figure B.1: Moment–deflection responses of the bare steel and fully prestressed FE models corresponding to the cross-section profiles Pr={1, 2, 3, 4, 5, 6} and the thicknesses t={1.00, 1.25, 1.50} mm.

Bare steel

Prestressed ($P_\mathrm{i}/P_\mathrm{max}$=1.0)

Figure B.2: Moment–deflection responses of the bare steel and fully prestressed FE models corresponding to the cross-section profiles Pr={1, 2, 3, 4, 5, 6} and the thicknesses t={1.75, 2.00, 2.25} mm.
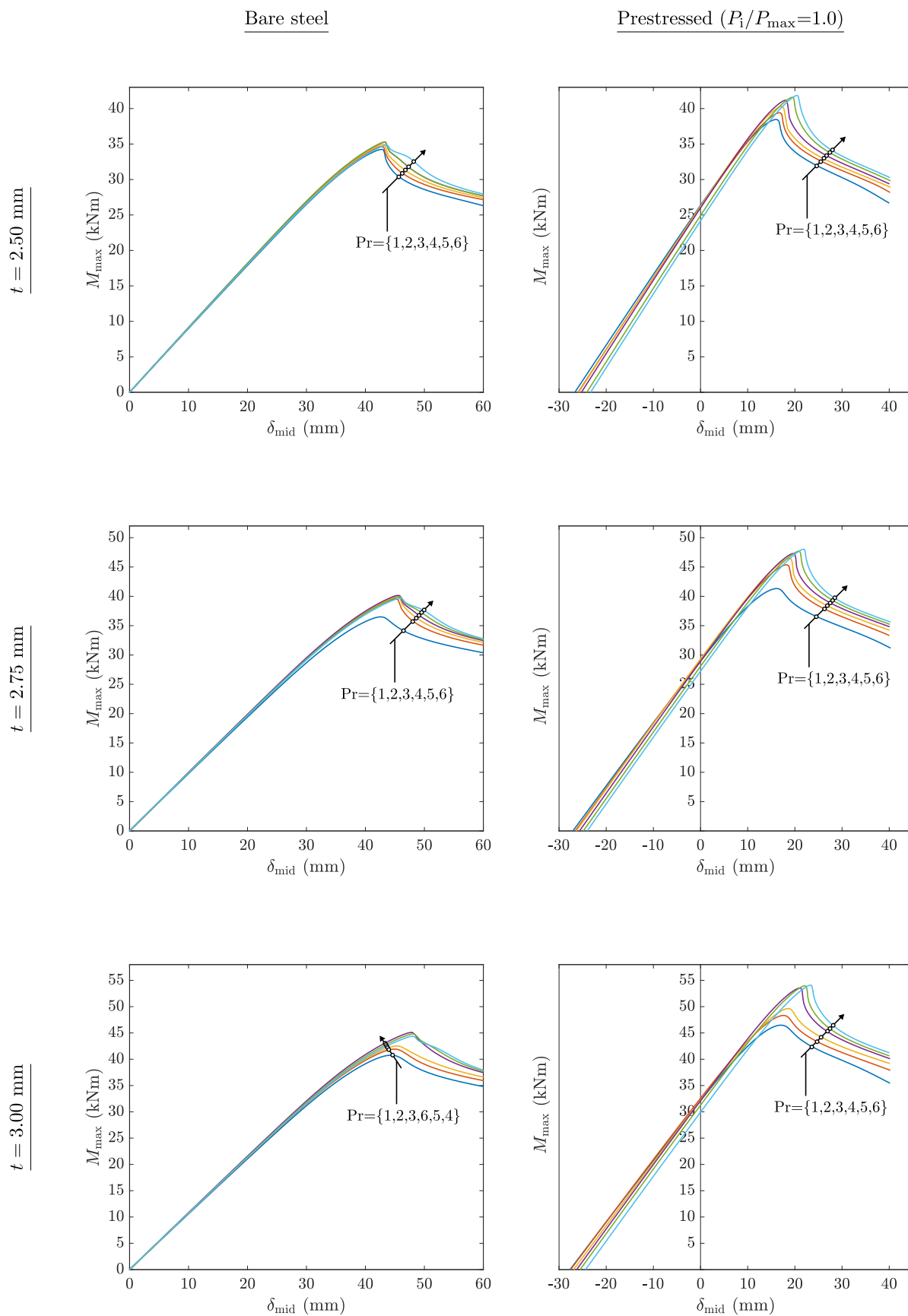
Figure B.3: Moment–deflection responses of the bare steel and fully prestressed FE models corresponding to the cross-section profiles Pr={1, 2, 3, 4, 5, 6} and the thicknesses t={2.50, 2.75, 3.00} mm.